2000

Structure-Function Studies on Human Epithelial Cystic Fibrosis Chloride Channels Expressed in Xenopus Laevis Oocytes

Laszlo Csanady

STRUCTURE-FUNCTION STUDIES ON HUMAN EPITHELIAL CYSTIC FIBROSIS CHLORIDE CHANNELS EXPRESSED IN *XENOPUS LAEVIS* OOCYTES

by

László Csanády

A thesis submitted in partial fulfillment of the

requirements for the degree of

Doctor of Philosophy

at

The Rockefeller University

April 2000

DEDICATION

To my wife Agatha for her love, understanding and patient support

ACKNOWLEDGEMENTS

I would like to thank most of all my advisor and mentor Dr. David C. Gadsby, for his patient and persistent guidance throughout this study, for sharing his knowledge along with his honest and steady commitment to an unbiased search for the truth; as well as for being a model of a humane, generous and tolerant leader.

I would like to thank Dr. Angus C. Nairn for closely following my progress and for sharing with us his expertise and his resources. I am also indebted to Drs. Roderick MacKinnon and Christopher Miller for giving their time and attention to read and criticize the Thesis, and help improve its quality.

I thank Dr. Bruce Knight for generously investing his time and expertise to reveal to me many of the beauties of applied mathematics; much of this work has benefited from our interaction over the years. I thank Drs. Olaf S. Andersen and Benoît Roux for their support in reviewing my first manuscript.

I thank Dr. Bruce McEwen for his tutoring during my first year, Dr. Alexander Tomasz for being a friend and support to me and my family, Dr. Steven K. Sullivan for helping me getting started with the *Xenopus* oocyte system, and Roberto Sánchez and Andrej Šali for lending their expertise in structural modeling.

I would like to acknowledge Peter Hoff for innumerable instances of patient technical support and help with the preparation of the oocytes, David C. Kopsco for cheerful technical assistance, and Kate Hall for careful management of all manuscripts.

I am also grateful to all members of the Gadsby laboratory: to Dr. Kim W. Chan for his professional advice in molecular biology and the joy of our friendship and fruitful scientific collaboration, to Donna Seto-Young for her persistent biochemical support, to Paola Vergani for help with some of the thesis figures, to Drs. Pablo Artigas, Claudia Basso, Cristina Cenciarelli, Lain F. Diaz, and Masayuki Sakaguchi for good-spirited team-work, for many exciting discussions, and for a brotherly atmosphere.

TABLE OF CONTENTS

LIST OF FIGURES

LIST OF TABLES

ABBREVIATIONS

a_{locked} ...fractional amplitude of slowly relaxing current component after AMPPNP removal

AMPPNP ..... 5'-adenylylimidodiphosphate

a_{sh}, a_l ....fractional amplitudes of short and long components of burst-duration distribution

ATP .....adenosine 5'-triphosphate

CDTA..... trans-1,2-diaminocyclohexane-N,N,N',N'-tetraacetic acid

CFTR .....Cystic Fibrosis Transmembrane conductance Regulator

CTP .....cytidine-5'-triphosphate

EGTA..... ethylene glycol-bis(β-aminoethyl ether) N,N,N',N'-tetraacetic acid

GTP ..... guanosine-5'-triphosphate

HEPES ..... N-[2-hydroxyethyl]piperazine-N'-[2-ethanesulphonate]

NBD .....nucleotide binding domain

NMG .....N-methyl-D-glucamine

PKA.....cyclic AMP-dependent protein kinase

R domain.....regulatory domain

P_o ..... open probability

PP_i .....pyrophosphate

τ_{AMPPNP} ..... time constant of slowly relaxing current component after AMPPNP removal

τ_b .....mean burst duration

τ_{ib}..... mean interburst duration

τ_{sh}, τ_l.....time constants of short and long components of burst-duration distribution

UTP ..... uridine-5'-triphosphate

STRUCTURE-FUNCTION STUDIES ON HUMAN EPITHELIAL CYSTIC FIBROSIS CHLORIDE CHANNELS EXPRESSED IN *XENOPUS LAEVIS* OOCYTES

László Csanády

Submitted on April 1st, 2000, in partial fulfillment of the requirements for the degree of Doctor of Philosophy

ABSTRACT

The cystic fibrosis transmembrane conductance regulator (CFTR) Cl^- channel is an ATP-binding cassette protein, comprising two transmembrane domains, two nucleotide binding domains (NBD1, NBD2) and a regulatory (R) domain. Channel gating is controlled by R-domain phosphorylation and by ATP binding and/or hydroysis at the NBDs. Exon 13 of the CFTR gene encodes residues 590 to 830, originally ascribed to the R domain. Here, CFTR channels were severed near likely N- or C-terminal boundaries of NBD1 or the R domain. Channel activity, assayed via two-microelectrode voltage clamp monitored successful assembly of pairs of channel segments as the sever point was systematically shifted along the primary sequence. Substantial activity indicated successful assembly; such constructs were further studied in excised patches, by correlating macroscopic and single-channel kinetics.

The C-terminus of NBD1 was found to extend beyond residues 590 and lies between residues 622 and 634, while the N-terminus of NBD1 lies between residues 432 and 449. In excised patches, channels severed just before (between a.a.s 432 and 433) or after NBD1 (between residues 633 and 634) displayed the usual hallmark characteristics of wild-type (WT) CFTR: requirement of phosphorylation by protein kinase A (PKA) and

exposure to ATP for gating, ability to be locked open by pyrophosphate or AMPPNP, small single-channel conductances, and high apparent affinity of channel opening by ATP; although bursts of 1-633 plus 634-1480 channels were ~40% shorter than in WT.

Channels severed near the R domain's C-terminus, 1-835 plus 837-1480, displayed low, PKA-independent, activity, enhanced apparent affinity for ATP, and destabilized binding site for the locking action of AMPPNP. R-domain-less split channels 1-633 plus 837-1480 were functionally similar to 1-835 plus 837-1480, including enhanced apparent ATP affinity and less tight binding of AMPPNP, but were more active before phosphorylation. Intriguingly, 1-633 plus 837-1480 channels, lacking the R domain, were still stimulated by PKA; and AMPPNP or pyrophosphate still prolonged bursts.

The kinetic analysis exploited a new method that rapidly extracts single-channel transition rate constants from multichannel patch-clamp recordings, using a simultaneous maximum-likelihood fit to the dwell-time distributions for all conductance levels (after successfully testing it on simulated current traces).

1. INTRODUCTION

1.1. Cystic Fibrosis (CF) and the Cystic Fibrosis Transmembane Conductance Regulator (CFTR)

Cystic fibrosis (CF), one of the most frequent inherited diseases among the caucasian population, is a multi-symptom disorder, which originates from a dysfunction of secretory epithelia. A deficiency in salt transport as a primary cause of CF was first suggested in 1983, based on the finding that CF epithelia were relatively impermeable to chloride (Quinton, 1983). In 1989 the CFTR gene was identified, by positional cloning (Riordan et al., 1989), as the single gene mutated in CF patients. Although its direct function was initially unclear, its predicted topology, from hydropathy analysis, identified it as a twelve-transmembrane protein. Since its cloning, extensive studies have shown that CFTR functions as a regulated chloride channel in the apical plasma membrane of secretory epithelia, and hundreds of mutations have been identified among its 1480 residues. Mutations have been categorized over the years, based on their effects on the CFTR protein, as: a) truncation mutations that result in premature termination of protein translation (e.g. G542X, Ng. et al., 1991), b) processing mutants that fail to fold properly and do not pass the quality control in the endoplasmic reticulum (e.g. ΔF508, Cheng et al., 1990), c) targeting mutants that are properly folded but not shuttled to the apical membrane (e.g. S1455X, Moyer et al., 1999), d) conduction mutants with decreased channel conductance from altered pore structure (e.g. R347P, cf. Tabcharani et al., 1993), e) gating mutants that pass chloride ions normally once they are open, but spend very little time in the open state (G551D, Yang et al., 1993), and, f) stability mutants that

are made properly by the cells and seem functionally intact, but have severalfold decreased lifetimes at the plasma membrane (Q1412X, Haardt et al., 1999). Although it is clear that a functional CFTR targeted to its proper location (apical membrane) is required for normal homeostasis of various secreting epithelia, the physiological role of CFTR in maintaining this homeostasis, as well as the pathophysiology of CF, a consequence of lack of normal CFTR function, is still debated (Guggino, 1999).

1.2. CFTR as a Cl- channel

Initially named "regulator", CFTR was suspected early on to be itself a chloride channel. Expression of the CFTR gene in a variety of heterologous expression systems (e.g. chinese hamster ovary (CHO) cells, Tabcharani et al., 1991; HeLa cells, NIH 3T3 fibroblasts, Anderson et al., 1991; Xenopus oocytes, Bear et al., 1991; Sf9 insect cells, Kartner et al., 1991) gave rise to chloride conductances, that could be activated by stimulating the protein kinase A (PKA) pathway, did not show time- or voltage dependence and exhibited similar anion selectivities. In single-channel experiments these channels were characterized by an ohmic ~10 pS conductance, linear single-channel current-voltage relationship in symmetrical high-[Cl^-] solutions, an absolute requirement of phosphorylation by PKA and of the presence of hydrolyzable nucleoside triphosphate for channel gating. Final proof that CFTR itself was the protein forming these channels came from experiments in which CFTR, purified to homogeneity, was reconstituted into a lipid bilayer to form regulated chloride channels closely similar to the ones described above (Bear et al., 1992).

1.3. CFTR as a regulator

Although few other ion channels bear a name as complicated as CFTR, recent demonstrations that CFTR may indeed influence the activity of other channels has validated its initial assignment as Regulator. The most convincing evidence for such a putative role is the demonstration, in excised patches, of altered gating of the epithelial sodium channel (ENaC), when co-expressed with CFTR (Stutts et al., 1995; Stutts et al., 1997).

Outwardly rectifying Cl^- channels (ORCCs, another subclass of Cl^- channels present in epithelia) are activated when the PKA pathway is triggered, but this activation only occurs in cells that co-express wild type (WT) CFTR; co-expression of the non-functional CFTR mutant G551D is insufficient to support ORCC activation in the same cells (Schwiebert et al., 1995). The stimulation of the ORCC channels, probably via activation of purinergic receptors, seems dependent on nanomolar concentrations of extracellular ATP, released by the cells upon PKA activation, since extracellular apyrase, or hexokinase in conjunction with glucose, both of which degrade ATP, abolishes activation of ORCCs by PKA (Schwiebert et al., 1995). The role of CFTR in this complicated process is still unclear. The suggestion that CFTR itself may be the means by which the cells release ATP is widely debated. Reports in the literature, using different cell types, include suggestions that CFTR itself is an ATP-channel with a common pore for conducting Cl^- and ATP^- (Schwiebert et al., 1995), demonstration of no ATP-flux supported by CFTR (Grygorczyk et al., 1996), or, recently, association of an ATP channel with CFTR, giving two distinct pores but a common gate (Sugita et al., 1998).

While the mechanism of such a variety of actions attributed to the same CFTR molecule is still very much controversial, advances in our understanding of how such interactions might take place came from recent biochemical identification of a growing number of proteins that interact with CFTR, to form what seems to be a huge, multiprotein complex at the apical membrane, composed of channels, anchoring proteins for cellular kinases, and signalling molecules, organized for efficient teamwork. Although CFTR's N-terminus has also been implicated in binding another membrane protein, syntaxin 1A (Naren et al., 1998), the organizing business end of the CFTR molecule seems to be its C-terminus, in particular the last four amino acids, forming a DTRL motif, compatible with binding to PDZ-domain containing proteins. One such protein, EBP50 (ERM binding phosphoprotein 50), has been identified in the apical membrane of epithelial cells, and found to colocalize with, and to coimmunoprecipitate, CFTR (Short et al., 1998). Since EBP50 contains two PDZ domains, one of which binds CFTR with nanomolar affinity, the other PDZ domain could serve to anchor some other membrane protein in the vicinity of CFTR. Furthermore, the C-terminus of EBP50 binds ezrin, and ezrin binds actin, providing a possible link to the cytoskeleton. Ezrin is also an AKAP (A-kinase anchoring protein), serving as a targeting protein for the type II regulatory subunit of PKA (Sun et al., 1999). Accordingly, CFTR could be successfully activated in excised patches by applying a cAMP analog to the cytosolic surface, indicating that PKA remained associated with the membrane after patch excision (Huang et al., 1998). Other players implicated in this submembrane compartment are the β_2-adrenergic receptor (Hall et al., 1998), the Na^+-H^+ exchanger (Yun et al., 1997), protein phosphatase 2C (PP2C, Zhu et al., 1999), AMP-activated protein kinase (Hallows et al.,

1999), and Munc 18 (Naren et al., 1998). Understanding this increasingly complex network of proteins will be an exciting challenge for the next years of CFTR research.

1.4. CFTR structure

In the continuing absence of a high resolution structure of CFTR, little is known about its three-dimensional fold. Sequence alignment immediately identified it as a member of the large family of ATP-binding cassette (ABC) transporters (Riordan et al., 1989; cf. Higgins, 1992). This family, prominent members of which are P-glycoprotein (PgP) and the sulfonylurea receptor (SUR), is characterized by an overall topology comprising two transmembrane domains, and two cytoplasmic nucleotide binding domains (NBDs). The topology of CFTR (Figure 1), as suggested by Riordan et al. (1989), contains two six-transmembrane domains (TMD1, *dark blue*, TMD2, *cyan*, Figure 1) each followed by an intracellular NBD (NBD1, *red*, NBD2, *yellow*, Figure 1); and the two halves are linked by a single domain, termed "regulatory" based on its large number of consensus phosphorylation sites for PKA (R domain, *green*, Figure 1). This overall topology has since been confirmed by a variety of means, including engineering of artificial glycosylation sites throughout the protein sequence (Chang et al., 1994).

The NBDs, a part of the fingerprint of all ABC transporters, contain three highly conserved motifs. The Walker A motif (GXXXXGKS/T) forms the so-called P-loop, a structure found in virtually all ATPases (Walker et al., 1982) and GTPases, involved in accomodating the β and γ phosphate of the bound nucleotide in all of these molecules. The conserved aspartate residue of the Walker B motif (LYLLD in CFTR) has long been implicated in coordinating the Mg^{2+} ion necessary for ATP hydrolysis. The third motif is

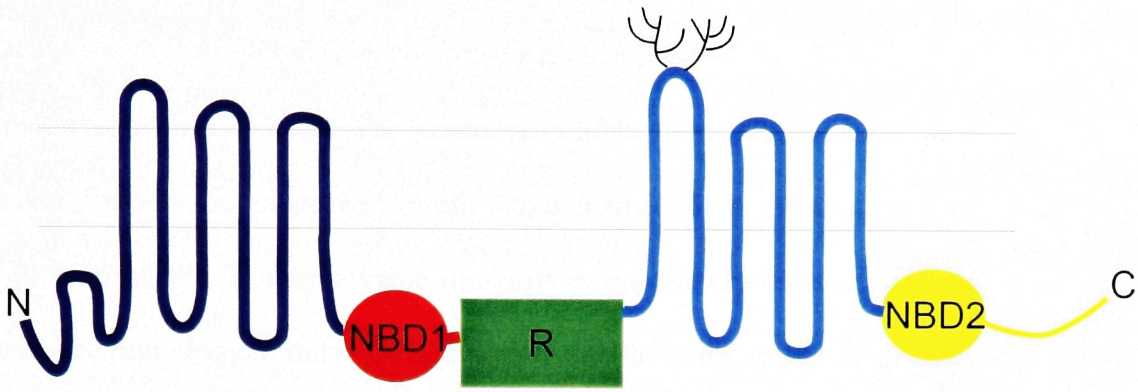

Figure 1. Topology of wild-type CFTR. Membrane domains, each comprising 6 transmembrane α-helixes, are colored *dark blue* (TMD1) and *cyan* (TMD2), NBD1 (*red*), R domain (*green*), and NBD2 (*yellow*) are indicated. Asparagines 894 and 900 in the fourth extracellular loop are the sites of in vivo glycosylation. (*Top*, extracellular face, *bottom*, intracellular face of plasma membrane.)

the so-called C-motif (LSGGQ), also highly conserved among ABC transporters, the function of which has been, and remains, debated. Recently, the crystal structures of the NBDs of two bacterial ABC transporters were solved: the N-terminal NBD in RbsA, part of the ribose transporter from *E. coli* (Armstrong et al., 1998), and the NBD of histidine permease, HisP (from *S. typhimurium*, Hung et al., 1998). These structures, identical to each other in their global fold, comprise a broken β barrel surrounding a central helix upon which the ATP binds. The structures confirm the suggested functions of the Walker A and B motifs, but place the C-motif into a distinct helical domain, far away from the ATP binding site. The remarkable similarity of the two crystal structures, despite a low sequence homology of only ~20%, suggests that these structures are good models for the NBDs of all ABC transporters, including CFTR. However, it is still unclear how the NBDs can tightly interact with each other, as suggested by function, and with other parts of the protein. The possibility exists that the crystal structures contain only incomplete binding sites, since the ATP lies in a shallow groove in both structures, and very few contacts between the nucleotide and the protein could be identified.

The R domain contains 9 serines located in classical consensus sequences (R/KR/KXS) for being good substrates for PKA. In addition to these "dibasic" sites, there are several more "monobasic" ones (R/KXS), also potential substrates of PKA. At least 8 of these sites have been shown to be phosphorylated in vivo or in vitro (Cheng et al., 1991; Picciotto et al., 1992; Townsend et al., 1996). Protein kinase C (PKC) phosphorylation of the R domain has also been demonstrated (Piciotto et al.). The only structural data on the R domain is CD spectral analysis of an R-domain peptide (Dulhanty

and Riordan, 1994), which suggested that conformational changes occur upon phosphorylation.

Identification of the CFTR channel pore so far has not been as successful as in the families of cation channels. Part of the difficulty is that all known homologs of CFTR are transporters, not ion channels. Also, the lyotropic anion selectivity of Cl^- channels appears to be a more distributed feature of the pore (reviewed in Dawson et al., 1999), in contrast to the highly localized selectivity filter of K^+ channels (Doyle et al., 1998), which therefore provided a consensus fingerprint of the pore, long before a crystal structure was obtained (Heginbotham et al., 1992; reviewed e.g., in MacKinnon, 1995). In CFTR, transmembrane helices TM1, 5, 6, and 12 have been implicated in contributing pore-lining residues, based on changes in conductance, anion-selectivity sequence, or pore blockage properties upon mutating individual residues (e.g. Anderson et al., 1991c; McDonough et al., 1994; Tabcharani et al., 1997; Mansoura et al., 1998). The most extensive studies were done on TM6, in which all residues were individually mutated to cysteines, and solvent accessibility was probed with thiol reagents (Cheung and Akabas, 1996). The results were consistent with an overall alpha-helical arrangement, with accessible residues following each other in frameshifts of ~3. More studies will be needed to definitively identify the chloride conducting pathway of CFTR.

As obvious a question as it seems, the stoichiometry of CFTR molecules within one channel is still not agreed on, to date. It has been widely accepted for a long time that CFTR monomers form chloride channels individually. This was based on a failure to co-immunoprecipitate two biochemically distinct forms of CFTR with each other, following co-expression and membrane solubilization with either ionic or non-ionic detergents

(Marshall et al., 1994). Recently, tandem constructs of two CFTR molecules, reconstituted in a lipid bilayer, were found to give rise to single unitary chloride conductances, and mixed-property single channels were formed from tandem constructs of WT and mutant CFTR, raising the possibility that CFTR may dimerize to form one channel (Zerhusen et al., 1999). Estimation of particle sizes in freeze-fracture micrographs were also consistent with 24 transmembrane helices forming a "CFTR particle" (Eskandari et al., 1998), although the close homolog PgP was predicted to be monomeric by cryoelectron microscopy (Rosenberg et al., 1997). A dimeric structure would necessitate reinterpretation of many of the functional data, since such a channel would contain two R domain- and four NBD-sequences, which may combine in any of several possible ways to form what is functionally observed as an ATP binding site, or a regularory particle.

1.5. Overview

Methods used for expressing wild type (WT) and mutant human epithelial CFTR channels in *Xenopus* oocytes, for recording currents from whole oocytes and from patches of excised membrane, and for analysis of the records are presented first. An algorithm specifically developed to allow kinetic analysis of records containing several channels, together with the results of extensive tests performed on simulated data (Csanády, 2000), is discussed in detail in a separate chapter, since it provided the basis for the kinetic analysis of CFTR channels presented in later sections. Chapter 4 provides a general functional characterization of WT human epithelial CFTR channels expressed in *Xenopus* oocytes, and also introduces the functional assays used in later chapters for

comparing structurally altered channels to WT. A subsequent chapter is dedicated to the evaluation of possible gating models with respect to their ability to explain both the experimental findings of the previous section, and some additional data taken from the literature. Only models compatible with most experimental results, based on qualitative arguments, are discussed further, more quantitatively, in the last chapter. The last two chapters describe and discuss two extensive series of experiments, aimed at characterizing CFTR molecules effectively severed in their protein backbone by co-expression of complementary channel segments. More specifically, using this approach, functional boundaries of CFTR's N-terminal NBD (NBD1) are defined in the first of those two chapters, while the role of the R domain in channel regulation is addressed in the last chapter.

2. METHODS

2.1. Molecular biology

pGEMHE-WT was constructed by subcloning a CFTR cDNA fragment, excised from pBQ4.7 (a gift from Dr. Johanna Rommens), into the *Sma*I and *Xho*I (BioLabs Inc.) sites of pGEMHE (Liman et al., 1992). A Flag epitope (M-DYKDDDDK) followed by a leucine was added to the N-terminus of a CFTR fragment containing amino acids 3 to 835 by running two consecutive PCR reactions using a GeneAmp PCR system 2400 (Perkin Elmer). In the first PCR reaction, FlagFW1 (5'-TACAAAGACGACGACGACAAGCTTAGGTCGCCTCTGGAAAAGGC) and 835RV (5'-CCG*CTCGAG*CTAATCAAAAAAGCACTCCTTTAAGTC) were used with pGEMHE-WT as template. In the second PCR reaction, FlagFW2 (5'-TCC*CCCGGG*CCG CCATGGATTACAAAGACG ACGACGACAAG) and 835RV were used with the purified PCR product, obtained from the first reaction, as template. The PCR product from the second reaction was subcloned into the S*ma*I and *Xho*I sites of pGEMHE to make pGEMHE-Flag3-835. pGEMHE-Flag3-589 was made by PCR using T7 FW primer (5'-TAATACGACTCACTATAGGGCGAATT) and a specific reverse oligonucleotide primer 589RV (5'-CCG*CTCGAG*CTAGCTTTCAAATATTTCTTTTTC) with pGEMHE-Flag3-835 as template, followed by subcloning into pGEMHE. pGEMHE-Flag3-611, pGEMHE-Flag3-622, pGEMHE-Flag3-633, pGEMHE-Flag3-432 and pGEMHE-Flag3-414 were similarly constructed using T7 FW and the corresponding specific reverse primers. pGEMHE-590-1480 was made by PCR using 590FW (5'-TCC*CCCGGG*CCGCCATGTGTGTCTGTAAACTGATGGCTAACAAAA) and SP6 RV

(5'-CGCCAAGCTATTTAGGTGACACTATAG) with pGEMHE-WT as template followed by subcloning. pGEMHE-449-1480, pGEMHE-433-1480, pGEMHE-634-1480, pGEMHE-668-1480, and pGEMHE-837-1480 were similarly constructed using specific forward primers. pGEMHE-FlagWT was constructed by subcloning a *Bsp*EI/*Xho*I fragment from pGEMHE-WT, which encodes part of TM6 and all the domains which follow, into *Bsp*EI and *Xho*I sites of pGEMHE-Flag3-835. pGEMHE-1-432, pGEMHE-1-633, and pGEMHE-1-835 were constructed by PCR reactions using forward primer T7 FW, specific reverse primers, and pGEMHE-WT as template. CFTR-K1250A was a gift of Dr. David Dawson, and was subcloned into pGEMHE to give pGEMHE-K1250A. pGEMHE-837-1480(K1250A) was made using pGEMHE-K1250A as template, primers SK837FW (5'-TCC*CCCGGG*CCGCCATGGAGAGCATACCAGCAGTGACT) and SP6 RV, followed by subcloning. All PCR reactions used Pfu polymerase (Stratagene) and a low number (15-20) of PCR cycles, and all constructs were confirmed by automated sequencing. Plasmid DNAs were linearized with *Nhe*I, and cRNAs were produced by in vitro transcription using a T7 mMessage mMachine kit (Ambion) and then run on denaturing gels to check size and quality. RNA concentration was estimated by comparison with a known amount of 0.24-9.5 kb RNA ladder (GIBCO).

2.2. Isolation and injection of Xenopus oocytes

Stage V-VI oocytes were isolated from adult female *Xenopus laevis* (Nasco, WI) by partial ovariectomy under Tricaine (1% solution) anaesthesia and were defolliculated by treatment, at room temperature (21-23°C) for up to 2 hr, with ~2 mg/ml collagenase (Worthington Type II or GIBCO Type I) in Ca^{2+}-free oocyte Ringer's solution (82.5 mM

NaCl, 2 mM KCl, 1 mM $MgCl_2$, 5 mM HEPES, pH 7.5). Defolliculated oocytes were rinsed extensively with Ca^{2+}-free Ringer's (3-5 washes, 50 ml each), and then incubated at 18°C for several hours in Ringer's with 1.8 mM Ca^{2+} and 50 μg/ml gentamycin (GIBCO) before they were pressure-injected (nanojet, Drummond) with cRNAs. Injection pipettes were pulled (Narishige, PP83) from glass capillaries (# 3-000-203-G/X, Drummond) and their tips were broken to an internal diameter of 10-20 μm. Usually, and unless otherwise specified, 2.5 ng of each cRNA, premixed if for co-expression, in a constant total volume of 50 nl, were injected per oocyte. Injected oocytes were further incubated at 18°C for 2-3 days before they were used for recording or for preparation of membranes.

2.3. Preparation of oocyte membranes

Oocytes injected with cRNA were incubated for 48 hr, then frozen in liquid nitrogen and stored at -80°C. Aliquots of ~150 frozen oocytes were homogenized at 4°C with 1 ml lysis buffer, containing 10 mM HEPES (pH 7.5 with NaOH), 6 mM EDTA, 50 mM NaCl, 1 mg/ml BSA, 1 mM PMSF, and protease inhibitor cocktail (Calbiochem; final concentrations were 1 mM AEBSF HCl, 300 nM aprotinin, 2 μM E-64, 2 μM leupeptin hemisulfate), and the suspensions centrifuged at 3000 *g* for 10 min. Supernatants were kept and centrifuged again at 3000 *g* for 10 min. 2 ml of lysis buffer was added to the resulting supernatants before centrifugation at 173,600 *g* for 1 hr. The pellets were washed with 3 ml modified lysis buffer (with 10% glycerol instead of BSA, and only 0.5 mM PMSF), the centrifugation repeated, and the pelleted membranes resuspended in 0.2 ml modified lysis buffer and stored at -80°C.

2.4. Western blotting and co-immunoprecipitation

Membrane proteins (75 μg total membrane protein per lane) were resolved by 7.5% SDS-PAGE and blotted onto nitrocellulose membranes using a semi-dry transfer cell (Bio-Rad). Protein bands containing the R domain were detected with anti-R-domain Ab (Picciotto et al, 1992) and HP-conjugated goat anti-rabbit IgG as the secondary Ab. N-terminal fragments were detected either using anti-Flag M2 monoclonal Ab (Sigma) with HP-conjugated goat anti-mouse IgG as the secondary Ab or, in co-immunoprecitation experiments, using an anti-N-terminal Ab (A_2; kindly provided by Dr. W. Skach) with HP-conjugated goat anti-rabbit IgG as secondary Ab. Protein bands were visualized with the ECL Western blotting kit (Pharmacia).

Co-immunoprecipitation was by a procedure modified from that of Ostedgaard et al. (1997). 450 μg of each total membrane protein sample were solubilized for 1 hr in 1 ml solubilization buffer (1.25% digitonin, 150 mM NaCl, 50 mM Tris/HCl, pH 7.5) and the suspensions centrifuged at 173,600 *g* for 1 hr. Each supernatant of soluble proteins was mixed with 200 μl of anti-Flag M2 affinity gel (Sigma), pre-washed with solubilization buffer, and the mixtures rocked overnight and then centrifuged at 26,000 *g* for 5 min. The pellets, containing anti-Flag M2 affinity gel with bound proteins, were washed 3 times with solubilization buffer, 3 times with high-salt buffer (500 mM NaCl, 50 mM Tris/HCl, pH 7.5), and then twice with 50 mM Tris (pH 7.5). The co-immunoprecipitated proteins were eluted with 150 μl Laemmli buffer.

2.5. Deglycosylation and protein determination

Oocyte membrane protein samples (75 μg) were treated with N-glycosidase-F and endoglycosidase-H for 1 hr at 37°C following the supplier's protocol (Boehringer Mannheim). Protein concentrations were measured with bicinchonic acid (Pierce).

2.6. Two-microelectrode voltage clamp recordings

For two-microelectrode voltage-clamp measurements, oocytes in a plexiglass recording chamber (volume ~150 μl) were continuously superfused (~2 ml/min) at ~22°C with gravity-fed solutions selected by manual valves (Hamilton). The dead volume was ~100 μl, and solutions were completely exchanged in <8 s. The standard bath solution was Ca^{2+}-free Ringer's solution. The chamber was connected to virtual ground circuitry through Ag/AgCl electrodes in 2.5% agar/3M-KCl bridges. Currents were measured by a voltage-clamp amplifier (OC-725A Oocyte clamp, Warner Instrument Corp.), filtered at 50 Hz by an 8-pole Bessel filter (Frequency Devices), digitized on-line at 100 Hz using a Digidata 1200 board (Axon Instruments) with pCLAMP 6.0.2 software (Axon), and stored on disk. Microelectrodes, pulled from glass capillaries (Drummond, cat # 3-000-210-G), were filled with 3M KCl and had resistances of 0.5-2 MΩ. Voltage steps were applied via the amplifier's toggle switch (duration 0.5-1 s) or using pCLAMP software. Steady-state currents were averaged over 200 ms near the ends of 1-s voltage steps, and plotted against voltage. Conductance was calculated from linear fits to the steady currents between -60 and -20 mV. Average values were from at least 5 oocytes. CFTR current was activated by superfusion with Ringer's solution supplemented with 50 μM forskolin (Sigma) and 1 mM 3-isobutyl-1-methylxanthine (IBMX, Sigma).

2.7. Excised patch recording

For recording single-channel or macroscopic currents, excised inside-out patches were pulled from oocytes preinjected with 0.1-5 ng of cRNA for each segment. Oocytes were shrunk for ~2 min in standard bath solution (138 mM NMG, 2 mM Mg-sulfamate, 5 mM HEPES, 0.5 mM EGTA, 134 mM sulfamic acid, pH=7.1 with sulfamic acid) supplemented with 100 mM NaCl, the vitelline membranes removed manually, and the cells transferred to a recording chamber containing standard bath solution. Patch pipettes were pulled from borosilicate glass (Drummond, cat.# N-51A) using a vertical pipette puller (Narishige, PP-83). Tips were fire-polished to a diameter of 1-2 μm (4-7 MΩ), or 5-6 μm (~1 MΩ), for single-channel or macropatch recordings, respectively. Pipette solution contained 138 mM NMG, 2 mM $MgCl_2$, 5 mM HEPES, 136 mM HCl (pH=7.4 with HCl). 100-300-GΩ seals were obtained by gentle suction. Patches were excised and transferred to a flow chamber, where the cytoplasmic surface was continuously superfused with standard bath solution containing various test substances. Switching between solutions was implemented by computer-driven electric valves (General Valve Corporation). With the dead volume of ~20 μl and flow rate of ~0.5 ml/min complete solution exchange took 2-4 s. The kinetics of solution exchange was characterized by a delay of ~1 s, followed by a transition period with a time constant of 200-600 ms; as verified at the end of each recording by applying a brief pulse of 2 mM Ca-sulfamate, and observing the rate of decay of endogenous Ca^{2+}-activated Cl^--channel current upon Ca^{2+} removal. The bath electrode (Ag/AgCl pellet in 100 mM KCl) was connected to the flow chamber by an agar bridge (4% agar in 100 mM KCl). Outward currents were recorded at

a pipette potential of -40 mV (V_m = +40 mV) via an Axopatch 200A amplifier (Axon Instruments), filtered at 100 Hz with an 8-pole Bessel filter (Frequency Devices), digitized on-line at 1 kHz using an ITC-16 board (Instrutech Corporation) and recorded on disk by PULSE software (Heka Elektronik). CFTR channels were activated by 300 nM catalytic subunit of protein kinase A (PKA) purified from bovine heart (Kaczmarek et al., 1980). MgATP (Sigma) was added from a 400 mM stock solution (pH=7.2 with NMG). At the end of each experiment channels were counted by locking them in the open state with 2 mM NMG-pyrophosphate (PP_i; Fluka) in the presence of 100 μM MgATP and 300 nM PKA, supplemented by 2 mM Mg-sulfamate. Li_4-AMPPNP (Sigma) was added from a 400 mM stock solution. Unless specified, recordings were done at ambient room temperature, which varied between 21-26°C, and was recorded on each experimental day. In particular, temperature was 21-23°C for the experiments described in Chapter 6 (NBD1 structure and function). The studies in Chapter 7 (R-domain function) were done either at ~24°C (studies on locking by AMPPNP and on apparent affinities for ATP), or between 21-26°C (steady state recordings used for kinetic analysis).

2.8. Analysis of single-channel and multichannel records

2.8.1. Baseline subtraction

Initial baseline value and single-channel current amplitude *i* were specified following visual inspection. Sections without channel openings were digitally filtered at 1 to 7 Hz, depending on the speed of the baseline drift, to create baseline currents for such

sections. Sections with k open channels were digitally filtered at 0.5 Hz to 3 Hz, followed by subtraction of k times the single-channel current amplitude, to extrapolate concomitant baseline currents. The number of open channels at the jth datapoint, $k(j)$, was obtained by comparison with $k(j\text{-}1)$. The obtained baseline current was then subtracted from the raw current trace. The result is equivalent to digital high-pass filtering (corner frequencies adjustable) by sections within two adjacent jumps, followed by reconstruction of the series of sections. In every case the extrapolated baseline trace was inspected visually to avoid artifacts. Although in most cases baseline current was stable, this algorithm allowed successful idealization of even multichannel patches with considerable baseline instability. Figure 2 illustrates such an example. The *top* trace shows a rather poor quality current record (seal resistance was only 7GΩ in this case, V_m=+20 mV), with considerable baseline drifts. The *green* trace is the extrapolated baseline (offset for better view), the *red* trace is the difference between the *black* and *green* traces, used for idealization; *blue* trace illustrates the idealized event sequence. *Black arrows* mark an artifact, introduced by insufficient baseline correction, but without effect on the idealized trace.

2.8.2. Idealization and fitting

Baseline-subtracted current traces were idealized using a simple half-amplitude threshold crossing criterion. Events lists from records with 1 to 7 channels were fitted with a simple model in which all principal gating transitions were pooled into a closed-open scheme, and flickery closures modeled as pore blockage events (Ishihara and Welsh, 1997), resulting in the three-state closed-open-blocked scheme (*C-O-B*). The best set of rate constants r_{CO}, r_{OC}, r_{OB}, and r_{BO} was extracted (cf. Csanády, 2000) from a

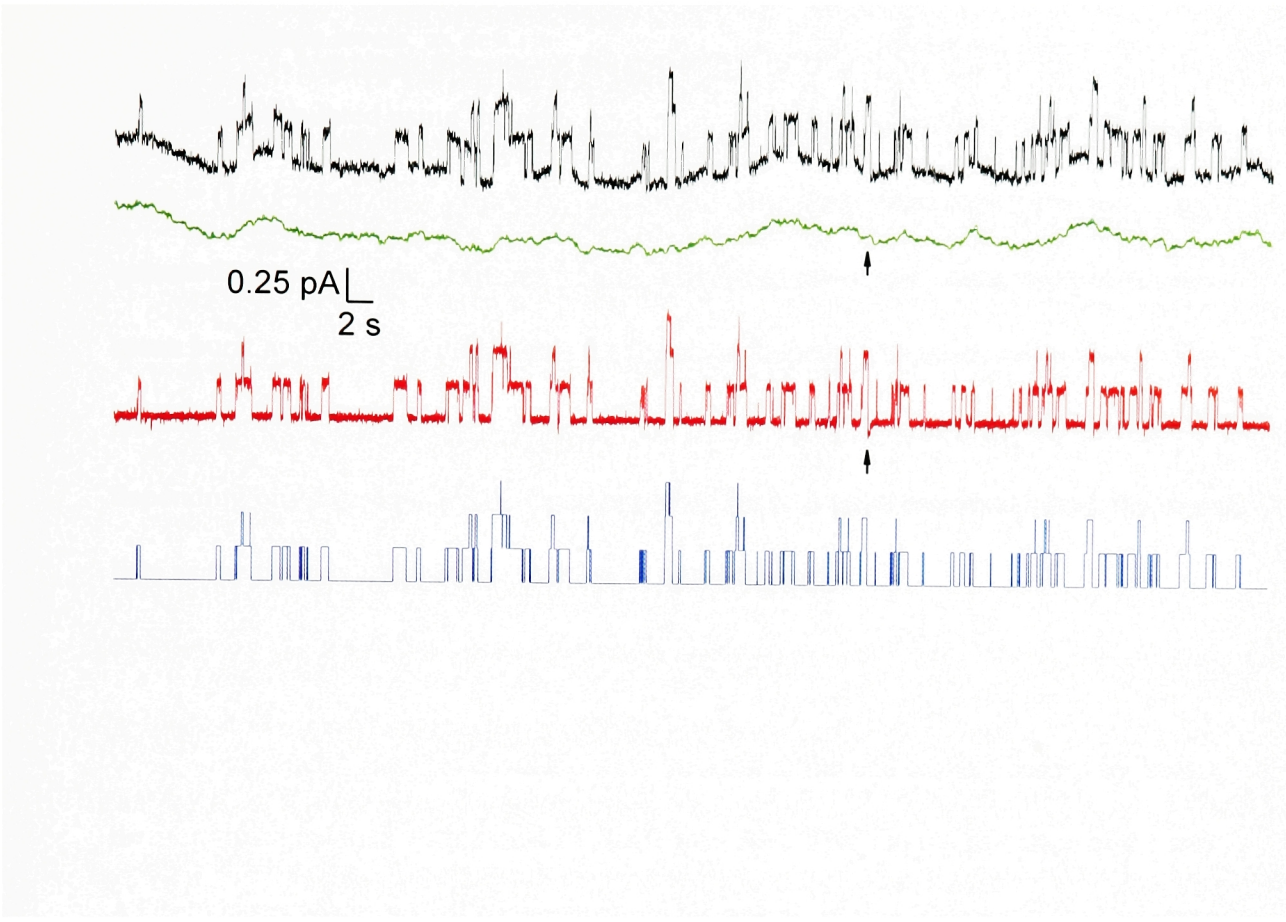

Figure 2. Illustration of the baseline correction procedure. The top trace (*black*) illustrates a segment of record with considerable baseline instability. Reconstructed baseline current is shown in *green*, offset for clarity. *Red* trace shows the baseline-corrected record, obtained by subtracting the *green* trace from the raw current trace (*black*). Idealized event sequence (*blue*) was obtained from the *red* trace by half-amplitude treshold crossing analysis. *Black arrows* locate an instance where the baseline-extrapolation was insufficient, introducing an artifact in the baseline-corrected trace, which, however did not affect the idealization procedure.

simultaneous maximum likelihood fit to the dwell-time histograms obtained from all of the conductance levels, as described in detail in Chapter 3. Mean interburst durations were then calculated using the relationship $\tau_{ib} = 1/r_{CO}$, mean burst durations were given by $\tau_b = (1/r_{OC})(1+ r_{OB}/r_{BO})$. As a control, when a closed-closed-open scheme was assumed, the same type of fitting yielded a different set of rate constants, but identical mean burst and interburst durations for the same records. The dead time t_d was 4-6 ms, typical rates of CFTR gating were r_{OB}=~3s^{-1}, r_{BO}=~100s^{-1}, r_{CO} and r_{OC} on the order of 1s^{-} depending on [ATP] and PKA. Open probabilities (P_o) were calculated from the events lists as the time-average of the fraction of open channels.

2.8.3. Determination of the number of channels

For kinetic analysis channels were counted at the end of each record by locking them in the open state with 2 mM PP_i (or 1 mM AMPPNP) in the presence of 0.1 mM ATP. In cases where not all channels could be locked, as was frequently the case for constructs 1-835 plus 837-1480, 1-633 plus 837-1480 and Flag3-633 plus 837-1480, statistical tests, developed for identical and independent channels with a simple closed-open scheme, were used to test the hypothesis that the number of channels in the patch (N) did not exceed the maximum number of channels observed simultanously open (N').

One such test was based on the argument that the presence of N channels ($N>N'$) is not likely, if the total observed time with N' channels simultanously open is long compared to the apparent opening rate of N-N' channels. In particular, if β' is the single-channel opening rate extracted assuming N' channels, then $\beta^*_{N-N'}$, the apparent opening rate of N-N' channels assuming that there are N channels in the patch, is given by

$\beta^*_{N-N'} \approx \left(\frac{N'}{N}\beta'\right)(N-N')$. If $T_{N'}$ is the total observed time during which N' channels were simultanously open, then the *a posteriori* probability that a simultanous opening of an additional channel is not observed during this time, provided that there are N channels, is given by $e^{-\beta^*_{N-N'}T_{N'}}$. Hence, the hypothesis that N channels ($N>N'$) are present in the patch can be rejected with confidence 1-ε, if

$$e^{-\beta^*_{N-N'}T_{N'}} < \varepsilon .$$

For N'=1 and P_o<<1 this test reduces to that derived by Colquhoun and Hawkes, 1995.

A different test was used in cases where the *number* of N'-events (termed l') was very small, but the total *time* observed with N'-1 simultanously open channels ($T_{N'-1}$) was very long, based on the argument that the presence of N channels ($N>N'$) is not likely if the number of expected N'-events (assuming N channels) greatly exceeds l'. In particular, if β' is the single-channel opening rate extracted assuming N' channels, then $\beta^*_{N-(N'-1)}$, the apparent opening rate of N-(N'-1) channels assuming the presence of N channels, is given by $\beta^*_{N-(N'-1)} \approx \left(\frac{N'}{N}\beta'\right)(N-(N'-1))$. If the openings of the remaining N-(N'-1) channels are viewed as point events (which means neglecting the total length of the N'-events compared to $T_{N'-1}$, as well as the possibility of two such openings occurring in overlap), the probability P_k that *exactly* k N'-events occur during the total timespan $T_{N'-1}$, assuming the presence of N channels, is given by $P_k \approx \frac{(\beta^*_{N-(N'-1)} \cdot T_{N'-1})^k}{k!} \cdot e^{-\beta^*_{N-(N'-1)} \cdot T_{N'-1}}$.

The probability that the number of N'-events is *more than* l', assuming the presence of N channels, is obtained by summing P_k for all $k>l'$. Thus, the hypothesis that N channels

($N>N'$) are present is rejected with 1-ε confidence, if that would predict a probability larger than 1-ε for observing *more than* l' N'-events, i.e., if

$$e^{-\beta^*_{N-(N'-1)}\cdot T_{N'-1}} \cdot \sum_{k=0}^{l'} \frac{(\beta^*_{N-(N'-1)} \cdot T_{N'-1})^k}{k!} < \varepsilon$$

Since these tests assume a simple closed-open scheme, β' was taken as r_{CO} (the inverse of the mean interburst duration, see above) obtained assuming N' channels, and l' was taken as the number of N' events after excluding flickery closures. Records for which the number of channels could be estimated with >90% confidence (by either of the two tests) were included for kinetic analysis. Although these tests proved reliable for simulated data, they are likely less accurate in real situations where the implicit assumption of identical and independent channels may not be valid. Nevertheless, they are expected to eliminate the likelihood of grossly underestimating channel number, which could easily happen otherwise when many channels are present, each with a very low open probability.

2.8.4. Burst analysis

Bursts were isolated from single-channel records by suppressing closures shorter than a specified cutoff t_c. The method of Jackson et al. (1983) was used to choose the value of t_c individually for each record. This method minimizes the total probability of mis-assigning a closed event, and provides t_c in the form of $t_c = \frac{\tau_1 \tau_2}{\tau_2 - \tau_1} \ln\left(\frac{\tau_2 a_1}{\tau_1 a_2}\right)$, where τ_1, τ_2, a_1, and a_2 are time constants and relative amplitudes of a two-exponential fit to the closed time histogram. (Typically t_c was 30-80 ms; but 400-800 ms for construct 1-633

plus 837-1480(K1250A).) The distributions of the durations of the bursts obtained in this way were fitted by single exponentials or mixtures of two exponential distributions using an unbinned maximum likelihood approach (e.g. Colquhoun and Sigworth, 1995). The need for introducing a second component was evaluated based on the Schwarz criterion, which penalizes models with too many parameters. This method was found effective by Ball and Sansom (1989) for model identification when comparing likelihoods of a series of dwell times. Since here (after exclusion of flickery closures) model identification at this stage was reduced to a choice between a simple closed-open model or a model with one closed and two open states, for both of which the log likelihood of the whole time series separates into the sum of the log likelihoods of the closed and open time intervals (see Ball and Sansom, 1989), in this case, applying the Schwarz criterion to the likelihood of the (relevant) open time intervals, instead of to the likelihood of the series of dwell times, is expected to give similar results. Accordingly, the two-exponential fit (3 parameters) was preferred over the single-exponential (1 parameter), if the increase in the log likelihood satisfied $\Delta LL > \ln(2M)$, where M was the number of bursts fitted (corresponding to a time series of $2M$ events). Isolated bursts obtained from low activity records with more than one channel were included if the mean length of those bursts was at least 80% of the mean burst duration obtained from the same patch using multichannel fitting (see above).

2.8.5. Reconstruction of the time sequence of unlocking events

CFTR channels that are normally gated by ATP can assume bursts of openings prolonged by orders of magnitude when they are exposed to mixtures of ATP and AMPPNP (Hwang et al., 1994; Gunderson and Kopito, 1994; Carson et al., 1995). The

duration of these "locked" events can be precisely estimated in macropatches from the time constant of the current decay following abrupt removal of nucleotides. Under these same conditions, the individual unlocking events can be discerned in patches with few channels. It is of interest to measure the mean locked time in small patches, and to see whether it agrees with the time constant of current decay observed in macropatches. Consider a situation in which there are several (5-10) channels in a patch, under conditions where each channel can transit from a common closed state (C) either to a relatively short-lived open state (O), or to a very long-lived conducting state (L, for "locked"). State L also communicates with a brief blocked (B) state. At steady state the rates are suddenly changed such that rate r_{CL}=0, and r_{CO} is made extremely small. The system can now be described by the scheme

$$[B \underset{r_{LB}}{\overset{r_{BL}}{\rightleftarrows}} L \overset{r_{LC}}{\rightarrow} C \underset{r_{OC}}{\overset{r_{CO}}{\rightleftarrows}} O] \quad X \quad N,$$

where initially N_o channels are in L, and N-N_o in C. The task is to reconstruct the time sequence $t_{N_o} < t_{N_o-1} < ... < t_k < ... t_1$ of unlocking ($L \rightarrow C$) events. A technical difficulty in identifying unlocking timepoints t_k is that channels in L undergo frequent brief transitions to B (~50-80 ms, longer than the flickers within normal bursts). When many channels are in L, these flickers can add up to apparent gaps of hundreds of milliseconds in the record, as if a channel had unlocked but then re-opened. In addition, real re-openings (to O) also occur occasionally, due to the combined difficulties of completely washing away all nucleotide molecules and of the high affinity of the channels for ATP. To circumvent this problem, a strategy was adopted in which the kth channel was considered unlocked, once

a gap to lower conductance levels was observed with a duration exceeding a defined cutoff. The cutoff was chosen separately for each conductance level, such that the choice equated the probabilities of assigning a particular unlocking event too early or too late. These error probabilities were based on estimates of r_{LC} and r_{CL}, and of the apparent reopening rate r_{CO}, observed after all channels were unlocked. This procedure assigns longer cutoff times for higher conductance levels, since flickery closures of more locked channels are more likely to add up to longer gaps, and since the channels that are locked are not yet available for reopening. Typical cutoffs ranged from ~500 ms for conductance level 1 (i.e. the unlocking of the last channel) to ~2000 ms for conductance level 10 (unlocking of the first of 10 locked channels). Results were satisfactory (in contrast to the use of a fixed cutoff for all levels) on simulated current traces, and afforded the additional benefit of providing the estimated probabilities for committing an error at each decision. The latter estimates were in good agreement with the fraction of mis-assigned unlocking events in individual simulated traces. A disadvantage is that the procedure relies on the estimate of the re-opening rate r_{CO}, based on the very small number of re-openings typically observed, and is thus prone to inaccuracy. Nevertheless, in practice the results obtained using this procedure agreed well with the rates obtained from fitting exponentials to macroscopic current decays.

2.8.6. Single-channel conductances

Single-channel conductances were estimated from amplitude histograms of 10-s excised-patch current segments recorded at holding potentials of -80, -40, 0, +40, and +80 mV, in symmetrical 140 mM [Cl^-]. (High-Cl^- bath solution contained 139.3 mM NMG, 2 mM $MgCl_2$, 5 mM HEPES, 0.5 mM EGTA, 136 mM HCl, pH=7.1 with HCl.) The

distances between adjacent peaks, from fits to sums of Gaussians, were plotted against voltage, and straight lines fitted to yield conductances.

2.8.7. Calculation of apparent affinities and fitting of macroscopic current relaxations

Macroscopic currents typically originating from hundreds or thousands of channels were digitally re-filtered at 10 Hz using a Gaussian filter, and then sampled at 50 Hz. The average steady-state current during 10-30-s applications of test concentrations of MgATP was normalized to the mean of the steady currents at 2 mM MgATP before and after the test, and the ratios used to estimate apparent affinities for ATP. Decay currents were fitted by single or double exponentials using a least-squares fitter (SigmaPlot 4.0), and the need for a second component was judged empirically.

2.8.8. Temperature dependence

Records used for kinetic analysis of CFTR constructs severed around the R domain (see Chapter 7), were segregated into pools recorded between 21 to 23 °C (termed 22°C), or 24 to 26°C (termed 25°C), and burst and interburst durations averaged separately. Though this temperature range is too small for accurate estimation of temperature dependence, approximate Q_{10} values were tentatively calculated from the Arrhenius equation as $Q_{10} = (k_2 / k_1)^{10/(T_2 - T_1)}$, with corresponding enthalpic activation energies given by $E_a = R\frac{T_1 T_2}{T_1 - T_2}\ln\frac{k_1}{k_2}$, where R=8.31 J mol^{-1} K^{-1}, and k_1 and k_2 are rates measured at absolute temperatures T_1 and T_2, respectively.

2.8.9. Statistics

Results are presented as mean ± s.e.m. of ≥5 experiments for kinetic data and for macroscopic measurements of AMPPNP off-rate, and ≥3 experiments for apparent affinities and single-channel conductances. Statistical significances were evaluated by Student's t-test.

3. KINETIC ANALYSIS OF MULTICHANNEL RECORDS

3.1. Motivation

Gating of single ion channels can be modeled by transitions among a finite number of conducting and non-conducting states, connected in some specified pattern. At any moment a single channel will be in one of these states, and can undergo transitions into adjacent ones in a stochastic fashion. Such a system is conveniently described by a continuous-time Markov process (Colquhoun and Hawkes, 1977 and 1981). Patch-clamp recording allows measurement of the conductance of single ion channels. Since more than one state of a channel may be characterized by the same conductance, such states can be grouped into classes, transitions within which remain undetected. The observable signal is modeled by an aggregated Markov process. The challenge for the experimenter is to identify the model underlying the observed sequence of transitions, and to estimate the rate constants.

The classical approach to kinetic analysis of single-channel data consists of constructing dwell-time histograms for the open and closed times of a single channel, and then fitting them with exponential functions (Colquhoun and Sigworth, 1983, 1995). This approach is widely used because of its simplicity and relatively small computational demand.

In many cases, however, it may be impractical to restrict analysis to single-channel records. If the channels of interest tend to cluster, for example, most patches may contain multiple channels. Also, if the open probability is low, long records are required to amass enough events from a single channel. In some cases it might be hard to maintain

steady-state conditions for a sufficiently long time to collect enough events from a single channel. Some of these factors are real concerns when studying CFTR channels in *Xenopus* oocytes. Given the slow gating of CFTR, together with exquisite sensitivity to phosphorylation level, records with sufficiently numerous events from a single channel at steady state are rare. Most of the data presented in later chapters, for instance, were obtained from patches with several channels.

As shown by Blunck et al. (1998), if the gating scheme is already known or assumed, data from patches containing multiple channels can be analyzed by a simultaneous fit of the dwell-time histograms for all the conductance levels. These authors used a least-squares fit to the observed set of histograms and showed that, in many cases, reasonable estimates of the parameters can be obtained after only short processing times. Unfortunately, the scatter of the estimates was considerable, and the approach failed for noisy data whenever the signal-to-noise ratio was too low for correct event detection.

This chapter presents an approach similar to the one introduced by Blunck et al. (1998), but with improvements that result in broader applicability and enhanced reliability. First, instead of least-squares fitting, which produces biased estimates depending on whether the fits are made to linear, semi-log or log-log histograms, a simultaneous maximum likelihood fit is made to the set of dwell-time histograms obtained from all conductance levels. Second, an effective correction for missed events is included, based on theory developed by Roux and Sauvé (1985) for a single channel, together with a practical implementation of a fixed dead time for multichannel records. This feature permits use of a range of filter settings, and hence, effective analysis of noisy

data with fairly low signal-to-noise ratio. Good results were obtained even with relatively small numbers of events (typically hundreds, for all but extreme ratios of rate constants).

A drawback of such one-dimensional histogram fitting is that the information contained in cross correlations between neighboring events is ignored. As a result, the number of extractable parameters is limited, and the method cannot distinguish between alternative connectivities. More powerful methods exploit these cross correlations. Maximum likelihood fitting of the whole time series, first introduced by Horn and Lange (1983), is based on calculating the likelihood of an observed sequence of sample points (Horn and Lange, 1983) or dwell times (e.g. Qin et al., 1996, 1997), given a kinetic model and a set of rate constants. The likelihood is then maximized with respect to the rate constants. However, the computational task involved is considerable, even if the likelihood is computed over dwell times only, and it increases dramatically with the number of states in the model. Processing time and required memory space also increase with the length of the record. Alternatively, correlations are explored by two-dimensional dwell-time histograms for pairs of adjacent events (Magleby et al., 1992; Rothberg et al., 1997). The above maximum likelihood approaches can be applied directly to multiple channels by treating the system as a single large Markov scheme (Horn and Lange, 1983; Qin et al., 1996). However, even for simple single-channel gating models, the size of the compound scheme grows rapidly with channel number, making those computations extremely slow for more than *3* channels, especially for long records.

As for all histogram fitting methods, the approach presented here assumes that the gating scheme is specified at the outset, since correlations remain unused. However, for a given model, the reliability of the fit is ensured by the wealth of information exploited by

considering the entire set of all dwell-time distributions. Attractively, computational time and required memory space do not depend on the length of the data, while the quality of the fit improves with more events.

Suitable applications are records with many active channels obeying fairly simple, but non-trivial, gating schemes, where more advanced routines, like fitting the event sequence, become impractical. In reality, the full gating scheme of CFTR, like that of most ion channels, is very complex (see Chapter 5). Frequently, however, gating schemes can be simplified by pooling certain states, while still retaining many essential features. In particular, CFTR gating at steady state is described by bursts of openings. As a first measure, mean burst and interburst durations, under various conditions, can be extracted from multichannel records using the present approach, by fitting a simple Closed-Open-Blocked (*C-O-B*) or Closed-Closed-Open (*C-C-O*) scheme (see below). Single-channel records can then be used to dissect more complicated details of the slow gating steps.

Here, the general theory underlying the approach is developed first, and then the method is extensively tested under a variety of conditions.

3.2. General theory

3.2.1. A many-channel system as a single Markov system

It is well known that a patch with multiple channels can be treated as a single Markov system (e.g. Horn and Lange, 1983; Qin et al., 1996). One "state" of this large system ("macroscopic state") is a particular pattern of partitioning the individual channels among the single-channel states ("microscopic states").

A simple important case, solved by Horn and Lange (1983), is when N channels are assumed to be identical and independent. If there are n microscopic states for a single channel, a macroscopic state of the system is represented by a vector of n entries, the i^{th} component of which specifies the number of individual channels in the i^{th} single-channel state. The entries of the macroscopic state vector sum to N. The number of macroscopic states is equal to $\binom{n+N-1}{N}$, the number of ways in which N can be divided into n parts. The transition rate from state $(N_1,\ldots N_i,\ldots N_j,\ldots N_n)$ to $(N_1,\ldots N_i-1,\ldots N_j+1,\ldots N_n)$ is

$$N_i \cdot r_{ij}, \tag{1}$$

where r_{ij} is the transition rate constant of a single channel from state i to j. Macroscopic states are numbered such that those belonging to the same conductance level are clustered, allowing partitioning of the transition matrix **Q** into submatrices relevant to each conductance level.

If the channels are distinguishable, the system can be described by a (usually much bigger) state space of n^N dimensions (see Qin et al., 1996). The concepts of this chapter are presented for N identical and independent channels, but should be equally applicable to the more general case.

3.2.2. Dwell-time distributions of the various conductance levels

For a Markov system described by the matrix **Q**, the distributions of dwell times in any subset of states can be calculated (Colquhoun and Hawkes, 1981). To obtain the dwell-time distribution of a conductance level k, a subset $\{k\}$ is defined as the set of all

macroscopic states with k channels open, $\{\bar{k}\}$ as the set of all other macroscopic states. Defined as $surv_{\{k\}}(t) = P(\text{no leaving from } \{k\} \text{ before time } t \mid \text{entered } \{k\} \text{ at time } 0)$, the survivor functions are given by

$$surv_{\{k\}}(t) = \mathbf{p}_k(0)^T e^{\mathbf{Q}_{kk}t}\mathbf{1}_k, \tag{2}$$

where $\mathbf{Q}_{kk}$ is the sub-matrix of $\mathbf{Q}$ describing transitions within $\{k\}$, $\mathbf{1}_k$ is the summation vector matching $\{k\}$ in dimensions. $\mathbf{p}_k(0)^T$ (matching $\{k\}$ in dimensions) is the row vector of probabilities of entering $\{k\}$ via any one of its component (macroscopic) states,

$$\mathbf{p}_k(0)^T = \frac{\mathbf{p}_{\bar{k}}(\infty)^T\mathbf{Q}_{\bar{k}k}}{\mathbf{p}_{\bar{k}}(\infty)^T\mathbf{Q}_{\bar{k}k}\mathbf{1}_k}, \tag{3}$$

where submatrix $\mathbf{Q}_{\bar{k}k}$ describes transitions from $\{\bar{k}\}$ to $\{k\}$, $\mathbf{p}_k(\infty)^T$ and $\mathbf{p}_{\bar{k}}(\infty)^T$ are row vectors of steady-state occupancy probabilities for macroscopic states in $\{k\}$ and $\{\bar{k}\}$ respectively. ($\mathbf{p}^T$ in general denotes the row vector corresponding to the column vector $\mathbf{p}$.) For binned maximum likelihood fitting (see Sigworth and Sine, 1987) it is convenient to use the survivor function, because the probability of a dwell time falling into a bin $t_i \le \textit{dwell time} < t_{i+1}$ is given by $surv(t_i) - surv(t_{i+1})$.

3.2.3. Simultaneous maximum likelihood fitting of a set of histograms

Binned maximum likelihood fitting (Sigworth and Sine, 1987), consists of a search for the set of kinetic parameters, which maximizes the likelihood that a series of dwell times in one particular conductance level yields the experimentally observed dwell-time histogram. Here, this approach is extended to the set of dwell-time histograms

constructed for all the conductance levels, which can be thought of as one "generalized histogram", each bin of which represents a range of dwell times for a certain conductance level. Figure 3 illustrates this concept, showing the generalized dwell-time histogram for a simulated current trace (described in more detail later, in Figure 9A), from *3* channels. The fit (solid black lines) was found by the method described here.

The likelihood function for an events list is defined as the likelihood of obtaining the observed generalized histogram (Figure 3) given a model and a set of rate constants. The likelihood estimate is based on the calculation of the probability that an observed event belongs to level k **and** falls into the i^{th} bin of the level k dwell-time histogram:

$$P(k,i) = P(\text{event is level } k \textbf{ and } t_{k,i} \le \textit{dwell time} < t_{k,i+1}).$$

This is easily obtained using conditional probabilities:

$$P(k,i) = pctlvl(k) \cdot p_{ki} \quad , \tag{4}$$

where $pctlvl(k)$ specifies what fraction of all observed events is expected to be at level k:

$$pctlvl(k) = P(\text{observed event is level } k) = \frac{\mathbf{p}_{\bar{k}}(\infty)^{T}\mathbf{Q}_{\bar{k}\bar{k}}\mathbf{1}_{k}}{\sum_{j=0}^{N}\mathbf{p}_{\bar{j}}(\infty)^{T}\mathbf{Q}_{\bar{j}\bar{j}}\mathbf{1}_{j}} \quad , \tag{5}$$

and p_{ki} is the fraction of all observed level k events predicted to fall into the i^{th} bin:

$$p_{ki} = P(t_{k,i} \le \textit{dwell time} < t_{k,i+1} | \text{event is level } k) = surv_{\{k\}}(t_{k,i}) - surv_{\{k\}}(t_{k,i+1}). \tag{6}$$

If the level k histogram contains r_k bins and $n_{k,i}$ is the occupancy of the i^{th} bin, the likelihood function can be calculated as follows:

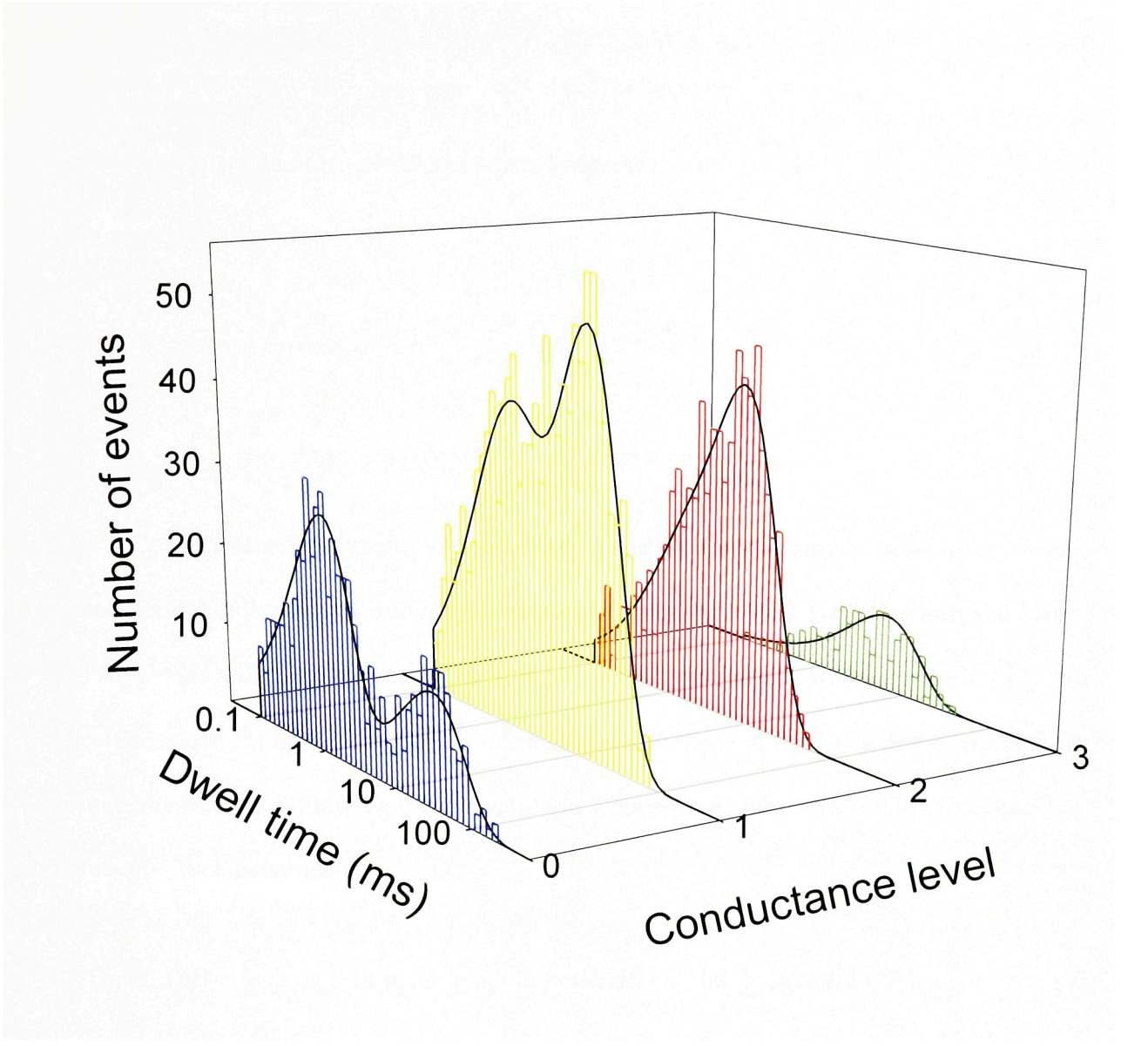

Figure 3. The concept of the generalized histogram. Set of dwell-time histograms (and fit, solid black lines) for all conductance levels of a simulated current record from 3 channels obeying the *C-O-B* scheme (see text for details). Rate constants (in s^{-1}) used for simulation: r_{CO} =10, r_{OC} =20, r_{OB}=40, and r_{BO}=1000. Estimates from fit: r_{CO} =10, r_{OC} =20, r_{OB}=38, and r_{BO}=918. Dead time: 0.1 ms (see text).

$$L(\Theta) = \prod_{k=0}^{N} \prod_{i=1}^{r_k} P(k,i)^{n_{k,i}} = \prod_{k=0}^{N} \prod_{i=1}^{r_k} \left[pctlvl(k) \cdot p_{k,i} \right]^{n_{k,i}} \quad , \tag{7}$$

where Θ represents the model and the set of rate constants. Both $pctlvl(k)$ and $p_{k,i}$ are functions of Θ. In practice the logarithm of the likelihood is used,

$$LL(\Theta) = \sum_{k=0}^{N} \sum_{i=1}^{r_k} n_{k,i} \cdot \ln p_{k,i} + \sum_{k=0}^{N} n_k \cdot \ln pctlvl(k) \quad , \tag{8}$$

where n_k is the total number of events in the level k histogram: $n_k = \sum_{i=1}^{r_k} n_{k,i}$.

Sometimes it is useful to exclude some events from binning by specifying lower and upper bin limits $t_{k,min}$ and $t_{k,max}$ for each conductance level k (see Sigworth and Sine, 1987). This will alter the scaling factors for the different levels, which can be compensated for by defining quantities analogous to those in Eqs. 5, 4, and 6, conditional on being binned. Following the derivation in Appendix A, the corrected log likelihood function then becomes

$$LL'(\Theta) = \sum_{k=0}^{N} \sum_{i=1}^{r_k} n_{k,i} \cdot \ln p_{k,i} + \sum_{k=0}^{N} n_k \cdot \ln pctlvl(k) - n_t \cdot \ln \left[\sum_{k=0}^{N} pctlvl(k) \cdot P_{k,binned} \right], \tag{9}$$

where

$$\begin{aligned} P_{k,binned} &= P(\text{event is binned} \mid \text{event is level } k) = \\ &= surv_{\{k\}}(t_{k,min}) - surv_{\{k\}}(t_{k,max}) \, , \end{aligned} \tag{10}$$

and $n_t = \sum_{k=0}^{N} n_k$ is the total number of binned events. Compared to the original expression for $LL(\Theta)$ in Eq. 8, the introduction of binning limits results in only one additional

term, even though the binning limits may be different for each level. $p_{k,i}$, $pctlvl(k)$, and $P_{k,binned}$ depend on the set of parameters Θ through Eqs 6, 5, and 10, respectively.

The approach presented in this section discards the information contained in the correlations between neighboring events. This is the penalty accepted for the much smaller computational task of having to deal with only a number of terms equal to the total number of all histogram bins (a few tens typically, independent of the length of the events list) for the calculation of the likelihood, compared to the total number of events (some thousands typically, proportional to the length of record) involved in fitting the whole dwell-time series (see Qin et al., 1996, 1997). Even so, a lot of information is still exploited. If n_c and n_o are the numbers of closed and open states, respectively, of a single channel, then the dwell-time distribution of level k for a record with N channels contains $\binom{n_o+k-1}{k}\cdot\binom{n_c+N-k-1}{N-k}$ exponential components. The time constants and relative amplitudes of each component for all levels, plus, for $N>1$, the relative scaling factor for each level provide a total number of $\left[2\cdot\sum_{k=0}^{N}\binom{n_o+k-1}{k}\cdot\binom{n_c+N-k-1}{N-k}\right]-1$ constraints used for restraining the fit. For a linear three-state scheme with 2 closed states and 1 open state there are 4 rate constants to be found. The number of parameters required to describe all dwell-time histograms are 4 for a single-channel record, 11 for a record with 2 channels, and 55 for a record with 6 channels. All of these parameters are functions of the 4 single-channel rate constants, providing strong constraints for accurate fitting. This does not necessarily mean that models which are unidentifiable from single-channel histogram fitting will become solvable from multichannel fitting. For instance,

the loop model of *CCO* cannot be solved by single-channel histogram fitting, since the likelihood surface has no unique maximum, and it is easy to show that this property is propagated to the likelihood of the set of histograms of a multichannel patch as well.

3.2.4. Correction for missed events

Limited bandwidth of the patch-clamp recording system is the price paid for filtering to achieve an acceptable signal-to-noise ratio. As a result of the filter delay, short events remain undetected, distorting the distribution of observed dwell times. A general theory for the treatment of the "missed event problem" was developed by Roux and Sauvé (1985), who assumed an absolute dead time (t_d): all events shorter than t_d remain undetected; all events longer than t_d are detected. Because of noise, such a fixed t_d cannot be calculated simply from the response characteristics of the filter, but it can be imposed retrospectively, by choosing t_d larger than the filter dead time, and by concatenating to the preceding sojourn any dwell time shorter than t_d (see Qin et al., 1996).

Following Roux and Sauvé (1985), given a fixed t_d, the survivor function for the observed dwell-time distribution of a conductance level k is defined as

$$surv^{R\&S}_{\{k\}}(t,t_d) = P(\text{no observable leaving from } \{k\} \text{ before time } t| \\ \text{entered } \{k\} \text{ at time 0 after an observable stay in } \{\bar{k}\}) \quad . \tag{11}$$

where "observable" means longer than t_d. With the additional assumption that the total duration of missed event(s) within an observed event is negligible, the authors were able to write down the probability density function (pdf), which, when integrated from t to ∞, yields the survivor function. In the present notation

$$surv^{R\&S}_{\{k\}}(t,t_d) = [\mathbf{initial}^{R\&S}]^T_k e^{\hat{\mathbf{Q}}_{kk}t}\mathbf{1}_k \quad , \tag{12}$$

where

$$[\mathbf{initial}^{R\&S}]_k^T = \frac{\mathbf{p}_k(\infty)^T \mathbf{Q}_{k\bar{k}} e^{\mathbf{Q}_{\bar{k}\bar{k}} t_d} (-\mathbf{Q}_{\bar{k}\bar{k}}^{-1}) \mathbf{Q}_{\bar{k}k}}{\mathbf{p}_k(\infty)^T \mathbf{Q}_{k\bar{k}} e^{\mathbf{Q}_{\bar{k}\bar{k}} t_d} (-\mathbf{Q}_{\bar{k}\bar{k}}^{-1}) \mathbf{Q}_{\bar{k}k} \mathbf{1}_k} \quad , \tag{12a}$$

$$\hat{\mathbf{Q}}_{kk} = \mathbf{Q}_{kk} - \mathbf{Q}_{k\bar{k}} (\mathbf{I}_{\bar{k}} - e^{\mathbf{Q}_{\bar{k}\bar{k}} t_d}) \mathbf{Q}_{\bar{k}\bar{k}}^{-1} \mathbf{Q}_{\bar{k}k} \quad . \tag{12b}$$

As noted by Qin et al. (1996), Eq. 11 does not take into account that no leaving can occur at all between time 0 and t_d after entering $\{k\}$, since that would produce a "short" $\{k\}$ event which would be concatenated to the preceding event. The fact that a $\{k\}$ event is detected means that its initial section (between time 0 and t_d) is free of transitions. To account for this, an additional condition has to be introduced into the definition of the survivor function:

$$\begin{aligned} surv_{\{k\}}(t, t_d) = P(&\text{no observable leaving from } \{k\} \text{ before time } t \mid \\ &\text{entered } \{k\} \text{ at time 0 after an observable stay in } \{\bar{k}\} \textbf{ and} \\ &\text{stayed in } \{k\} \text{ until time } t_d) \quad . \end{aligned} \tag{13}$$

Using this definition, and following the steps described in Appendix B, the correct form of the survivor function is

$$surv_{\{k\}}(t, t_d) = \begin{cases} 1 & \text{for } t < t_d \\ [\mathbf{initial}]_k^T e^{\hat{\mathbf{Q}}_{kk}(t - t_d)} \mathbf{1}_k & \text{for } t \geq t_d \end{cases} \quad , \tag{14}$$

where

$$[\mathbf{initial}]_k^T = \frac{\mathbf{p}_k(\infty)^T \mathbf{Q}_{k\bar{k}} e^{\mathbf{Q}_{\bar{k}\bar{k}} t_d} (-\mathbf{Q}_{\bar{k}\bar{k}}^{-1}) \mathbf{Q}_{\bar{k}k} e^{\mathbf{Q}_{kk} t_d}}{\mathbf{p}_k(\infty)^T \mathbf{Q}_{k\bar{k}} e^{\mathbf{Q}_{\bar{k}\bar{k}} t_d} (-\mathbf{Q}_{\bar{k}\bar{k}}^{-1}) \mathbf{Q}_{\bar{k}k} e^{\mathbf{Q}_{kk} t_d} \mathbf{1}_k} \quad , \tag{14a}$$

$$\hat{\mathbf{Q}}_{kk} = \mathbf{Q}_{kk} - \mathbf{Q}_{k\bar{k}} (\mathbf{I}_{\bar{k}} - e^{\mathbf{Q}_{\bar{k}\bar{k}} t_d}) \mathbf{Q}_{\bar{k}\bar{k}}^{-1} \mathbf{Q}_{\bar{k}k} \qquad \text{(as in Eq. 12b).} \tag{14b}$$

Thus, the additional condition results in a corrected initial vector and a translation of the survivor function along the time axis. The survivor function now takes on the value of 1 at time $t = t_d$, as expected. This correction is equivalent to the adjustment made by Qin et al. (1996); but merging the correction into the initial vector rather than the main operator seems more natural in the present application, and is required for the proper scaling of the survivor functions.

The relative scaling factor for each conductance level, required for simultaneous fitting, can be calculated by analogy to Eq. 5 :

$$pctlvl(k,t_d) = \frac{\mathbf{p}_k(\infty)^T \mathbf{Q}_{k\bar{k}} e^{\mathbf{Q}_{\bar{k}\bar{k}} t_d} (-\mathbf{Q}_{\bar{k}\bar{k}}^{-1}) \mathbf{Q}_{\bar{k}k} e^{\mathbf{Q}_{kk} t_d} \mathbf{1}_k}{\sum_{j=0}^{N} \left[\mathbf{p}_j(\infty)^T \mathbf{Q}_{j\bar{j}} e^{\mathbf{Q}_{\bar{j}\bar{j}} t_d} (-\mathbf{Q}_{\bar{j}\bar{j}}^{-1}) \mathbf{Q}_{\bar{j}j} e^{\mathbf{Q}_{jj} t_d} \mathbf{1}_j \right]} \quad . \tag{15}$$

For $t_d = 0$ Eqs. 14 and 15 reduce to Eqs. 2 and 5, respectively.

3.2.5. Implementation of a fixed dead time

Some thought needs to be given to how the fixed dead time is implemented in practice. Qin et al. (1996) suggested imposing a fixed dead time (preferably longer than the filter dead time) retrospectively by concatenating each event shorter than the chosen t_d to the preceding sojourn. As pointed out by the authors, if a channel undergoes many short transitions in a row ("buzz mode") the fixed dead time cannot be enforced in the above way. However, even in the absence of a buzz mode, when many channels are present, other types of event sequences will appear for which the above method violates the definition in Eq. 13. These cases can be dealt with in the way discussed below, even though "buzz mode" events will still resist idealization.

For instance, as illustrated in Figure 4A (left), a leaving from $\{k\}$ to $\{\bar{k}\}$ much longer than t_d would be ignored by the above simple procedure, if it consisted of a series of dwells - each shorter than t_d - at different conductance levels in $\{\bar{k}\}$, before returning to $\{k\}$. This is contrary to Eq. 13, and would result in concatenation of the two bracketing $\{k\}$ events plus the intervening sojourn in $\{\bar{k}\}$ into one long $\{k\}$ event, leading to underestimation of the rates. A different, but smaller, problem is that according to Eq. 13 a $\{k\}$ event should be considered terminated once there is a leaving into $\{\bar{k}\}$ longer than t_d. However, as illustrated in Figure 4A (right), if the new sojourn in $\{\bar{k}\}$ begins with an event shorter than t_d in a particular conductance level of $\{\bar{k}\}$ (or a series of such events) that event (series) would be concatenated to the end of the last $\{k\}$ event. Note that both of these problems arise only if there are more than two conductance levels.

To circumvent these problems, the following strategy was used (see flow chart in Figure 4B) for imposing a fixed t_d in a manner that more closely follows the assumptions of Eq. 13. (Since in this study half-amplitude threshold-crossing was used for idealization of raw current traces, the algorithm could be applied "on line", yielding an events list with the required properties. For other methods of idealization this can be done retrospectively.) Scanning along the record, events are written to the output events list until a "short" ($\leq t_d$) event is reached. Incoming "short" events are temporarily stored in a buffer, until the next "long" ($>t_d$) event is reached or the conductance returns to the level of the last "long" event. At this point there are three options.

If the new ("long") event belongs to a different conductance level than the last "long" event, the contents of the buffer are discarded, and a flag is written to the events list stating the total length of discarded time, followed by the new "long" event.

If the new event belongs to the same conductance level as the last "long" event, and the total time stored in the buffer is shorter than t_d, the contents of the buffer and the bracketing events are concatenated into a single event of conductance level given by the bracketing events and of duration given by the sum of the three sources.

If the new event belongs to the same conductance level as the last "long" event, but the total time stored in the buffer exceeds t_d, the last "long" event is written to the events list. If the new event is "short", it is added to the buffer, otherwise the buffer is discarded, a flag is written to the events list, and the new event is considered separately.

The flow chart in Figure 4B summarizes the strategy described above. Figure 4A provides a visual comparison of the resulting idealized event sequences obtained in the conventional way or "correctly", according to the above algorithm.

As a result, the only concatenated events are of the type $\{k\} \rightarrow \{\bar{k}\} \rightarrow \{k\}$, where the total time spent in $\{\bar{k}\}$ is shorter than t_d, as required by Eq. 13. The first sojourn in every "detected" event still has to be longer than t_d (see Eq. 13), otherwise it would be discarded from the buffer. The flags can be thought of as dividing the record into small sections – considered separately – within which the fixed dead time can be imposed consistently, while the regions where this is impossible are discarded. The final histograms can be viewed as the sums of the histograms for the "good" sections. This approach improved the results of subsequent histogram fitting substantially, especially in cases where, because of frequent rapid gating events and many channels, sequences of the type shown in Figure 4A occurred often (cf. Figure 8).

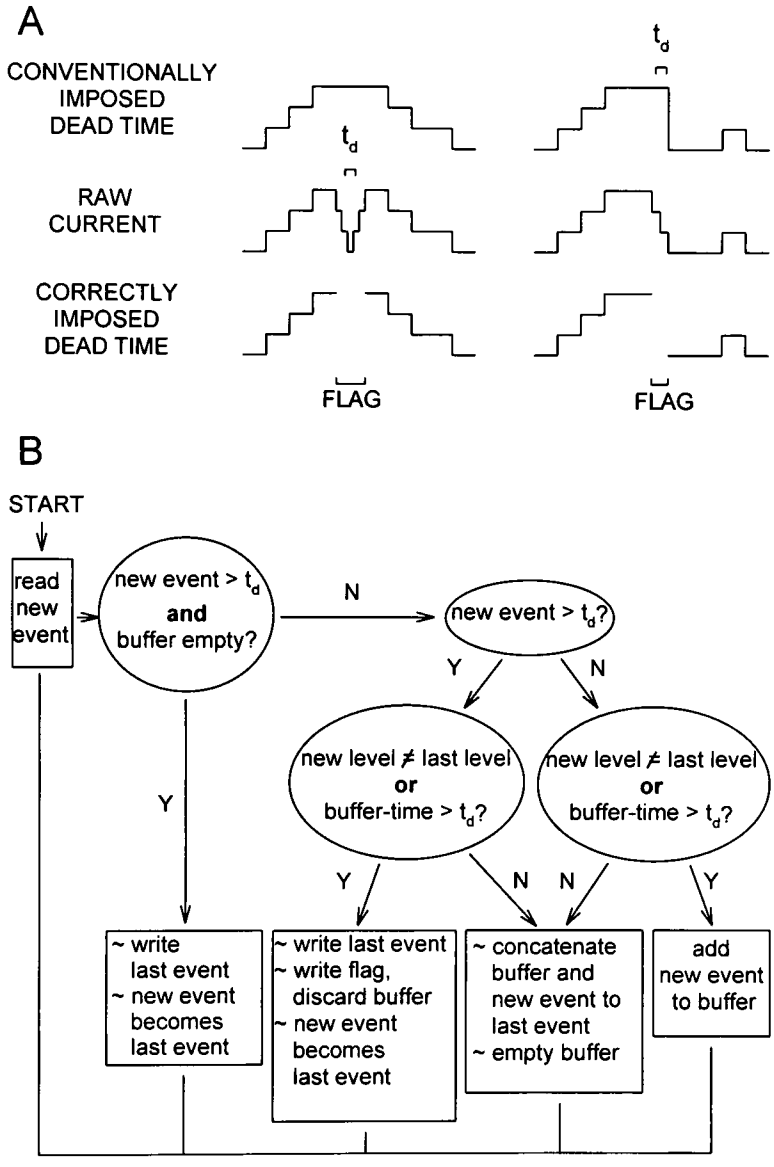

Figure 4. Application of a fixed dead time. A, Two examples of raw event sequences where conventional concatenation of brief events (top) is inappropriate: left, a leaving from level 3 longer than t_d is incorrectly ignored because it comprises only sub-dead-time components; right, a level 3 event is prolonged by incorporation of a series of brief sojourns ("staircase"), although the latter are part of a long dwell in $\{\overline{3}\}$. For comparison, idealized event sequences generated by the algorithm described in the text and in B are shown below. **B**, Flow chart of the algorithm used to avoid inappropriate concatenations.

3.2.6. Program cycle

To implement the procedures just described, a computer program (see Figure 5) was written in *C* language. The inputs for this analysis program are a) the model gating scheme, b) an events list with sub-dead-time events suppressed, c) the value of t_d, d) the number of channels, and e) an initial guess at the single-channel rate constants. Figure 5. illustrates the program cycle in the form of a flow chart.

First, the program scans through the events list and constructs the dwell-time histograms, with logarithmic time axes (Sigworth and Sine, 1987), for each conductance level. Unless $t_d = 0$, the lower binning limit is t_d for all levels (i.e. no short events are excluded from binning). Bin density is 6 per *e*-fold. The maximum number of bins is *60* for each level, which usually accomodates all events. If the range of dwell durations exceeds e^{10} ($2 \cdot 10^4$), some long events may remain unbinned, in which case the correction explained in Eqs. 9-10 is implemented. Event binning is the only step whose processing time depends on the actual length of the events list. Since this step represents only about one percent of the computational time, the latter is largely independent of the length of the record, in contrast to routines that fit the event sequence (see Horn and Lange, 1983; Qin et al., 1996, 1997).

Next, the program enters a loop of iterations aimed to maximize the likelihood of the set of histograms. The loop starts with the construction of the transition rate matrix **Q** for the model macro-system, as given by Eq. 1. The survivor functions of the conductance levels are calculated according to Eq. 14, with scaling factors given by Eq. 15. Finally, the log likelihood function is calculated according to Eq. 9. The likelihood is

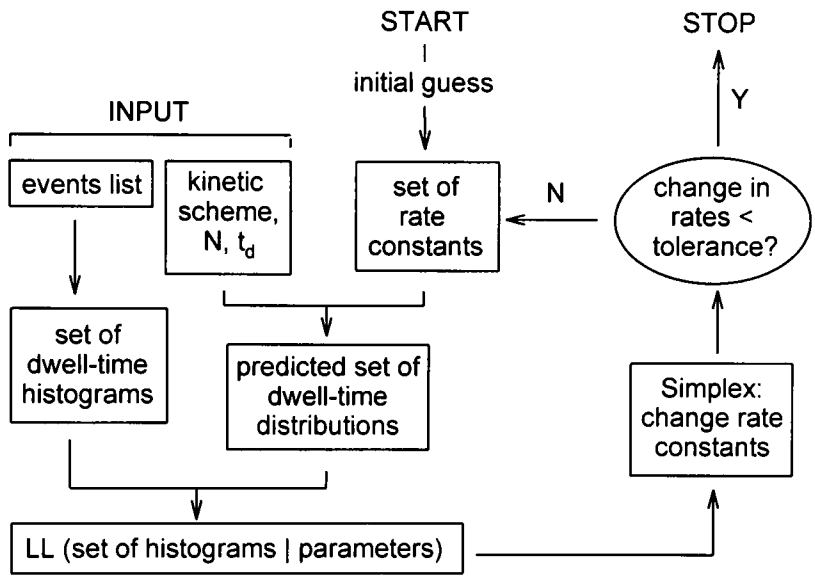

Figure 5. Flow chart illustrating the program cycle of the fitting software.

maximized with respect to the rate constants using the simplex algorithm (Caceci and Cacheris, 1984), chosen because of its simple programming code and proven robustness.

The key step is evaluation of the survivor function, of the form $\mathbf{p}^{\mathrm{T}}e^{\mathbf{Q}t}\mathbf{1}$. The row vector $\mathbf{p}^{\mathrm{T}}e^{\mathbf{Q}t}$ is calculated as a power-series, truncated when when a term drops below a predefined error: $\mathbf{p}^{\mathrm{T}}e^{\mathbf{Q}t} = \mathbf{p}^{\mathrm{T}} + \mathbf{p}^{\mathrm{T}}\mathbf{Q}t + (\mathbf{p}^{\mathrm{T}}\mathbf{Q}t)(\frac{t}{2}\mathbf{Q}) + [(\mathbf{p}^{\mathrm{T}}\mathbf{Q}t)(\frac{t}{2}\mathbf{Q})](\frac{t}{3}\mathbf{Q})+...$ Each term is obtained from the previous one as a vector-matrix product, involving $n_{\mathbf{Q}}^2$ add-multiply operations, $n_{\mathbf{Q}}$ being the dimension of $\mathbf{Q}$. Thus, processing time is proportional to the square of the number of macroscopic states.

3.3. Testing on simulated current traces

The analysis program was tested on a range of simulated multichannel current traces to establish how the efficiency depends on the gating model, relative sizes of the rate constants, channel number, dead time, noise, and length of the record. For "reasonable" schemes, i.e. if all "microscopic" states were visited at some non-negligible frequency by the individual channels, the iterations converged, starting from a broad range of initial values.

The C_1-O-C_2 model was chosen first, to test the efficiency of the routine given a variety of parameter combinations. Since this is the scheme used to describe open-channel block, the following nomenclature will be adopted:

$$C \underset{r_{\mathrm{OC}}}{\overset{r_{\mathrm{CO}}}{\rightleftarrows}} O \underset{r_{\mathrm{BO}}}{\overset{r_{\mathrm{OB}}}{\rightleftarrows}} B$$

This single-channel scheme has one conducting state *O* (open), and two non-conducting states *C* (closed) and *B* (blocked). Because of the symmetry of the scheme (exchanging r_{OC} with r_{OB} and r_{CO} with r_{BO} yields a scheme indistinguishable from the original one) the likelihood surface is also symmetrical, with two peaks mirroring each other. Depending on the seed parameters, the program ends up at one of the two peaks.

3.3.1. Simulation of multichannel currents and noise

Channel currents were constructed using the macroscopic Markov scheme described earlier, and a simulator similar to that described by Blunck et al (1998). Channel current traces were overlaid by noise synthesized with specified Gaussian amplitude distribution and Lorentzian power spectrum, to mimic the signal that arises after low-pass filtering broad bandwidth noise whose initial power spectrum is flat in the pass-range of the filter. Variance σ^2 and corner frequency $f_{c,n}$ were adjustable. A typical setting for $f_{c,n}$ was 5 kHz, a bandwidth at which patch-clamp data are commonly acquired. To test the validity of the dead-time correction, noisy data traces were Gaussian-filtered at a corner frequency $f_{c,G}$, chosen to achieve a signal-to-noise ratio sufficient for idealization by half-amplitude threshold-crossing (see Figure 9A).

3.3.2. Distribution of the parameter estimates

To establish the nature of the scatter of the estimates, 100 simulations were carried out using the *C-O-B* scheme, with a fixed set of parameters (in s^{-1}, r_{CO}=50, r_{OC} =10, r_{OB} =50, r_{BO} =1000; *N*=3, 900 events), but different random seed values. Figure 6 shows the fit results, for all parameters, normalized to the simulated values and collected into bins of width 0.05. The histograms were fitted reasonably well by Gaussian

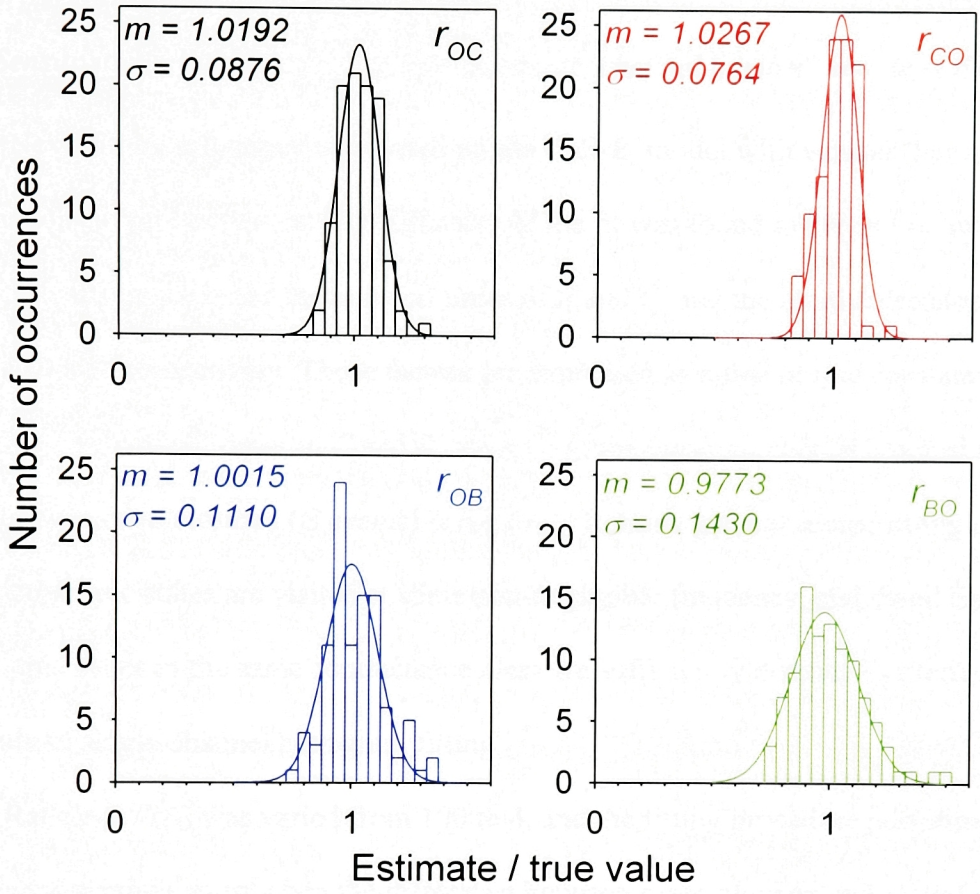

Figure 6. Histograms describing the scatter of the estimates. 100 simulations with different random seed values (900 events each) were made for 3 channels obeying the *C-O-B* scheme, r_{CO} =50, r_{OC} =10, r_{OB} =50, r_{BO} =1000 (in s^{-1}). Dead time was 0.4 ms. Parameter estimates, normalized to the respective true values, were collected into bins of width 0.05. Distributions of the estimates were fitted by Gaussian functions (solid lines) of the form $A \cdot e^{-(x-m)^2/2\sigma^2}$.

functions (solid lines in Figure 6). In subsequent sections results will be depicted as the mean of the estimates normalized to the simulated values, with error bars representing the normalized standard deviations.

3.3.3. Sensitivity to relative values of rate constants, channel number, and dead time

Next, fitting efficiency was tested on the *C-O-B* model with various combinations of rate constants. The difficulty of the fit was found to depend on two factors: the difference in the mean dwell times of *B* and *C*, and the relative frequencies of entering *C* or *B*, respectively. These factors are expressed as ratios of rate constants: the ratio of the mean dwell times in *C* and *B* is r_{BO} / r_{CO}, the mean number of blocked (*B*) events between two closures (*C events*) is r_{OB} / r_{OC}. In more general terms, fitting is easy if all microscopic states are visited at some non-negligible frequency, and dwell times of microscopic states in the same conductance class are sufficiently distinct – criteria that also apply to single-channel histogram fitting.

Ratio r_{BO} / r_{CO} was varied from 100 to 4, and the fitting procedure performed well over the entire range, even when the difference between mean blocked and closed times was as small as 4-fold. As an example, after simulating 2500 events with 4 channels, with input parameters (in s^{-1}) r_{CO}=50, r_{OC}=10, r_{OB}=50, and r_{BO}=200, followed by idealization with a dead time of 1 ms, the fitting yielded estimates r_{CO}=60, r_{OC}=13, r_{OB}=39, and r_{BO}=185, respectively.

Next, ratio r_{OB} / r_{OC} was varied in a total of 1800 experiments. While r_{BO} / r_{CO} was set to either 100 or 20, r_{OB} / r_{OC} values of 0.1, 0.2, 1, 5, and 10 were tested. Each combination of rate constants was tried with 1 to 6 channels, and dead times of 0, 0.1, 0.2, 0.3, 0.4, and 0.5 times the mean blocked time. (Since for *N* channels the fastest

macroscopic rate constant is $N \cdot r_{BO}$, a dead time of $0.5 / r_{BO}$ is three times longer than the mean dwell time of the shortest lived state, when N=6.) Each of these 360 parameter combinations was simulated five times, starting with different random seed numbers. For a single channel 600 to 2200 transitions were simulated, and traces with multiple channels were simulated for the same length of time as the corresponding single-channel ones.

Figure 7 is a summary of 300 experiments. Results were similar for all channel numbers ranging from 1 to 6, those for 2 (Panel A) and 5 channels (Panel B) are shown. With r_{BO} / r_{CO} =20, r_{OB} / r_{OC} was varied (x axis) between 0.1 and 10, with t_d ranging (y axis) from 0 to 0.5 times the mean blocked time $(1 / r_{BO})$. Means and standard deviations of the fit results for the individual rate constants are shown (z axis) normalized to their simulated values. A symbol at height 1 means accurate estimation, values higher or lower than 1 represent over- and underestimates, respectively. The solution surfaces tend to be close to 1; i.e., good estimates were obtained over a broad range of input parameters.

For r_{OB} / r_{OC} small, transitions between O and B are rare, and many of these are lost if t_d is long compared to the mean blocked time (i.e. $r_{BO} \cdot t_d$ is comparable to 1). Under these conditions the likelihood surface is relatively insensitive to r_{OB} and r_{BO}, the estimates of which become uncertain, while r_{CO} and r_{OC} are still estimated precisely. This is verified in Figure 7, where the error bars of r_{OB} and r_{BO} increase for $r_{OB} / r_{OC} < 0.2$. When r_{OB} / r_{OC} is large, transitions between states O and B of the individual channels are prevalent. While estimation of r_{OB} and r_{BO} becomes easy even for long t_d, the error on r_{CO} and r_{OC} increases (but remains around 20% even for $r_{OB} / r_{OC} = 10$). Overall errors become smaller with larger numbers of fitted events (see later).

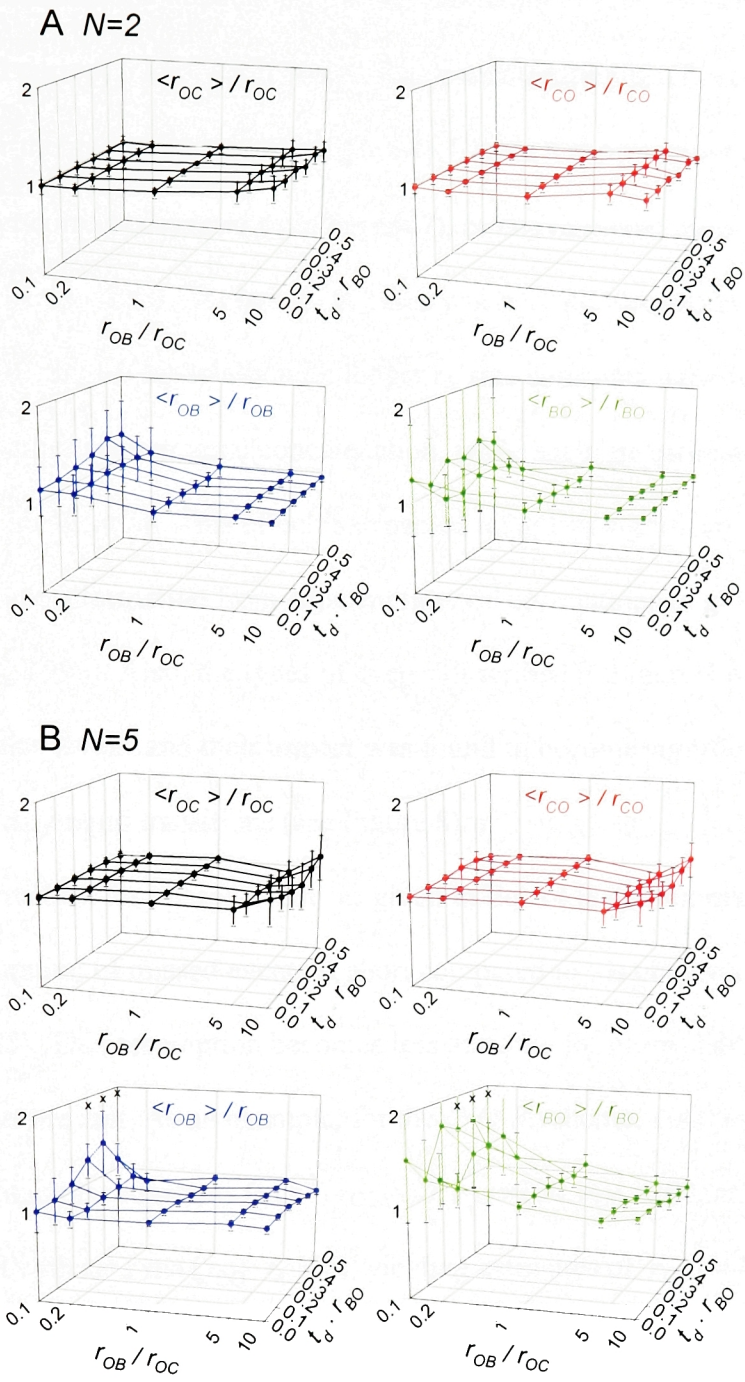

Figure 7. Performance with different rate constants. Means ± s.d. of parameter estimates from 5 simulations, normalized to true values, plotted against r_{OB}/r_{OC} and $t_d \cdot r_{BO}$. A symbol at height 1 means accurate estimation. Error bars of r_{OB} and r_{BO} are large when r_{OB}/r_{OC} is small, while those of r_{CO} and r_{OC} increase somewhat for large r_{OB}/r_{OC}. **A**, N=2. **B**, N=5; in three cases, marked with x, estimation of r_{OB} and r_{BO} was impossible: for those combinations, symbols and error bars represent only 4 simulations.

To demonstrate the impact of the implementation of t_d on subsequent fitting, the same simulated current traces were idealized by concatenating brief events either in the conventional or the improved way (cf. Figure 4). Figure 8 shows parameter estimates for 6 channels, after correct (depicted as in Figure 7), or conventional idealization (cyan symbols, error bars omitted for clarity). In cases where rapid blocked events were frequent (r_{OB} / r_{OC} high), especially with longer t_d, rate constants were seriously underestimated after conventional concatenation, while accurate estimates were obtained after improved idealization. This effect is expected to be less significant for methods which also exploit information from adjacent interval correlations (e.g. Horn and Lange, 1983; Qin et al., 1996). Also, the types of events described in Figure 4 only arise for 3 or more conductance levels, and their impact was found to become significant only with 5-6 channels and many rapid transitions (see Figure 8).

The correction for missed events as given in Eq. 14 is approximate, it assumes that the total duration of missed events is short compared to the observed event (Roux and Sauvé, 1985). This assumption becomes less accurate for more channels, especially if all rate constants are fast. As an example, for the *C-O-B* scheme, 1000 events simulated with 1 channel and rate constants (in s^{-1}) r_{CO}=50, r_{OC}=100, r_{OB}=200, and r_{BO}=1000, were well fitted with t_d=1 ms ($r_{BO} \cdot t_d = 1$), yielding estimates of r_{CO}=44, r_{OC}=91, r_{OB} =163, and r_{BO}=838, although more than 50% of the events were omitted. For the same scheme with 6 channels and 6000 events the estimates were good with t_d=0.5 ms (r_{CO} =57, r_{OC}=118, r_{OB}=150, r_{BO}=1208), but started to deviate at t_d=1 ms (r_{CO}=46, r_{OC}=98, r_{OB}=83, and r_{BO}=855). When three of the rates were slowed down, but r_{BO} left unchanged, the fit worked well even for 6 channels and t_d=1 ms, although 60% of the

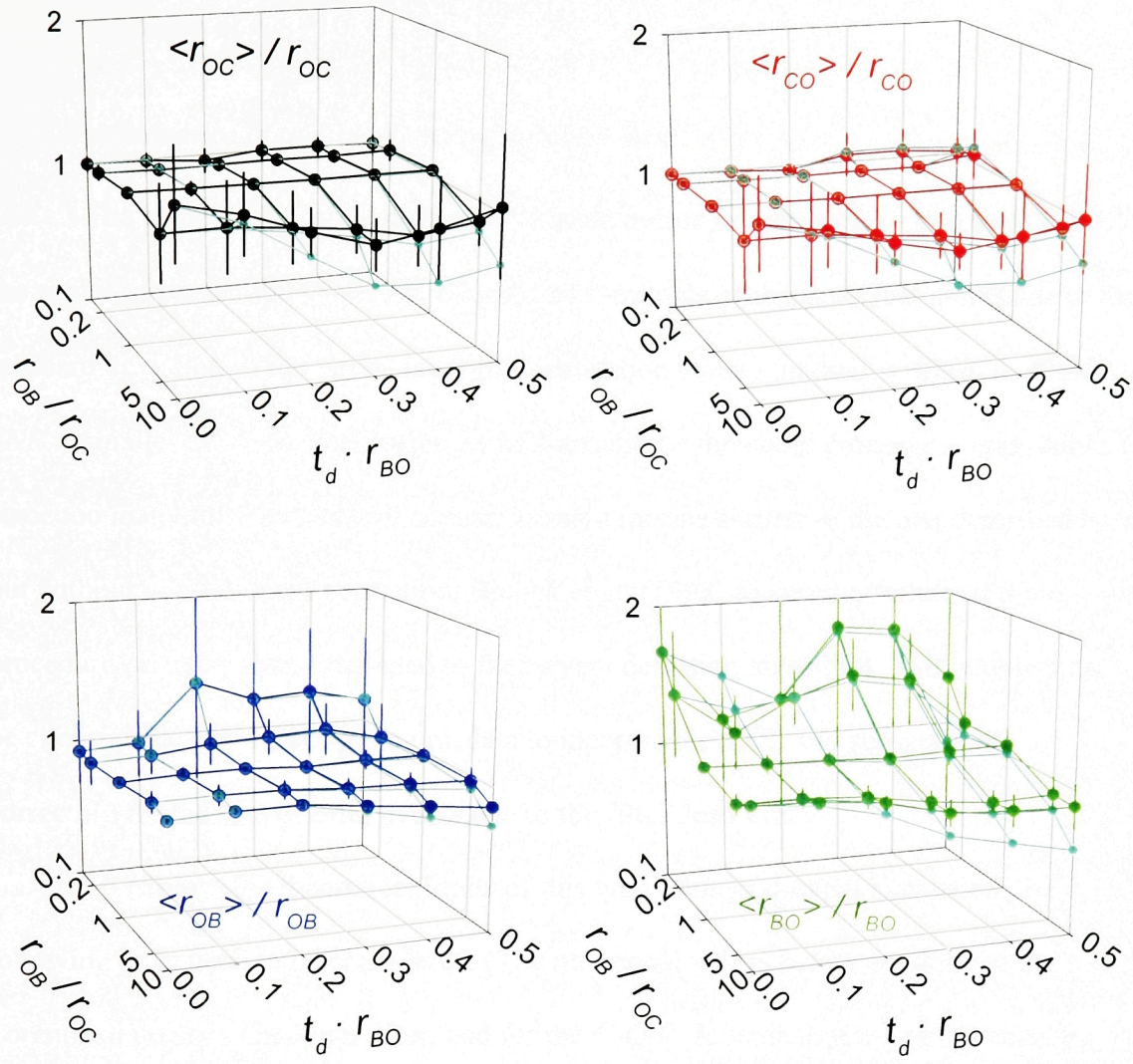

Figure 8. Impact of the implementation of the fixed dead time on subsequent fitting. Comparison of fit results for 6 channels after conventional (cyan symbols) or correct (depicted as in Figure 7.) implementation of a fixed t_d. For $r_{OB} / r_{OC} \geq 5$ and $t_d \cdot r_{BO} \geq 0.3$ conventional idealization resulted in considerable underestimation of the rate constants.

events was lost, yielding, for simulated parameters r_{CO}=10, r_{OC}=20, r_{OB}=100, and r_{BO}=1000, estimates of r_{CO}=10, r_{OC}=19, r_{OB}=83, and r_{BO}=834.

3.3.4. Performance of the fit procedure on noisy data

The advantage of a correction for missed events is applicability to noisy data. If the signal-to-noise ratio (*SNR*; i.e. the ratio of the single-channel current amplitude to the standard deviation of the noise) is small, idealization by any method is difficult. If the *SNR* is smaller than ~5, idealization by half-amplitude threshold crossing is impossible, since too many false events will appear. Using a routine similar to the one described here, but without missed-event correction, Blunck et al. (1998) reported a failure of their procedure on noisy data, attributed to their event detection algorithm. This problem can be circumvented by filtering the raw data to increase the *SNR*, and subsequently correcting for the loss of brief events due to the filter dead time.

To explore the theoretical limits of this type of missed-event correction, the following facts need to be considered. (The numerical values below are derived for Lorentzian noise, a Gaussian filter, and for the *C-O-B* scheme, but the same reasoning applies with only minor variations to other types of noise, filters, and schemes.) First, t_d cannot be very long compared to the shortest lived state in the kinetic scheme. For the *C-O-B* scheme the analysis worked well with all parameter combinations tested, for up to 6 channels, with $t_d \leq 0.5 / r_{BO}$. (Longer dead times also worked as long as r_{CO} and r_{OC} were not very fast.) This imposes a lower limit to the corner frequency used for filtering. For a Gaussian filter, with corner frequency $f_{c,G}$, $t_d \approx 0.18 / f_{c,G}$. Hence, the constraint

$f_{c,G} \gtrsim 0.36 \cdot r_{BO}$ is obtained. Second, reliable idealization by half-amplitude threshold

crossing requires a $SNR \gtrsim 8$. In the common case where the corner frequency of the noise ($f_{c,n}$) is much greater than $f_{c,G}$, the relationship between the *SNR*s before (SNR_n) and after (SNR_G) filtering is

$$SNR_G^2 = SNR_n^2 \cdot (\pi \cdot \ln 2)^{1/2} \cdot f_{c,n} / f_{c,G} \quad . \tag{16}$$

Combining this result with the above inequalities yields

$$SNR_n^2 \cdot f_{c,n} \gtrsim 8^2 \cdot 0.36 \cdot (\pi \cdot \ln 2)^{-1/2} \cdot r_{BO} \approx 16 \cdot r_{BO} \quad . \tag{17}$$

This is an approximate guideline for the quality of the raw data, required for efficient use of this approach. As an example, if r_{BO}=1000s^{-1} (i.e. the mean blocked time is 1 ms), raw data acquired at an initial bandwidth of 5 kHz will have to satisfy $SNR_n \gtrsim 1.8$. On the other hand, SNR_n at 5 kHz can be as low as 1, if the mean blocked time is longer than 3 ms. (For other schemes r_{BO} is replaced by the fastest rate constant, and for different noise characteristics and filters the numerical values will be somewhat modified.)

To test the missed-event correction algorithm on more realistic records than the noise-free simulations used for Figs. 4, 5, and 6, the fit procedure was tested on noisy current traces. The testing was structured as illustrated in Figure 9A. Channel currents were simulated and overlaid by noise. *SNR*s as low as 3, 2 and 1 were tested, in which cases idealization by threshold crossing was impossible. Noisy traces were Gaussian-filtered digitally to increase the *SNR* to 8 -10. Filtered traces were idealized by half-amplitude threshold crossing combined with the imposition of a fixed t_d, about twice the

dead time of the filter, to minimize uncertainties caused by noise (see representative noisy, filtered, and idealized traces in Figure 9A). Finally, events lists were fitted to yield estimates of the rate constants.

The program performed well on noisy data after filtering. Figure 9B provides a summary of one such series of 150 experiments, structured like the one shown in Figure 9A. With a fixed ratio of $r_{BO} / r_{CO} = 20$, r_{OB} / r_{OC} was varied between 0.1 and 10 (x axis), with channel numbers ranging from 1 to 6 (y axis). Each parameter combination was simulated 5 times. Initial noise was characterized by $SNR_n = 2$ and $f_{c,n} = 5.0 \cdot r_{BO}$. Noisy traces were filtered at $f_{c,G} = 1.0 \cdot r_{BO}$, and idealized with $t_d = 0.4 / r_{BO}$. A sampling rate of 20 times $f_{c,G}$ was used. From Figure 9B, the performance of the analysis under these conditions is comparable to that seen for noise-free simulations (cf. Figure 7), confirming the applicability of the approach in realistic situations.

It is of interest to visualize the impact of missed-event correction. The same set of noisy traces described in the previous paragraph were also filtered at $f_{c,G} = 0.45 \cdot r_{BO}$, resulting in a filter dead time of $0.4 / r_{BO}$, equal to t_d above. These traces were then idealized by simple half-amplitude threshold crossing, without imposing any artificial dead time. The events lists were then analyzed without missed-event correction, i.e. Eqs. 2 and 5 were used in the program cycle instead of Eqs. 14 and 15. The resulting estimates for the rate constants are plotted in Figure 9B in cyan. (Error bars are omitted for clarity.) Roux and Sauvé (1985) showed that for a single channel with a *C-O-B* scheme, as long as t_d is short compared to the mean duration of sojourns in *C*, the estimates of r_{CO} and r_{OC} remain undistorted, even if most blocked events are filtered out. This is verified in Figure 9B, where, for 1 channel, lack of missed-event correction

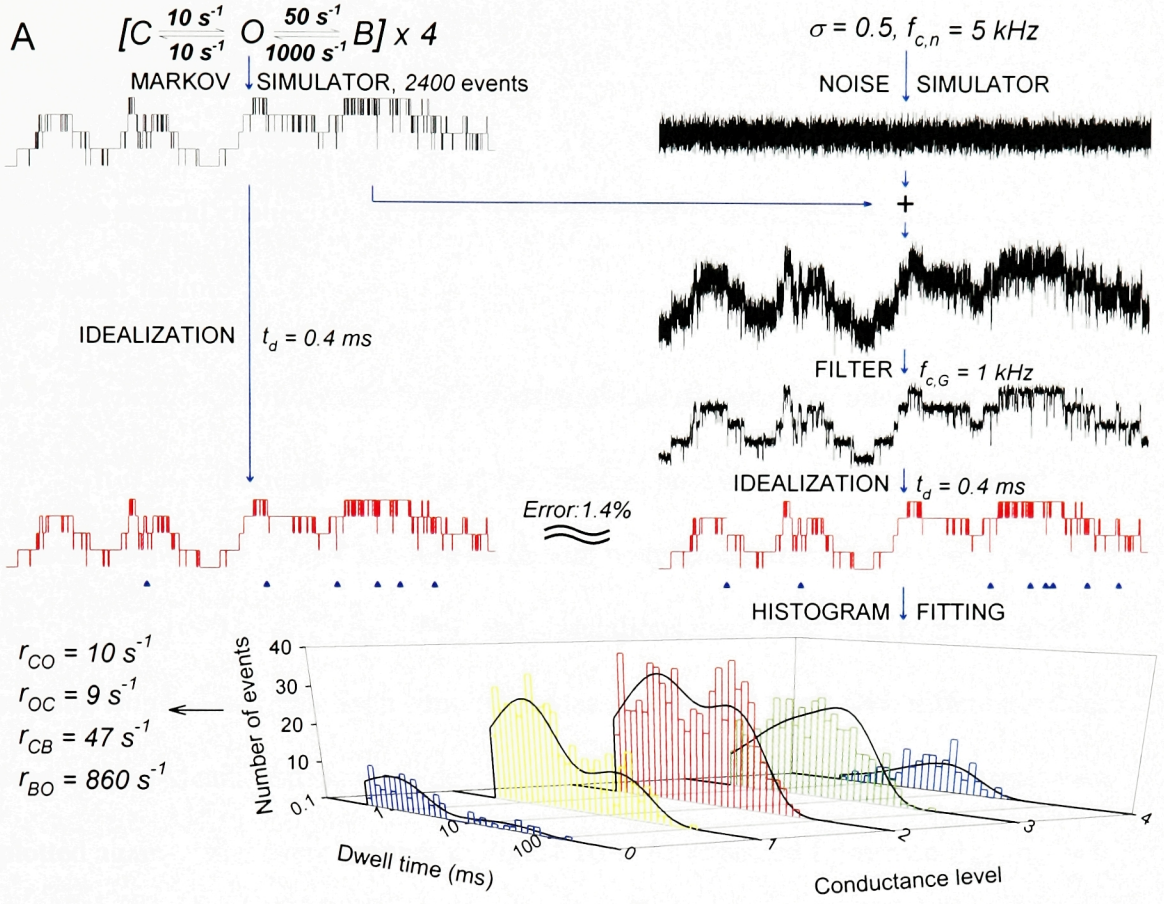

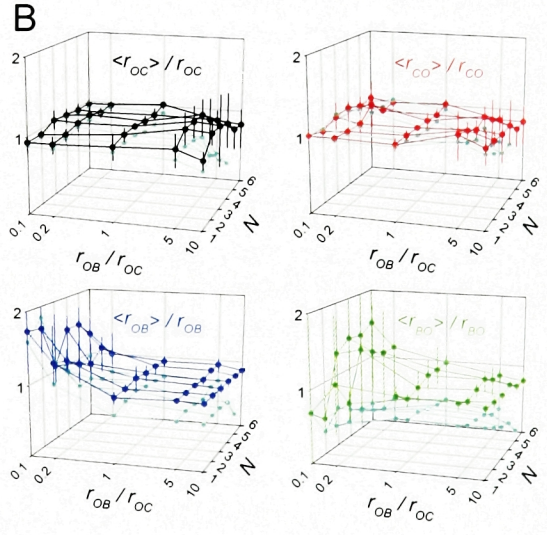

Figure 9. Testing of the fit procedure on noisy current traces. Simulated noise was added to channel currents. Noisy traces were Gaussian-filtered digitally, idealized by half amplitude threshold crossing, and events lists fitted to extract rate constants. **A,** Test structure. Idealization, with the same t_d, of noise-free channel currents and noisy traces after filtering gave 98.6% identical results. ▲, "flags" (see text). **B,** Summary of 150 tests like in **A**. Means of parameter estimates from 5 simulations, normalized, plotted against r_{OB}/r_{OC} and N. Error bars are s.d. Simulation parameters: *C-O-B* scheme, r_{BO}/r_{CO}=20, SNR_n=2, $f_{c,n} = 5.0 \cdot r_{BO}$. Filter: $f_{c,G} = 1.0 \cdot r_{BO}$. Idealization: $t_d = 0.4/r_{BO}$. Cyan symbols are estimates obtained without missed-event correction: r_{CO} and r_{OC} are well estimated for N=1, but less so for N>1.

results in underestimation of r_{OB} and r_{BO} only. However, with many channels, lack of correction results in underestimation of r_{CO} and r_{OC} as well. This is because, even if r_{CO} and r_{OC} are slow compared to the dead time, transitions between C and O are lost when there are several channels, if mirroring transitions of two different channels occur close to each other in time.

3.3.5. Dependence of the scatter of the estimates on the length of the record

It is useful to establish for a given scheme, how many events are required for reliable fitting. The *C-O-B* model was chosen with fixed parameters r_{CO}=50 , r_{OC}=10, r_{OB}=2, r_{BO}=1000, t_d=0.2 / r_{BO}, N=4, and simulations were done with event numbers ranging from 40 to 5000. Each simulation was repeated 10 times with different random seed values. Means and standard deviations of the normalized parameter estimates are plotted against total event number in Figure 10A. As expected from ratio $r_{OB} / r_{OC} = 0.2$, the errors of the estimates of r_{OB} and r_{BO} exceed those of r_{CO} and r_{OC}. For all rate constants, however, the scatter becomes smaller with increasing numbers of events. Figure 10B shows the sizes of the error bars from Figure 10A plotted against the number of events. The dependence of the errors of r_{OB} and r_{BO} on total event number is shifted to the right compared to the errors of r_{CO} and r_{OC}. From the total number of events the expected number of individual transitions along any of the four pathways is easily calculated. These numbers are plotted in red as an alternative abscissa in Figure 10B. The shift of r_{OB} and r_{BO} compared to r_{CO} and r_{OC} is less dramatic from the perspective of this new abscissa. The standard deviations of r_{CO} and r_{OC} decrease to ~20% with ~200 corresponding transitions, and a similar number of respective transitions brings the errors of r_{OB} and r_{BO} also down below 30%.

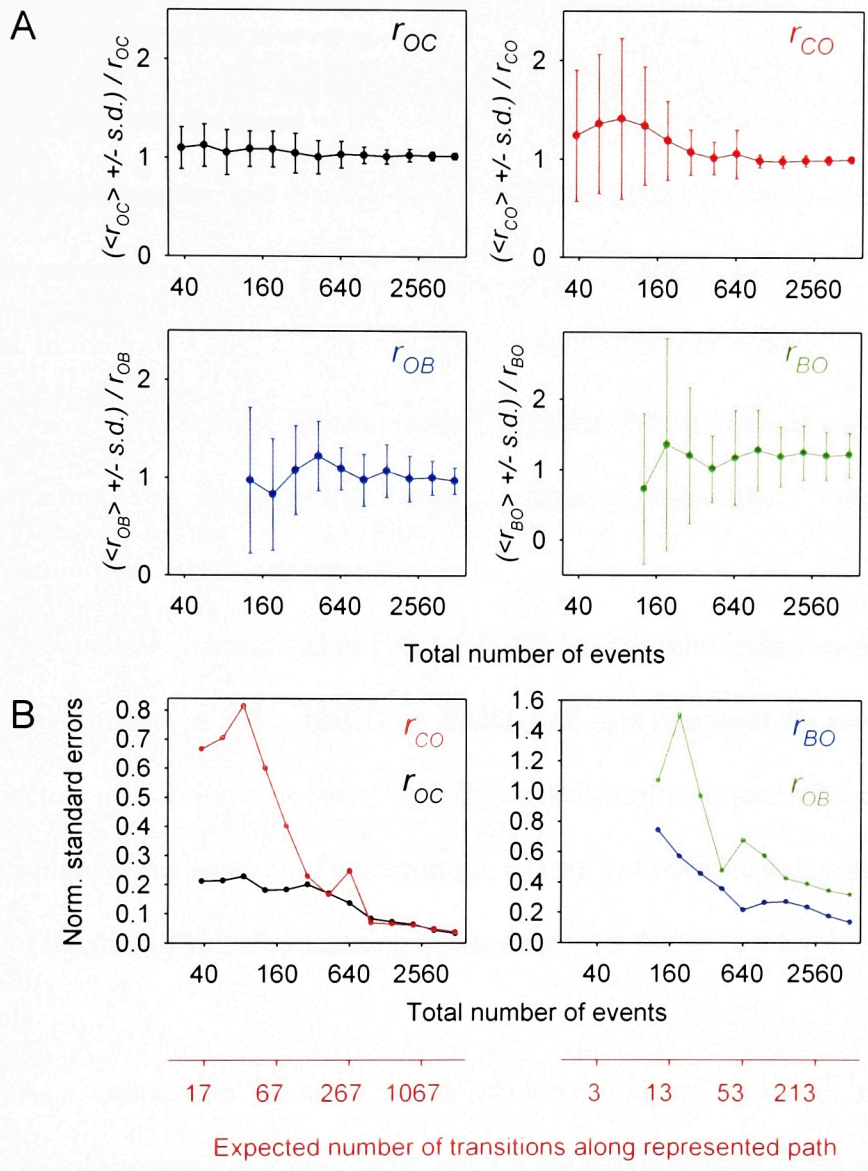

Figure 10. Dependence of the scatter of the estimates on the length of the record. Channel currents of different lengths were simulated with the same set of parameters (*C-O-B* scheme, r_{CO} =50 , r_{OC} =10, r_{OB} =2, r_{BO} =1000, N=4), idealized with t_d=0.2 / r_{BO}, and fitted. **A,** Normalized parameter estimates vs. total event number, means ± s.d. from 10 simulations. Since r_{OB}/r_{OC} =0.2, errors of r_{OB} and r_{BO} exceed those of r_{CO} and r_{OC}. All errors decrease with larger numbers of events. **B,** Lengths of the error bars from **A** vs. total event number. Alternative abscissa (red) describes expected numbers of transitions along represented pathways. Errors are more uniform with respect to alternative abscissa: <20% for r_{CO} and r_{OC}, and <30% for r_{OB} and r_{BO} for ~200 corresponding transitions.

3.3.6. Dependence of the processing time on channel number and length of record

To illustrate the speed of the fitting, the processing time was measured on events lists of various lengths, and different numbers of channels. The processing time depends on many parameters including kinetic scheme, rate constants, and initial parameter guesses. In the following experiments the *C-O-B* scheme was used with r_{CO}=50, r_{OC}=10, r_{OB}=50, r_{BO}=1000. Seed parameters were chosen based on a quick estimate of the cycle-time, obtained by counting the number of transitions per unit time. Fitting was performed on a *Pentium* 266 MHz machine.

Results are summarized in Figure 11. Channel number was varied from 1 to 6, with event numbers of 3300, 10000, or 30000. Red bars represent the mean of three trials. As expected, processing time (note logarithmic ordinate) increases with channel number (as the square of the number of macroscopic states), but remains independent of the length of the data. Typical processing times were ~1 s for 1, ~6 s for 4, and ~33 s for 6 channels.

As a comparison, the same events lists were analyzed with *MIL*, part of the *QuB* single channel analysis package, which maximizes the likelihood of the joint probability density for the whole dwell time series (Qin et al. 1996, 1997). Results are shown as blue bars in Figure 11. Large differences in processing time are apparent for N=4 and 5, where *MIL* typically converged after ~500 s and ~5000 s respectively, compared to ~6 s and ~14 s for the present histogram method. With 6 channels *MIL* failed to initialize, but the extrapolated processing time is ~50000 s (14 hours, cyan bars in Figure 11) as opposed to ~30 s with the method given here. The resulting estimates were essentially identical for the two approaches.

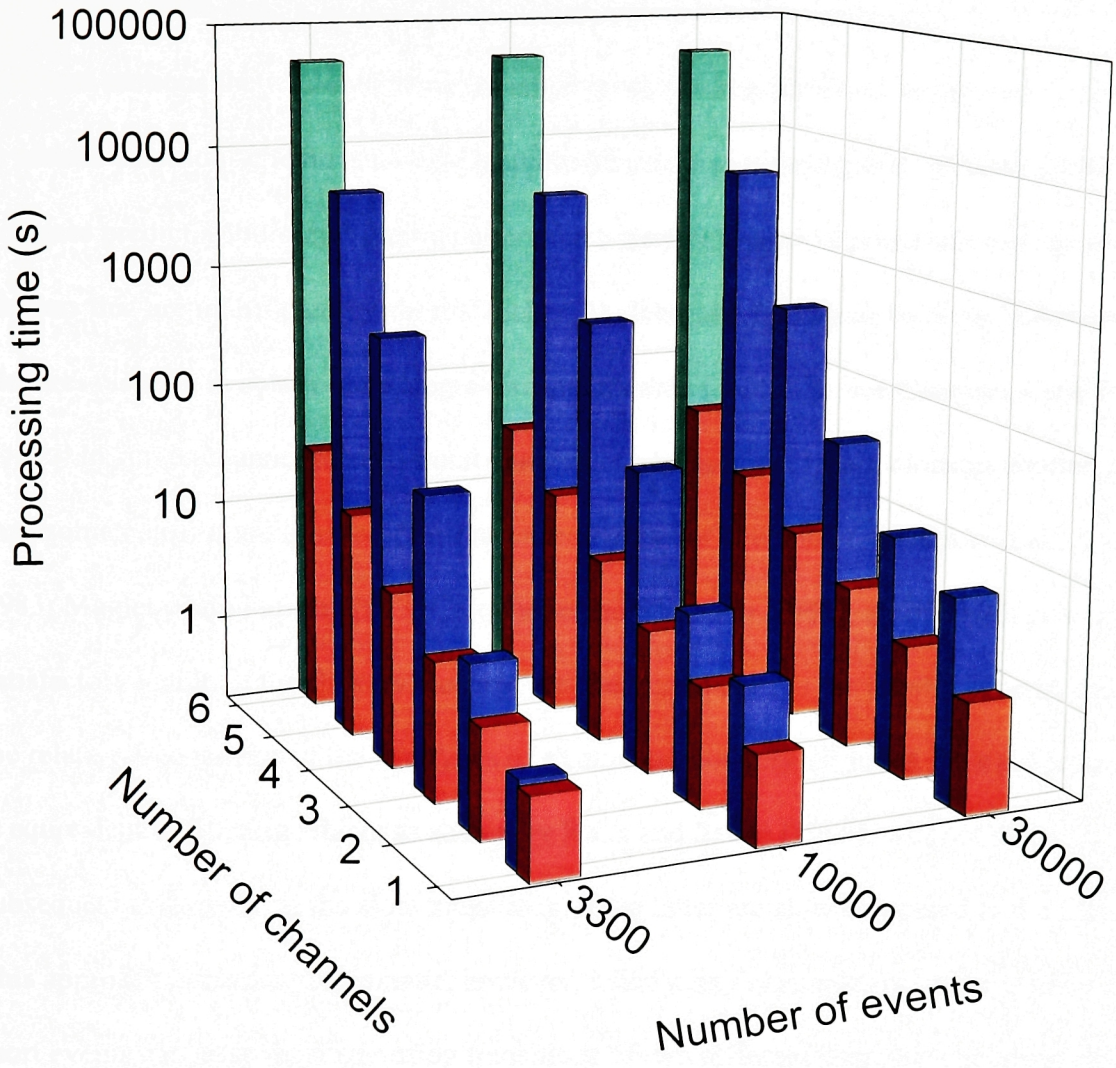

Figure 11. Speed of the fitting process. Comparison of processing times for simultaneous histogram fitting (red bars) and complete time series fitting (*MIL*, blue bars). Bars are means of three measurements. Processing time for simultaneous histogram fitting increases proportionally with the square of the number of macroscopic states, but is independent of the length of the record. Typical processing times were 1, 2, 3, 6, 14, 33 s for N=1, 2, 3, 4, 5, and 6 respectively. For comparison, *MIL* produced identical estimates after processing times of 3, 6, 50, 500, and 5000 s for N=1, 2, 3, 4, and 5 respectively, and 10000 events. Extrapolated processing time for N=6 (cyan bars) is ~50000 s (14 hours) with *MIL*.

3.3.7. Applicability to different gating schemes

Two three-state schemes are encountered frequently in ion-channel physiology. In previous sections the *C-O-B* scheme (open-channel block model) was tested extensively. A second common scheme is C_1-C_2-O, applicable, e.g., to ligand-gated channels. Both schemes predict a "bursting" gating pattern for a single channel, where openings occur in clusters that are interrupted by short ("flickery") closures and flanked by long "interburst" closures, as seen in steady-state single-channel records for CFTR (see Chapters 4 and 5).

In single-channel records burst analysis can be applied, where closings shorter than some cutoff t_c are ignored. Various criteria exist for choosing t_c (Jackson et al., 1983; Magleby and Pallota, 1983; Colquhoun and Sakmann, 1985), all of which give satisfactory results if the flickery closures are short compared to the interburst time, and the relative frequencies of the two types of closure are not very different. This procedure is equivalent to filtering which, as shown by Roux and Sauvé (1985), will not distort subsequent estimation of the slow transitions, if the latter are slow compared to the filter. This approach becomes problematic, however, when many channels are present, since short events can arise from mirroring transitions of two different channels occurring close to each other in time. As shown earlier in this chapter, even short dead times can seriously distort the estimation of slow rate constants in multichannel patches, unless appropriate care is taken (see, e.g., Figure 9B, cyan symbols).

In records with multiple channels, if the open probability of a single channel is very low, such that the average number of open channels at any given time is small, Jackson (1985) showed that the rate constants can be estimated from the distribution of closed times (all channels closed) and open times (one channel open, no superimposed

openings). If the activity of the channels is high, however, such events become rare, limiting the applicability of that approach.

The method described here was also tested on the C_1-C_2-O model, with channel numbers ranging from 1 to 6, and, as with the *C-O-B* scheme, it was found to perform well regardless of the open probability ($0.01 \leq P_o \leq 0.99$) of the channels. Table I summarizes the results of a limited range of fitting experiments for the C_1-C_2-O scheme. Essentially identical results were obtained for this scheme, although after much longer processing times (like in Figure 11), using the more sophisticated program *MIL* (Qin et al. 1996, 1997). The remaining two linear three-state schemes, C-O_1-O_2 and O_1-C-O_2, were also tested with success on a few simulated records, but those schemes have less relevance for the study of CFTR channels, and are not discussed here.

3.4. Summary and recommendations

A procedure has been developed for quickly and reliably extracting rate constants of channel gating from patch recordings containing multiple channels. The algorithm is based on a simultaneous maximum likelihood fit to the dwell-time histograms for the various conductance levels. It does not exploit correlations between adjacent events, but results in a greatly reduced computational task and, hence, processing time. This feature makes it attractive for the analysis of multichannel patches, in cases where the gating scheme itself is already known and relatively simple. Of course, patches with multiple channels, and analyses using this algorithm, are not the tools of choice for solving complicated schemes, nor for distinguishing between rival gating models. For those

purposes single-channel records are desirable, along with correlation analysis using event sequence fitting or two-dimensional histograms.

The theory is illustrated for N identical and independent channels, but can be applied straightforwardly to more general cases; for such systems (e.g., non-identical channels, or channels influencing each other) the **Q** matrix of the macroscopic system will have to be constructed using the full, n^N-dimensional, state-space (instead of Eq. 1, cf. Qin et al., 1996). The algorithm is tested on two common three-state schemes, *C-O-B* and C_1-C_2-O, both of which yield a burst-type gating pattern, but it is expected to work on other simple (e.g. three-state) schemes as well. It can be recommended for such schemes when 3 or more channels contribute to the recorded current, since a considerable decrease in processing time is gained in comparison to more advanced routines (see Figure 11 for a comparison with *MIL*, the fitting routine in the *QuB* package), without any loss of accuracy.

Accurate parameter estimates are obtained from as little as a few hundred events, if there are no large discrepancies between the frequencies of occurrence of the single-channel gating steps. On the other hand, the accuracy increases with longer recordings, without any cost in processing time or memory space requirement.

A robust correction for missed events due to filtering allows the algorithm to be applied to noisy data. Limitations for such cases are summarized in Eq. 17, which provides acceptable limits for the relationship between speed of channel gating and magnitude and bandwidth of noise.

TABLE I **Parameter estimates for the C_1-C_2-O_3 scheme.**

Rates are s^{-1}, t_d is ms, errors are s. d. (n=5 simulations).

	r_{12}	r_{21}	r_{23}	r_{32}	N	t_d
True value	50	800	200	100	2	0.2
Estimate	56±11	750±215	171±55	97±5		
True value	50	500	500	100	2	0.2
Estimate	50±4	480±103	437±67	97±4		
True value	50	200	800	100	2	0.2
Estimate	49±9	189±26	721±25	95±2		
True value	50	800	200	100	4	0.2
Estimate	47±3	616±14	166±17	99±2		
True value	50	500	500	100	4	0.2
Estimate	50±8	446±90	420±30	95±3		
True value	50	200	800	100	4	0.2
Estimate	48±4	179±16	701±94	94±5		
True value	50	800	200	100	6	0.2
Estimate	51±3	616±50	152±11	98±2		
True value	50	500	500	100	6	0.2
Estimate	52±6	480±99	439±43	96±2		
True value	50	200	800	100	6	0.2
Estimate	40±5	138±26	644±66	94±1		
True value	50	200	800	100	4	0.0
Estimate	52±7	244±29	894±60	100±4		
True value	50	200	800	100	4	0.2
Estimate	48±4	179±16	701±94	94±5		
True value	50	200	800	100	4	0.4
Estimate	49±5	231±45	960±192	108±10		

4. FUNCTIONAL CHARACTERIZATION OF WILD TYPE HUMAN EPITHELIAL CFTR EXPRESSED IN *XENOPUS* OOCYTES

4.1. Whole-oocyte conductances measured by two-microelectrode voltage clamp

Xenopus oocytes have proven to be a convenient expression system for functional and biochemical analysis of a variety of ion channels, including CFTR (e.g. Bear et al., 1991; Smit et al., 1993; Wilkinson et al., 1996; Naren et al., 1999). Two-electrode voltage clamp is a handy way of assaying the total conductance of a large number (typically millions, for CFTR) of such heterologuously expressed channels, and remains, despite its crude nature, an important initial screening strategy for channel function.

4.1.1. Wild type CFTR channels display basal activity in resting Xenopus oocytes

Since large ionic currents (tens of microamperes) can be elicited in oocytes overexpressing an ion channel, it may be expected that over prolonged recordings intracellular ion concentrations will shift. To avoid Cl^--loading/depletion of the oocytes during long recordings, time courses of CFTR activation were routinely measured while holding the membrane potential close to E_{Cl}, with brief applications of ±60 mV voltage pulses every 1-2 minutes to assay changes in conductance. Healthy, uninjected (or H_2O-injected) oocytes have typical resting conductances of ~2 μS (0.5 MΩ). Two to three days after injection of 2.5 ng cRNA encoding WT CFTR, oocytes display a significantly higher (10±1 μS) resting conductance when compared to uninjected control cells. The resting potential in these oocytes is found to lie close to the expected reversal potential for Cl^- (E_{Cl},-20 to -30 mV). Most of this resting conductance can be abolished by

injection of RpcAMPS (~2 mM final concentration, see also below, Chapter 7). RpcAMPS is a structural analog of cAMP, resistent to phosphodiesterases, which binds to the regulatory subunits of PKA, without causing the release of the catalytic subunit. The result is inhibition of PKA activity. The resting conductance in CFTR-expressing oocytes is hence a Cl^- conductance that depends on PKA activity, and that is absent from uninjected oocytes. The simplest interpretation of these results is that the ~10-μS resting conductance of CFTR-injected oocytes reflects CFTR channel activity corresponding to some basal level of phosphorylation, maintained at equilibrium by opposing resting activities of PKA and of phosphatase(s).

4.1.2. Maximally activatable CFTR conductances

When the cAMP/PKA pathway is stimulated in oocytes expressing WT CFTR by superfusing them with 1 mM IBMX and 50 μM forskolin, a large CFTR current is activated in 2 to 4 minutes. The maximum conductance in the presence of forskolin and IBMX is 173±4 μS. Current activation is reversible, to resting levels, when IBMX and forskolin are washed away. (IBMX washes off slowly, in ~20 minutes, likely due to its redistribution into the lipid environment of the yolk). Faster washoff (~5 minutes), but smaller maximal currents are obtained if forskolin alone (50 μM) is used as the activator. This stimulation of CFTR current by forskolin and IBMX presumably reflects activation of the channels by PKA-mediated phosphorylation (e.g. Bear et al., 1991; Smit et al., 1993), and possibly also by a direct stimulation by IBMX (Al-Nakkash and Hwang, 1999).

4.1.3. Saturation of whole-oocyte conductances, interpretation of two-electrode data

When titrating the amount of injected cRNA, both basal and maximally activatable conductances increase linearly with the amount of cRNA, up to injected amounts of ~0.5 to 1 ng. Above this range, however, while basal conductance continues to increase in proportion to the amount of cRNA, maximally activatable conductance saturates at the above-mentioned ~180 μS. Preliminary results of Western blots of total oocyte membrane protein indicate that CFTR protein expression levels still increase with injected cRNA well above 1 ng. This suggests that activation, not production, of the channels becomes rate-limiting. Since channels are activated via the endogenous PKA pathway, saturation may occur at any one of several steps, and is not yet understood. For this reason the two-electrode measurements may be viewed as a crude, *yes*-or-*no* type assay of channel expression. Only mutant constructs that gave sizeable whole-oocyte conductances were routinely selected for further detailed study.

4.2. Hallmarks of CFTR in excised patches

4.2.1. Background conductances in the oocyte membrane

After patch excision, under ionic conditions where the only permeant ion is pipette Cl^- (NMG^+, the cation in both pipette and bath solutions is too large to pass through most cation channels, and bath sulfamate does not permeate through most anion channels), at a membrane potential of +40 mV ($V_{pipette}$ = -40 mV), a small seal current of <0.4 pA was routinely recorded, indicative of a seal resistance of >100 GΩ. Under these conditions, the only endogenous current that can be readily activated in the oocyte membrane is that through Ca^{2+}-activated chloride channels. Figure 12 shows, under these ionic conditions

but at V_m= 0 mV, reversible activation of a large outward current upon superfusion of the cytoplasmic surface of the patch with 2 mM Ca sulfamate. Conductances before, during, and after the Ca^{2+} pulse were assessed by a voltage ramp protocol. Panel B shows the current/voltage relationship of the Ca^{2+}-dependent component, obtained by subtracting ramp current obtained before Ca^{2+} application from that measured in the presence of Ca^{2+}, and plotting the difference against voltage. The plot shows a slightly outwardly rectifying current, which does not reverse at the lower ramp voltage of -50 mV, consistent with a conductance highly selective for chloride (over sulfamate). Unitary currents underlying this conductance could never be resolved. The conductance diminished immediately when Ca^{2+} was removed (cf. I/V plot c-a), and the time course of this current decay was used to estimate the speed of solution exchange in individual patches. This rate of current decay, possibly rate-limited by the speed of deactivation of the Ca^{2+}-dependent Cl^--channels, and hence conceivably slower than the real solution exchange rate, was nevertheless fast enough (typically 2 to 5 s^{-1}) compared to the rates of CFTR gating studied using concentration jumps (off-rate of AMPPNP from CFTR, 0.02 to 0.2 s^{-1}, see below). This current was not seen while CFTR channel currents were recorded, since bath free [Ca^{2+}] was kept in the nanomolar range by 0.5 mM EGTA.

Apart from the Ca^{2+}-dependent Cl- current, large non-selective, presumably stretch-activated, channels were observed occasionally, which were easily distinguished from CFTR by their many-fold larger unitary current size.

4.2.2. Single-channel conductance of CFTR

In patches excised from oocytes injected with small amounts (0.01 to 0.1 ng) of cRNA encoding WT CFTR, unitary currents were readily observed. Figure 13 shows

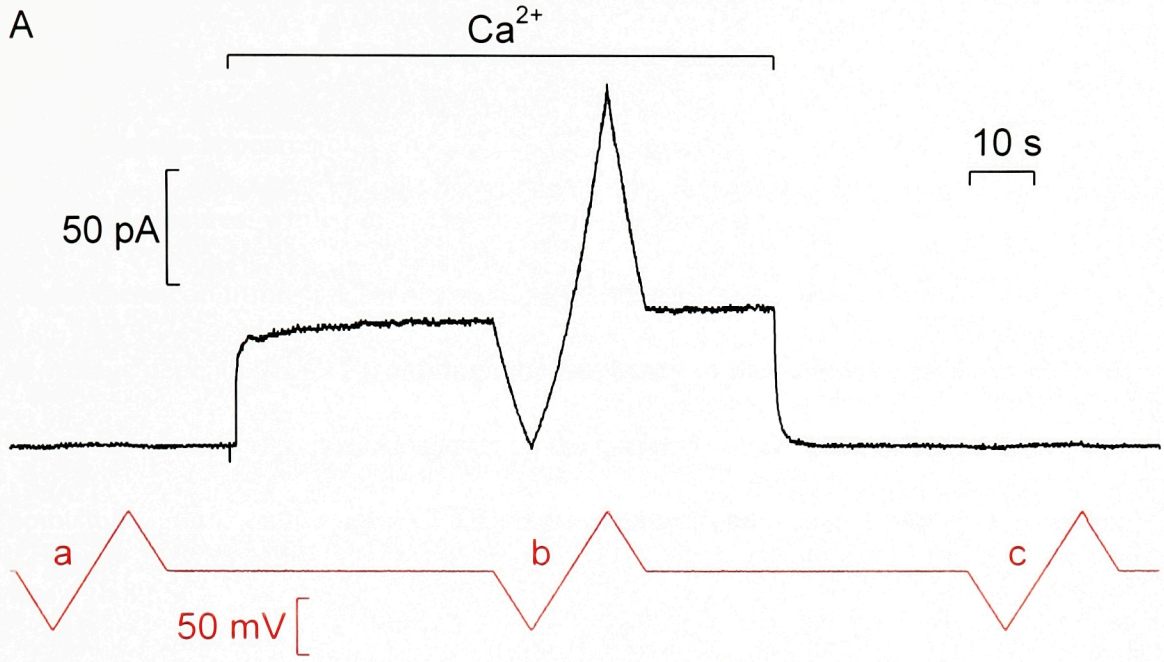

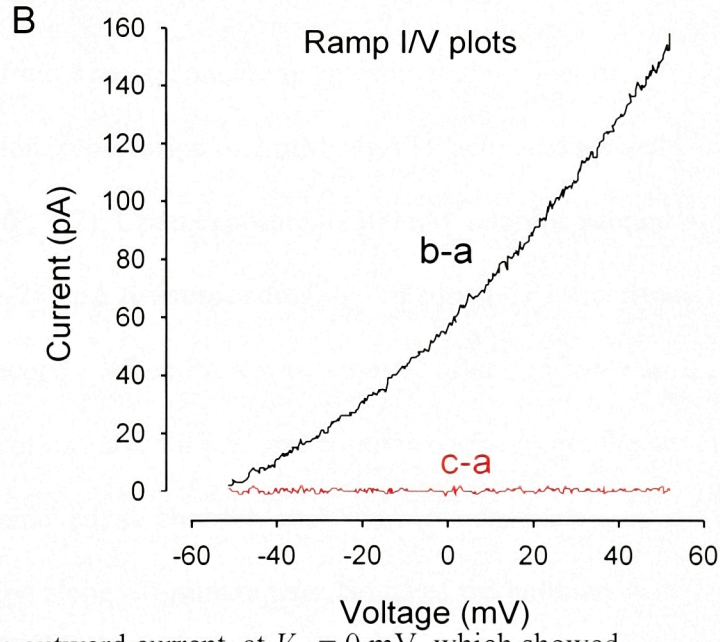

Figure 12. Endogenous Ca^{2+}-activated Cl- channel current in the oocyte membrane. A, Current (*black*) and voltage (*red*) traces recorded from a patch under bi-ionic conditions (pipette, Cl^-, bath, sulfamate$^-$). Small current response to an initial voltage ramp protocol (*a*, 12 s ramp between -50 and +50 mV), R_{seal} = 100GΩ. 2mM Ca-sulfamate induced a large outward current, at V_m = 0 mV, which showed outward rectification in response to a second voltage ramp (*b*). The current inactivated immediately, and completely, after Ca^{2+} was removed; current response to a third voltage ramp after Ca^{2+} washoff (*c*) was indistinguishable from the initial response. **B,** Difference I/V plots from ramp currents, demonstrating high Cl^- vs. sulfamate$^-$ selectivity ($p_{Cl}/p_{Sulfamate} > 10$, assuming $E_{rev} < -60$ mV) of the Ca^{2+}-dependent current component (*b-a*, *black*), as well as complete reversibility after Ca^{2+} washoff (*c-a*, *red*).

representative traces of prephosphorylated CFTR channels, recorded in symmetrical 140 mM Cl^- with 2 mM MgATP in the bath, at holding potentials of -80, -40, 0, +40, and +80 mV. Openings appeared clustered into bursts comprising openings separated by short "flickery" closures, while bursts themselves were flanked by longer, interburst closures. Under these conditions CFTR channels appeared essentially ohmic, with no obvious time or voltage dependence of P_o, although the frequency of short flickery closures was clearly higher at negative voltages. As shown on the current /voltage plot, obtained from the all-points histograms on the right, CFTR single-channel conductance under these conditions was 6 to 8 pS.

4.2.3. Phosphorylation dependence of channel activity

Figure 14A shows a current trace from a patch containing an estimated number of ~2000 CFTR channels. After patch excision, superfusion of 2 mM MgATP activated a small number of channels in this case ($NP_o \sim 2$). Upon exposure to 300 nM catalytic subunit of PKA, however, a large current of ~250 pA (corresponding to ~700 open CFTR channels) developed in little more than 10 seconds. When PKA was removed after ~35 seconds, the current rapidly diminished to ~1/3 of its maximal size, and continued to decrease thereafter at a slower rate. When ATP was removed, all channels shut, but some channels were still activatable when ATP was reapplied alone, ~1 minute later. Some of the hallmark characteristics of CFTR gating, that emerge already from this simple experimental protocol, are that no channel opening is observed unless CFTR is phosphorylated by PKA, and that phosphorylated channels are capable of opening in the absence of PKA as long as MgATP is supplied, but not in the absence of ATP. Since channels were not opened initially by ATP, but were so following exposure to PKA, it seems likely that at

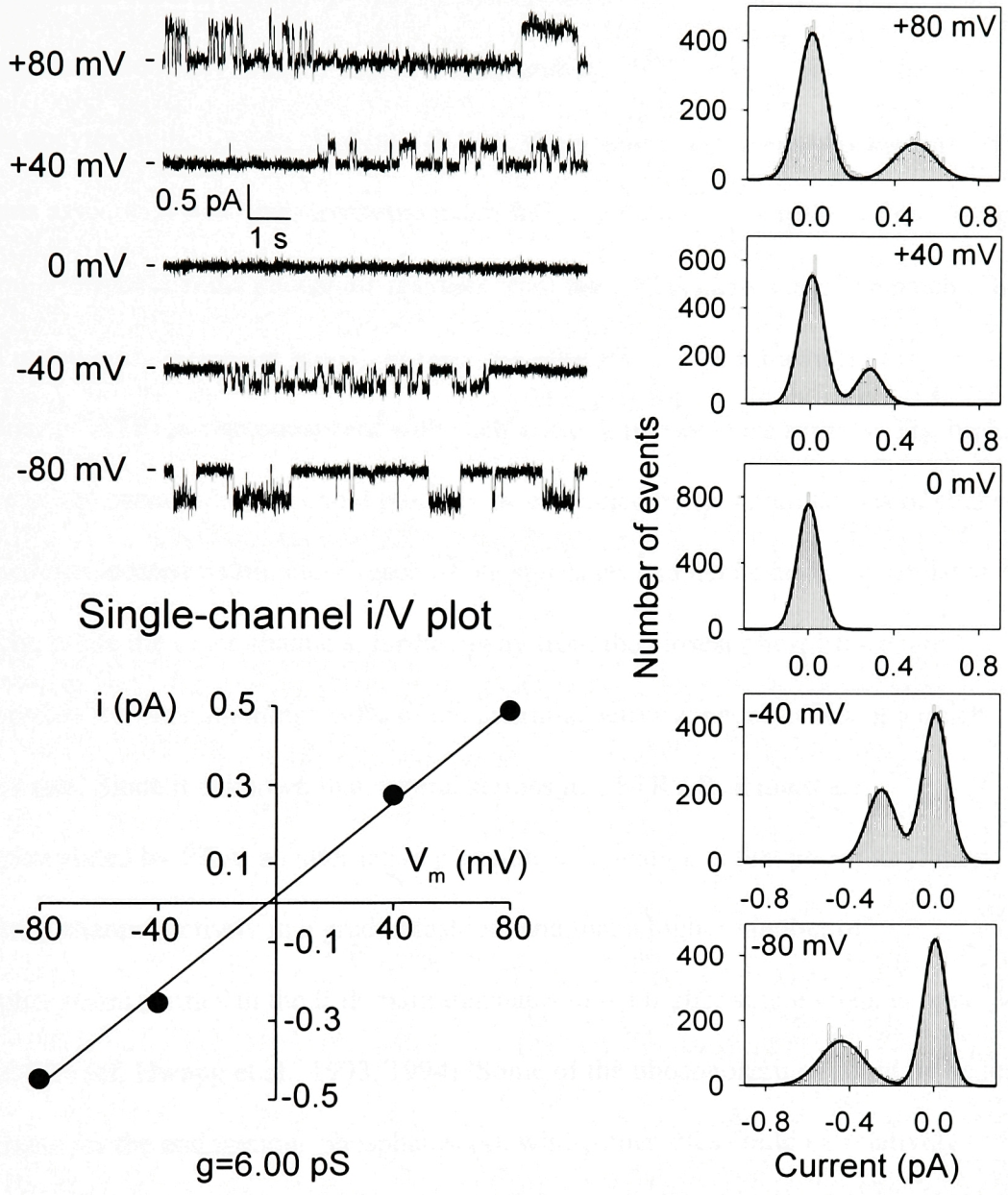

Figure 13. Single-channel conductance of WT human epithelial CFTR. Current segments at holding potentials of -80, -40, 0, +40, and +80 mV, recorded in the presence of 2 mM MgATP, in symmetrical 140 mM Cl^-, from a patch containing WT CFTR channels. Gaussian fits to all-points histograms (shown on the right) were used to estimate unitary current sizes at the various holding potentials. The slope of a linear fit to the plot of unitary current amplitude versus voltage, shown below, revealed a single-channel conductance of 6 pS in this case (6.8±0.3 on average, from 4 experiments).

the start of the record, ~2 minutes after patch excision, CFTR channels were in a dephosphorylated state. Since small, but measurable, CFTR activity is recorded from whole oocytes in the resting state (see above), this implies that a phosphatase activity remains associated with the membrane patch following excision, capable of removing, within ~2 minutes, most phosphate residues from the CFTR channels in the patch. The rapid initial current decline seen in Figure 14A after PKA is withdrawn (in the continued presence of ATP) is also consistent with such a strong phosphatase activity. The biphasic nature of the current decline could possibly be explained by two populations of channels, one perhaps located within close reach of phosphatases and hence dephosphorylated quickly, while the other channels, further away from the closest phosphatase, are responsible for the remaining ~30% of the maximal activity, which is lost at a much slower rate. Since it is known that several serines in CFTR's R domain are phosphorylated by PKA, an alternative plausible explanation is that phosphorylation regulates channel activity in a graded fashion, and that a higher number of phosphorylated serines in the R domain translates into a higher single-channel open probability (cf. Hwang et al., 1993, 1994). Some of the phosphoserines could be better substrates for the endogenous phosphatase(s), while other sites could be relatively phosphatase resistent and so could account for the longer lasting residual activity.

The latter possibility is supported by experiments like that shown in Figure 14B, illustrating an experimental paradigm similar to the one in panel A, but for a patch containing only a small number of channels. Kinetic analysis of such patches reveals a rapid shortening of burst durations after PKA is removed (from ~800 ms to ~250 ms), accompanied by a slower increase, over time, in the interburst durations (from ~1500 ms,

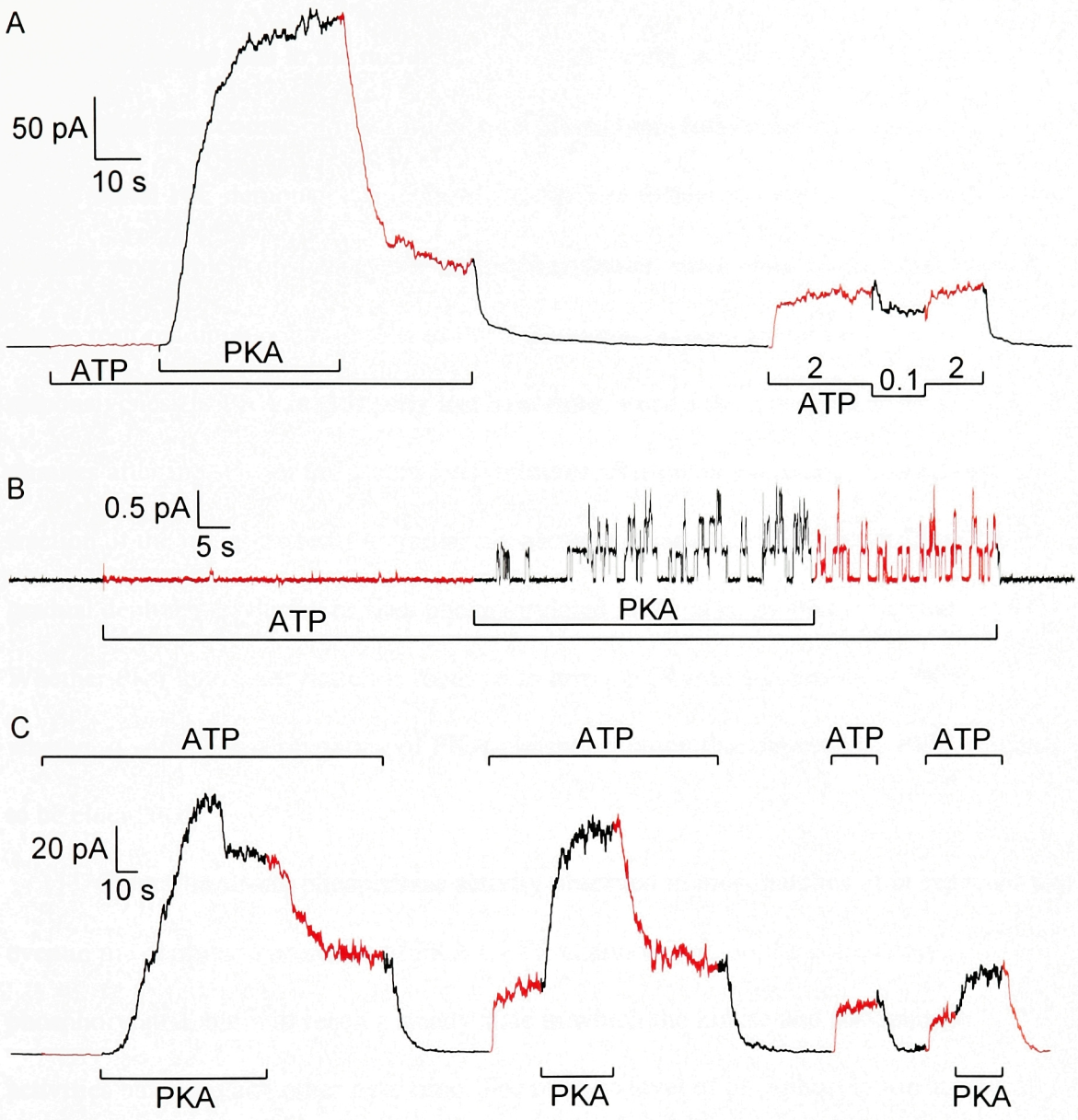

Figure 14. Phosphorylation dependence of WT CFTR activity. A, PKA activates CFTR channels in a macropatch. Some channel activity is seen in the continued presence of ATP following removal of, but not before exposure to, PKA. The magnitude of the residual current is sensitive to ATP concentration, as seen from alternating exposures to 2 mM or 100 μM ATP. **B,** Experiment similar to **A**, but in a patch with few CFTR channels. Shortened bursts are observed after withdrawal of PKA. **C,** The current decline following PKA removal is initially reversible, as most of the activity is restored by a second exposure to PKA, but less so by a third exposure ~ 10 minutes after patch excision.

in the presence of PKA) . Thus, a biphasic decrease in the single-channel open probability, rather than in the number of active channels, is responsible for the biphasic deactivation time course of macroscopic CFTR currents following PKA removal.

Panel 14C demonstrates that the activity loss following removal of PKA is at least partially reversible, consistent with dephosphorylation, since close to maximal activity can be restored upon reapplication of PKA. However, as seen in the same record, responsiveness to PKA is gradually lost over time, since a third reapplication of PKA ~8 minutes after the start of the record (~10 minutes after patch excision) restored only a fraction of the initial current. A similar phenomenon was observed, and attributed to gradual dephosphorylation of sites phosphorylated in the cells by PKC (Jia et al., 1997). Whether PKC-phosphorylation is required to turn CFTR into a substrate of PKA, or whether it is the effect on gating of PKA-phosphorylation that depends on PKC, remains to be elucidated.

Given the strong phosphatase activity observed in most patches, it is expected that even in the continued presence of PKA CFTR channels will not be completely phosphorylated, but will reach a steady state in which the kinase and phosphatase activities balance each other over time. The relative level of phosphorylation at which this steady state occurs (anywhere between 0 and ~15 phosphoserines may coexist in the R domain, in theory) will depend on the rates of phosphorylation and dephosphorylation. Ideally, experiments should be done under conditions in which at least the rate of phosphorylation is reproducible. To this end, the responses to PKA were recorded and compared over a range of [PKA]. Figure 15A shows a representative trace, from a patch containing four CFTR channels, in which [PKA] was incrementally increased from 0 nM

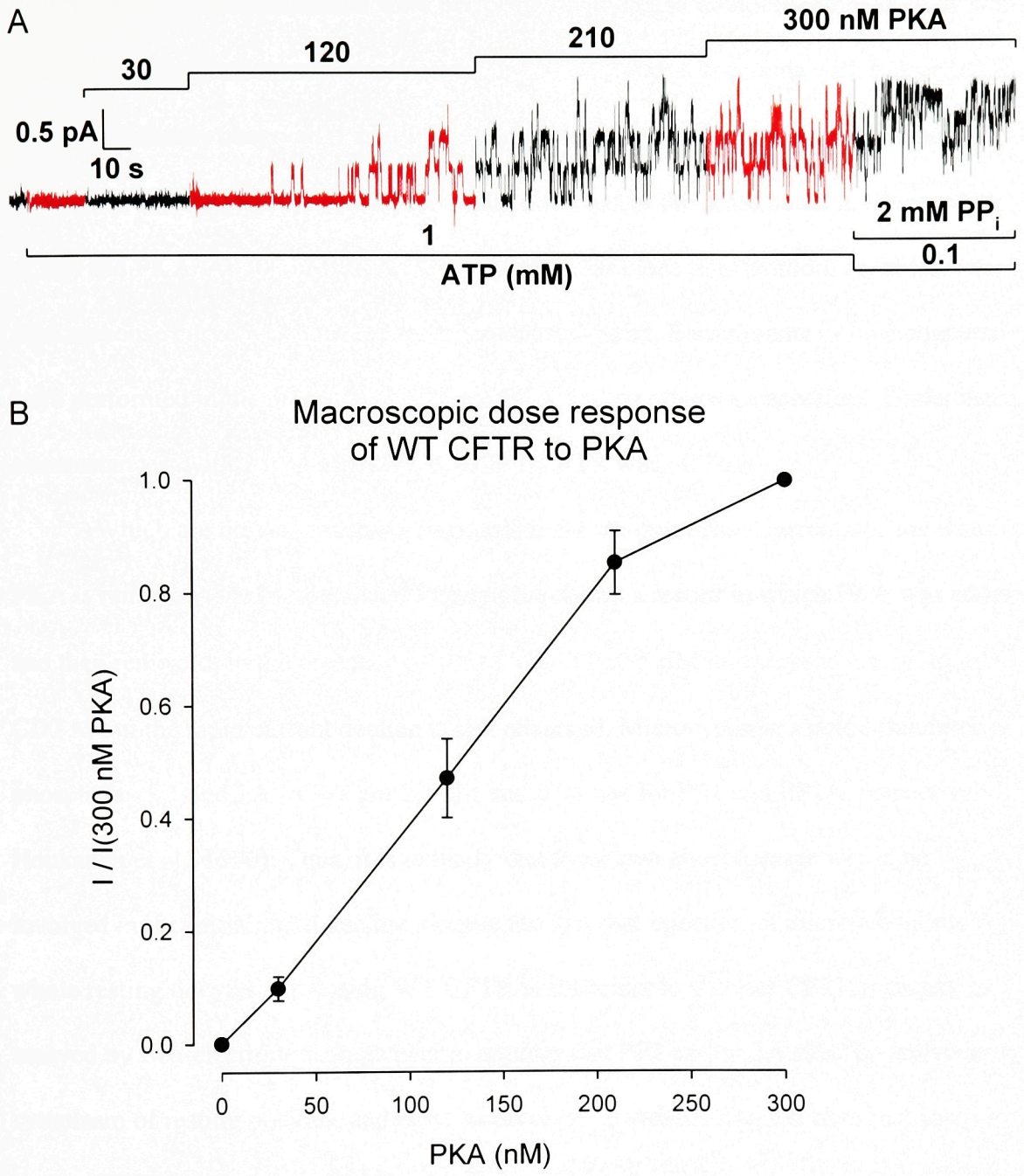

Figure 15. Dose response of WT CFTR current to PKA. A, Current record from a patch containing 4 CFTR channels, as counted at the end of the record by locking the channels open with PP_i. Increasing concentrations of PKA incrementally increase P_o. **B,** Dose response of steady-state macropatch currents to [PKA], normalized to the current at 300 nM PKA.

to 300 nM. Similar experiments were performed with larger numbers of channels as well, where the relaxations to new steady states upon switching to solutions with higher [PKA] were more clearly observed. Panel B shows a dose response curve of steady channel currents at various [PKA] normalized to that observed in the same patch in the presence of 300 nM PKA. At 300 nM PKA CFTR activity was close to saturation, or, at least the dose response curve was not very steep around this point. Experiments in later chapters were performed in the presence of 300 nM PKA, unless otherwise specified. Under these circumstances, with 2 mM MgATP, P_o of WT CFTR was ~0.36.

Which are the phosphatases responsible for the immediate current decline when PKA is removed (see Figure 14A)? Figure 16A shows a record in which PKA was added, and then removed, in the presence of 1 mM MgATP, 0.5 μM microcystin, and 2.45 mM CDTA, but the rapid current decline is still observed. Microcystin is a potent inhibitor of phosphatases 1 and 2A (IC_{50}'s are 1.7 nM and 0.04 nM for PP1 and PP2A, respectively, Honkanen et al., 1990): Thus, it is unlikely that those two phosphatases would be involved in the initial rapid decline, despite the fact that injection of microcystin into whole resting oocytes expressing WT CFTR is sufficient to activate CFTR currents, as assayed by two-electrode voltage clamp, arguing that PP1 and/or 2A must be active in the cytoplasm of resting oocytes, and must be involved in maintaining the observed low resting CFTR conductance. PP2C, a Mg^{2+}-dependent phosphatase, has also been demonstrated to dephosphorylate CFTR expressed in various cell types (Travis et al., 1997; Luo et al., 1998). In the presence of 1 mM MgATP and 2.45 mM CDTA (plus 0.5 mM EGTA and 2 mM Mg^{2+} from the standard bath solution), calculated free [Mg^{2+}] is ~100 μM. Hence, even if the fast-acting phosphatase is Mg^{2+}-dependent, lowering the

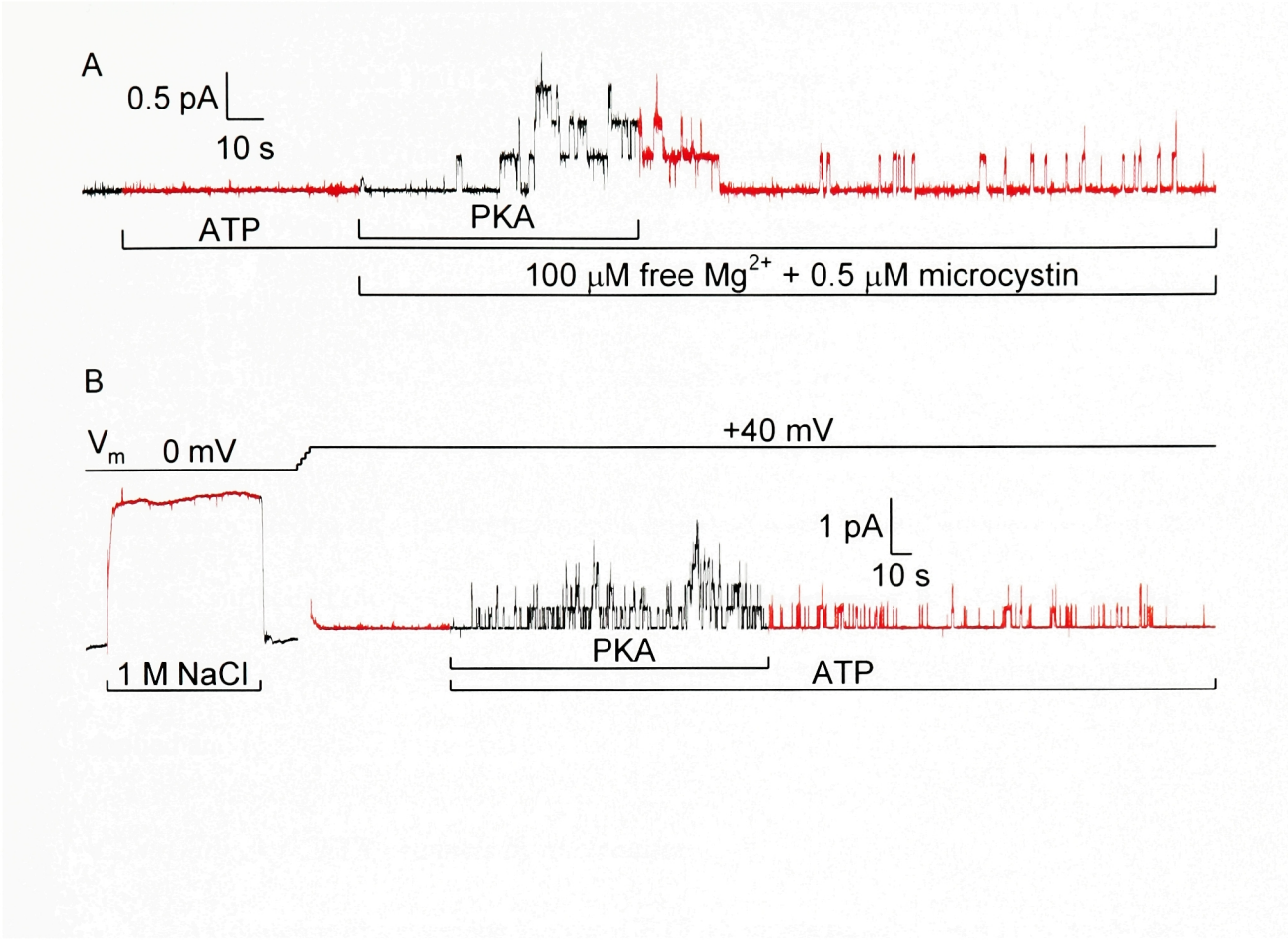

Figure 16. Which are the phosphatases in the oocyte membrane? A, Rapid decline of P_o after PKA withdrawal is not prevented by 0.5 μM microcystin and lowered (to 100 μM) free [Mg^{2+}]. Note prolonged bursts induced by low Mg^{2+} in the presence of PKA, but not after PKA removal. **B,** The fast-acting phosphatase activity seems tightly associated to the patch membrane, since it survives a high-salt wash by exposure to 1M NaCl for ~80 s. The rapid initial decline in P_o, accompanied by shortening of burst durations, is still observed after PKA removal, subsequent to the high-salt wash.

free [Mg^{2+}] to 100 μM is insufficient to prevent its action. On the other hand, under the above conditions, almost half (45%) of the total ATP is in the form of free ATP, competing with MgATP for CFTR's NBDs. This has been shown to alter CFTR gating (Dousmanis, 1996a), consistent with the slow gating kinetics seen in Figure 16A (cf. long openings and long closed times, compare to time bar). (Note that open times become short following PKA removal, despite maintained low free [Mg^{2+}]; the likely explanation for this will be discussed in sections 5.2.2. and 7.3.) The phosphatase in question seems tightly associated to the membrane, since a high-salt wash, by an ~80-s exposure of the cytosolic surface of the patch to a bath solution supplemented with 1 M NaCl, did not prevent rapid channel deactivation in the same patch, when PKA was subsequently applied and removed (Figure 16B).

4.2.4. Gating of CFTR channels by nucleotides

As shown in the previous figures, CFTR channels require MgATP to open, even once they have been phosphorylated. To understand how gating is regulated by ATP, the dependence of channel P_o on [ATP] was examined. For these experiments the relatively steady residual current that survived the removal of PKA was used, reflecting activity of partially phosphorylated channels. As illustrated in Figure 14A, macropatch currents were sampled at test [ATP] (0.1 mM in that case), bracketed by applications of 2 mM [ATP]. Steady-state currents at test [ATP] were then normalized to the average of that at 2 mM ATP, to provide the normalized dose response of channel activity (NP_o) to [ATP], shown in Figure 17A. The data were well fitted by a Michaelis-Menten curve (solid line), with a K_m of 51±2 μM. A Hill fit to the same data gave a Hill coefficient of 0.98±0.06. Experiments like the one in Figure 14A were also done on patches with smaller numbers

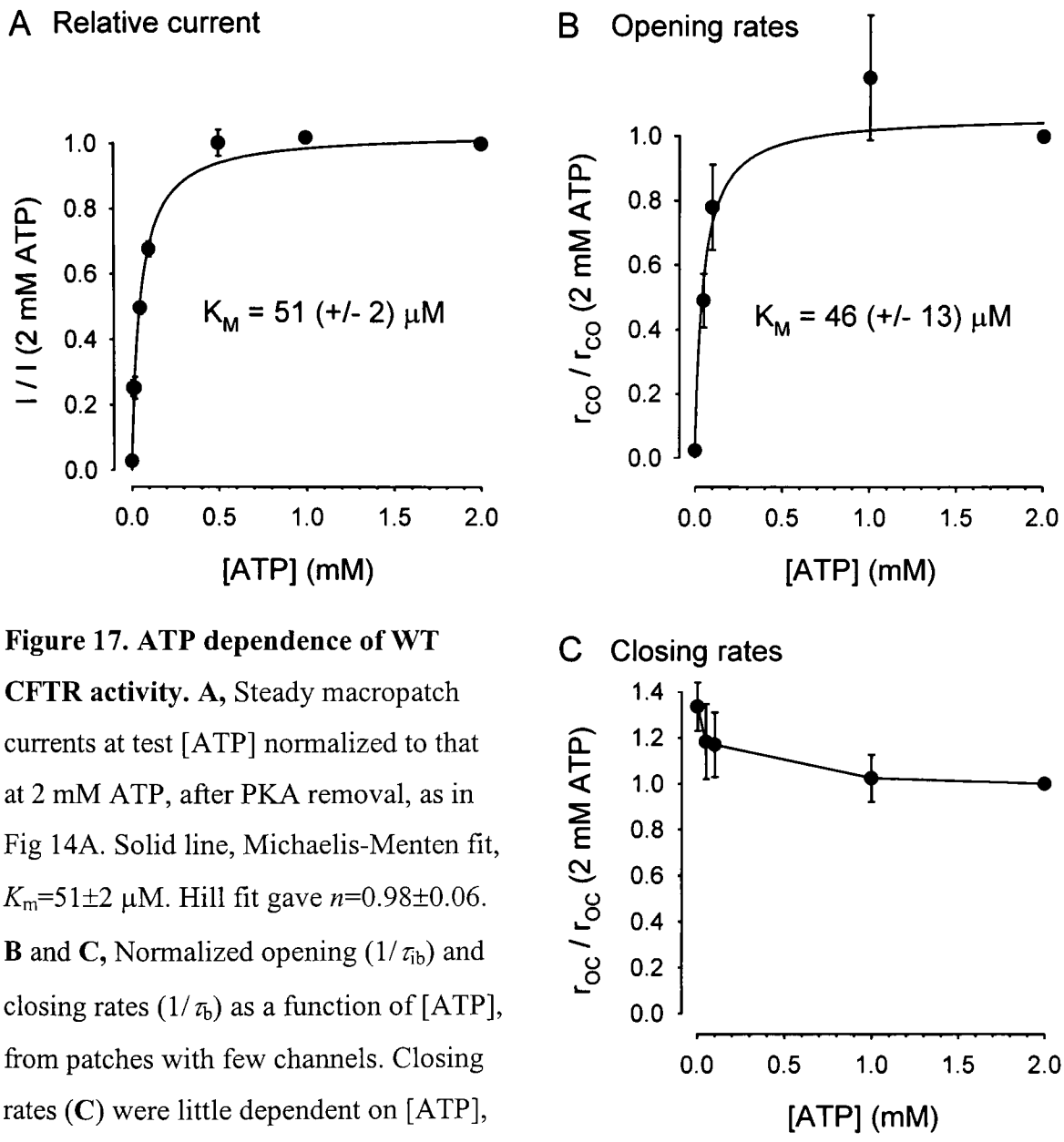

Figure 17. ATP dependence of WT CFTR activity. A, Steady macropatch currents at test [ATP] normalized to that at 2 mM ATP, after PKA removal, as in Fig 14A. Solid line, Michaelis-Menten fit, K_m=51±2 μM. Hill fit gave n=0.98±0.06. **B** and **C,** Normalized opening ($1/\tau_{ib}$) and closing rates ($1/\tau_b$) as a function of [ATP], from patches with few channels. Closing rates (**C**) were little dependent on [ATP], opening rates (**B**) were Michaelis-Menten-fitted (solid line, K_m=46±13 μM). Data at 2 μM ATP are from 3 tests on a macropatch, in which PKA activated a 130 pA current (NP_o=360), predicting $N \approx 1000$ (assuming $P_o \approx 0.36$). After PKA removal, at [ATP]= 2 μM, NP_o was ~ 1, with ≤6 superimposed openings during ~1 minute tests. Dwell-time histograms, obtained after imposing t_d=30 ms (see Chapter 3), were fitted with a *C-O* scheme assuming N=10. Extracted opening rates were then corrected for a true N =1000. Kinetic parameters for the bracketing applications of 2 mM ATP, used for normalization, were estimated from NP_o, assuming N=1000 and a closing rate typical for 2 mM ATP.

of channels, followed by kinetic analysis. Panels B and C of Figure 17 show opening (B) and closing rates (C), normalized to their respective values at 2 mM ATP, plotted against [ATP]. The Michaelis-Menten type dependence of the opening rate (K_m=46±13 μM) is in reasonable agreement with, and sufficient to explain, the macroscopic data. Under the above conditions channel closing rate (~4 s^{-1}) was largely independent of [ATP], maximal opening rate was ~0.35 s^{-1}.

AMPPNP, a non-hydrolyzable analog of ATP, does not open CFTR channels (Anderson et al., 1991a; Nagel et al., 1992; Carson and Welsh, 1993; Hwang et al., 1994), however, when applied together with ATP, it causes long bursts lasting for up to a minute at room temperature (Gunderson and Kopito, 1994; Hwang et al., 1994). This effect of AMPPNP, referred to as "locking" (in the open state), has been attributed to tight binding of AMPPNP to a site on the channel. A convenient way to study this phenomenon in the *Xenopus* oocyte system, is to apply ATP and AMPPNP to patches containing thousands of CFTR channels. Upon removal of the nucleotides, the rate of current decay reflects the off-rate of AMPPNP from its binding site on CFTR. Figure 18A shows such an example. After activating CFTR channels with 300 nM PKA and 2 mM ATP, AMPPNP (1 mM) was applied while [ATP] was lowered to 0.1 mM. The current, activated ~2 fold by AMPPNP, declined slowly when nucleotides were removed. A single exponential fit to the decay current (*blue line*) gave a time constant of 47 s. The inset shows rapid activation and inactivation of Ca^{2+}-dependent Cl^- current elicited by a brief pulse of 2 mM Ca sulfamate, verifying that the slow decay of AMPPNP-activated current was not due to slow solution exchange. Pyrophosphate (PP_i) has somewhat similar effects on CFTR to those of AMPPNP, in that it does not support channel openings when added

alone, but elicits long lasting bursts when provided in a mixture with ATP. This is demonstrated in the experiment in Figure 18B, roughly analogous to the experiment in Panel A. In contrast to the experiment above, superfusion of PP_i (2 mM) was continued for ~10 s after ATP and PKA were withdrawn. As is suggested by the kink in the current decay upon subsequent removal of PP_i, the initial decay in the presence of PP_i appeared slower than that in the absence of PP_i (τ=72 s for the fit of the PP_i-free section). However, essentially no current was activated when PP_i was re-applied alone, following the brief Ca^{2+}-pulse used to verify the rate of solution exchange. Thus, PP_i alone is unable to open CFTR channels, but may act by itself to slow closure of channels previously locked open by ATP plus PP_i.

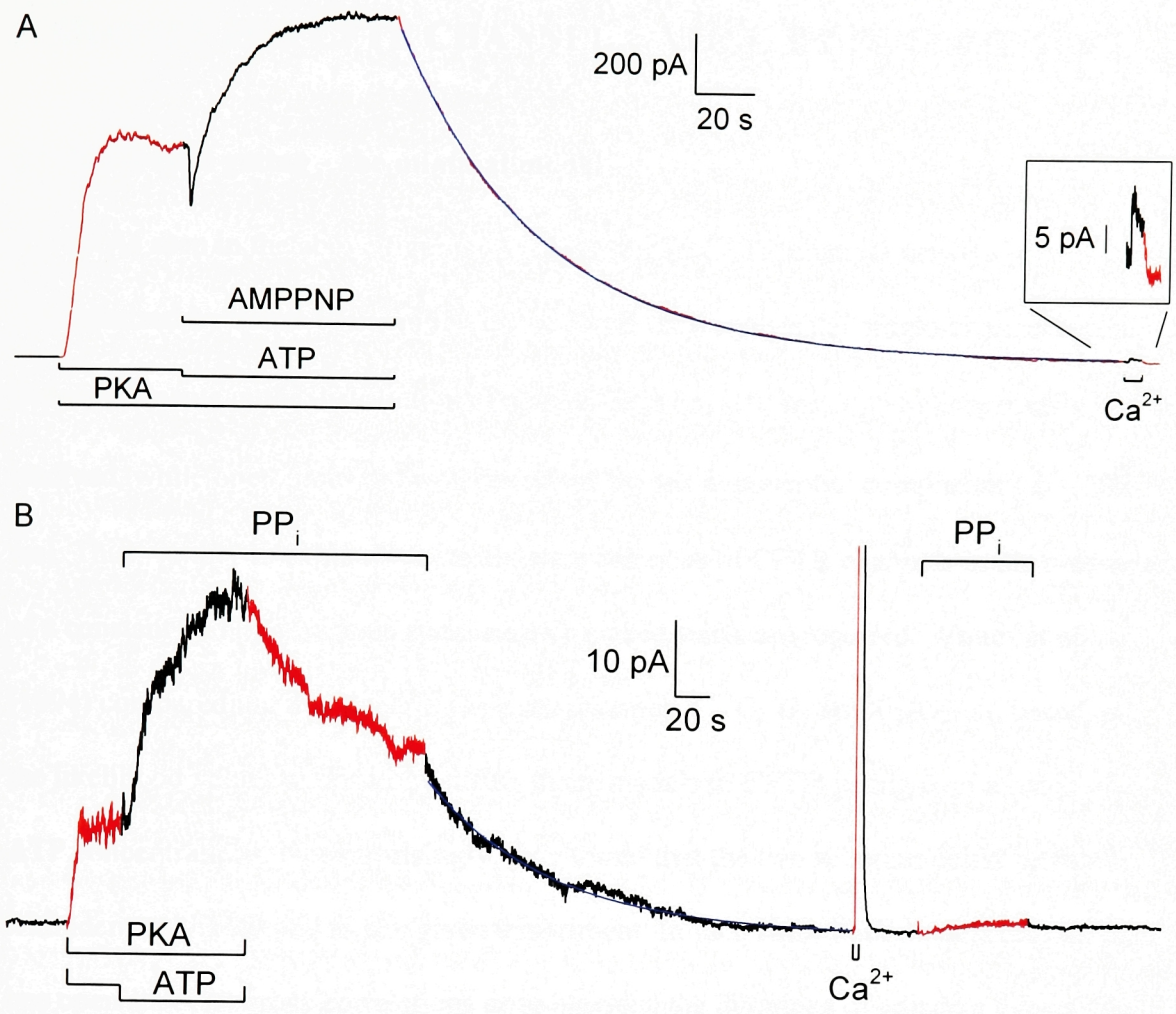

Figure 18. Locking in the open state of WT CFTR channels by AMPPNP and PP_i. **A,** 300 nM PKA and 2 mM MgATP activate ~6000 CFTR channels in a macropatch. Current is further stimulated by application of 1 mM AMPPNP, concomitantly to lowering of [ATP] to 100 μM. Upon nucleotide-washoff the noise-free decaying current is well fit by a single exponential (*blue*) with time constant τ=47 s. Inset, prompt activation and deactivation of Ca^{2+}-dependent Cl^- current in response to a brief Ca^{2+} pulse. **B,** Protocol similar to **A**, using 2 mM PP_i instead of AMPPNP. Prolonged exposure to PP_i alone slows the decay of the current after removal of ATP (and PKA), but reapplication of PP_i alone does not reactivate the channels once they are all closed. Fit by a single exponential (*blue*) of the decay following removal of PP_i gave τ=72 s.

5. MODELS FOR CFTR CHANNEL GATING BY NUCLEOTIDES

5.1. Burst-type gating – the minimal model

As seen in the above figures (e.g. Figure 13), CFTR channel activity is characterized by bursts of openings. From dwell-time analysis of single-channel records two components in the distribution of closed times (τ_{cs} ~10 ms, τ_{cl} >1 s) are readily resolved, while open times are well described by one exponential component (τ_o ~ 200 ms). Thus, simply to explain the steady-state behavior of CFTR channels in the presence of a constant [ATP], one open state and two closed states are required. Winter et al. (1994) compared the two linear three-state schemes, C_1-C_2-O_3 and C_1-O_2-C_3, based on the likelihood values obtained by fitting those models to CFTR gating over a range of ATP concentrations. Not surprisingly, they found that the two schemes could be fitted with identical likelihood to any given experiment. In fact, since both models contain only one open state, no cross-correlations arise between the durations of adjacent events, and, for any set of rate constants describing C_1-C_2-O_3, it is easy to find another set of rate constants for C_1-O_2-C_3 that will generate a record, and hence open and closed time distributions, indistinguishable from the first one. Those authors then proceeded to choose C_1-C_2-O_3, after showing that only the interburst durations changed with [ATP], which, with that scheme, allowed them to postulate rate r_{12} as the only adjustable parameter, while they claimed that three [ATP]-dependent parameters were required to fit the data with C_1-O_2-C_3 over the whole range of [ATP]. This claim, however, is rather surprising, since a change in interburst duration simply requires changing r_{12} for the second scheme as well. For example, the rates for C_1-C_2-O_3 (in s^{-1}), used by those authors

to describe the two extremes of [ATP] tested (0.1 mM and 3 mM), r_{12}=2, r_{21}=80, r_{23}=214, r_{32}=52, and r_{12}=15, r_{21}=98, r_{23}=245, r_{32}=54, respectively, predict results indistinguishable from those obtained with scheme C_1-O_2-C_3, and rates r_{12}=1.44, r_{21}=14.15, r_{23}=37.85, r_{32}=294, and r_{12}=10, r_{21}=15.43, r_{23}=38.57, r_{32}=345, respectively. Thus, the argument based on parsimony is not valid, and no steady-state measure distinguishes these two schemes; nor are "jump" experiments, like measuring first latencies following step application of ATP, feasible given the negligibly short life time of the flickery closed state compared to the interburst duration.

It remains, then, to evaluate the two possibilities based on qualitative arguments. C_1-C_2-O_3 is the scheme used to describe ligand-gated channels, in which C_1 is the unliganded, C_2 the liganded (activated), but closed, state from which the channel can open. There is, however, increasing evidence that CFTR is not simply gated by ATP binding, rather by irreversible gating steps, involving ATP hydrolysis. On the other hand, C_1-O_2-C_3 is the scheme used to describe open-channel block. In this view the flickery closures (C_3) are interpreted as pore-blockage events, e.g. by some large anion "sticky" enough to dwell in the pore for a few milliseconds. Some support for this latter possibility is the much higher frequency of brief closures at negative voltages (cf. Figures 13, 23), as well as the demonstration of pore block by negatively charged buffer molecules, such as HEPES or MOPS, in CFTR and other chloride channels (cf. Ishihara and Welsh, 1997). Based on these arguments, the latter view was adopted, and the closed-open-blocked scheme (termed *C-O-B* for simplicity, see Chapters 3 and 4) was used for data analysis. This implies, however, that all relevant gating transitions are pooled into the simple *C-O* part of the model, and hence that details of gating can be studied only by burst analysis,

after exclusion of the "irrelevant" flickery closures. (This does not mean that the flickery closures themselves are not related to gating at all; in fact, Ishihara and Welsh (1997) showed that the characteristics of MOPS-block changes asymmetrically during a burst of openings, consistent with some irreversible change in the shape of the pore during the gating cycle.)

5.2. More complex models based on interactions with nucleotides and PKA

Since the simple *C-O* model falls far short of explaining the complexity of CFTR gating, even after exclusion of flickery closures, a number of models have been suggested over the years. Below is a summary of a few such models, together with a brief discussion about strengths and shortcomings. Towards the end of the discussion, the search will be narrowed down to a subset of models capable of describing most of the data. Some further refinement will be provided in the last chapter.

5.2.1. Models involving one ATP binding site

Venglarik et al. (1994) evaluated gating parameters of prephosphorylated CFTR channels, in the absence of PKA, over a range of [ATP], by performing noise analysis in the frequency range of 0.096-31 Hz; this largely excluded the impact of flickery closures which lasted for ~3 ms at the temperature used in that study (~35°C). After obtaining good fits for all data by single Lorentzians, and calculating channel number based on statistics, the authors extracted opening and closing rates from the corner frequencies of the Lorentzians, and found that a simple Michaelis-Menten type dependence of the opening rate (i.e. interburst duration) and a constant closing rate (i.e. burst duration) gave

an excellent description of their data, and compared well with the dependence on [ATP] of P_o calculated directly from the traces. (Similar data are shown above in Figure 17.) The authors explained their data in terms of Model 1 (see Figure 19), where C_1 is an unliganded, C_2 an ATP-bound closed state, and open state O_3 is ATP-bound as well; i.e., channels simply have to bind ATP to assume an activated state compatible with opening. Note, that this scheme is not identical to C_1-C_2-O_3 discussed in the previous section, since it is meant to explain gating after exclusion of flickery closures. In particular, rates r_{23} and r_{32} were assumed slow, consistent with mean burst and interburst durations at saturating ATP. With a relatively fast rate r_{21}, and apparent rate r_{12} linear with [ATP], gating occurs between C_2 and O_3, while C_1 serves to diminish the relative occupancy of C_2 at low [ATP]. Although this scheme predicts two distinct (positive) components in the distribution of interburst durations at any [ATP], not observed in the power spectra, this can be amended by assuming $r_{21} >> r_{23}$, in which case the distribution of interburst durations essentially reduces to a single component with decay rate $r_{23}(r_{12}/(r_{12}+r_{21}))$, i.e. r_{23} times the fractional occupancy of state C_2 within an interburst interval.

An alternative three-state scheme, also consistent with the hyperbolic dependence of opening rate on [ATP], was suggested e.g. by Zeltwanger et al. (1999; Model 2 in Figure 19). Also in this model, rate r_{12} is linear with [ATP] while all other rates are constant, C_1 is the "empty" and C_2 the ATP-bound closed state; however, transition $C_2 \rightarrow O_3$ is postulated to involve ATP hydrolysis, i.e. O_3 is a state in which the hydrolysis products ADP and P_i are bound to the channel. Closure always proceeds from O_3 to C_1, by dissociation of the hydrolysis products. Note that the mere schematics of Models 1 and 2 are very similar, except that Model 1 closes to state C_2, while Model 2 closes to

state C_1. While these two models predict identical dependencies of the *mean* interburst duration on [ATP], they differ in their predictions of the shape of the *distribution* of interburst intervals.

Model 1 is a reversible scheme, and hence all exponential components describing the interburst duration are predicted to be positive (or zero in the limit). Model 2 is irreversible, and forces all interbursts to transit through at least two states (C_1 and C_2). Thus, it predicts a negative component in the distribution of interburst durations, i.e. a lack of very brief interburst events; noticeably under conditions where r_{12} is slow (at low [ATP]). Verification of such a paucity of brief interburst closures is greatly hampered by the need to discard very brief "flickery" closures, but has been noted by Zeltwanger et al. (1999) who compiled a large number of single-channel records at 100 μM ATP, and obtained a peak at 200 ms in the pdf of the interburst durations (flickery closures <80 ms were excluded), consistent with the irreversible mechanism in Model 2. Also in favor of Model 2, as opposed to Model 1, is the observation that AMPPNP does not open CFTR channels, although it clearly binds to closed channels, since exposure to AMPPNP (or ADP) alone, delays their subsequent activation by ATP (Weinreich et al., 1999), consistent with competition between AMPPNP and ATP for a common site important in channel opening. Furthermore, free ATP, in the absence of Mg^{2+}, does not open the channels, although free ATP can also bind, and even compete with Mg^{2+}ATP under conditions where a mixture of free ATP and Mg^{2+}ATP is present (Dousmanis et al., 1996a). All of these arguments are consistent with channel opening being rate limited by ATP hydrolysis, or at least by a Mg^{2+}-dependent step after ATP binding.

An alternative irreversible three-state scheme (Model 3), in which a rate limiting

Models with one binding site

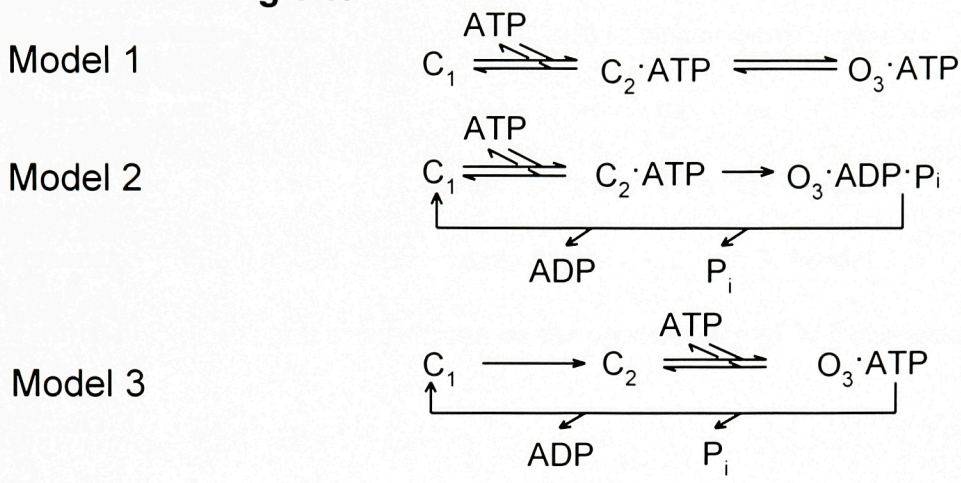

Models with two binding sites

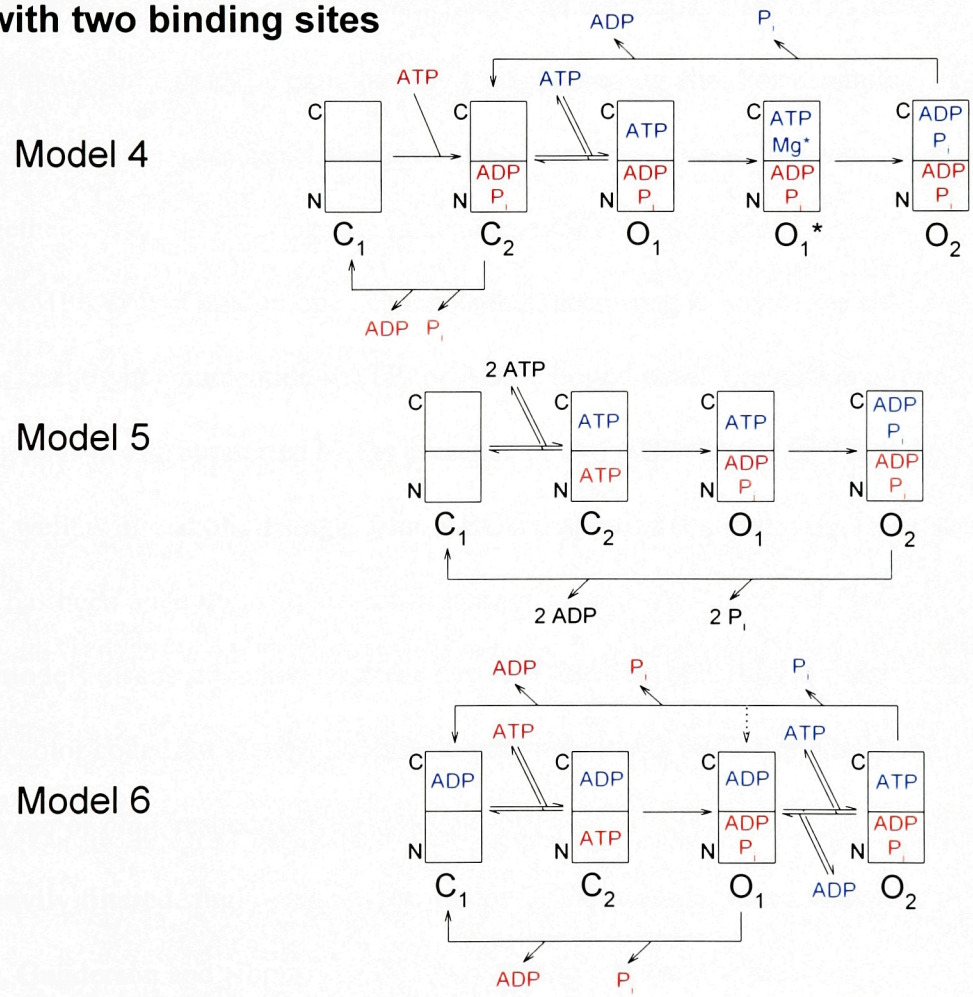

Figure 19. Models of CFTR gating by nucleotides. Models 1 to 3 involve only one, Models 3 to 6 two ATP binding sites. For the latter models *red* and *blue* mark nucleotides interacting with NBD1 or NBD2, respectively.

step would precede nucleotide binding, predicts that similar maximal opening rates should be observed at saturating concentrations of various nucleoside-triphosphates. This is certainly not the case for CTP and UTP, both of which can open CFTR channels, but at a much slower rate (at saturating concentrations) than ATP or GTP (Shawn Zeltwanger, personal communication). Thus, among Models 1, 2, and 3, Model 2 is favored, since it fits all experimental observations on the opening rate of WT channels.

5.2.2. Models involving two ATP binding sites

The schemes considered above involve only one binding site for ATP. Some observations, however, cannot be explained by a single binding site. For example, AMPPNP, which cannot open the channels by itself, can delay channel closure when supplied together with ATP (locking; the same is true for PP_i, see Figure 18). This implies that AMPPNP can bind to open channels that, according to any of the above schemes, are already in a nucleotide- (ATP- or ADP-) bound state. The notion of two ATP-binding sites is also supported by the presence of two NBDs in the CFTR sequence, as well as in that of all single-gene ABC transporters (binding of ATP to both sites of PgP has been unequivocally demonstrated, cf. review by Senior and Gadsby, 1997). The models discussed below consider two ATP binding sites, and are illustrated in Figure 19, color coded for clarity: nucleotide interacting with NBD1 or NBD2 is marked with *red* or *blue*, respectively.

In heavily filtered single-channel records of CFTR channels reconstituted in a lipid bilayer, Gunderson and Kopito (1995) observed the asymmetric presence of two distinct subconductance states: channels mostly opened to conductance level O_1, but briefly transited to a state with ~10% larger conductance (O_2) before closing. This

phenomenon, a filter artifact explained by more frequent flickery closures during the initial part of the bursts (Ishihara and Welsh, 1997), nevertheless provided a wealth of new information, first of all, by shedding light on an irreversible step during the open (burst) state. Those authors went on to show that the long locked events elicited by non-hydrolyzable AMPPNP, never proceeded to the O_2 state, and the same applied when free [Mg^{2+}] was lowered to submicromolar levels. Furthermore, when the conserved lysine in the Walker A motif of NBD2 (see Chapter 1) was mutated to an alanine, a mutation that abolishes ATP hydrolysis in all known ABC transporters including CFTR (Loo and Clarke, 1995; Müller et al., 1996; Ramjeesingh et al., 1999), the resulting K1250A channels were opened by ATP to bursts that lasted for ~ 1 minute, without proceeding to O_2, reminiscent of AMPPNP-induced lock of WT channels. Based on the dramatic effect on gating of this NBD2 mutation, while the analoguos mutation in NBD1, K464A, left channels with seemingly normal gating but for a two-fold slowed opening rate, Gunderson and Kopito postulated a primary role of NBD2 in CFTR gating (Model 4). In this model, binding of ATP to NBD2 opens the channels (O_1), while closing is linked obligatorily to hydrolysis (O_2), once ATP, in the presence of Mg^{2+}, has assumed a tightly bound prehydrolysis complex (O_1*). The NBD1 hydrolysis cycle is assigned a secondary role, keeping the channels in an active state. While this Model explains locking by AMPPNP, as well as the effect of the K1250A mutation, it fails to explain several other features of CFTR gating. One of the main problems is that at sufficiently high [ATP] Model 4 would force every channel, after closing from O_2 to C_2, to immediately proceed to O_1 again. Thus, at high [ATP] interburst durations would decrease to zero, and P_o would increase to ~1, in contrast to the experimentally observed

saturation of opening rate and P_o (cf. Figure 17). An obligatory role of ATP binding at NBD2 in channel opening is also not supported by the finding (Zeltwanger et al., 1999) that the same K1250A mutant, which opens to bursts ~100 times longer than WT at 1 mM ATP, has burst durations indistinguishable from WT (~250 ms) at low (10μM) ATP, suggesting, that those short bursts do not involve ATP binding to NBD2 at all.

After noting the dramatically prolonged bursts of K1250A mutant channels, and , in their case, a 5-fold slower opening rate of the NBD1 mutant K464A, Carson et al. (1995) proposed a scheme (Model 5), in which ATP hydrolysis at NBD1 opens, while ATP hydrolysis at NBD2 closes a CFTR channel. But, because binding is postulated to occur at both ATP-binding sites before channel opening, Model 5 would allow for tight binding of AMPPNP to NBD2 of closed channels. Thus, exposure to AMPPNP alone should not open the channels (as it does not), but subsequent exposure to ATP alone should occasionally result in long locked-open events, whenever ATP binds and is hydrolyzed at NBD1 of a channel that still has AMPPNP bound at its NBD2. This, however, has not been observed (cf. Hwang et al., 1994), suggesting that binding at the two NBDs is strictly sequential, the second binding site (presumably NBD2) becoming available only in channels already opened by ATP hydrolysis at NBD1. The absolute requirement for ATP hydrolysis at NBD2 for channel closure, also postulated in Model 5, is inconsistent with the brief openings of the K1250A mutant at low [ATP] (see above), as well as with the lack of stabilizion by AMPPNP of openings of partially phosphorylated channels (Hwang et al., 1994).

All of the above experimental findings, and more, are explained by a scheme that involves sequential binding of ATP to two sites (Model 6). Note that Model 6 is an

extension to two binding sites of single-site Model 2. Binding (C_2) and hydrolysis of ATP at the first site (presumably NBD1) opens the channels (O_1). Open channels can either close directly to C_1 by loss of the hydrolysis products, or proceed to bind ATP at the second site (presumably NBD2, state O_2). ATP is tightly bound at the second site, and so channels normally stay in O_2 until that second ATP is hydrolyzed to allow exit from O_2. Two versions of this scheme have been proposed by Zeltwanger et al. (1999) and Gadsby and Nairn (1999; slightly modified in Weinreich et al., 1999), differing in whether ATP hydrolysis at NBD2 propels channels from O_2 directly to C_1 (hydrolysis products at both NBDs are lost; Gadsby and Nairn, 1999), or only back to O_1 (only P_i from NBD2 is lost initially, several O_1 to O_2 transits per burst are possible; Zeltwanger et al., 1999; *dotted arrow* in Model 6). There is also room for argument about where ADP leaves NBD2 in Model 6. One possibility is a strict exchange for ATP in step $O_1 \rightarrow O_2$, ensuring that NBD2 is always occupied by nucleotide. Alternatively, ADP could leave NBD2 together with P_i during step $O_2 \rightarrow C_1$ (or $O_2 \rightarrow O_1$), leaving NBD2 empty for the next NBD1 half-cycle. At present, no experimental result allows a distinction to be made between these possibilities.

Since Model 6 is an extension of Model 2, it explains all opening rate-related observations already discussed; such as the Michaelis-Menten type relationship between [ATP] and opening rate, the requirement for Mg^{2+} for channel opening, the paucity of short interburst events at low [ATP], competition of AMPPNP (or ADP) with ATP for channel opening, as well as failure to "load" the high-affinity second binding site with AMPPNP in closed channels.

Closing rate-related observations depend on the ratio of the rates for ATP-binding at the second site ($O_1 \rightarrow O_2$) and for dissociation of the hydrolysis products from the first site ($O_1 \rightarrow C_1$). In highly phosphorylated channels the transition from O_1 to O_2 is favored, explaining the observed longer bursts of WT channels in the presence of PKA (discussed above, cf. Figures 14B, 16; Hwang et al., 1994; Dousmanis et al., 1996b) as well as the dependence of closing rate on [ATP] under such conditions (Zeltwanger et al., 1999), locking by AMPPNP of phosphorylated channels (Hwang et al., 1994), prolonged bursts of K1250A channels, and similarly prolonged bursts of WT channels at low (micromolar) Mg^{2+} (Figure 16A; Dousmanis et al., 1996a). However, at low [ATP], even phosphorylated channels close directly from O_1 to C_1 without binding ATP at the second site, explaining the brief openings of K1250A (and WT) channels at 10 μM ATP (see above). Apparently, the on-rate of ATP to the second site is greatly slowed when channels become partially dephosphorylated following removal of PKA. Under such conditions Model 6 essentially reduces to Model 2, which explains the observed constant closing rate over a range of [ATP] in the absence of PKA (Figure 17C), the failure of AMPPNP to lock open channels under such conditions (Hwang et al., 1994), as well as the brief openings of WT channels even at low (micromolar) Mg^{2+} following PKA removal (see Figure 16A; cf. Dousmanis et al., 1996a). Vanadate has been shown to lock open even partially dephosphorylated CFTR channels (Baukrowitz et al., 1994). This is explained by Model 6 (or 2) as a prolonged dwell in state O_1, due to vanadate-induced trapping of ADP at the first site, presumably NBD1. (Vanadate-induced trapping of the hydrolysis product α-^{32}P-8-azido-ADP at both sites of PgP has been demonstrated; reviewed in Senior and Gadsby, 1997.)

The structural assignment of the "first" and "second" binding site is still problematic. The large effect of the K1250A mutation on burst duration, together with the (much smaller) effect on opening rate of the analogous NBD1 mutation K464A, led to the assignment of NBD1 as the "first" site, i.e. the site responsible for channel opening, and of NBD2 as the "second" site, involved in stabilizing the open state. Other consequences of these same mutations, however, are not so easy to fit into this framework. In particular, K1250A is also ~10-fold slowed in opening (Carson et al., 1995), and K464A, a mutant with greatly reduced ATPase activity, is comparatively little affected in its opening rate (Ramjeesingh et al., 1998). The possibility that more than a single NBD amino acid sequence is needed to complete a functional binding site was raised by the small number of contacts between ATP and its binding pocket identified in the crystal structures of RbsA and HisP, and is not inconsistent with the recent proposal that CFTR may function as a dimer (Zerhusen et al., 1999). Because of this uncertainty, in following chapters the binding site responsible for channel opening will be termed NBD-A, and the site stabilizing the open state NBD-B, to distinguish these functionally defined sites from NBD1 and NBD2 of the primary sequence of CFTR.

6. NBD1 STRUCTURE AND FUNCTION

6.1. Introduction

Apart from the R domain, the large unique linker domain connecting CFTR's N- and C-terminal halves, CFTR's overall predicted domain structure identifies it as a member of the very large family of ABC transporters (see also Chapter I, Figure 1). There are several other well known eukaryotic ABC proteins such as P-glycoprotein (Pgp) and multi-drug resistance related protein (MRP), both associated with multi-drug resistance in mammalian tumor cells, and STE6, the **a**-mating factor transporter of yeast. In all these examples, both membrane-spanning domains and the two NBDs are encoded by a single large gene. But, in the much larger number of procaryotic ABC transporters the NBDs may be expressed from individual genes (as for HisP, the NBD of histidine permease; e.g., Hung et al., 1998), or two NBDs may be fused in a single gene product (as for RbsA, the NBDs of the ribose transporter; e.g., Armstrong et al., 1998), while the transmembrane domains may be expressed from yet other genes. One implication of this post-translational assembly of functional transporters in bacteria is that the separate domains must each possess all the information needed to fold correctly and to interact with the complementary domains that make up a functioning transporter.

CFTR is the only known ABC protein which functions as an ion channel. As discussed in some detail in Chapters 4 and 5, regulation of opening and closing of CFTR channels by phosphorylation of the R domain and nucleotide binding and hydrolysis at the NBDs is extremely complex, and not yet fully understood. Nevertheless, it is clear

that interactions between the two NBDs, and between the NBDs and the R domain, play important roles in its gating.

Further dissection of these roles would greatly benefit from structural information on each of these domains, which is presently lacking. This is so, despite the expression of peptide models of the R domain (Picciotto et al., 1992; Dulhanty and Riordan, 1994), of the N-terminal NBD (NBD1; Hartman et al., 1992; Ko and Pedersen, 1995; Yike et al., 1996; Ko et al., 1997; Clancy et al., 1998), and of the C-terminal NBD (NBD2; Randak et al., 1996, 1997). A valid concern with several of these constructs is the sparse knowledge of the location of the domain boundaries. As a first step towards addressing this concern, we attempted to define the boundaries of NBD1 of CFTR by exploiting a functional approach. It has already been shown that the CFTR channel protein can be severed near the C-terminal end of the R domain, and the two halves co-expressed to form a functional complex (Ostedgaard et al., 1997). Therefore, given the modular design of ABC transporters in general, we reasoned that judicious cuts in the links flanking NBD1 ought to be tolerated. Indeed, cuts between three of the four domains of STE6 did not abrogate its function (Berkower et al., 1996). This chapter describes our search for the boundaries of NBD1 by co-expressing contiguous, or near contiguous, segments of CFTR in *Xenopus* oocytes and assessing function with two-microelectrode voltage clamp and excised-patch recordings. Expression and physical association of the CFTR protein segments were assayed using immunoblots and co-immunoprecipitation. Using this approach, we find that the N-terminus of NBD1 lies between amino acids (a.a.) 432-449 and the C-terminus lies between a.a.s 622-634. Moreover, regions spanning a.a. 415-432 and a.a. 634-667 can be deleted without destroying CFTR channel function.

6.2. Results

6.2.1. Defining the C-terminal boundary of NBD1 by assessing function of co-expressed severed CFTR segments

The location of the boundary between NBD1 and the R domain in CFTR is presently unclear. The initial suggestion was that exon 13 of CFTR, comprising a.a. 590-830, encoded the R domain, and hence that the exon 12/13 junction marked the boundary between NBD1 and the R domain (Riordan et al., 1989). If that were so, it might reasonably be expected that functional CFTR channels could be reconstituted by co-expression of the two contiguous segments of CFTR severed between residues 589 and 590, viz. Flag3-589 plus 590-1480. The N-terminal Flag epitope was incorporated to facilitate immunoprecipitation and detection of the expressed proteins (see below). Injection of oocytes with a mixture of the two cRNAs encoding these two segments resulted in conductances that were negligible under both basal (2 ±1 μS) and activated (2 ±1 μS) conditions, just as in control, uninjected oocytes (Figure 20A and Table II). On the assumption that NBD1 likely stretches beyond a.a. 589, a series of contructs were made in which the C-terminus of Flag3-589 was incrementally extended. Each of these constructs in turn was co-expressed with the 590-1480 segment, and basal and activated conductances were measured to assess channel function (Figure 20A). These conductances mimicked those of uninjected oocytes until the Flag-tagged CFTR segment was extended to a.a. 633. Thus basal and activated conductances were 2±1 μS and 3±1 μS for oocytes injected with Flag3-622 plus 590-1480, but jumped to 8 ±1 μS and 91 ±7 μS in oocytes co-expressing Flag3-633 plus 590-1480. However, the basal and activated conductances produced by Flag3-633 plus 590-1480 constructs were both smaller than

those attained by WT CFTR (173±4 μS, *n*=37, Figure 20A, and Table II). We speculated that this shortfall might be attributable to the repetition of residues 590 to 633 upon co-expression of Flag3-633 plus 590-1480, and so we removed the overlapping residues by co-expressing Flag3-633 with segment 634-1480, which yielded basal and activated conductances of 17 ±1 μS and 182 ±4 μS respectively, comparable to those of oocytes expressing WT CFTR (Figure 20A, and Table II).

These results show that robust CFTR channel function is obtained when the C-terminus of the segment Flag3-589 is extended to a.a. 633 (but not to a.a. 622) and that construct is co-expressed with the appropriate complementary segment, suggesting that the C-terminus of NBD1 lies between a.a. 622 and 634. (In other words, it could lie at a.a. 623, or 624, or 625, etc., but could extend as far as a.a. 633.) An alternative possibility, that a crucial part of NBD1 extends beyond a.a. 633 but can nevertheless associate with the Flag3-633 segment to form a complete NBD1 domain, is ruled out by our finding that strong CFTR channel activity was reconstituted by co-expression of Flag3-633 with 668-1480: despite this deletion of a.a. 634-667, basal and activated conductances (16 ±1 μS and 175 ±7 μS, respectively; Figure 20A and Table II) were similar to those of WT CFTR. On the other hand, oocytes co-expressing Flag3-622 plus 634-1480, in which any CFTR channels must lack a.a. 623-633, displayed negligible basal and activated conductances like those of uninjected oocytes, supporting our conclusion that the C-terminal boundary of NBD1 falls between a.a. 622 and 634.

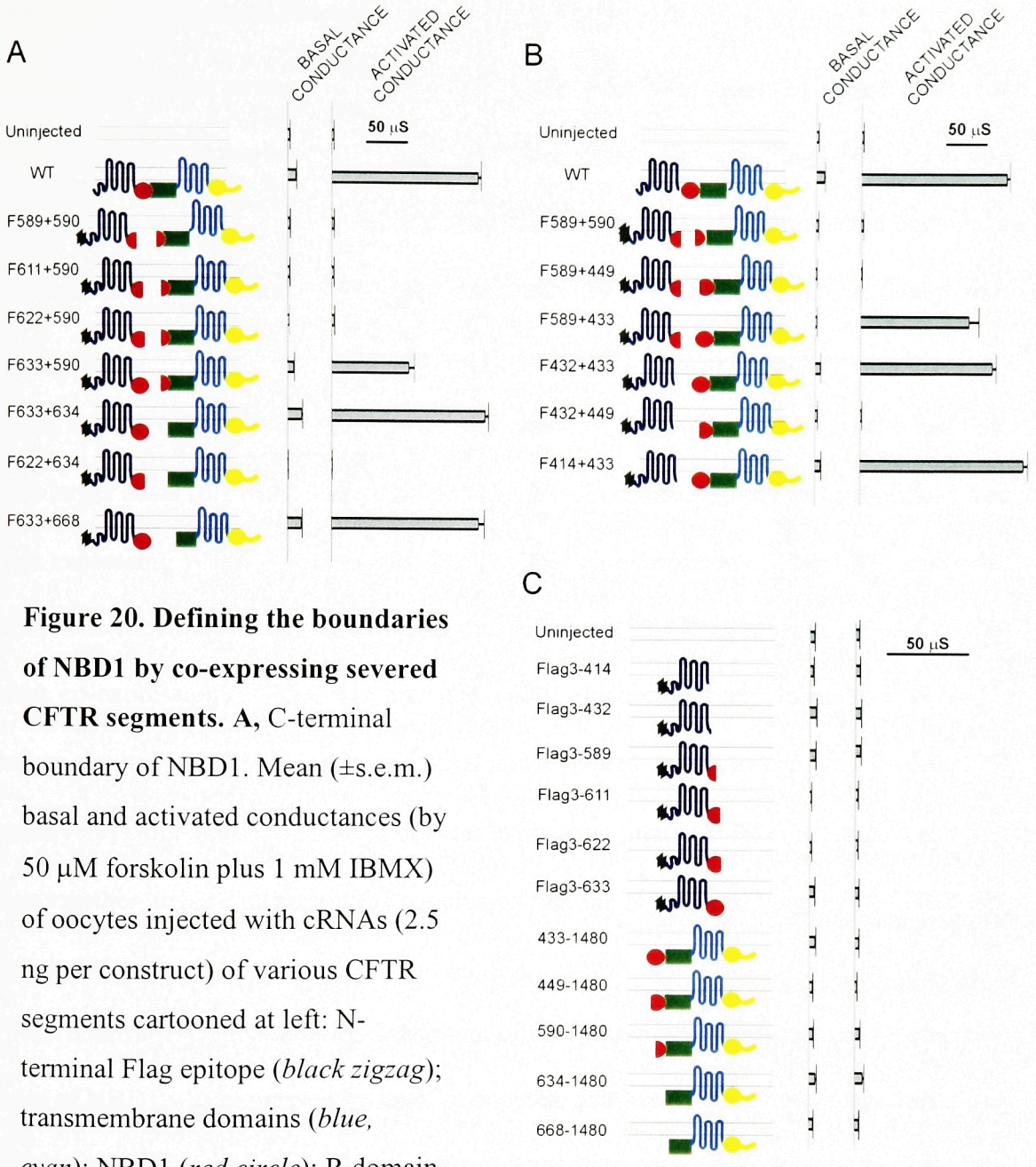

Figure 20. Defining the boundaries of NBD1 by co-expressing severed CFTR segments. A, C-terminal boundary of NBD1. Mean (±s.e.m.) basal and activated conductances (by 50 µM forskolin plus 1 mM IBMX) of oocytes injected with cRNAs (2.5 ng per construct) of various CFTR segments cartooned at left: N-terminal Flag epitope (*black zigzag*); transmembrane domains (*blue, cyan*); NBD1 (*red circle*); R domain (*green rectangle*); NBD2 (*yellow circle*). Conductances were calculated from linear fits to steady-state I-V data between -60 and -20 mV; average values are from at least 5 oocytes. The C-terminus lies between residues 622 and 633. **B,** N-terminal boundary of NBD1. Methods and symbols are as in **A**. The N-terminus lies between residues 433 and 449. **C,** Negligible basal and activated conductances of oocytes expressing single truncated CFTR channel segments. Methods and symbols are as in **A**.

6.2.2. Defining the N-terminal boundary of NBD1

We used a similar strategy to incrementally extend the N-terminus of segment 590-1480 in an attempt to build a complete NBD1 there. Upon co-expression with Flag3-589, the extended segment 449-1480 yielded conductances indistinguishable from those of uninjected oocytes, but extended segment 433-1480 gave substantial activated (129 ±12 μS) conductance, though still smaller than that of WT CFTR-injected oocytes (Figure 20B). However, omission of the overlapping section (residues 433-589) by co-expression of Flag3-432 plus 433-1480 resulted in somewhat larger basal (6 ±1 μS) and activated (157 ±5 μS) conductances that approached those of oocytes expressing WT CFTR channels. The fact that co-expression of Flag3-432 plus 449-1480 yielded no functional channels confirms that segment 433-448 is an essential part of NBD1. In contrast, co-expression of Flag3-414 plus 433-1480, which effectively deleted a.a. 415-432, nevertheless resulted in oocytes displaying basal and activated conductances (7±1 μS and 195 ±5 μS, respectively) comparable to those of oocytes expressing intact CFTR (Figure 20B and Table II). Taken together, these data permit the conclusion that the N-terminal boundary of NBD1 lies between a.a. 432 and 449.

As a control test, each individual segment of CFTR used to investigate the functional boundaries of NBD1 was expressed by itself in oocytes, and basal and activated conductances were measured in the usual manner. In all cases, the resulting conductances were similar to those of uninjected oocytes (Figure 20C, and Table II), confirming that none of these truncated CFTR fragments readily forms viable channels when expressed alone in *Xenopus* oocytes.

TABLE II **Basal and activated membrane conductances of oocytes expressing CFTR constructs severed around NBD1.**

Conductances, mean ± s.e.m., are in μS, numbers of observations are given in parentheses.

Construct	*Basal conductance*		*Activated conductance*	
uninjected oocyte	3 ± 0.3	(21)	2 ± 0.2	(34)
WT	10 ± 1	(16)	173 ± 4	(37)
Flag3-414 (F414)	2 ± 1	(5)	3 ± 0.2	(5)
Flag3-432 (F432)	4 ± 0.4	(8)	3 ± 0.4	(8)
Flag3-589 (F589)	3 ± 0.3	(5)	3 ± 0.4	(5)
Flag3-611 (F611)	1 ± 0.1	(5)	2 ± 0.1	(5)
Flag3-622 (F622)	1 ± 0.1	(5)	2 ± 0.1	(5)
Flag3-633 (F633)	3 ± 1	(14)	2 ± 0.2	(15)
433-1480 (433)	4 ± 1	(14)	2 ± 0.2	(10)
449-1480 (449)	2 ± 0.3	(5)	1 ± 0.2	(5)
590-1480 (590)	4 ± 0.4	(5)	3 ± 0.5	(8)
634-1480 (634)	4 ± 1	(9)	5 ± 1	(10)
668-1480 (668)	3 ± 0.3	(5)	3 ± 0.3	(5)
F589+590	2 ± 1	(6)	2 ± 0.4	(13)
F611+590	2 ± 1	(8)	3 ± 0.3	(14)
F622+590	2 ± 0.3	(5)	3 ± 0.4	(9)
F633+590	8 ± 1	(11)	91 ± 7	(21)
F633+634	17 ± 1	(9)	182 ± 4	(11)
F622+634	1 ± 0.1	(5)	1 ± 0.1	(5)
F633+668	16 ± 1	(8)	175 ± 7	(8)
F589+449	2 ± 0.2	(5)	2 ± 0.2	(5)
F589+433	2 ± 0.2	(11)	129 ± 12	(9)
F432+433	6 ± 1	(16)	157 ± 5	(18)
F432+449	3 ± 0.4	(9)	2 ± 0.2	(10)
F414+433	7 ± 1	(5)	195 ± 5	(10)

6.2.3. Expression and maturation of severed CFTR segments

Western blots of proteins resolved from total oocyte-membrane preparations were used to evaluate expression of intact or truncated CFTR proteins. C-terminal fragments were recognized by an anti-R-domain antibody, N-terminal fragments by the M2 anti-Flag antibody. Glycosylation of C-terminal fragments (the native glycosylation sites of CFTR are located in the fourth extracellular loop, between transmembrane helices 7 and 8, see Figure 1) was identified as a decrease in mobility on SDS-PAGE, and was further studied by treatment with endoglycosidase-H and N-glycosidase-F. Because endoglycosidase-H removes glycosyl moieties only from proteins not yet modified by the early Golgi enzyme mannosidase II, whereas N-glycosidase-F removes all asparagine-linked glycosyl groups, resistance to endoglycosidase-H was interpreted as a sign of full glycosylation, as distinct from endoglycosidase-H sensitive core-glycosylated forms, predicted to originate from the endoplasmic reticulum (ER). Interactions between complementary fragments were also assayed by co-immunoprecipitation using anti-Flag affinity beads.

cRNAs for all CFTR segments, whether injected alone or as non-functional or functional pairs, were translated in the oocytes, since protein corresponding to these segments was recognized in Western blots of total oocyte-membrane preparations, although some of the segments seemed highly unstable (e.g. 449-1480). However, C-terminal fragments were fully glycosylated only when they were co-expressed with their cognate N-terminal counterparts, in pairs already recognized by two-microelectrode voltage clamp as forming functional combinations. Co-expression of such pairs also resulted in much higher protein levels in every case, consistent with mutual stabilization.

Interestingly, even non-functional pairs (like Flag3-622 plus 634-1480) were able to co-immunoprecipitate with each other, even though C-terminal segments in such cases were merely core-glycosylated. These results suggest that interaction between complementary segments starts already in the ER, but pairs in which, because of non-tolerated cuts (or gaps), NBD1 cannot fold properly fail to exit the ER.

6.2.4. The N-terminal Flag epitope lowers the P_o of CFTR channels by slowing opening

As activation of CFTR channels by forskolin occurs via an indirect pathway involving adenylyl cyclase and PKA holoenzyme (and might therefore be subject to saturation in the oocyte), and IBMX at millimolar concentrations likely directly stimulates CFTR channel activity (Al-Nakkash and Hwang, 1999), we view our two-microelectrode recordings as coarse assays of the function of the various severed constructs. So, we directly activated the channels by applying catalytic subunit of PKA to the cytoplasmic surface of inside-out patches excised from oocytes, and evaluated their behavior in detail. And, because the N-terminal CFTR segments described so far had all been tagged with the Flag M2 epitope, we characterized the unitary currents of the three respresentative channel types, WT CFTR, CFTR severed just before NBD1, and CFTR severed just after NBD1, in each case with and without the Flag tag (e.g., Figure 21). The representative recordings in Figure 21 show that WT and Flag-WT CFTR channels share several of the accepted hallmark characteristics, such as single channel conductance, the requirement for ATP and prior phosphorylation by PKA for channel activity, relatively slow channel gating (interburst and burst durations on the order of seconds), and locking of the channels in the open state by PP_i (2 mM, in the presence of 0.1 mM MgATP) or by AMPPNP (data not shown). However, kinetic analysis revealed that the P_o of Flag-WT was ~1/3 that of WT

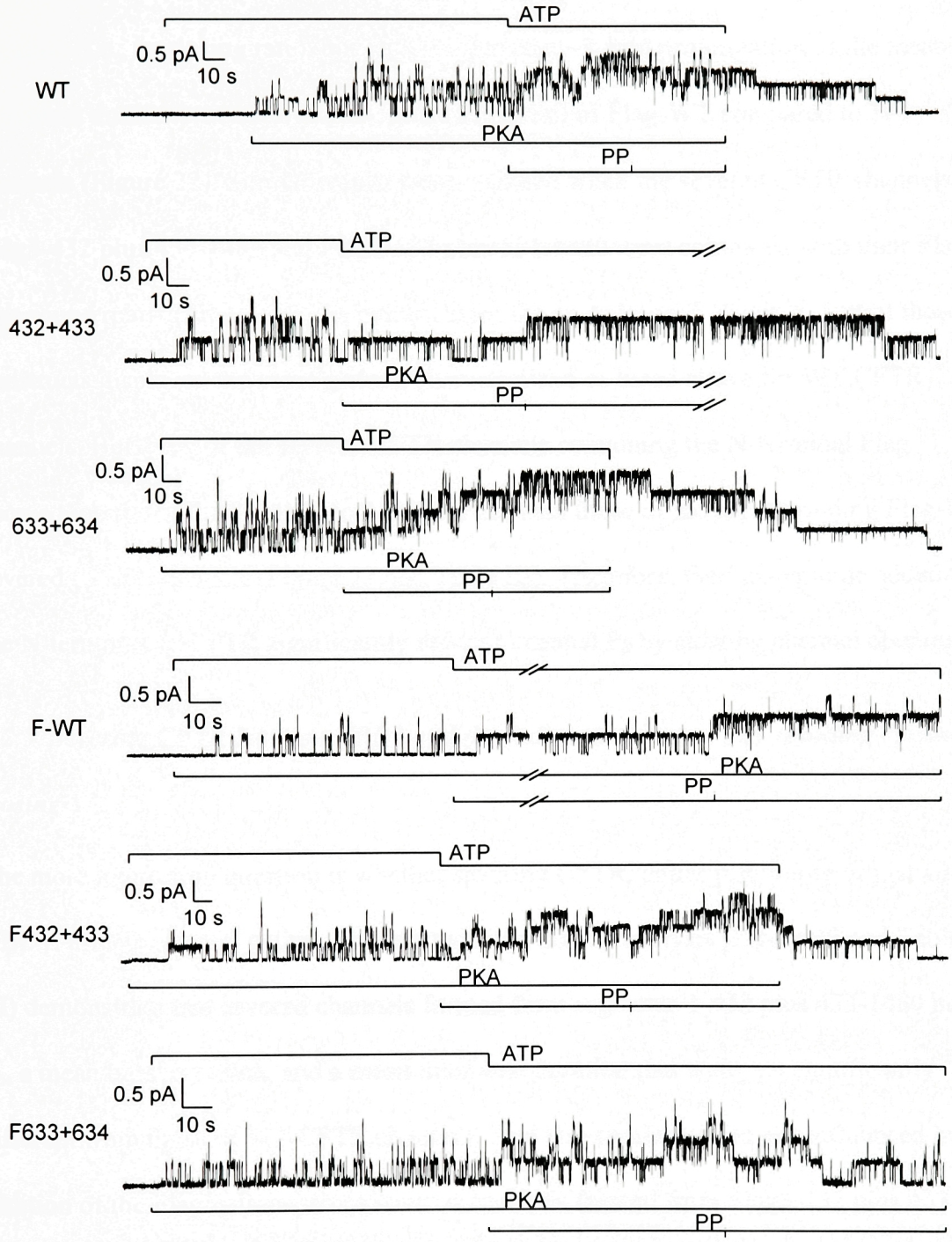

Figure 21. Representative excised-patch current records comparing WT CFTR and CFTR channels severed around NBD1. 1-432+433-1480, 1-633+634-1480, Flag-WT, Flag3-432+433-1480, and Flag3-633+634-1480 channels all shared hallmark features of WT CFTR including requirement of phosphorylation by PKA and exposure to MgATP for opening, slow burst kinetics, and locking in the open state by mixtures of ATP + PP_i.

(Figure 22 and Table III). This reduction in P_o was not due to any change in mean burst duration (i.e., in closing rate), but rather reflected a ~3-fold prolongation of the mean interburst duration (i.e., ~3-fold lower opening rate) of Flag-WT compared to WT channels (Figure 22). Similar results were obtained when the severed CFTR channels Flag3-432 plus 433-1480 and Flag3-633 plus 634-1480 were compared with their Flag-less counterparts (Figure 22). As evident from the recordings in Figure 21, all of these constructs displayed the same general characteristics as listed above for WT CFTR channels. But, both of the severed CFTR channels containing the N-terminal Flag showed interburst durations 2- to 3-fold longer than those of the corresponding Flag-less severed CFTR channels (Figure 22 and Table III). Therefore, the Flag epitope added to the N-terminus of CFTR significantly reduces channel P_o by slowing channel opening.

6.2.5. Severing CFTR between NBD1 and the R domain lowers P_o by speeding channel closing

The more interesting question is whether severing CFTR, either just before or just after NBD1, affects channel gating. The results of the kinetic analysis (Figure 22 and Table III) demonstrate that severed channels formed from segments 1-432 plus 433-1480 had a P_o, a mean burst duration, and a mean interburst duration that were not significantly different from those of WT CFTR channels. And this similarity was not influenced by addition of the Flag epitope, since severed channels formed from Flag3-432 plus 433-1480 segments showed P_o, and burst and interburst durations, closely similar to those of Flag-WT channels (Figure 22 and Table III). However, severed channels formed from CFTR segments 1-633 plus 634-1480 had a smaller P_o than WT or 1-432 plus 433-1480 channels, attributable to a reduced burst duration (i.e., to an increased closing rate). This

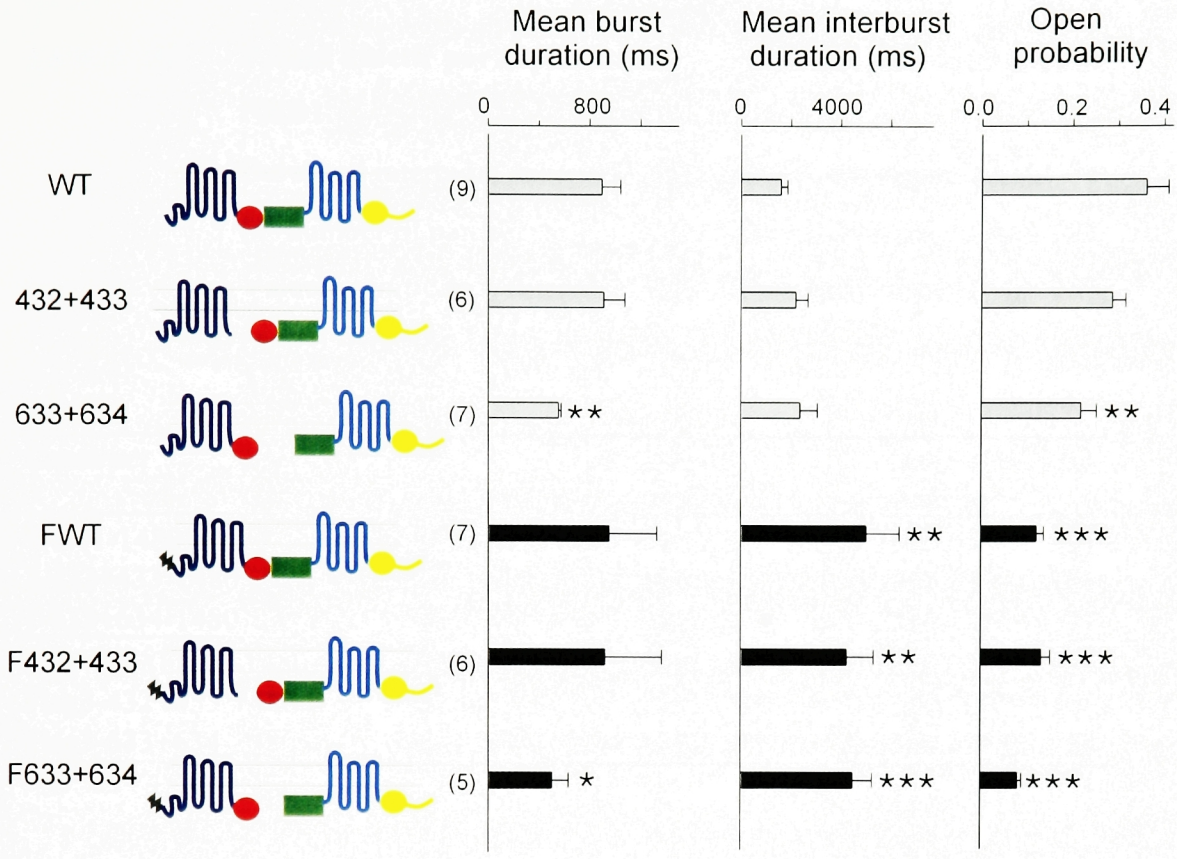

Figure 22. Kinetic analysis of WT CFTR and CFTR channels severed around NBD1. Kinetic parameters for WT, 1-432+433-1480, 1-633+634-1480, Flag-WT, Flag3-432+433-1480, and Flag3-633+634-1480 channels were extracted from records of patches containing 1-7 channels, exposed to 2 mM MgATP and 300 nM PKA. Mean burst durations of constructs severed between NBD1 and the R domain (1-633+634-1480 and Flag3-633+634-1480) were significantly shorter than those of WT, or Flag-WT, respectively. All constructs containing the Flag epitope (Flag-WT, Flag3-432+433-1480, and Flag3-633+634-1480) showed significantly prolonged interburst durations and, hence, significantly reduced P_o compared to WT. Significance levels are denoted by * (p<0.1), ** (p<0.05), or *** (p<0.01).

TABLE III **P_o and kinetic parameters of CFTR constructs severed around NBD1.**

Burst and interburst durations (in ms) and P_o are mean± s.e.m. (*n*=number of patches) at 2 mM MgATP and 300 nM PKA at ~22°C. Values significantly different from WT are marked with * ($p<0.1$), ** ($p<0.05$), or *** ($p<0.01$).

Construct	*Burst duration*	*Interburst duration*	*Open probability*	*(n)*
WT (1-1480)	896±145	1604±253	0.36±0.05	(9)
1-432+433-1480	910±166	2211±485	0.29±0.03	(6)
1-633+634-1480	554±21**	2380±703	0.22±0.03**	(7)
Flag-WT (Flag3-1480)	954±375	5050±1326**	0.12±0.02***	(7)
Flag3-432+433-1480	921±447	4279±1078**	0.13±0.02***	(6)
Flag3-633+634-1480	505±128*	4526±775***	0.08±0.01***	(5)

effect of severing CFTR channels just after NBD1 was independent of the presence or absence of the Flag epitope, because the mean burst duration of channels comprising segments Flag3-633 plus 634-1480 was significantly shorter than that of either Flag-WT or Flag3-432 plus 433-1480 channels (Figure 22 and Table III). These findings indicate that severing CFTR just before NBD1 has no measurable effect on channel P_o or gating kinetics, whereas severing CFTR between NBD1 and the R domain leads to a reduction in P_o due to an increase in channel closing rate.

6.2.6. Neither adding the Flag epitope, nor severing CFTR before or after NBD1, affects single-channel conductance or the apparent affinity for ATP

To verify that neither incorporating the Flag epitope, nor severing CFTR before or after NBD1, causes a major structural alteration in the channel pore, we measured single-channel conductances of WT and Flag-WT CFTR channels, and of severed channels formed from segments 1-432 plus 433-1480, or Flag3-432 plus 433-1480, or 1-633 plus 634-1480, or Flag3-633 plus 634-1480, in excised patches exposed to symmetrical 140 mM Cl^- solutions. Under these conditions, as illustrated for WT and for 1-432 plus 433-1480 channels, each channel type was characterized by an ohmic single-channel conductance: its average magnitude was ~7 pS, and there was no significant difference between the conductance of WT CFTR channels and that of any of the other constructs ($p=0.1$; Figure 23). This argues that severing CFTR, or adding the N-terminal Flag, did not grossly alter the pore architecture.

Assuming that hydrolysis of ATP at one of the binding sites (NBD-A) drives channel opening, there are two possible explanations for the observation that opening rate, and hence P_o, are decreased in Flag-tagged CFTR channels. This decrease could

Figure 23. Single-channel conductances of WT CFTR and CFTR channels severed around NBD1. WT, 1-432+433-1480, 1-633+634-1480, FlagWT, Flag3-432+433-1480, and Flag3-633 +634-1480 channels were assayed in symmetrical 140 mM Cl^-. **A, B,** Segments of records, illustrated for WT and 1-432+433-1480, at holding potentials of -80, -40, 0, +40, and +80 mV, were used to create amplitude histograms, fitted by sums of Gaussians (right). Distances between adjacent peaks, plotted against potential gave linear i/V plots. (Note shoulder in -80 mV histogram in **B**, due to excessive flickery closures at negative voltages.) **C,** Fitted slopes gave conductances (in pS) of 6.8±0.3 (WT, n=4), 7.1±0.2 (1-432+ 433-1480, n=4), 6.3±0.2 (1-633+634-1480, n=3), 6.64±0.26 (Flag-WT, n=3), 7.0±0.2 (Flag3-432+433-1480, n=3), and 7.0±0.1 (Flag3-633+634-1480, n=3), none of which differed significantly from WT at p<0.1.

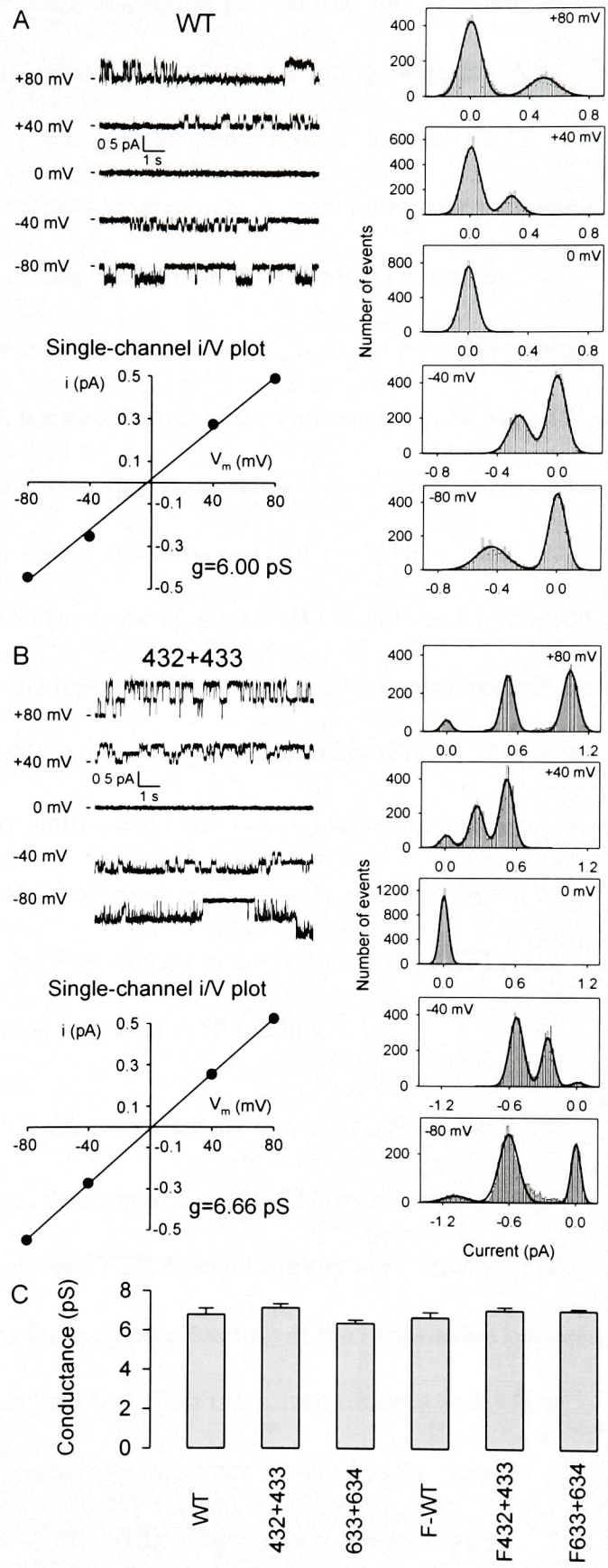

result from a reduction either in the binding affinity for ATP at that site, or in the rate of a step after binding (such as hydrolysis, or transmission of the gating conformational change to the pore). To distinguish between these two possibilities, for each CFTR construct we measured macroscopic currents in large patches containing many channels, and compared the current magnitude during exposure to 50 μM MgATP with that obtained at 2 mM (Figure 24). The ratio of these currents ($I_{50\mu M}$ /I_{2mM}) provides a rough measure of apparent affinity for ATP, because for all of the constructs 2 mM MgATP proved to be a saturating concentration: thus, I_{1mM} /I_{2mM} ratios were 1.02±0.01 (n=6) for WT, 0.94±0.03 (n=3) for 1-432+433-1480, 1.30±0.10 (n=4) for 1-633+634-1480, 1.02±0.04 (n=3) for FlagWT, 0.96±0.03 (n=3) for Flag3-432+433-1480, and 1.15±0.09 (n=3) for Flag3-633+634-1480. Both the representative macroscopic current records for each of these constructs (Figure 24 A-C) and the bar graph summary (Figure 24E) show that the $I_{50\mu M}$ /I_{2mM} ratios were all very similar and close to 0.5, indicating that $K_{1/2}$ (ATP) for activation of P_o was ~50 μM for all these constructs. Hence, the observed reduction in P_o following addition of the Flag epitope to the N-terminus of CFTR is likely to reflect slowing of a rate-limiting step after ATP binding.

6.2.7. Deletion of a.a. 415-432 in CFTR does not alter the apparent affinity for ATP

The demonstration that effective deletion of a.a. 415-432, by co-expression of segments Flag3-414 and 433-1480, impairs CFTR channel activity very little, if at all (Figure 20B, above), has ramifications for our understanding of the relationship between the structure of these channels and their function. This is because residues 415-432 in CFTR align with those comprising a structurally important β-strand in the recently solved high-resolution structures of HisP, the NBD of histidine permease (from *S.*

Figure 24. Apparent affinities for activation of P_O by MgATP for WT CFTR and CFTR channels severed around NBD1. Representative macropatch currents are shown for WT and Flag-WT (**A**), 1-633+634-1480 and Flag3-633+634-1480 (**B**), 1-432+433-1480 and Flag3-432+433-1480 (**C**), and Flag3-414+433-1480 (**D**) channels. After pre-phosphorylation by PKA, and removal of both PKA and ATP, once all channels had closed, 50 μM ATP was applied for 10-30 s, bracketed between exposures to 2 mM ATP. **E,** The ratios of the mean steady currents, $I_{50\mu M}$ /I_{2mM}, were 0.50+0.02 (WT), 0.56±0.03 (Flag-WT), 0.51±0.02 (1-633+634-1480), 0.42±0.01 (Flag3-633+634-1480), 0.49±0.02 (1-432+433-1480), 0.44±0.01 (Flag3-432+433-1480), and 0.45±0.01 (Flag3-414+433-1480). None of the constructs differed significantly from WT at $p<0.05$.

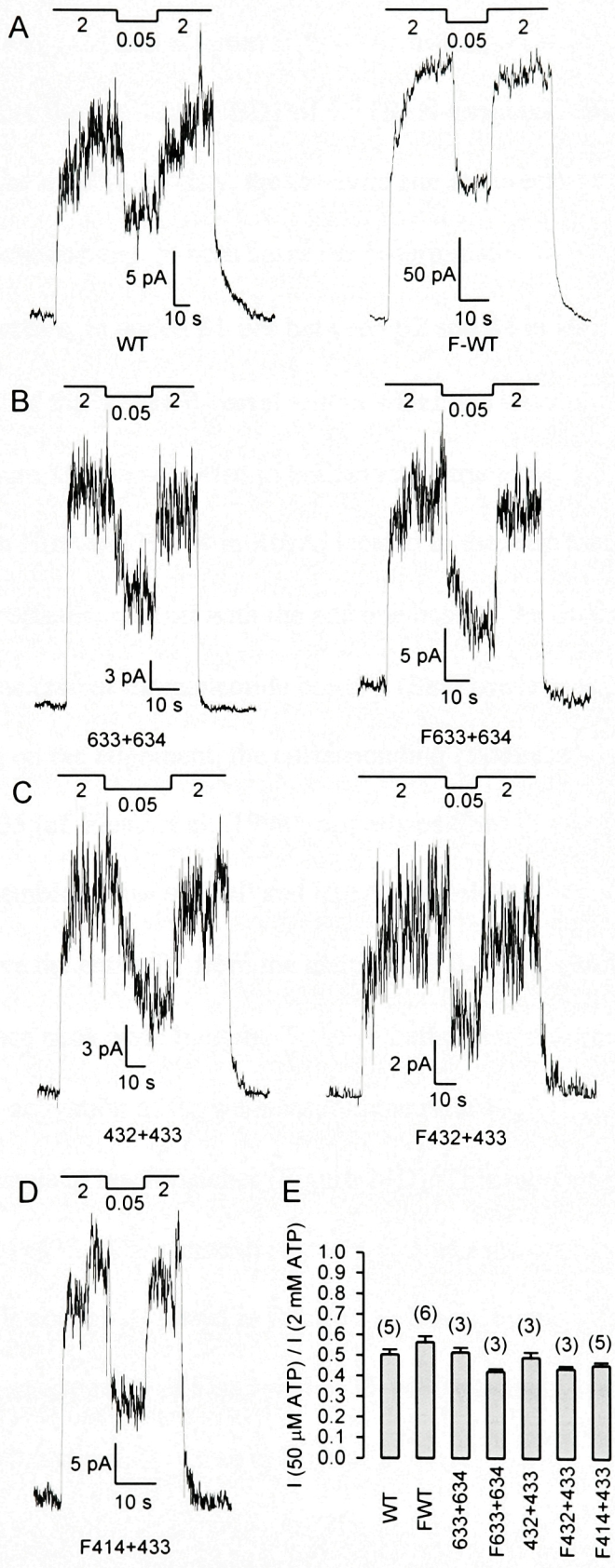

typhimurium; Hung et al., 1998), and of the N-terminal NBD in RbsA, which incorporates the two NBDs of the ribose transporter (from *E. coli*; Armstrong et al., 1998). Although the sequences of these three NBDs (NBD1 of CFTR, N-terminal NBD of RbsA, HisP) share only on the order of 20% identity, the catalytic site architectures of HisP and RbsA are closely similar. In particular, in both cases the N-terminal ≤70 residues form a β1-β2-β3-α1-β4 structure, in which β1 lies between β2 and β4 in an antiparallel sheet that forms one wall of the broken β-barrel within which the helix α1 lies and the nucleotide binds (cf. Figure 25, below). Also in both crystal structures, a conserved aromatic residue, Tyr16 in HisP and Phe14 in RbsA, located in the loop that links β1 to β2, makes extensive hydrophobic contact with the adenine base of the bound nucleotide and, at least in HisP, seems crucial for nucleotide binding (Shayamala et al., 1991; Hung et al., 1998). Depending on the alignment, the corresponding residue in NBD1 of CFTR is likely to be Leu435 (cf. Hung et al., 1998), or perhaps Phe433. Insofar as the structure of NBD1 resembles those of HisP and RbsA, the deletion of a.a. 415-432 may be anticipated to remove the entire β1 from the antiparallel β-sheet, which, in turn, would be expected to influence nucleotide binding. To see whether this deletion affects the apparent affinity for ATP activation of P_o, we measured the ratio $I_{50\mu M}/I_{2mM}$ for Flag3-414+433-1480 CFTR channels in macropatches (Figure 24D). This ratio was found to be close to 0.5 for Flag3-414+433-1480 channels, the same value as observed for WT (as well as all the other CFTR constructs tested in Figure 24). Since, in one experiment, I_{1mM}/I_{2mM} was 1.02 in a macropatch of Flag3-414+433-1480 channels, we may conclude that $K_{1/2}$(ATP) was ~50 μM also for these channels.

6.3. Discussion

The above experiments establish that physical and functional association of complementary segments of CFTR, severed just before or just after NBD1, results in split channels with microscopic properties closely similar to those of intact WT CFTR. Further, by systematically shifting the sever point, we have been able to define the domain boundaries of NBD1 to within 10-15 amino acids. The newly defined boundaries have important ramifications for structural and functional studies of CFTR's NBDs, whether as isolated polypeptides or in their native state, incorporated into full-length CFTR.

That a severed membrane transport protein may nevertheless function has been demonstrated previously. For example, *E. coli* cells expressing both putative hexahelical halves of *lac* permease, severed within its central cytoplasmic loop, transport lactose at about one third the rate of cells expressing intact permease, but no transport is seen in cells expressing either half alone (Bibi and Kaback, 1990). Similarly, co-expression in *Xenopus* oocytes of up to three complementary segments (severed within cytoplasmic or extracellular loops) comprising the full-length human erythrocyte anion exchanger (band 3, or AE1) resulted in Cl influx levels comparable to those observed after expression of intact WT band 3 (Groves et al., 1998). Although the domain organization of band 3 is not yet known, it is remarkable that the protein backbone can be cut at at least four sever points (and at least two of them simultaneously) with little detectable loss of Cl transport function. It is perhaps less surprising that a multi-domain protein like the voltage-gated Na channel, which has four repeats each with six putative membrane-spanning helices, can still function with a single cut between two repeats (at least in two of the three

linking loops; Stühmer et al., 1989). Eukaryotic ABC transporters are also multi-domain proteins with homologous internal repeats, a consequence of their evolution from procaryotic ancestors in which the individual domains are often expressed from separate genes (e.g. Higgins, 1992). So it is not surprising that ABC molecules such as the yeast **a**-factor transporter, STE6, can also function when co-expressed as two separate halves (Berkower and Michaelis, 1991), nor that co-immunoprecipitation experiments demonstrate that those two halves physically interact (Berkower et al., 1996). Representatives of the two families of multidrug resistance ABC proteins, Pgp (Loo and Clarke,1994) and MRP (Gao et al., 1996) have also been shown to survive being cut in half, between NBD1 and the second transmembrane domain, and to retain at least partial function: severed MRP transported substrate at least a third as well as intact MRP (a fraction possibly simply reflecting the efficiency of simultaneous transfection of the insect cells used; Gao et al., 1996), whereas severed Pgp supported substrate-induced ATPase activity about half that of intact Pgp, but showed no sign of drug transport in NIH-3T3 cells, possibly due to defective trafficking to the cell membrane (Loo and Clarke, 1994). Physical and functional association between N- and C-terminal halves of CFTR (residues 1-835 and 837-1480; cut after the R domain) was demonstrated by Ostedgard et al. (1997), who found that the severed construct supported intracellular cAMP-activated anion fluxes, assayed by measurements of SPQ fluorescence, that were comparable to those of WT CFTR.

Our detailed single-channel measurements show that individual severed CFTR channels, cut just before (1-432 plus 433-1480) or after NBD1 (1-633 plus 634-1480), have the same unitary conductance as WT CFTR channels (Figure 23) and almost

identical gating characteristics in the presence of PKA catalytic subunit (Figure 22). Both severed constructs had the same opening rate as WT channels, and the same apparent affinity for opening by MgATP, and both were locked open by PP_i (Figure 21) or AMPPNP. Only the closing rate of channels cut after NBD1 differed from that of WT, and was ~40% faster, indicating that the bursting state is somewhat destabilized by that cut, likely reflecting slight acceleration of the rate-limiting step in the ATP hydrolysis cycle at NBD2 (see in more detail in Chapter 7, below). So we can conclude that the normal function of NBD1 (which we infer to be major structural contribution to the ATP-binding site that controls channel opening, NBD-A; see Chapters 4 and 5) does not depend on its covalent linkage either to the first transmembrane domain, nor to the R domain, since the maximal opening rates are the same for intact channels as for channels cut before or after NBD1. Nor does channel opening require segments 415-432 (Figures 20B, 24D) or 634-667 (Figure 20A). On the other hand, we were surprised to see the comparatively large effect of incorporating the 8-residue Flag tag at the N terminus of CFTR, which consistently slowed channel opening ~2-3 fold, resulting in a ~2-3-fold reduction in P_o for both severed and intact constructs, without affecting the mean burst duration, conductance, or locking of any of the channels. Surprisingly, Moyer et al. (1998) found that attaching the 238-residue polypeptide GFP to the N terminus of CFTR affected neither single-channel conductance (assayed in bilayers) nor macroscopic whole-cell conductance in transfected NIH-3T3 cells. But it remains unclear whether channel P_o was affected by the large GFP tag, because the bilayer experiments did not address channel number or gating kinetics, and no comparison was made between the levels of CFTR protein expressed in cells transfected with WT CFTR and those transfected with

GFP-CFTR. Interestingly, an interaction between an acidic region of CFTR's N-terminal cytoplasmic tail and the R domain was recently demonstrated, which stabilized the open state of the channel (Naren et al., 1999); disrupting the interaction by mutating the acidic residues resulted in shorter bursts. It is not yet clear whether, or how, that finding relates to our observation here that incorporation of the largely acidic Flag at the N-terminus of CFTR stabilized the channel *closed* state (both for intact and for severed channels). We have found, however, that this effect is also mediated via the R domain, since addition of an N-terminal Flag does not alter the opening rate of severed CFTR channels from which the entire R domain (a.a. 634-836) is missing (see Chapter 7, below).

None of the half molecule constructs gave measurable basal or activated Cl^- conductance in two-microelectrode recordings of macroscopic currents, regardless of whether the oocytes were expressing the N-terminal half with (construct Flag3-835; see Chapter 7) or without (Flag3-633; Figure 20C) the R domain, or the C-terminal half with (CFTR construct 634-1480; Figure 20C) or without (construct 837-1480; see Chapter 7) the R domain. However, because we did not record from patches excised from those oocytes, we cannot rule out the possibility that an extremely low density of channels might be formed from certain half molecules. Our macroscopic current results contrast with a recent report that expression of only the C-terminal half of CFTR, either with or without the R domain, gave macroscopic, intracellular cAMP-activated, whole-cell currents in injected oocytes and in transfected IB3 cells, as well as unitary currents activated by PKA and ATP in patches excised from the IB3 cells (Devidas et al., 1998). Although a major procedural difference was the injection of 50 ng cRNA per construct in those experiments (vs. 2.5 ng in ours), it seems unlikely that protein expression was

correspondingly high because the activated conductance of WT CFTR was only ~5 μS (Devidas et al., 1998), more than 30-fold smaller than the average in the present experiments (Figure 20, Table II). Sheppard et al. (1994) did observe channel currents in patches excised from HeLa cells expressing just the N-terminal half of CFTR truncated after the R domain (segment 1-835), though channel formation was far less efficient than for WT CFTR, which presumably accounts for the fact that no change in SPQ fluorescence could be detected when the same cells were challenged with cAMP-elevating cocktail (Ostedgaard et al., 1997).

Assaying the function of severed molecules to define domain boundaries is an approach ideally suited to single-gene eukaryotic ABC transporters, since their individual domains may be expected to fold separately, and there are already examples of links between domains being severed without destroying the overall function (as described above). In general, if severing the backbone of a protein does not detectably impair its function it is reasonable to conclude both that covalent linkage at that point is not required for the assayed function, and either that the cut occurs between functional domains, or that the sever point lies within a domain but the native fold and function are nevertheless retained. The latter possibility may be virtually eliminated if function remains unaffected when a small deletion is introduced on one side or the other of the sever point. Because that was precisely our finding when we effectively deleted residues 415-432 (by co-expressing Flag3-414 plus 433-1480; Figure 20B) from the N-proximal side of NBD1, or residues 634-667 (by co-expressing Flag3-633 plus 668-1480; Figure 20A) from the C-proximal side of NBD1, we believe the domain boundaries of NBD1 of

CFTR can be confidently assigned to lie within residues 433-448, and within residues 623-633, at the N- and C-termini of NBD1 respectively.

How do these functionally defined boundaries of CFTR's NBD1 compare with the crystal structures of the HisP and RbsA NBDs, whose close similarity supports their being considered reasonable models for the structure of all ABC NBDs, including those of CFTR? Figure 25 shows a cartoon of a structural model of CFTR's NBD1 (built by Roberto Sánchez and Andrej Šali), based on alignment with the sequences of the crystallized homologs RbsA and HisP. Intervals within which our functional assays pinpointed N- and C-terminal boundaries of CFTR's NBD1 were mapped on the model, and are colored *blue*. The tolerated sever points close to the N- and C-termini are colored *green*, and the non-tolerated cut points are highlighted in *red*. Regions that could be discarded without apparently altering function (residues N-terminal of Phe433 and C-terminal of Leu633) are colored *gray*. Although the safe boundaries of CFTR's NBD1 circumscribe only 200 residues, whereas the crystallized NBDs of HisP and RbsA included 259 and 241 residues, respectively, the boundaries still compare reasonably well because alignments (e.g. Hung et al., 1998) indicate that NBD1 of CFTR lacks a stretch of 10-20 amino acids present in the other NBDs just after strand β4. Moreover, the safe sever points can be rationalized on the basis of such alignments. Thus, Phe433 (Figure 25, *green*) would be predicted to occur in a loop linking β1 to β2, distant from the γ-phosphate of bound ATP (although nearby Leu435, if not Phe433 itself, is implicated in binding of the nucleotide base; cf. Hung et al., 1998), and Leu633 (Figure 25, *green*) would be expected to occur after the final beta strand in the NBD1 structure, between it and a final helix (which is arranged slightly differently in HisP and RbsA). In

contrast, the non-tolerated sever point Glu449 (Figure 25, *red*) occurs 2 residues before a highly conserved glycine that in HisP and RbsA begins β3, where severing might disrupt the 6-stranded beta sheet that forms the major wall of the catalytic site, since β3 lies at the center of that wall. At the C terminus, Gly622 (Figure 25, *red*) is predicted to lie in the loop connecting the last two (antiparallel) beta strands of that large beta sheet, where severing might perturb stabilizing interactions between those two strands. Overall, that the structures of HisP and RbsA afford reasonable interpretations of our results with NBD1 of CFTR supports the notion that the NBDs of all ABC transporters are likely to share the same general fold. If so, our findings have importance for design of peptide models of CFTR's NBDs and imply, for instance, that CFTR NBD1 constructs truncated at or near residue 589 would be disadvantaged (cf. Hartman et al., 1992; Ko and Pedersen, 1995; Ko et al., 1997; Clancy et al., 1998), as might CFTR NBD2 constructs truncated at Leu1399 (corresponding to NBD1 Leu602; Randak et al., 1996, 1997).

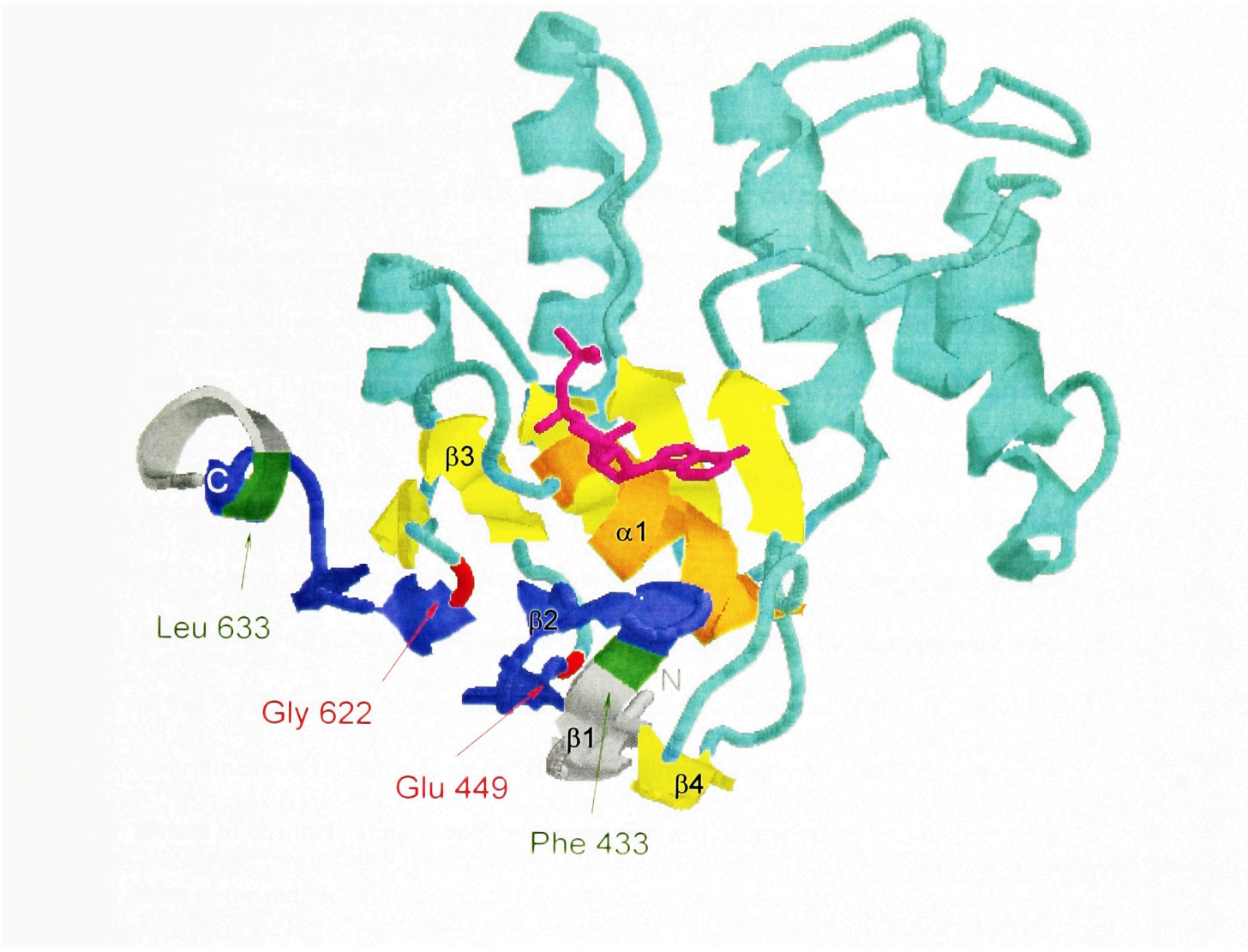

Figure 25. Cartoon of a structural model of CFTR's NBD1. The model was built based on sequence alignment with crystallized homologs RbsA and HisP. A β-barrel (*yellow*) with an α-helix in its center (*orange*) forms the core of the ATP-binding pocket; *magenta*, ATP. *Blue*, intervals within which functional domain boundaries were pinpointed (434-448, N-terminus; 623-632, C-terminus), mapped on the model structure. *Green*, Phe433 and Leu633, representing tolerated cut sites, *red*, Glu449 and Gly622, representing non-tolerated cut sites. *Grey*, regions that could be discarded without major functional consequences (regions N-terminal of Phe433, or C-terminal of Leu633).

7. R-DOMAIN FUNCTION

7.1. Introduction

Based on characteristics of gating of WT CFTR channels, described in Chapter 4 and in the literature, we have evaluated in Chapter 5 possible models that could account for the multitude of observations. A picture involving the interaction of the R domain with two ATP binding sites was found to fit most of the data, and was summarized in Model 6 of Figure 19. Accordingly, phosphorylation of the R domain by PKA (and probably PKC) is required before ATP binding, and likely hydrolysis, at NBD-A causes a CFTR channel to open. Depending on the channel's phosphorylation status, a second ATP may then bind at NBD-B and stabilize the open state of the channel until hydrolysis of that ATP prompts channel closure. The primary sequence of NBD1 is likely to contribute most of NBD-A, while NBD-B is formed mostly by NBD2. However, this picture of channel gating is both oversimplified and controversial, and neither the precise roles of the individual domains nor the details of the interactions between them are yet clear.

This chapter presents our studies aimed at clarifying the nature of these interactions between the R domain and the NBDs in regulating CFTR channel gating. One question is whether activation of CFTR channels via R-domain phosphorylation reflects disinhibition or stimulation, or both. Because opening of WT CFTR channels by ATP requires phosphorylation, it was suggested that the dephosphorylated R domain inhibits channel function (e.g., Cheng et al., 1991). This was further supported by the finding that CFTR channels with much of the R domain deleted, CFTR-ΔR(708-835),

were gated by ATP in the absence of phosphorylation, albeit with a poor open probability (Rich et al., 1991, 1993; Ma et al., 1997). The low opening rate of ΔR(708-835) channels, compared to WT, went hand in hand with their apparent inability to interact with AMPPNP or PP_i (Ma et al., 1997), substances that stabilize open bursts of phosphorylated WT channels (e.g. Figure 18, above). These deficiencies of ΔR(708-835) channels, together with a stimulation of their activity caused by phosphorylated exogenous R-domain peptides, led to the conclusion that the R domain inhibits CFTR-channel gating in its dephosphorylated state, but stimulates gating when phosphorylated (Winter and Welsh, 1997; Ma et al., 1997). In addition, all of the stimulation caused by PKA was ascribed to phosphorylation of the R domain, because PKA no longer influenced ΔR(708-835) channels once the residual R-domain serine, Ser 660, was mutated to alanine (Rich et al., 1993).

Although deletion of a domain is a useful strategy for discerning its function, the selection of appropriate boundaries for the deletion, to avoid steric distortion when non-adjacent residues are linked, is difficult unless the structure is already known. To circumvent this difficulty, the approach of exploiting split constructs, already used successfully for defining structural boundaries of NBD1 (see Chapter 6), was extended here to probe the interactions of the R domain with the NBDs responsible for regulating CFTR channel gating.

WT CFTR channels, and severed CFTR channels with a single cut close to either the N- or the C-proximal end of the R domain, as well as severed CFTR channels lacking the entire R domain between those cut sites, were expressed in *Xenopus* oocytes and studied by two-microelectrode voltage clamp and excised inside-out patch recordings.

Channel gating kinetics in patches were estimated from fits to macroscopic current relaxations and from analysis of steady-state single-channel dwell times. We found all these split channels to be efficiently processed in the oocytes. Severing CFTR between NBD1 and the R domain resulted in only a small change in gating properties, whereas a cut near the C terminus of the R domain allowed a small amount of phosphorylation-independent activity, enhanced the apparent affinity for ATP (at NBD-A), and appeared to destabilize the binding site for nucleotides at NBD-B. Split channels with no R domain were functionally similar to channels cut just after the R domain, except for a more pronounced activity without phosphorylation. Intriguingly, these severed channels lacking the entire R domain could be locked in the open state, although less efficiently than WT channels, by AMPPNP or PP_i, and could still be partially activated by PKA, suggesting that stimulation of WT CFTR by PKA may involve phosphorylation of sites outside the R domain. Because the opening rates were the same after phosphorylation for WT channels and split channels without an R domain, it seems unlikely that the phosphorylated R domain normally stimulates CFTR channel opening.

7.2. Results

7.2.1. Dependence on phosphorylation of currents in severed channels in resting and stimulated oocytes

CFTR channels severed near either the N-proximal (between residues 633 and 634; Chapter 6) or the C-proximal (between residues 835 and 837; Ostedgaard et al., 1997) boundary of the R domain show robust activity when stimulated by PKA. A

continuous CFTR construct in which residues 708-835 were deleted (ΔR(708-835); i.e. 707 and 836 linked; Rich et al., 1991, 1993; Ma et al., 1997) was previously found to show activity that no longer requires phosphorylation by PKA. So, we reasoned that co-expression of segments 1-633 and 837-1480 ought to yield severed CFTR channels without an R domain but with constitutive activity. We injected cRNA encoding WT or severed CFTR molecules into *Xenopus* oocytes and first measured membrane conductance under two-microelectrode voltage clamp as an assay of channel function (Figure 26). Stimulation of the cAMP/PKA pathway by 50 μM forskolin and 1 mM IBMX, which did not affect control uninjected oocytes (cf. Figure 20), elicited similarly large conductances in oocytes injected with 2.5 ng WT CFTR cRNA (173±4 μS, n=37), or 2.5 ng each of cRNAs encoding Flag3-835 plus 837-1480 (165±9 μS, n=14), or 2.5 ng each of cRNAs encoding Flag3-633 plus 837-1480 (179±5 μS, n=5), comparable to those we found for CFTR constructs severed before or after NBD1 (Chapter 6, cf. Figure 20). Resting oocytes expressing WT CFTR display a small but significant (~5-10 % of maximal) conductance that reflects a low level of phosphorylation by basally active PKA (cf. Chapter 4), because injection of RpcAMPS, an inhibitor of PKA, reduced that conductance (here from 14±1 μS, n=4 to 6±0.5 μS, n=5) to near the level seen in resting uninjected oocytes (3±0.3 μS, n=21; Figure 26): this implies that constitutively active phosphatases in the resting oocytes are able to dephosphorylate and inactivate the channels following RpcAMPS injection.

Unlike the small basal conductance of oocytes expressing WT CFTR channels (or Flag3-633 plus 634-1480 channels; Figure 20A), the conductances of resting oocytes injected with severed constructs Flag3-835 plus 837-1480 or Flag3-633 plus 837-1480

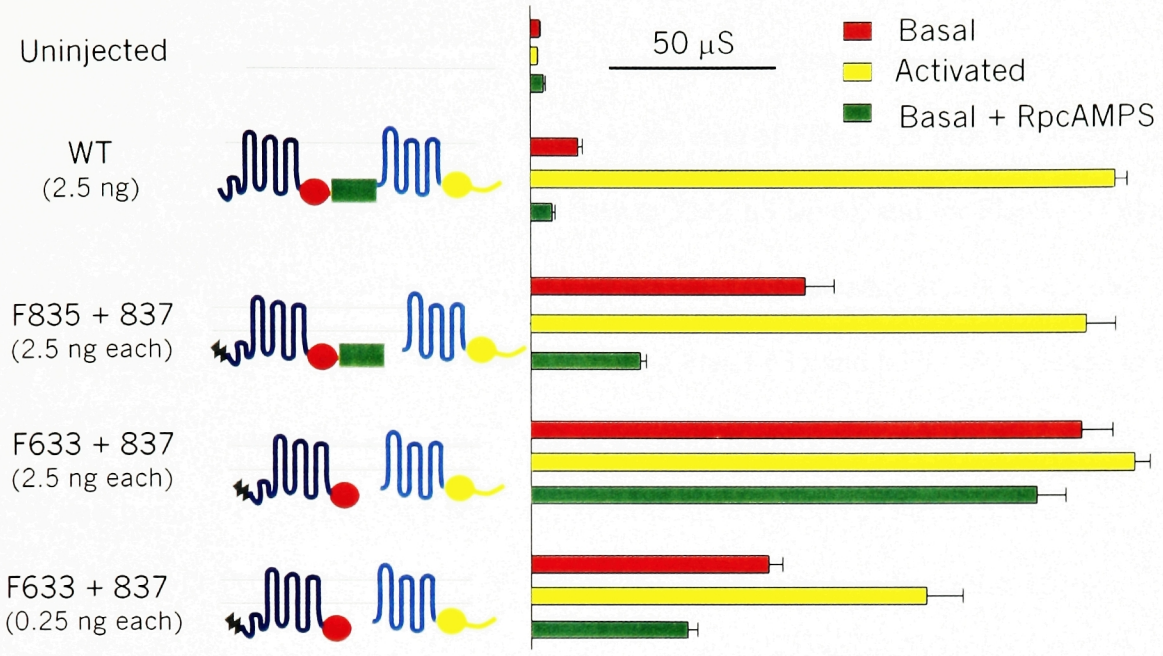

Figure 26. Dependence on phosphorylation by PKA of membrane conductance in oocytes expressing WT CFTR and CFTR channels severed around the R domain. Bars show mean (±s.e.m.) resting (basal, *red bars*) and activated (by 50 μM forskolin plus 1 mM IBMX, *yellow bars*) conductances, as well as conductances after RpcAMPS injection (2 mM final, *green bars*), of oocytes expressing WT, Flag3-835 plus 837-1480, or Flag3-633 plus 837-1480 CFTR (2.5 or 0.25 ng cRNA / construct, as indicated); as cartooned at left: N-terminal Flag epitope (*black zigzag*); TM domains (*blue*, *cyan*); NBD1 (*red circle*); R domain (*green rectangle*); NBD2 (*yellow circle*). Conductances were calculated from linear fits to steady-state I-V data between -60 and -20 mV. Maximal conductances of oocytes expressing any of the half-molecules alone was close to that of uninjected oocytes (2±1 μS, n=34). In μS: Flag3-633, 2±0.2 (n=15); Flag3-835, 3±0.4 (n=10); 634-1480, 5±1 (n=10); and 837-1480, 3±0.4 (n=9).

were relatively large, 82±9 μS (n=9) or 164±9 μS (n=4), respectively (Figure 26). Moreover, in contrast to the abolition of basal conductance that followed injection of RpcAMPS in oocytes expressing WT CFTR, in the case of Flag3-835 plus 837-1480 RpcAMPS reduced the basal conductance only to 33±2 μS (n=6), and for Flag3-633 plus 837-1480 channels RpcAMPS hardly reduced the basal conductance at all (150±9 μS, n=9). Use of only 0.25 ng of each cRNA encoding Flag3-633 and 837-1480 resulted in a smaller basal conductance (71±4 μS, n=5), again only slightly reduced (to 46±3 μS, n=2) by injection of RpcAMPS, but there was a significant activation of these channels by forskolin and IBMX (117±11 μS, n=5; Figure 26). These results indicate that PKA-mediated phosphorylation makes a substantial contribution to both the low level of activity of WT CFTR channels, and the greater activity of Flag3-835 plus 837-1480 channels, in resting unstimulated oocytes, whereas the comparatively large basal activity of Flag3-633 plus 837-1480 channels, which lack an R domain, is practically independent of phosphorylation by PKA, i.e., constitutive. Surprisingly, these Flag3-633 plus 837-1480 channels could still be stimulated by PKA, even though they had no R domain. However, the enhanced ratio of the (smaller) basal and activated conductances obtained with 0.25 ng cRNA suggests that the ~180-μS, apparently maximal, activated conductance (Figure 26) seen after injecting 2.5 ng (or more) of cRNA encoding a variety of CFTR channel constructs (cf. Figure 20) might reflect saturation, e.g., of some component in the cAMP/PKA pathway. Further analysis was therefore carried out using excised patches in which the channels could be directly phosphorylated with PKA catalytic subunit.

In addition, although the N-terminal Flag provides a convenient tag for co-immunoprecipitation of these severed constructs and will be important, e.g., for examining

possible phosphorylation of the channels with no R domain, it slows CFTR channel opening 2- to 3-fold (Figure 22). We therefore characterized mainly non-Flagged constructs, but also included Flag3-633 plus 837-1480 channels in all tests for later comparison with biochemical data.

7.2.2. Differential dependence on phosphorylation of macropatch currents of various severed channels

In excised patches the strong, membrane-coupled, endogenous phosphatase activity rapidly diminished to negligible levels the small basal activity of WT CFTR channels, and of those formed by segments 1-633 plus 634-1480, so they could not be activated by MgATP alone (e.g. Figure 28A, below, cf. Figures 14 and 21). But both of these channel types were similarly activated, over 10-20 s, by 300 nM PKA catalytic subunit in the presence of 2 mM MgATP, giving large macropatch currents (Figures 27A, B). Also in both cases, channel activity immediately (within 3-5 s) declined ~3 fold upon removal of PKA in the continued presence of ATP, but was then relatively stable, the remaining current declining much more slowly over several minutes. This biphasic decline is interpreted as extremely quick dephosphorylation by endogenous phosphatases of some phosphorylated residues, resulting in partially phosphorylated channels with lower activity, whereas other residues, supporting that residual current, are dephosphorylated with a much slower time course (cf. Chapter 4). As expected, all channels shut when ATP was withdrawn.

Patches containing severed 1-835 plus 837-1480 channels generated a sizeable current when MgATP alone was applied, even prior to PKA exposure (Figure 27C).

Nevertheless, subsequent application of PKA caused a robust several-fold increase in this macroscopic current.

Severed channels Flag3-633 plus 837-1480 (Figures 27D, 31E), and 1-633 plus 837-1480 (Figure 31D), both of which lack an R domain, displayed substantial activity in the presence of MgATP alone. Furthermore, superfusion with PKA increased current ~30-50% in patches containing Flag3-633 plus 837-1480 channels (Figure 27D), an effect also found for 1-633 + 837-1480 channels (cf. Figure 31D, E). This response to PKA was unexpected, since these constructs lack the entire R domain (residues 634-836), suggested to contain all, or most, of the phosphorylation sites responsible for channel activation (e.g. Seibert et al., 1995, 1999; Rich et al., 1993).

Figure 27E summarizes the relative amplitudes of the initial currents in the presence of MgATP alone (*black bars*), normalized to the maximal currents subsequently recorded in the same patches in the presence of PKA (*red bars*), for the three constructs that gave measurable currents before PKA application. This initial current, the component of basal whole-oocyte current that survives patch excision, likely reflects phosphorylation-independent activity, because preinjection of oocytes with RpcAMPS (which effectively abolished basal activity of WT channels; Figure 26) 10-20 minutes before patch excision, did not alter the fractional response of Flag3-633 plus 837-1480 channels to subsequently applied PKA (cf. *gray* vs. *black bars*; Figure 27E). This implies that by the time (typically ~2 min) recordings were begun in excised patches any basally phosphorylated residues capable of supporting channel activity had already been dephosphorylated by membrane-associated phosphatases.

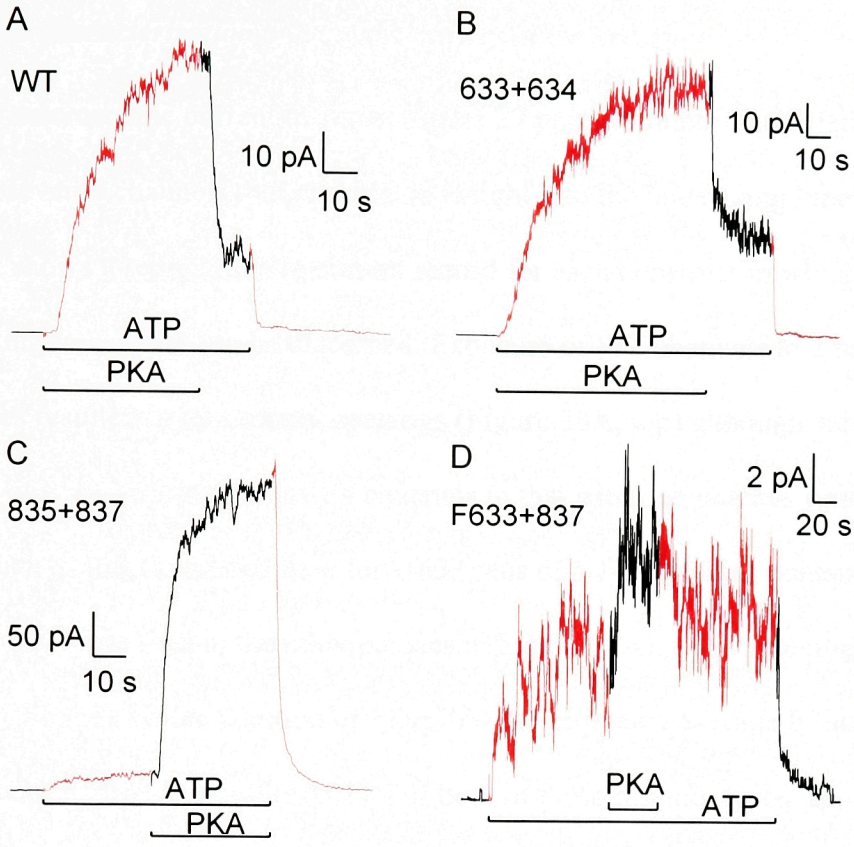

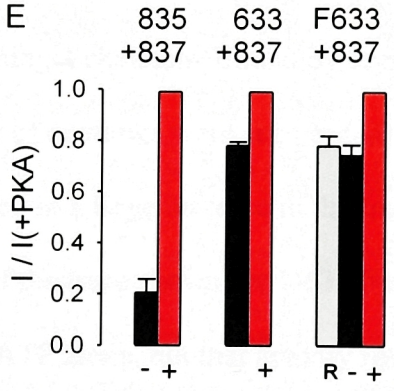

Figure 27. Macropatch currents of WT CFTR and CFTR channels severed around the R domain recorded before, during, and after exposure to 2 mM MgATP with and without 300 nM PKA. A, WT channels. **B,** 1-633 plus 634-1480 channels. **C,** 1-835 plus 837-1480 channels; note significant current activated by ATP alone, and robust stimulation by PKA. **D,** Flag3-633 plus 837-1480 channels; note strong activation by ATP alone, and small stimulation by PKA. **E,** Summary, currents activated by ATP alone (*black bars*, labeled "-"), normalized to currents subsequently measured in the same patches in the presence of PKA (*red bars*, labeled "+"), for constructs 1-835 plus 837-1480, 1-633 plus 837-1480, and Flag3-633 plus 837-1480; normalized basal current of Flag3-633 plus 837-1480 channels was unaltered in patches from oocytes preinjected with RpcAMPS (2 mM final, *gray bar*, labeled "R") to inhibit endogenous PKA.

7.2.3. Kinetic characterization of channel activity in the presence and absence of PKA

The macroscopic current traces in Figure 27 point to important differences among the various severed channels, but provide no insight into the underlying kinetic changes. Figure 28A shows a representative current record for each construct in which individual channel gating transitions can be discerned. Exposure of WT channels to 2 mM MgATP for 3 minutes resulted in no channel openings (Figure 28A, top) although subsequent application of PKA activated at least 4 channels in that patch. In patches containing many channels, such as that illustrated here for 1-633 plus 634-1480 (which contained ~15 channels, many more than in the other patches in Figure 28A), a few openings could occasionally be seen before addition of PKA, but the estimated average P_o under those conditions was negligibly small (≤ 0.01). For both of these channel types, application of PKA induced robust channel activity, a fraction of which survived after PKA removal. In the center trace, recorded from a patch containing 4 channels formed by segments 1-835 plus 837-1480, a small but significant number of openings were seen initially in MgATP alone, but subsequent exposure to PKA resulted in a large increase in the frequency of channel opening events. The initial segment of the trace shown for 1-633 plus 837-1480 also shows substantial channel activity in MgATP alone, but that activity resulted from the openings of only a single channel and so reflects a considerably higher constitutive P_o than that of the 1-835 plus 837-1480 channels. PKA caused an increase in the frequency of openings of the 1-633 plus 837-1480 channel, but the increase was much smaller than seen for 1-835 plus 837-1480. The trace representing the Flag3-633 plus 837-1480 construct demonstrates behavior comparable to that seen for its Flag-less counterpart. Figure 28 B-D summarizes the results of kinetic analyses performed on segments of records during

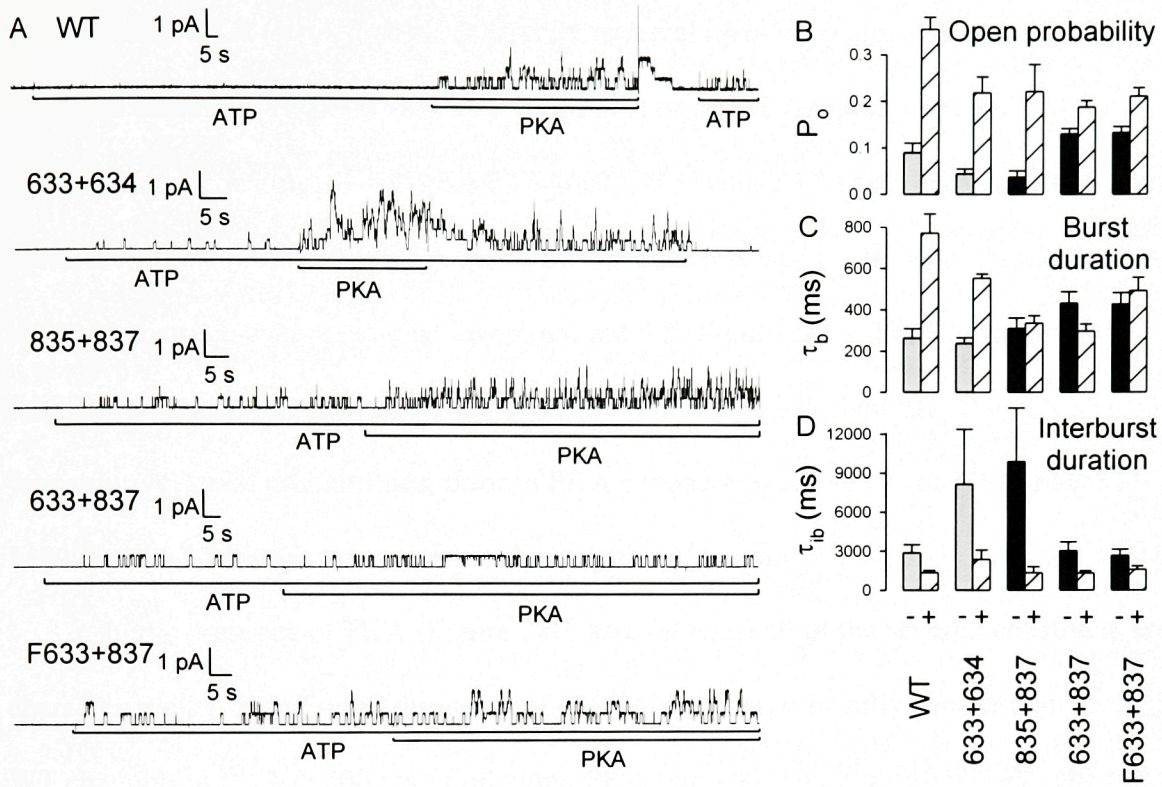

Figure 28. Kinetic parameters underlying phosphorylation-dependent changes in channel currents. A, Representative records from excised patches containing small numbers of WT and severed channels: 1-633 plus 634-1480, 1-835 plus 837-1480, 1-633 plus 837-1480, and Flag3-633 plus 837-1480. **B,** Open probability, **C,** mean burst duration, and **D,** mean interburst duration, from fits to steady-state multichannel dwell-time histograms for each construct (identified below each column): *striped bars*, estimates in the presence of 300 nM PKA and 2 mM MgATP; *black bars*, estimates in MgATP alone, before exposure to PKA, for constructs 1-835 plus 837-1480, 1-633 plus 837-1480, and Flag3-633 plus 837-1480; *gray bars*, estimates in MgATP alone, just after removal of PKA, for WT and 1-633 plus 634-1480 channels.

application of PKA (*striped bars*) or after its removal (*gray bars*) for WT and 1-633 plus 634-1480 channels, as well as before (*black bars*) or during (*striped bars*) PKA application for constructs 1-835 plus 837-1480, 1-633 plus 837-1480, and Flag3-633 plus 837-1480. In the presence of PKA the P_o of WT channels was ~0.36, whereas the P_o of the severed constructs was somewhat lower, around 0.2 (Figure 28B). The P_o dropped 3-4 fold for WT and 1-633 plus 634-1480 channels following PKA removal. The "constitutive" open probabilities, prior to PKA exposure, were ~0.04 for 1-835 plus 837-1480, and ~0.13 for the two constructs lacking the R domain.

In the presence of PKA (Figure 28C; *striped bars*) all of the severed constructs are characterized by open (burst) durations of ~300-500 ms, significantly shorter than those of WT channels in PKA (~800 ms). Following PKA removal, 1-633 plus 634-1480 channels, like WT channels, showed a considerable reduction of mean burst duration, in both cases resulting in bursts that lasted only ~200-250 ms (*gray bars*). However, the burst durations of channels 1-835 plus 837-1480, 1-633 plus 837-1480, and Flag3-633 plus 837-1480 changed little, if at all, when PKA was added or removed (Figure 28C; *black* vs. *striped bars* for those constructs).

The interburst durations (closed intervals) were similar (~1500 ms) for WT and all of the severed constructs in the presence of PKA (Figure 28D, *striped bars*). The sudden drop in P_o of WT and 1-633 plus 634-1480 channels following PKA removal (Figures 27A-B, 28A-B) is seen to partly reflect increased closed intervals (Figure 28D), not merely briefer openings (Figure 28C). The strong activation by PKA of 1-835 plus 837-1480 channels, as well as the more modest stimulation of the constructs with no R domain, was due to a shortening of the interburst durations which, in the absence of PKA, were

TABLE IV **P_o and kinetic parameters of CFTR constructs severed around the R domain.**

Mean±s.e.m. (*n*=number of observations) burst (τ_b) and interburst (τ_{ib}) durations (ms) and P_o at 2 mM MgATP with (+) or without (-) 300 nM PKA at 21 26 °C. Ratios were calculated individually only for patches tested under both conditions, and averaged.

Construct	WT	633+634	835+837	633+837	F633+837
$P_o(+)$	0.36±0.03(19)	0.22±0.03 (7)	0.22±0.06 (5)	0.19±0.01 (13)	0.21±0.02 (9)
$P_o(-)$	0.09±0.02 (5)	0.04±0.01 (4)	0.04±0.01 (3)	0.13±0.01 (18)	0.13±0.01 (13)
$P_o(+)/P_o(-)$	4.11±1.04 (5)	5.02±0.83 (6)	7.03±1.32 (6)	1.60±0.17 (15)	1.53±0.10 (11)
$\tau_b(+)$	771±92 (19)	554±21 (8)	336±36 (8)	297±35 (15)	493±64 (13)
$\tau_b(-)$	264±45 (5)	240±26 (6)	312±50 (7)	432±55 (24)	429±54 (18)
$\tau_b(+)/\tau_b(-)$	2.94±0.60 (5)	2.96±0.40 (6)	1.06±0.16 (6)	0.88±0.07 (15)	1.05±0.07 (12)
$\tau_{ib}(+)$	1364±158(19)	2380±703 (7)	1341±459 (5)	1297±181 (13)	1583±273 (9)
$\tau_{ib}(-)$	2900±606 (5)	8172±4187(4)	9895±4111(3)	3055±666 (18)	2678±467 (13)
$\tau_{ib}(+)/\tau_{ib}(-)$	0.62±0.16 (5)	0.55±0.11 (6)	0.17±0.05 (5)	0.58±0.07 (15)	0.67±0.06 (11)

very long (~10 s) for 1-835 plus 837-1480 channels, but less so (~3 s) for the constructs lacking the R domain (Figure 28D).

Table IV summarizes these kinetic parameters, and also their ratios when data were obtained with and without PKA in the same patch; these ratios agree well with those estimated in retrospect from the overall average parameters.

7.2.4. Macroscopic currents suggest increased apparent ATP affinity of channels cut after the R domain

If channel opening is the consequence of ATP binding to NBD-A followed by some irreversible rate-limiting step (e.g. ATP hydrolysis), then the affinity of NBD-A for ATP should be reflected by the dependence of channel P_o on ATP concentration. To see whether severing these CFTR molecules around the R domain influenced ATP binding, the apparent affinities of the severed constructs and of WT channels were assessed in macropatches by normalizing the steady-state currents at various [ATP] to that at 2 mM ATP. The tests were performed in the absence of PKA, i.e., in the constitutive, basal state for channels 1-633 plus 837-1480 and Flag3-633 plus 837-1480, but after PKA removal for WT, 1-633 plus 634-1480, and 1-835 plus 837-1480 (since for the latter construct pre-phosphorylation activity was fairly small).

Figures 29A and B show a series of such measurements for WT and 1-633 plus 837-1480 channels, with steps between 2 mM ATP and 2, 10, 20, 50, 100, 500 μM, or 1 mM ATP. Simple inspection of the traces reveals that half-maximal activity of WT channels requires ~50 μM ATP, whereas for 1-633 plus 837-1480 channels 20 μM ATP is sufficient. Results from experiments like these are summarized in Figure 29C for patches containing WT (*filled circles*), 1-633 plus 837-1480 (*empty triangles*), and Flag3-633 plus

837-1480 (*filled triangles*) channels. The *solid* and *dotted lines* are Michaelis-Menten fits to the data for WT and Flag3-633 plus 837-1480 channels respectively; the fit to the data for 1-633 plus 837-1480 overlies the *dotted line*, and was omitted for clarity. K_m estimates (in μM) from the fits were 51±2 for WT, 25±1 for 1-633 plus 837-1480, and 23±1 for Flag3-633 plus 837-1480. Fitting the same data to the Hill equation yielded Hill coefficients of 0.98±0.06 for WT, 0.84±0.05 for 1-633 plus 837-1480, and 0.99±0.08 for Flag3-633 plus 837-1480 channels.

Figure 29D summarizes relative currents at 50 μM ATP (normalized to those at 2 mM ATP) for all of the constructs, including 1-633 plus 634-1480 and 1-835 plus 837-1480 for which dose response curves were incomplete. The ratio $I_{50\mu M}/I_{2mM}$ provides a rough measure of apparent affinity, because 2 mM ATP was a saturating concentration for each construct (I_{1mM}/I_{2mM} ratios were: 1.02±0.01 (n=6) for WT, 1.34±0.10 (n=4) for 1-633 plus 634-1480; 1.03±0.02 (n=5) for 1-835 plus 837-1480, 1.05±0.02 (n=3) for 1-633 plus 837-1480, 1.06±0.01 (n=2) for Flag3-633 plus 837-1480). The $I_{50\mu M}/I_{2mM}$ ratio of 1-633 plus 634-1480 channels (0.51±0.02, cf. Figure 24B, E) was not significantly different (p>0.1) from WT (0.50±0.02), but that ratio for channels 1-835 plus 837-1480 (0.71±0.02), 1-633 plus 837-1480 (0.62±0.01), and Flag3-633 plus 837-1480 (0.66±0.02) was in each case significantly higher than for WT channels (p<0.01; Student's t-test).

7.2.5. The macroscopic response to ATP reflects [ATP] dependence of the opening rate

To see whether the changes in channel P_o with [ATP] (Figure 29A-C) reflected changes in burst or interburst duration, or both, we analyzed channel kinetics. WT channels were examined in their partially phosphorylated state, shortly after PKA removal, and Flag3-633 plus 837-1480 channels were studied in their constitutively active

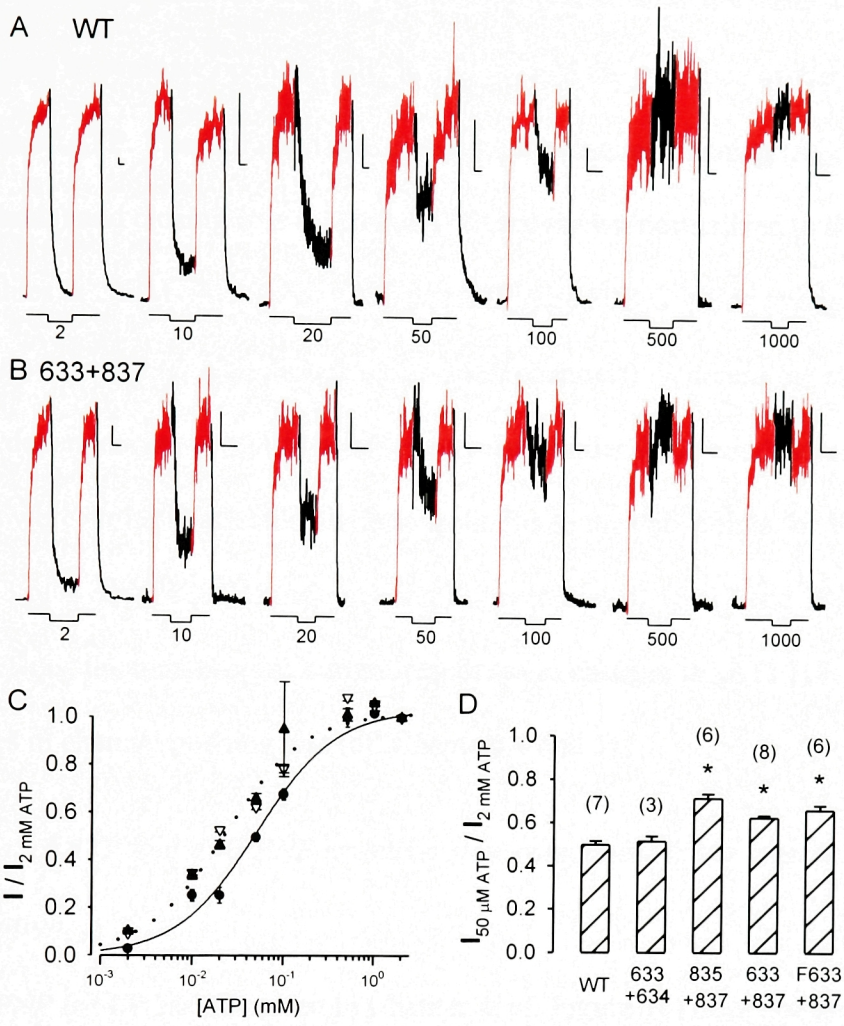

Figure 29. Apparent affinity for ATP as reflected by P_o, for WT CFTR and CFTR channels severed around the R domain. Tests were done following PKA removal for WT, 1-633 plus 634-1480, and 1-835 plus 837-1480, and before applying PKA for 1-633 plus 837-1480 and Flag3-633 plus 837-1480. **A, B,** Macroscopic currents of WT (**A**) and 1-633 plus 837-1480 (**B**) in response to step applications of 2 mM [ATP] with intervening 10-30-s test exposures to 2, 10, 20, 50, 100, 500 μM, and 1 mM [ATP], respectively; scale bars, 5 pA and 10 s. **C,** Summary, activation of macroscopic current by [ATP], normalized to that at 2 mM [ATP]. WT, *filled circles*; 1-633 plus 837-1480, *empty triangles*; Flag3-633 plus 837-1480, *filled triangles*. *Solid line*, Michealis fit for WT; K_m=51±2 μM. *Dotted line*, fit for Flag3-633 plus 837-1480; K_m=23±1 μM. The fit for 1-633 plus 837-1480, omitted for clarity, overlies the *dotted line*; K_m=25±1 μM. **D,** Summary, relative currents $I_{50\mu M}/I_{2mM}$; * means significantly higher (p<0.01) than WT.

state in the complete absence of PKA (Figure 30A). In both cases, the quasi-stationary activity was used to evaluate opening and closing rates in the presence of varying concentrations of ATP. The extracted rate constants for channel opening (r_{CO}; see *C-O-B* scheme, Methods) and closing (r_{OC}) at each [ATP] are shown normalized to their respective values at 2 mM ATP in the same patch (Figure 30B,C: *filled triangles*, WT channels; *empty triangles*, Flag3-633 plus 837-1480 channels). Whereas the closing rates showed little dependence on [ATP] for either construct under these conditions, the opening rates were strongly affected, the Michaelis fits to the data points for WT (*solid*) and Flag3-633 plus 837-1480 (*dotted*) yielding K_m estimates of 46±13 and 39±7 μM, respectively. Thus, the macroscopic current responses to changes in [ATP] (Figure 29) report changes in channel opening rate (cf. Chapters 4 and 5).

7.2.6. Removal of ATP and AMPPNP reveals a slow component in the macroscopic current relaxation

AMPPNP (or PP_i, as discussed in Chapter 4, cf. Figure 18) does not support channel opening by itself, but, when added with ATP, it can lock channels in the open state, due to tight binding of AMPPNP presumably to NBD-B; similarly long open bursts result from mutations at NBD2. WT channels may be locked open only when they are highly phosphorylated, implying that the high-affinity site for AMPPNP responsible for the effect is rarely accessible in poorly phosphorylated channels (Hwang et al., 1994).

We tested whether AMPPNP elicits a locking effect in the severed channels, by exposing macropatches containing the various constructs to 1 mM AMPPNP plus 0.1 mM ATP in the presence of PKA. Upon removal of all nucleotides no further channel openings are expected (e.g., Figure 27, above), and the relaxation rate of the current then reflects the

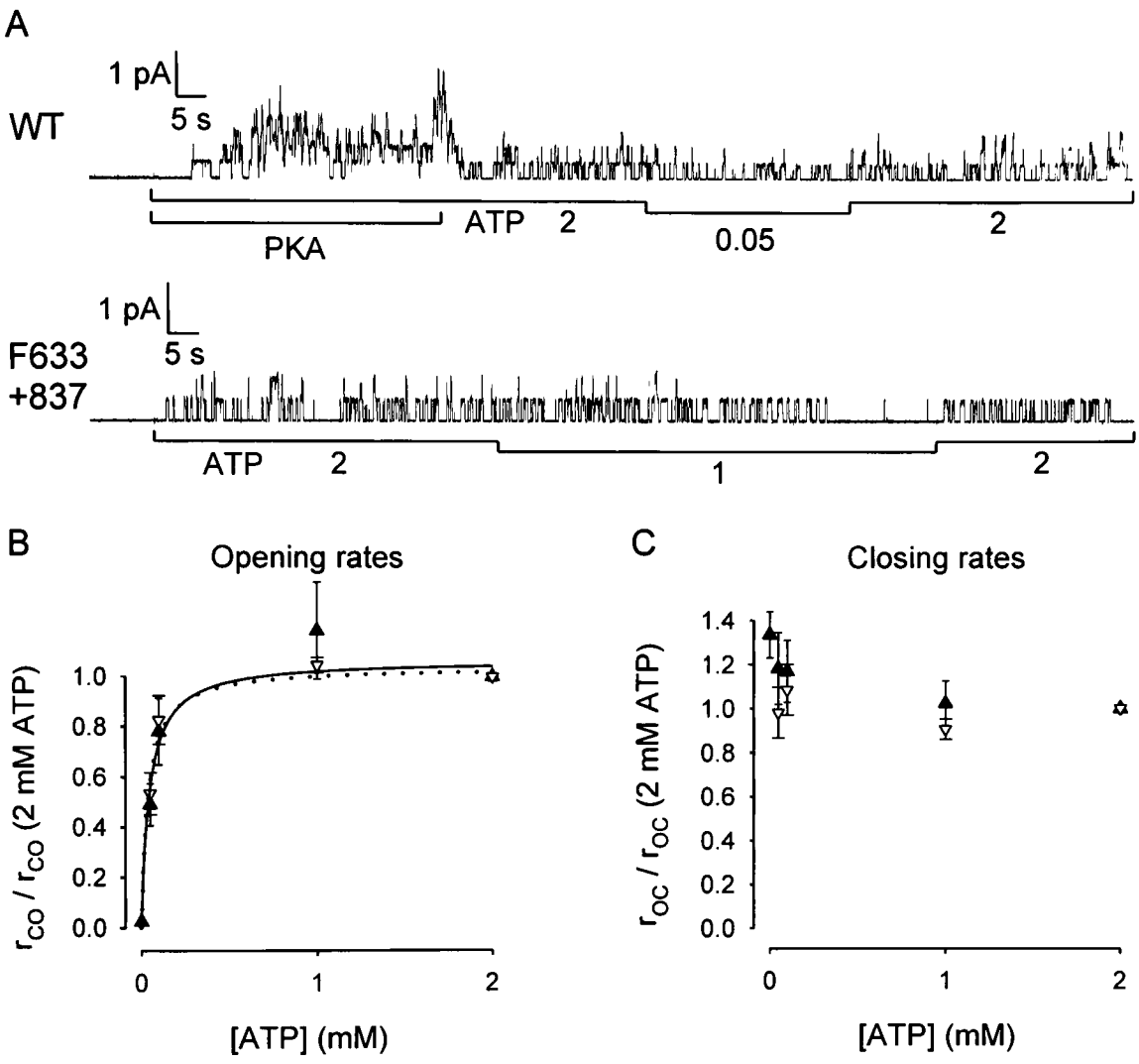

Figure 30. Dependence on [ATP] of opening and closing rates of WT and Flag3-633 plus 837-1480 CFTR channels. A, Representative recordings from patches with few channels: quasi-stable activity of WT (*top*) after initial rapid drop in P_o on removal of PKA; Flag3-633 plus 837-1480 (*bottom*) before exposure to PKA. **B, C,** Summary of opening and closing rates from the segments at test [ATP] (50 μM, 100 μM, and 1mM, for WT also 2 μM) normalized to the mean of the estimates obtained from the bracketing segments at 2 mM ATP, from experiments like in **A**, for WT (*filled triangles*) and Flag3-633 plus 837-1480 (*empty triangles*). *Solid* and *dotted lines* in **B** are Michaelis fits for WT and Flag3-633 plus 837-1480, giving K_m values of 46±13 μM and 39±7 μM, respectively.

rate of channel closure. A brief pulse of 2 mM Ca^{2+} at the end of each experiment opened and closed endogenous Ca^{2+}-activated Cl^- channels, the current relaxation providing a rough measure of solution exchange time (time constant 200-600 ms), which was an order of magnitude faster than the fastest unlocking rates found here.

Figure 31 shows a representative record for each construct at ~24 (23-25) °C. Once WT-channel current was steady in 300 nM PKA and 2 mM MgATP, the [ATP] was decreased to 0.1 mM and 1 mM AMPPNP was added (Figure 31A). An initial current drop, due to both the decreased [ATP] (cf. Figures 29, 30) and competition with AMPPNP for the site of channel opening, was followed by robust activation. After withdrawal of all nucleotides the current decayed to zero with an exponential time course (fitted *blue line*) of time constant 47 s, reflecting the mean dwell time of AMPPNP on the channels. A similar result was obtained with severed 1-633 plus 634-1480 channels (Figure 31B) for which the single-exponential fit to the current decay gave a time constant of 38 s.

For severed 1-835 plus 837-1480 channels, the AMPPNP test was bracketed by two applications of ATP alone, with or without PKA – the latter followed by the brief Ca^{2+} pulse – and fits were made to all four decay time courses (Figure 31C). The first, after removal of ATP plus PKA, required two exponential components for a good fit, with time constants τ_1=623 ms and τ_2=10.3 s, and amplitudes a_1=365 pA and a_2=25 pA, respectively. The relaxation following AMPPNP withdrawal also needed two exponential components, with time constants τ_1=337 ms and τ_2=11 s, and amplitudes a_1=63 pA and a_2=501 pA, respectively. But the last two current decays, following removal of ATP and of Ca^{2+}, were both well fit by single exponentials with time constants 429 ms and 568 ms, respectively. Because the time constants of the fast components in the first two relaxations

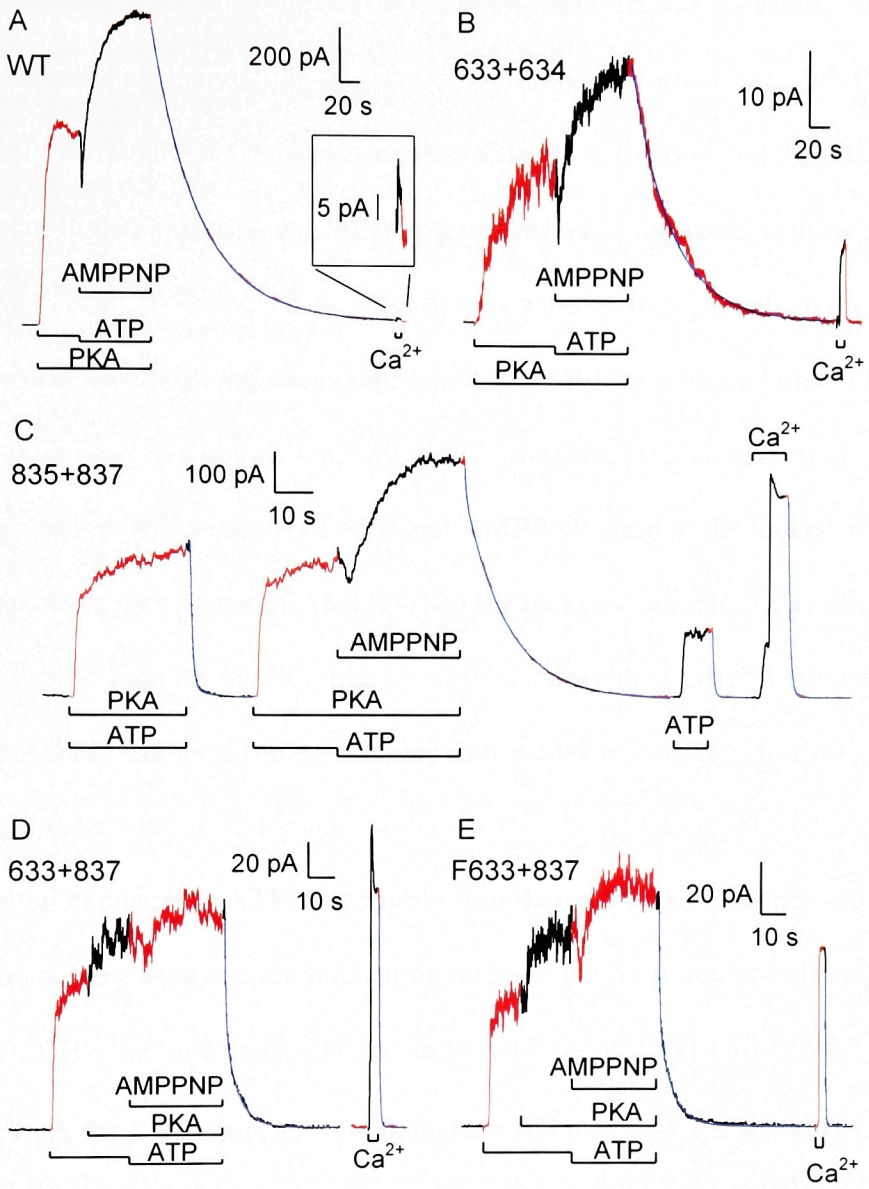

Figure 31. Slow current relaxation after removal of ATP and AMPPNP in WT and severed channels. Channels, activated by 2 mM MgATP with or without 300 nM PKA, were locked open with 1 mM AMPPNP plus 0.1 mM ATP in PKA; brief stimulation of Ca^{2+} activated Cl^- channels with 2 mM Ca sulfamate indicated solution exchange time. **A,** WT; *blue line*, single exponential fit, $\tau = 47$ s. **B,** 1-633 plus 634-1480; *blue line*, single exponential fit, $\tau = 38$ s. **C,** 1-835 plus 837-1480; double exponential fit after AMPPNP, $\tau_1 = 337$ ms, $\tau_2 = 11$ s, a_1=63 pA, a_2=501 pA. **D,** 1-633 plus 837-1480; double exponential fit after AMPPNP, $\tau_1 = 439$ ms, $\tau_2 = 4.7$ s, a_1=57 pA, a_2=59 pA. **E,** Flag3-633 plus 837-1480; double exponential fit after AMPPNP, $\tau_1 = 364$ ms, $\tau_2 = 5.2$ s, a_1=41 pA, a_2=40 pA.

and of the third decay were all comparable to that observed for Ca^{2+} washout, they all likely reflect solution exchange time and so were not studied further. AMPPNP, added in the presence of PKA and ATP, evidently caused a strong activation and introduced a large slow component in the current decay following its removal, compared to those after washout of ATP, or of ATP plus PKA. However, in contrast to the results with WT and 1-633 plus 634-1480 channels, the decay on removing AMPPNP also included a fast component, suggesting that not all 1-835 plus 837-1480 channels contributing to the steady-state current in the presence of ATP and AMPPNP were in the locked state. Further, the apparent dwell time of AMPPNP on the locked channels (11 s) was considerably shorter than for the WT-like constructs, implying a faster dissociation rate of AMPPNP from these channels (note expanded time scales in Panels 31C-E).

The channels with no R domain (with or without the Flag) displayed constitutive activity on initial exposure to ATP, discernible stimulation by PKA, further activation by AMPPNP, and current decays upon nucleotide removal that required double-exponential fits (Panels 31D, E): the time constants and amplitudes were τ_1=439 ms, τ_2=4.7 s, a_1=57 pA, and a_2=59 pA for 1-633 plus 837-1480, and τ_1=364 ms, τ_2=5.2 s, a_1=41 pA, and a_2=40 pA for Flag3-633 plus 837-1480. For these two patches the Ca^{2+}-washout time constants were 372 ms and 212 ms. Thus, AMPPNP consistently enhanced current and introduced a slowly decaying component after its removal, but the fraction of channels locked was smaller for the channels severed after the R domain and they became unlocked more rapidly than WT-like channels (Table V).

TABLE V **Time constant and fractional amplitude of slow component of current decay after AMPPNP removal.**

Mean±s.e.m. time constants (τ_{AMPPNP}; ms) and fractional amplitudes (a_{locked}), measured at ~24°C; n=number of patches.

Construct	τ_{AMPPNP}	a_{locked}	n
WT	39316±3646	0.90±0.07	9
633+634	58052±14447	1.00±0.00	4
835+837	7310±1027	0.59±0.09	9
633+837	5841±423	0.47±0.04	8
F633+837	8161±2203	0.65±0.11	5

7.2.7. Prolonged bursts in AMPPNP underlie the slow current decay following AMPPNP removal

In patches with few channels, AMPPNP added with ATP elicited long open bursts both for WT channels and for all the severed constructs. Removal of all nucleotides then resulted in a staircase-like current decay in which individual unlocking events could be identified, as illustrated by traces from WT (Figure 32A) and 1-633 plus 837-1480 channels (Figure 32C), both of which start 5 s after withdrawal of 1 mM AMPPNP and 0.1 mM ATP. The solid (*red*) lines represent the reconstructed idealized sequences of unlocking events (see Methods). Adding up such idealized unlocking sequences (excluding the first 5 s) from two tests on WT (Figure 32B), and from five tests on 1-633 plus 837-1480 channels (Figure 32D), all at ~24 °C, and fitting the resulting relaxations, yielded single exponentials with time constants of 31 s for WT and 6.4 s for 1-633 plus 837-1480; a similar procedure with four tests on Flag3-633 plus 837-1480 channels gave a time constant of 9.3 s. Thus, in these severed constructs, AMPPNP induces long open bursts with a mean duration in good agreement with the time constant of the slow component of the macroscopic current relaxations on AMPPNP removal (Figure 31, Table V).

7.2.8. Burst distributions imply different mechanisms of shorter mean burst durations of cut channels

In PKA, the mean burst durations of all the severed constructs were similarly shortened, compared to WT (Figure 28C), but their locking behavior with AMPPNP separated them into two groups. 1-633 plus 634-1480 channels resembled WT in that the

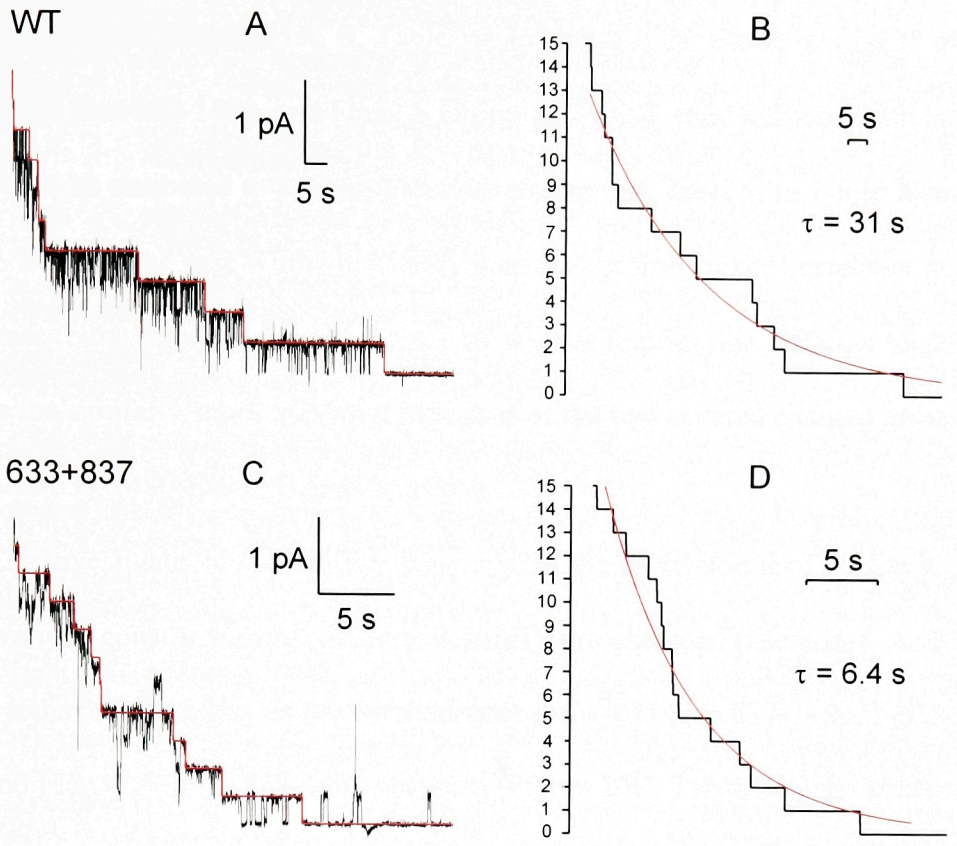

Figure 32. Long bursts of openings induced by AMPPNP. A, C, Delayed closure of WT (**A**) and 1-633 plus 837-1480 (**C**) channels after washout of 0.1 mM MgATP and 1 mM AMPPNP 5 s before the start of each trace. Solid *red lines* show unlocking events reconstructed using algorithm in Methods. **B, D,** Idealized sequences of unlocking events for WT (**B**) and 1-633 plus 837-1480 (**D**) channels, constructed by summing results of two WT and five 1-633 plus 837-1480 experiments like those at left. Note different time scales in **A**, **B** vs. **C**, **D**.

currents of both decayed as a single exponential with similar time constants following AMPPNP removal (Figure 31A, B; Table V). In contrast, for constructs 1-835 plus 837-1480, 1-633 plus 837-1480, and Flag3-633 plus 837-1480, only a fraction of that current decay could be attributed to a slow unlocking component, itself 5- to 7-fold faster than for WT. Because the ease with which WT channels become locked correlates with their open times (burst durations; Hwang et al., 1994), this implies that different mechanisms underlie the similarly shortened burst durations of the two severed channel groups, viz., 1-633 plus 634-1480 channels and the others.

To investigate this possibility, we analyzed the distributions of the burst durations for the various constructs, after flickery closures were excluded (Methods). As PKA seemed to have little effect on the burst durations of 1-835 plus 837-1480, 1-633 plus 837-1480, and Flag3-633 plus 837-1480 channels (Figure 28C; Table IV), and because of the limited number of true single-channel records, segments of records in the absence or presence of PKA were pooled for those three constructs. But, for WT and 1-633 plus 634-1480 channels segments recorded in the presence of PKA were analyzed separately from those in its absence. The distributions of the burst durations were maximum likelihood-fitted with both single exponentials and sums of two exponential distributions, and the need for the second component was accepted or rejected based on its improvement of the likelihood (Methods).

Figure 33 shows the distributions of burst durations obtained for each construct in the form of survivor functions, i.e., the probability that a channel is *still* in the bursting state after time *t*, provided it was in the burst state at time *zero*, is plotted against time. Solid *red lines* represent the best fits obtained by the above criterion. The *top* panels show

the distributions for WT and 1-633 plus 634-1480 channels in the presence ("+"; *1*st and *3*rd panels from left) and absence of PKA ("-"; *2*nd and *4*th panels). All four of these distributions were well fit by single exponentials, and introduction of a second component did not significantly improve the likelihood. The time constants of the fits were 778 ms and 461 ms in the presence of PKA for WT and for 1-633 plus 634-1480, respectively, in good agreement with the mean burst durations of these same constructs obtained from multichannel kinetic fits under the same conditions (771 ms, and 554 ms, respectively; Figure 28C, *striped bars*, and Table IV). In the absence of PKA the fitted time constants were 263 ms and 214 ms for WT and 1-633 plus 634-1480, close to the estimated mean burst durations of 264 ms and 240 ms, respectively, under those conditions (Figure 28C, *gray bars*, and Table IV).

The three *lower* graphs (Figure 33) display distributions and fits for constructs 1-835 plus 837-1480, 1-633 plus 837-1480, and Flag3-633 plus 837-1480. In all three cases introducing a second component into the fit significantly improved the likelihood. The brief components, accounting for the larger fraction of events in all three cases, were characterized by time constants reminiscent of those observed for WT and 1-633 plus 634-1480 channels in the absence of PKA. However, in all three cases there was also a clearly discernible long component with a time constant not very different from that for WT in the presence of PKA (*top* row, *left*).

7.2.9. Strong temperature dependence of burst durations and locking behavior

The experiments in Figures 27-28 and 33 were performed at ambient room temperature, which varied between extremes of 21 and 26 °C and was noted on each experimental day. Data were separated, in retrospect, into pools recorded at temperatures

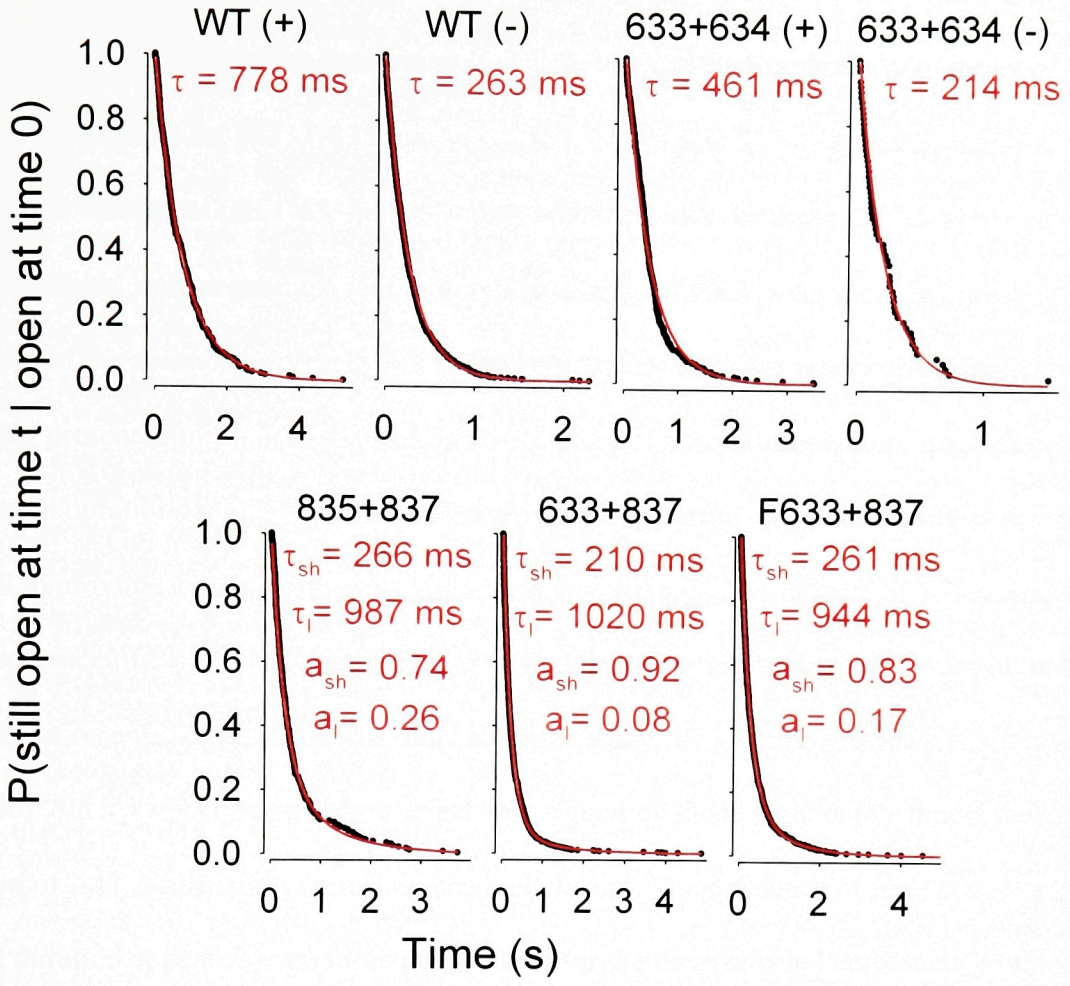

Figure 33. Distributions of burst durations of WT CFTR and CFTR channels severed around the R domain. Dwell times of inividual bursts, after omitting flickery closures, were ranked by duration in descending order, and rank numbers, divided by the total number of events, were plotted against duration. The resulting survivor functions for the distribution of burst durations, were fitted (*red lines*) by single or double exponentials using maximum likelihood; the need for a second component was evaluated from its improvement of the likelihood. Time constants and fractional amplitudes are printed in each panel. WT and 1-633 plus 634-1480 were analyzed separately in PKA and after PKA removal. Analysis for 1-835 plus 837-1480, 1-633 plus 837-1480, and Flag3-633 plus 837-1480, was done on pooled data including segments with and without PKA.

between 21 and 23 °C (referred to as 22 °C), and those obtained between 24 to 26 °C (referred to as 25 °C). Mean burst durations were re-evaluated separately for the two temperature pools for WT, 1-835 plus 837-1480, 1-633 plus 837-1480, and Flag3-633 plus 837-1480 constructs (all 1-633 plus 634-1480 data fell into the same, 22 °C, pool). For WT channels, only segments recorded in the presence of PKA were included, while records in the absence or presence of PKA were included for the other constructs. The results, presented in Figure 34A and Table VI, suggest a large temperature dependence of the burst durations for all constructs. Though the temperature range sampled was far too small to provide accurate estimates, these data suggest a Q_{10} for closure of WT channels in the presence of PKA of 2.8, predicting an enthalpic activation energy of 75 kJ/mol, not far from that recently determined in a more rigorous study (87 kJ/mol; Mathews et al., 1998b). Such a strong temperature effect was argued by those authors to support the notion of ATP hydrolysis controlling channel closure. The influence of temperature on burst duration appeared even more pronounced for the three severed constructs, giving Q_{10} estimates of 4.0, 4.0, and 5.3 for 1-835 plus 837-1480, 1-633 plus 837-1480, and Flag3-633 plus 837-1480 channels, corresponding to apparent enthalpic activation energies for channel closure of 100, 102, and 122 kJ/mol, respectively.

The effect of AMPPNP on 1-633 plus 837-1480 channels was tested at 20°C (under temperature control; Figure 34B). At this lower temperature, AMPPNP caused a larger amplitude activation (even in the complete absence of PKA; compare with 24°C, Figure 31D) and, in the patch illustrated, the decay after AMPPNP removal was well fit by a single exponential with a time constant of 18 s. In 5 experiments on 1-633 plus 837-1480 channels at 20 °C, the slow component averaged 0.71±0.08 of the total current decay, and

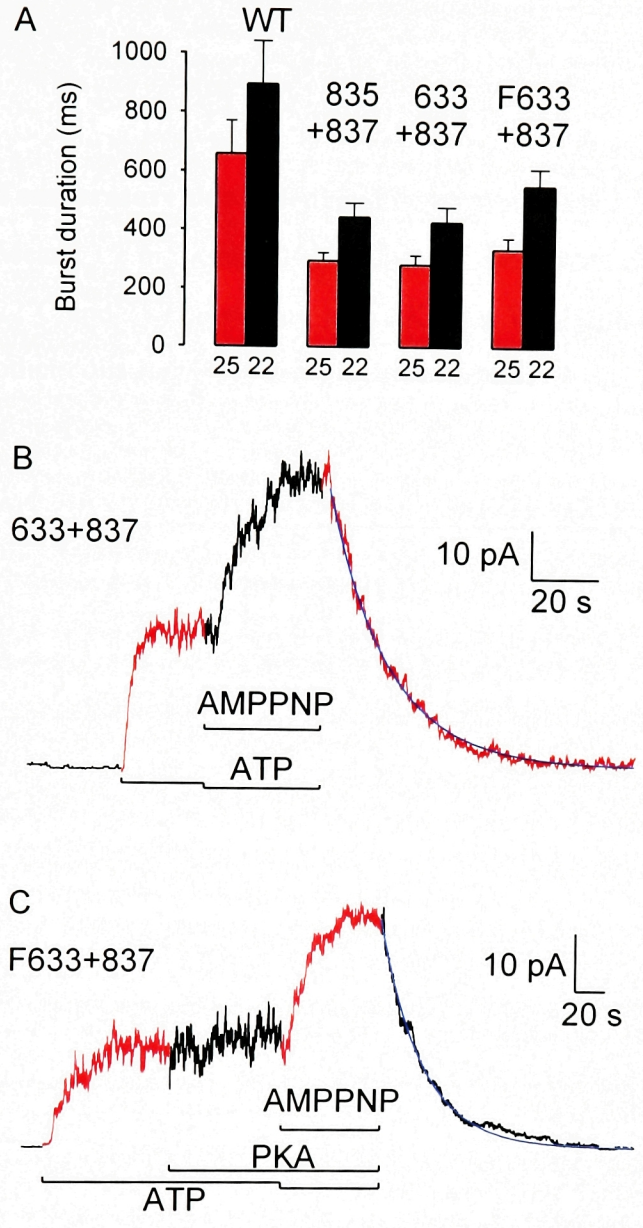

Figure 34. Influence of temperature on burst duration and locking by AMPPNP.

A, Summary of mean burst durations for WT, 1-835 plus 837-1480, 1-633 plus 837-1480, and Flag3-633 plus 837-1480 channels, calculated separately for records at 24-26 °C (*red bars*, labeled 25), and for records at 21-23 °C (*black bars*, labeled 22). **B,** Enhanced stimulation of 1-633 plus 837-1480 channel current by AMPPNP at 20°C, in the absence of PKA; decay after nucleotide removal was well fit by a single exponential (*blue line*), τ=18 s. **C,** Flag3-633 plus 837-1480 channels strongly stimulated by AMPPNP at 22°C; decay after nucleotide removal fit by single exponential (*blue line*), τ=28 s.

TABLE VI **Temperature dependence of burst durations.**

Mean± s.e.m. (*n*=number of observations) burst durations (ms) for the 22°C and 25°C pools are with PKA for WT, with or without PKA for the other constructs; apparent E_a is in kJ/mol.

Construct	τ_b(22 °C)	τ_b(25 °C)	$\tau_b(22)/\tau_b(25)$	Q_{10}	*Apparent* E_a
WT (+PKA)	896±144 (9)	659±113 (10)	1.36	2.8	75
835+837	445±49 (3)	295±29 (12)	1.51	4.0	100
633+837	429±52 (26)	282±33 (13)	1.52	4.0	102
F633+837	554±58 (17)	336±39 (14)	1.65	5.3	122

its average time constant was 13.5±2 s. Similarly, Figure 34C shows robust activation and a reasonable fit by a single exponential, with a 28-s time constant, of the current decay following exposure of Flag3-633 plus 837-1480 channels to AMPPNP at 22 °C.

7.2.10. Severed channels with no R domain, but with NBD2 Walker-A mutation, display prolonged bursts

Longer burst durations of WT CFTR channels in the presence of PKA, and the locking action of AMPPNP have been interpreted as signifying NBD2 function; i.e., NBD-B has been identified with NBD2, based on the locked-like prolonged bursts of CFTR(K1250A), mutated at the Walker-A lysine (Walker et al., 1982) in NBD2 (see Chapter 4). The response to AMPPNP of the severed channels with no R domain (Figures 31D, E, 32C, 34B, C), and the two components in the burst-duration distributions of the same constructs exposed to ATP (Figure 33), suggest that nucleotides do bind at NBD-B (presumably NBD2) in severed channels without an R domain, albeit less effectively than in WT channels. If so, then such a severed deleted-R channel bearing the Walker-A lysine mutation in NBD2, K1250A, is expected to show prolonged bursts whenever ATP binds at NBD2. Indeed, 1-633 plus 837-1480(K1250A) channels in excised patches showed similar conductance properties to WT CFTR, required MgATP for activity but (like the other severed constructs with no R domain) were active without being exposed to PKA, and their activity was dominated by long open bursts, interrupted by many flickery closures (Figure 35A; note time scale).

Kinetic analysis of these channels proved extremely difficult. Not only were the burst kinetics very slow (both burst and interburst durations were prolonged) hampering the collection of sufficient numbers of relevant gating transitions, but the distribution of

closed events was heavily dominated by the flickery closures (mean duration ~80 ms), some 6-8 flickery closures occurring on average between adjacent interburst events. Although kinetic parameters estimated for this construct are likely less accurate given these difficulties, multichannel histogram fits gave mean burst durations of 4969±654 ms at 25°C (n=5), and 9450±1419 ms at 20°C (n=3). As the prolonged bursts likely reflect non-hydrolytic binding of ATP at NBD2 of these channels, the mean burst durations provide a measure of the dwell time of ATP there, expected to be similar to the dwell time of AMPPNP at the analogous site on 1-633 plus 837-1480 channels. Accordingly, these mean burst durations of 1-633 plus 837-1480(K1250A) were comparable to the time constants of the slow components of current relaxation following exposure of 1-633 plus 837-1480 channels to AMPPNP at the corresponding temperatures (5841±423 ms and 13.5±2 s at 25°C and 20°C, respectively; Figures 31D, 34B, and Table V).

To circumvent the difficulties of steady-state kinetic analysis, the macroscopic current relaxation following ATP removal in patches containing 1-633 plus 837-1480(K1250A) channels was examined. Because patches with more than 10-20 channels were rare, ATP removal experiments were performed repeatedly and the records subsequently added up to produce quasi-macroscopic current relaxations. The current decay of Figure 35B, constructed from 9 ATP removal experiments at 25°C, yielded a single exponential fit with time constant 6.7 s, in reasonable agreement with the steady-state estimate of the mean burst duration at that temperature. The inset shows a similar trace, constructed from 7 experiments at 20°C, with a fit time constant of 10.1 s that likewise matches the corresponding steady-state estimate of mean burst duration. Considered together, these data support the hypothesis that ATP can, and does, bind at

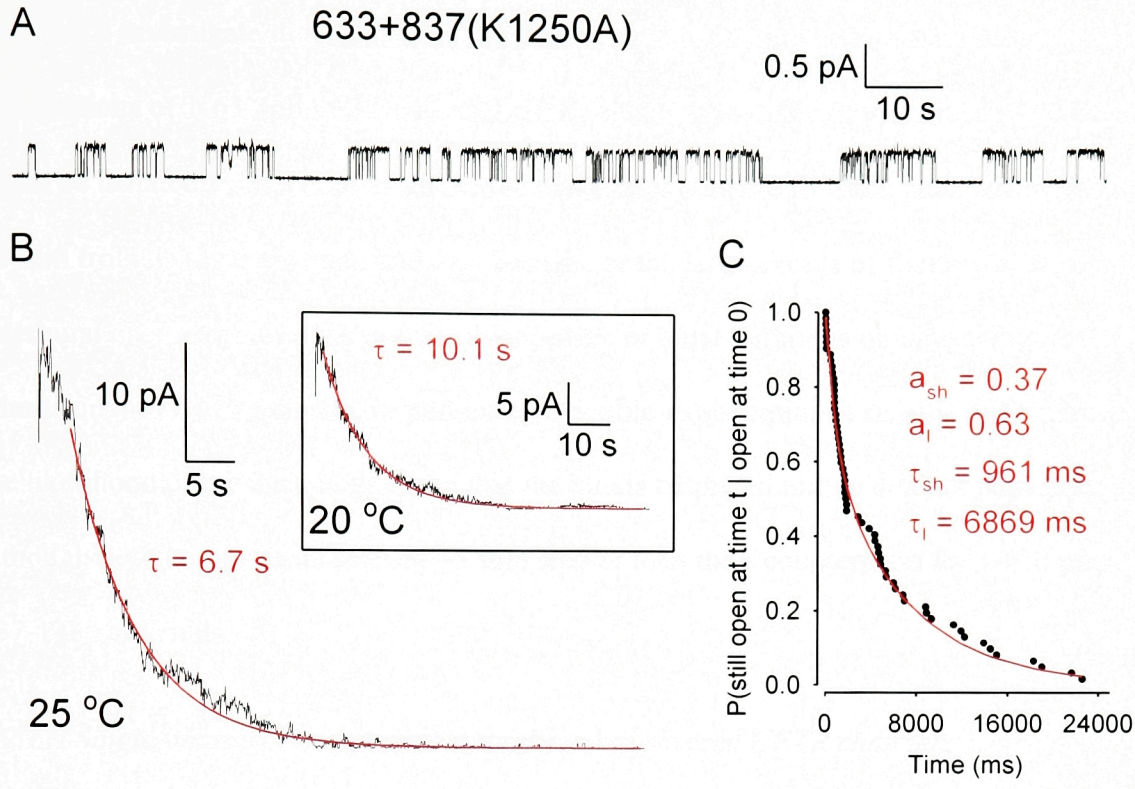

Figure 35. Walker-A mutant 1-633 plus 837-1480(K1250A) channels show prolonged open bursts. A, Representative record of single 1-633 plus 837-1480(K1250A) channel in 2 mM MgATP, no PKA, at 25°C. **B,** Current relaxation of 1-633 plus 837-1480(K1250A) channels following removal of 2 mM MgATP (no PKA), constructed by summing synchronized decay currents from 9 experiments, at 25 °C; single-exponential fit (*red line*) to quasi-macroscopic current decay gave $\tau = 6.7$ s. *Inset*, similar trace constructed from 7 experiments at 20°C with fit (*red line*) $\tau = 10.1$ s. **C,** Survivor function of burst durations, after exclusion of flickery closures, of 1-633 plus 837-1480(K1250A) channels in 2 mM MgATP was fit (*red line*) significantly better by two exponential components than by one.

NBD2 (NBD-B) in severed CFTR constructs lacking the R domain.

To investigate this further, an attempt was made to analyze burst-duration distributions of 1-633 plus 837-1480(K1250A) channels; a difficult task since <100 bursts could be isolated from a total of 16 min of recordings suitable for such analysis, including 10 min from a single channel; and also because of the large excess of flickery over interburst closures. Nevertheless, the distribution of burst durations obtained (Figure 35C) admits qualitative arguments. In particular, a double-exponential fit significantly increased the likelihood of the data, suggesting that the bursts belonged to two distinct populations, although both components seemed ~5 fold slower than their counterparts for 1-633 plus 837-1480 channels.

7.2.11. Single-channel conductance is unaltered in severed CFTR channels

Because of their kinetic differences, we examined whether severed channels 1-633 plus 634-1480, 1-835 plus 837-1480, 1-633 plus 837-1480, and Flag3-633 plus 837-1480 displayed conductance properties similar to WT CFTR channels. Figure 36A shows representative current records from a patch containing 1-633 plus 837-1480 channels held at different potentials in the presence of 2 mM MgATP and symmetrical 140 mM [Cl^-] solutions, all-points histograms, and the derived current-voltage plot, which reveals a slope conductance of ~7 pS. Figure 36B summarizes similar measurements for WT CFTR and all the severed channels: single-channel conductances were ~7 pS for all constructs, and none proved significantly different from WT ($p<0.05$), indicating that the gross pore architecture of the severed constructs remained intact.

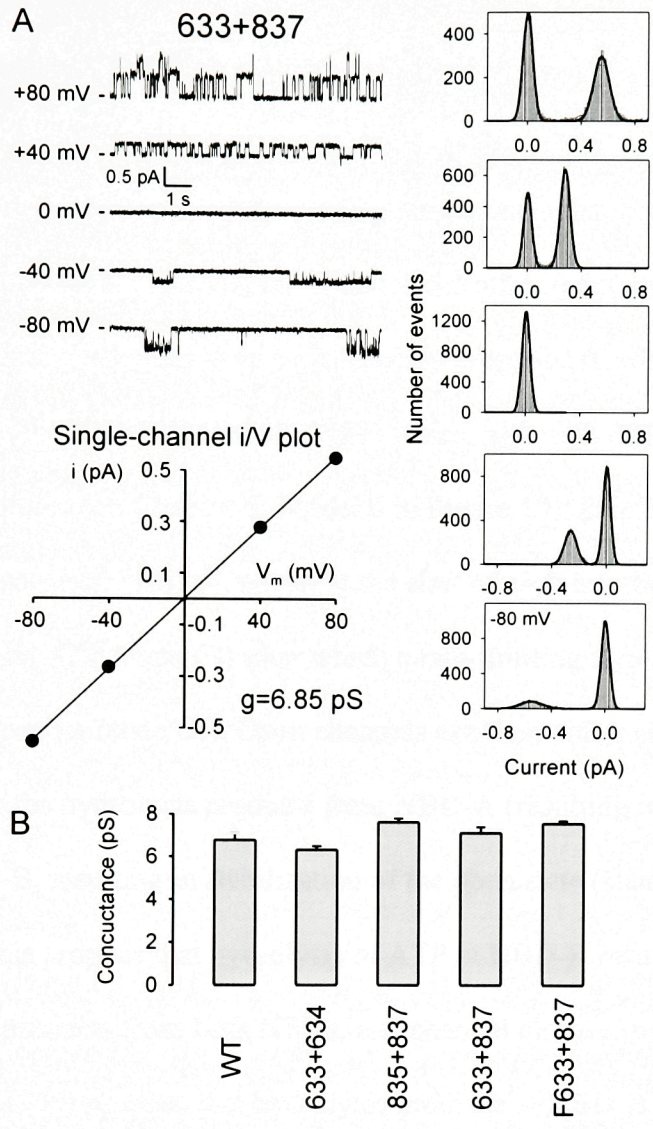

Figure 36. Single-channel conductances of WT CFTR and CFTR channels severed around the R domain. A, *Left*, currents recorded at -80, -40, 0, +40, and +80 mV from a patch containing 1-633 plus 837-1480 channels. *Right*, All-points histograms from the traces on the left, fitted with sums of Gaussians. *Bottom*, Distances between adjacent peaks of the Gaussian fit functions were plotted against holding potential and fit by a straight line, with slope 6.85 pS. **B,** Summary of single-channel conductances (in pS): 6.3±0.2 (n=3) for 1-633 plus 634-1480, 7.6±0.2 (n=3) for 1-835 plus 837-1480, 7.1±0.3 (n=4) for 1-633 plus 837-1480, and 7.6±0.1 (n=4) for Flag3-633 plus 837-1480, none of which differed significantly from WT (6.8±0.3, n=4) at $p<0.05$.

7.3. Discussion

7.3.1. Evaluation of models

The data presented are consistent with gating models that involve two binding sites for ATP, one responsible for opening the channel, the other for stabilizing its open (burst) state. Three such gating schemes have been recently proposed (Gadsby and Nairn, 1999; Weinreich et al., 1999; Zeltwanger et al., 1999) which, although differing in detail, share many common features (cf. Chapter 5; Model 6 in Figure 19). Briefly, channel openings are preceded by two steps: NBD-A, empty at the start of each interburst closure (state C_1), first reversibly binds ATP (state C_2) after which a rate-limiting step (related to hydrolysis) leads to channel opening (state O_1). Open channels can then either simply close (back to state C_1) by losing the hydrolysis products from NBD-A (resulting in brief openings), or bind ATP at NBD-B, resulting in stabilization of the open state (state O_2; long openings). The first two models propose that hydrolysis of ATP at NBD-B results in an obligatory loss of hydrolysis products from both NBDs, and channel closure (back to state C_1). Zeltwanger et al. (1999) propose that hydrolysis products at NBD-B are lost first, returning the channel to state O_1, from which it can either close (to state C_1) or rebind ATP at NBD-B (returning to state O_2; cf. Figure 19, Model 6, *dotted line*). The first two models can be simplified to Scheme I, while that of Zeltwanger et al. reduces to Scheme II.

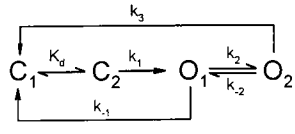

(Scheme I)

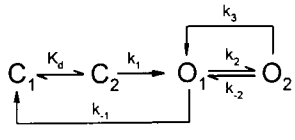

(Scheme II)

Forward and backward rate constants between states C_1 and C_2 are not made explicit, since there was no attempt to estimate them in the present study. By fitting the distribution of interburst durations, Zeltwanger et al. (1999) proposed a rapid equilibrium between the two closed states ($k_{off,ATP} = 6.5\ s^{-1}$), whereas Weinreich et al. (1999) suggested a slow k_{off} for nucleotides ($k_{off,ADP} \sim 0.4\ s^{-1}$, $k_{off,AMPPNP} \sim 0.05\ s^{-1}$), based on fits to macroscopic relaxations following step changes in nucleotide concentrations.

Most qualitative predictions of the two schemes are similar. Thus, both predict a simple Michaelis-Menten type dependence of channel opening rate on [ATP], consistent with the data presented (Figure 30B). The strong dependence on phosphorylation of WT burst durations (Figures 28C, 33) can be explained by an influence on the rate k_2: in poorly phosphorylated channels $k_2 << k_{-1}$, so most openings proceed directly from O_1 to C_1. In highly phosphorylated channels k_2 is large, so transition $O_1 \rightarrow O_2$ will be favored over transition $O_1 \rightarrow C_1$, producing an increase in burst duration (assuming $k_3 < k_{-1}$). When k_2 is comparable to k_{-1}, a mixture of short and long openings is expected; never observed for WT channels here, but shown in Figure 33 for constructs 1-835 plus 837-1480, 1-633 plus 837-1480, and Flag3-633 plus 837-1480 (cf. Dousmanis et al., 1996b). Rate k_{-2} represents the rate of dissociation of ATP from NBD-B. On the assumption that AMPPNP, which structurally resembles ATP (Yount, 1975), has comparable binding kinetics at that site, the low apparent dissociation rate of AMPPNP from WT channels (Figures 31, 32; cf. Figure 35) suggests that k_{-2} is very small ($\sim 0.02\ s^{-1}$), so that channels mostly exit from the O_2 state via the pathway characterized by rate k_3. Although drawn as one step in both schemes, this pathway transits through a series of states involving hydrolysis and release of products from NBD-B (also from NBD-A for Scheme I). Unlike the other explicit rate

constants, which are all first-order, rate k_2 characterizes binding of ATP to NBD-B and is pseudo-first-order, scaling with [ATP]. If that step were a simple bimolecular binding reaction, Scheme II would predict infinitely long burst durations at very high [ATP], because for $k_2 >> k_{-1}$ the channels would incessantly cycle between O_1 and O_2. Since the dependence of the burst durations on [ATP] was found to saturate in the study of Zeltwanger et al. (1999), those authors proposed that binding of ATP to NBD-B follows a rate-limiting dissociation of ADP from that site. (Strictly, if ADP leaves NBD-B during step $O_1 \rightarrow O_2$, then in the absence of ADP that step is irreversible, and channels unlocking from AMPPNP must close through a state distinct from O_1: the 4-state schemes are clearly oversimplified.) For high k_2, Scheme I predicts that most openings will proceed from O_1 to O_2, and then to C_1, producing a uniform population of openings with durations approximating the lifetime of state O_2, $\sim 1/k_3$.

Both Schemes I and II are consistent with the mean burst durations found here under various conditions. However, the two schemes differ in their predictions for the distribution of burst durations. As a first approximation, we may assume that k_2 is the only rate among the ones influencing open time (i.e., k_{-1}, k_2, k_{-2}, k_3) that is altered by phosphorylation in WT channels. If so, k_{-1} is the reciprocal of the mean burst durations of poorly phosphorylated channels (or of channels at very low [ATP]; see Zeltwanger et al., 1999), for which $k_2 << k_{-1}$. This argument predicts $k_{-1} \sim 4\ s^{-1}$ for WT CFTR. For Scheme II the mean burst duration is $\tau_b = (1/k_{-1}) \cdot (1 + (k_2 / (k_3 + k_{-2})))$. With fixed rate constants k_{-1} and k_{-2}, and a given observed τ_b, this equation puts a linear constraint on k_2 and k_3: $k_3 = (\tau_b k_{-1} - 1)^{-1} \cdot k_2 - k_{-2}$. Although any pair of values for k_2 and k_3 that satisfies this constraint will fit the mean of the observed burst durations, their distribution will vary for

different such pairs. With rates k_2 and k_3 on the order of those proposed by Zeltwanger et al. (~1 s^{-1}), and applying the above constraint to match τ_b measured here, Scheme II predicts a distribution with two components that ought to be distinguishable. For example, rates k_{-1}=3.8 s^{-1}, k_2=2 s^{-1}, k_{-2}=0.025 s^{-1}, k_3=1 s^{-1}, respectively, predict τ_b=777 ms, close to that observed here for WT channels in PKA, but they also predict a distribution with two components, with time constants τ_{sh}=161 ms, τ_l=1591 ms, and fractional amplitudes a_{sh}=0.57 and a_l=0.43, respectively, in contrast to the uniform distribution found (Figure 33). Simulating 160 events (far fewer than obtained in this study) for Scheme II with the above rates, and fitting the distribution of open times with two exponentials, gave estimates τ_{sh}=171 ms, τ_l=1276 ms, a_{sh}=0.51 and a_l=0.49, together with a 24-log-unit increase in the likelihood over that of a single-exponential fit, indicating a significantly better fit by two components. This set of rate constants is therefore not consistent with the uniform distribution of burst durations observed here for WT channels with PKA.

It is nevertheless possible to find a set of rates for Scheme II that predicts a uniform distribution of burst durations. As k_2 and k_3 are made faster, while respecting the above linear constraint, both time constants of the distribution progressively shorten, while the fractional amplitudes shift in favor of the longer component, until, with k_2 and k_3 very fast, the distribution becomes nearly uniform. Qualitatively, each opening contains many, but brief, passages to state O_2, while the observed apparent closing rate essentially becomes k_{-1} multiplied by the fraction of time open channels spend in the O_1 state. In practice, with k_2 ~20 s^{-1} and a corresponding k_3 of ~10 s^{-1}, identification of two components in the distribution of open times from simulated data became difficult. However, such rates are inconsistent with studies on macroscopic relaxations of WT

CFTR currents upon removal of ATP (Weinreich et al., 1999). Using high-speed solution exchange compatible with resolution of CFTR gating, those authors found a slow component in the current decay when ATP was removed together with, or shortly after, but not when long after, PKA. Scheme II with $k_3 >> k_{-1}$, however, predicts that all channels shut quickly, essentially with rate k_{-1}, once ATP is removed.

Scheme I thus seemed easier to fit to our data, with the assumption that, among the rates controlling burst duration, k_2 is the one most affected by phosphorylation in WT channels, and that it is much larger than k_{-1} in the presence of PKA but very small in poorly phosphorylated channels. So Scheme I will be used for subsequent discussion and interpretation of the data.

7.3.2. Phosphorylation dependence of channel activity for the severed constructs

The lack of activity of dephosphorylated WT CFTR channels has been attributed to an inhibitory effect on gating of the unphosphorylated R domain, since a deletion construct missing most of the R domain, ΔR(708-835)CFTR, was active without phosphorylation (Rich et al., 1991,1993; Ma et al., 1997). Consistent with those results, split channels with no R domain, 1-633 plus 837-1480 and Flag3-633 plus 837-1480, were active in the presence of MgATP following patch excision, before exposure to PKA (Figures 27D, E, 28A, B). This activity, not seen for WT channels, is inferred to reflect constitutive, PKA-independent, channel function because it was also observed in patches excised from oocytes preinjected with RpcAMPS, an inhibitor of PKA (Figure 27E); RpcAMPS suppressed activity of WT, but not of Flag3-633 plus 837-1480, channels in resting oocytes (Figure 26). For both severed channels without an R domain this constitutive activity corresponded to a P_o of ~0.13 (Figure 28B, and Table IV), roughly

35% of the P_o of WT channels in the presence of PKA (~0.36). Severed 1-835 plus 837-1480 channels, with no deletion but severed near the C terminus of the R domain, also displayed activity prior to phosphorylation (Figures 27C-E, 28A-B), but much smaller than the deletion constructs, corresponding to a basal P_o of ~0.04 (Figure 28B, and Table IV). Severing close to the N terminus of the R domain (1-633 plus 634-1480) did not result in any significant phosphorylation-independent activity (Figure 28A; cf. Figure 20A). On the basis of Scheme I, these effects on channel opening are interpreted as a dependence of rate k_1 on phosphorylation. Thus, in dephosphorylated WT (as well as 1-633 plus 634-1480) channels k_1=0, i.e. the rate-limiting step after ATP binding is inhibited by the unphosphorylated R domain. This inhibition is partially relieved by a cut close to the C terminus of the R domain and, presumably, fully relieved in severed channels with no R domain, or in WT channels by phosphorylation of the R domain.

1-835 plus 837-1480 channels, severed after the R domain, are activated several-fold on exposure to PKA, due to an increase in opening rate (Figure 28D and Table IV), which in PKA becomes indistinguishable from that of WT. Surprisingly, currents of severed channels 1-633 plus 837-1480 and Flag3-633 plus 837-1480, lacking the R domain, were still stimulated by 30-50% by exposure to PKA (Figures 27D, E, 28A, B, 31D, E, and Table IV), to a P_o of ~0.2, due to a near doubling of the opening rate, which closely approached that of WT in the presence of PKA (Figure 28D, and Table IV). This activation is intriguing, because the effect of PKA on CFTR has generally been attributed to phosphorylation of serine residues within the R domain, based on both biochemical and functional evidence: CNBr cleavage and peptide mapping experiments on CFTR protein prephosphorylated by PKA with γ-^{32}P ATP found no evidence for phosphorylation outside

the R domain (Seibert et al., 1995; Cheng et al., 1991; Picciotto et al., 1992), while PKA no longer stimulated ΔR(708-835) channels after mutation of serine 660 to alanine (ΔR(708-835)-S660A, Rich et al., 1993; cf. Ma et al., 1997). However, from a methionine map of CFTR, full CNBr cleavage might be expected to generate many small fragments (several <10 amino acids long), some including serines, and phosphorylation of such short fragments is unlikely to be detected by standard SDS-PAGE. Also, the lack of response of ΔR(708-835)-S660A channels to PKA could reflect steric constraints (see below) introduced by linking residues 707 and 836, which, in WT channels, might be far away from each other in space. Systematic mutation to alanines of R-domain serines known to be PKA substrates did decrease channel activity, and yet 10SA CFTR, with 10 of the most prominent sites mutated, could still be activated to a P_o ~50% that of WT (Chang et al., 1993; Mathews et al., 1998a); that P_o was further reduced only slightly (by ~40%) in 11SA CFTR (Seibert et al., 1995). So, at present, phosphorylation of CFTR by PKA on a site outside the R domain cannot be ruled out, and could account for the PKA-mediated stimulation of channel activity seen here for 1-633 plus 837-1480 and Flag3-633 plus 837-1480 channels. One candidate is serine 422 just before NBD1, a dibasic consensus site for PKA, also implicated in channel function (Chang et al., 1993), and phosphorylated in an NBD1-R peptide (Townsend et al., 1996) although not in WT CFTR (Neville et al., 1997). Preliminary data from autoradiograms of Flag3-633 plus 837-1480 CFTR, co-immunoprecipitated by an anti-Flag M2 monoclonal antibody and incubated in vitro with PKA and γ-^{32}P ATP, suggest that PKA can phosphorylate those channels. But more work will be needed to identify the site(s) phosphorylated, and address their in vivo significance. Whether or not they are phosphorylated, our observed stimulation by PKA of

split channels with no R domain could still reflect phosphorylation of ancillary proteins in the patch that somehow modulate CFTR activity.

In addition to its inhibitory effect on channel gating when dephosphorylated, a stimulatory effect of the R domain when phosphorylated was recently proposed based on a stimulatory action of phosphorylated R-domain peptides on ΔR channels, attributed to an increase in channel opening rate (Ma et al., 1997; Winter and Welsh, 1997). However, in the absence of the phosphopeptide the opening rate of ΔR(708-835)-S660A, with or without PKA, was only ~30% of that of phosphorylated WT, and increased only to ~45% of the latter, even in the presence of the phosphopeptide (Winter and Welsh, 1997; cf. Ma et al., 1997). In the present work severed channels 1-633 plus 837-1480 and Flag3-633 plus 837-1480, both lacking an R domain, had opening rates in the presence of PKA indistinguishable from that of phosphorylated WT channels (Figure 28D and Table IV), arguing against any stimulatory effect of the phosphorylated R domain in WT. The much lower opening rate of ΔR(708-835) channels compared to WT (or severed 1-633 plus 837-1480) suggests that the linkage of residue 707 to 836 impairs channel function, in which case addition of an exogenous R domain might help to normalize channel structure. Indeed, in preliminary tests, injection of 2.5 ng cRNA encoding ΔR(708-835) channels did not give rise to any measurable conductance in oocytes, although in excised patches single channels with very low activity were occasionally observed (with 5 ng cRNA), implying very inefficient processing of those channels under our conditions. In contrast, effectively severing ΔR(708-835) by coexpressing segments Flag3-707 plus 837-1480 (2.5 ng cRNA each) resulted in a construct that supported robust currents in resting unstimulated oocytes (conductance was 167±7 μS, n=6), supporting the notion that the linkage per se, rather

than the precise boundaries of the deletion, was responsible for the low P_o and poor expression of single-chain ΔR(708-835) in oocytes.

Chapter 6 described that attaching the 8-residue Flag epitope to the N terminus of WT CFTR, or of CFTR channels severed near either boundary of NBD1, selectively lowered the channel opening rate 2- to 3-fold. In contrast, Flag3-633 plus 837-1480, a severed channel lacking the R domain, showed functional characteristics roughly similar to its non-Flagged counterpart, 1-633 plus 837-1480 (e.g., Figures 28, 29, 31, 33 and Tables IV-VI). Interestingly, a likely alpha-helical section of CFTR's N terminus (within residues 46-60) was recently reported to bind to the R domain, and enhance channel activity (Naren et al., 1999): point mutations in that stretch of amino acids impaired the gating of WT (an effect apparently on channel closing rate), but not of ΔR(708-835)-S660A, channels. It is therefore tempting to speculate that our N-terminal Flag epitope slowed CFTR channel opening by interfering with the interaction between the helical region and the R domain, perhaps impairing phosphorylation or the gating response to phosphorylation.

For WT channels, in addition to the opening rate, the channel closing rate was strongly influenced by phosphorylation, as demonstrated by the shortening of the burst duration from ~800 ms to ~250 ms following PKA removal (Figure 28C, and Table IV; cf. Hwang et al., 1994; Dousmanis et al., 1996b). The tendency was similar for severed 1-633 plus 634-1480 channels, although their burst durations in PKA (~500 ms; Figure 28C, and Table IV) were shorter than for WT. However, there was little or no change in the burst durations of 1-835 plus 837-1480, 1-633 plus 837-1480, or Flag3-633 plus 837-1480 channels upon PKA exposure, and they all had shorter bursts on average than WT

channels in PKA. A plausible interpretation is that in WT channels the phosphorylated R domain stimulates ATP binding to NBD-B (Hwang et al., 1994; Gadsby and Nairn, 1999). In 1-835 plus 837-1480 channels, however, although the unphosphorylated R domain is evidently capable of substantial inhibition, judging from the several-fold stimulation of opening rate by PKA (Figure 28D, and Table IV), the mean burst duration was nevertheless unaffected by PKA. It seems likely, then, that the ATP-binding site of NBD-B (presumably NBD2) is structurally destabilized by severing the backbone near the C terminus of the R domain. Deletion of the entire R domain (in 1-633 plus 837-1480 and Flag3-633 plus 837-1480 channels) did not further alter burst duration.

7.3.3. Channels severed near C terminus of R domain have slightly increased apparent ATP affinities

Previous studies have revealed a dependence on phosphorylation of CFTR's apparent affinity for ATP, from comparisons of P_o vs. [ATP] relationships, either for WT CFTR channels with or without PKA (Winter and Welsh, 1997), or for phosphorylated WT channels versus mutants lacking one or more R-domain serines (Winter and Welsh, 1997, Mathews et al., 1998a). Correspondingly, pretreatment of purified, reconstituted WT CFTR with PKA lowered ~3-fold the K_m of the ATP hydrolysis rate, compared to untreated CFTR (Li et al., 1996). Based on these findings, and the effect of phosphorylated R-domain peptide on ΔR(708-835)-S660A channels, the phosphorylated R domain was proposed to stimulate channel activity by enhancing the affinity of CFTR for ATP (Winter and Welsh, 1997). In the present study, apparent ATP affinities for activating P_o in 1-633 plus 837-1480, and Flag3-633 plus 837-1480 channels were ~2-fold higher than in WT, when measured in the absence of PKA (Figure 29). Because WT channels

under these conditions are expected to be only partially phosphorylated (removal of PKA prompts an immediate drop in P_o; Figures 14 and 27A), this result is more consistent with the unphosphorylated R domain inhibiting ATP binding to CFTR, and with the increase in apparent affinity caused by PKA reflecting a graded disinhibition; full disinhibition occurs in severed channels with no R domain, as reported by their higher apparent affinity. Moreover, the higher $I_{50\mu M}/I_{2mM}$ ratio of severed 1-835 plus 837-1480 channels compared to WT (both following PKA removal), suggests that a simple cut close to the C terminus of the R domain, while only partially relieving the inhibitory effect of the unphosphorylated R domain on the rate-limiting step for channel opening (cf. low basal opening rate; Figure 28D), may still be sufficient to fully relieve the inhibition on ATP binding. Interestingly, a half-channel truncated at that same cut site (D836X; Sheppard et al., 1994) showed a low level of constitutive activity but was strongly activated by PKA, and also had an increased apparent affinity for ATP, properties reminiscent of those described here for 1-835 plus 837-1480 channels. In the present study a similar half-molecule, Flag3-835, gave no measurable conductance in resting or stimulated oocytes (see legend to Figure 26), and so was not examined in excised patches. Not inconsistent with the above data, when experiments like those of Figure 29 were performed on WT channels in the presence of PKA, a Michaelis- fit to a more limited data set yielded a slightly smaller K_m of 38±7 μM (compared to 51±2 μM after removing PKA; Figure 29).

Our dwell-time analysis revealed that the macroscopic (P_o) apparent affinity for ATP of both Flag3-633 plus 837-1480 channels and partially-phosphorylated WT channels in the absence of PKA, results from a Michaelis-type dependence of opening rate on [ATP], while closing rates were relatively unaltered (Figure 30B, C; cf. Venglarik et

al., 1994; Winter et al., 1994). This differs from a report (Zeltwanger et al., 1999) demonstrating longer bursts, though of presumed highly-phosphorylated WT CFTR channels, at higher [ATP]. The present data can be interpreted in terms of Scheme I by assuming that rate k_2 becomes very small in WT channels after PKA is removed, so that most openings close from O_1 directly to C_1 with rate k_{-1} which is independent of [ATP]. This would account for the short burst durations of ~250 ms of WT channels following PKA removal (Figures 28C, 33 and Table IV). The postulated reduction of apparent ATP affinity by the unphosphorylated R domain then likely reflects inhibition of ATP binding to NBD-A. Mean burst durations of Flag3-633 plus 837-1480 channels were not altered by PKA (Figure 28C, and Table IV), despite evidence that rate k_2 is non-zero, as nucleotide (e.g. AMPPNP, Figure 31E) could bind at NBD-B. This would, in turn, imply a dependence of the mean burst duration of Flag3-633 plus 837-1480 channels on [ATP], but this is not apparent in Figure 30C, suggesting that the transition from O_1 to O_2 in those channels is rate-limited by something other than ATP binding (perhaps dissociation of ADP from NBD-B; cf. Gadsby and Nairn, 1999; Zeltwanger et al., 1999).

If opening rate r_{CO} depends on [ATP] through $r_{CO} = r_{CO,max} \cdot [ATP]/([ATP]+K_{r_{CO}})$, while closing rate r_{OC} is independent of [ATP], then a similar Michaelis-type dependence ensues for P_o vs. [ATP], $P_o = P_{o,max} \cdot [ATP]/([ATP]+K_{P_o})$, where $P_{o,max} = r_{CO,max}/(r_{CO,max}+r_{OC})$, and $K_{P_o} = K_{r_{CO}} \cdot r_{OC}/(r_{CO,max}+r_{OC})$. This $K_{0.5}$, as measured by P_o, is hence expected to be somewhat smaller than the $K_{0.5}$ measured by opening rate. In the above conditions (i.e., after PKA removal), however, with $r_{CO,max}$ ~0.35s^{-1} and r_{OC} ~ 3s^{-1} (cf. Table IV), these relations predict $K_{P_o} \approx K_{r_{CO}}$, in reasonable agreement with the data (Figures 29C, 30B),

considering the errors in the kinetic measurements. From Scheme I, $K_{r_{CO}} = (k_{off,ATP} + k_1) / k_{on,ATP}$. Thus, $K_{r_{CO}}$ (and hence K_{P_o}) is expected to be close to the real affinity ($K_d = k_{off,ATP} / k_{on,ATP}$) of NBD-A for ATP, only if ATP binding at NBD-A is in rapid equilibrium compared to the subsequent step (related to hydrolysis) that rate-limits channel opening ($k_{off,ATP} >> k_1$). In any case, since k_1 in the experiments to estimate apparent affinity was comparable for all constructs (~0.35 s^{-1}; after PKA removal for WT and 1-835 plus 837-1480, before PKA exposure for 1-633 plus 837-1480 and Flag3-633 plus 837-1480), the observed differences in $K_{r_{CO}}$ (K_{P_o}) may, at least, be expected to reflect parallel changes in K_d.

7.3.4. Locking of severed channels in the open state by AMPPNP

AMPPNP, in the presence of ATP, enhanced the currents of WT and all severed channels tested, and elicited a slowly relaxing component in the current decay on nucleotide removal (Figure 31) due to prolonged bursts (cf. Figure 32). Similar results were obtained for all constructs when pyrophosphate (PP_i) replaced AMPPNP (Figure 21; cf. Csanády et al., 1999). If the prolonged bursts reflect AMPPNP binding to NBD-B, then, since AMPPNP cannot be hydrolyzed (i.e., k_3=0), Scheme I predicts that the time constant of the slowly decaying current component is given by $1/k_{-2}$. The faster rates measured for 1-835 plus 837-1480, 1-633 plus 837-1480, and Flag3-633 plus 837-1480 channels (Figures 31, 32, and Table V) suggest more rapid dissociation, and hence a destabilized binding site for AMPPNP, in those channels compared to WT or 1-633 plus 634-1480 channels. The fractional amplitude of the slow component gives the approximate fraction of open channels that, in the steady state, have AMPPNP bound at NBD-B. Though faster than WT, the dissociation of AMPPNP from 1-835 plus 837-1480,

1-633 plus 837-1480, and Flag3-633 plus 837-1480 channels is still too slow to account for the much smaller fractional amplitude of their slow component (Table V). This argues that an additional consequence of severing near the C terminus of the R domain is a reduction in k_2, possibly another reflection of relative structural instability of NBD-B in those channels. Nevertheless, the clear demonstration that severed channels with no R domain are locked open by either AMPPNP (Figures 31, 32, 34) or PP_i contrasts with their reported lack of effect on burst durations of ΔR(708-835) CFTR channels; PP_i did not affect bursts even in the presence of phosphorylated R-domain peptide (Ma et al., 1997), suggesting severe destabilization of NBD-B, possibly a further consequence of distortion imposed by linking residues 707 and 836.

7.3.5. Analysis of the distribution of burst durations

All severed constructs in this study had shorter mean burst durations in PKA than WT (Figure 28C, and Table IV). But the underlying mechanism differed between 1-633 plus 634-1480 channels, in which locking behavior mimicked WT, and the others, in which locking was altered. This grouping was confirmed by the distributions of burst durations. WT and 1-633 plus 634-1480 channels displayed uniform populations of bursts both with and without PKA, with long lifetimes in PKA (somewhat reduced for 1-633 plus 634-1480), and short lifetimes in its absence (Figure 33, *top* panels). These findings are explained by Scheme I if k_{-1} is similar (~$4s^{-1}$) for both channels, and for both k_2 is similarly low in the absence and similarly high in the presence of PKA, but k_3 is somewhat faster for 1-633 plus 634-1480 than for WT. Together with a similarly small k_{-2} this scheme also accounts for the similar locking behavior of the two constructs (Table V), despite different mean burst durations. In contrast, the burst durations of 1-835 plus 837-

1480, 1-633 plus 837-1480, and Flag3-633 plus 837-1480 channels were little affected by PKA (Figure 28C, and Table IV), and displayed double-exponential distributions indicating mixtures of two populations of bursts with different lifetimes. Interestingly, the two time constants in each case roughly matched the lifetimes of WT bursts with and without PKA (Figure 33, *bottom* row). Such behavior is predicted by Scheme I if k_2 is small but not zero (as already indicated by the locking behavior; Table V), and not altered much by PKA. As already mentioned, because burst durations of Flag3-633 plus 837-1480 channels did not increase with [ATP] (Figure 30C), whereas k_2 as written should, the (presumably compound) step represented by k_2 is likely rate-limited by something other than ATP binding in the above three constructs.

Caution is warranted in interpreting burst-duration distributions obtained by pooling data from several patches, despite their consistency with the macroscopic unlocking data. It is hard to exclude the possibility that the distributions and the macroscopic data both reflect mixtures of the behaviors of functionally different channels, rather than the complex behavior of individual channels. An extreme possibility is that 1-835 plus 837-1480, 1-633 plus 837-1480, and Flag3-633 plus 837-1480 constructs all give rise to two distinct channel populations, one behaving (with respect to NBD2 function) like WT in the presence of, the other like WT in the absence of, but neither population being affected by, PKA. While this seems unlikely, because short and long bursts were readily seen in individual single-channel records for these constructs, the extracted relative fractions of the two populations could be inaccurate, due to unpredictable bias introduced by differing impacts of records of unequal length, expected to scale with the number of contributed events. Nevertheless, the qualitative information derived from the pooled

distributions is likely valid, and improvement will remain difficult for a channel gated as slowly as CFTR.

7.3.6. Strong temperature dependence of gating of constructs severed at the C terminus of the R domain

The fairly large apparent Q_{10} for closure of WT channels in PKA (~2.8; Table VI), roughly guaged from burst durations collected in two narrowly separated temperature pools (21-23°C vs. 24-26°C), agrees with the more accurate estimate of Mathews et al. (1998b). Apparent Q_{10} values seemed even higher for 1-835 plus 837-1480, 1-633 plus 837-1480, and Flag3-633 plus 837-1480 channels (Figure 34A; Table VI). But, with evidently more than one open state, Q_{10} values of mean burst durations need not reflect the activation energy of a particular gating step. In Scheme I, for instance, four rate constants (k_{-1}, k_2, k_{-2}, and k_3) control mean burst duration, and so its temperature dependence is in general a complicated function of the temperature sensitivities of all four. For phosphorylated WT channels, though, our data are consistent with a very fast rate k_2 (compared to k_{-1}) and a slow rate k_{-2} (compared to k_3). The closing rate thus approximates k_3, and the apparent Q_{10} of channel closure may then reflect just that step (likely ATP hydrolysis at NBD-B, as also suggested by Mathews et al., 1998b). For 1-835 plus 837-1480, 1-633 plus 837-1480, and Flag3-633 plus 837-1480 channels, however, our data are consistent with Scheme I with k_2 small, comparable to k_{-1}, resulting in a mixture of $O_1 \rightarrow C_1$ and $O_1 \rightarrow O_2 \rightarrow C_1$ bursts. Changes in mean burst duration with temperature may then arise from changes not only in lifetimes, but also in the relative frequencies, of these two burst populations. Thus, the mean burst durations would shorten at higher temperatures if the (already small) rate k_2 increased more slowly than k_{-1} with temperature, resulting in an

even smaller fraction of the longer, $O_1 \rightarrow O_2 \rightarrow C_1$ type, bursts. So our findings with severed constructs 1-835 plus 837-1480, 1-633 plus 837-1480, and Flag3-633 plus 837-1480 could be explained if higher temperatures compromise the stability of NBD-B in those channels. This interpretation is supported by the locking behavior of those channels, which is consistent with the relative instability of NBD-B at 24 °C (Figures 31C-E), but increased fraction of locked 1-633 plus 837-1480, and Flag3-633 plus 837-1480 channels after cooling to 20 °C (Figures 34B, C), implying an enhanced ratio of k_2 to k_{-1} at the lower temperature. In sharp contrast to the data of Mathews et al. (1998b), and that presented here, the closing rate of phosphorylated WT CFTR channels examined in lipid bilayers was found to be only weakly temperature dependent, with a Q_{10} of ~1.1 and apparent activation energy of ~10 kJ/mol (Aleksandrov and Riordan, 1998). However, the mean burst durations in that study (220 ms at 23° C) were comparable to those found here for partially phosphorylated WT channels in the absence of PKA (264 ms; Figure 28C, Table IV), interpreted as representing mostly $O_1 \rightarrow C_1$ type bursts. Possibly, in terms of Scheme I, k_2 was small in the experiments of Aleksandrov and Riordan (1998), and the observed Q_{10} of channel closure reflects the smaller activation energy of rate k_{-1}.

7.3.7. ATP binding to NBD2 of severed channels lacking an R domain is supported by prolonged bursts of 1-633 plus 837-1480(K1250A)

Mutation of the conserved lysine residue in the Walker-A motifs has been shown to practically abolish ATP hydrolysis in CFTR as well as other ABC transporters (e.g., Loo and Clarke, 1995; Müller et al., 1996; Ramjeesingh et al., 1999). Introducing this mutation into CFTR's NBD2 (K1250A) results in extremely long bursts of openings, comparable to those seen in the presence of AMPPNP (Gunderson and Kopito, 1995;

Carson et al., 1995), interpreted as non-hydrolytic tight binding of ATP to NBD2; in the present schematic, NBD2 would then be expected to contribute the functionally defined binding site NBD-B. If ATP can indeed bind at NBD2 in severed channels lacking the R domain, then 1-633 plus 837-1480(K1250A) channels ought to show prolonged bursts (like those induced by AMPPNP in 1-633 plus 837-1480 channels) whenever ATP does bind to NBD2, since k_3=0. This expectation was confirmed (Figure 35A), and corroborated by the correspondingly slow relaxation of quasi-macroscopic currents following withdrawal of ATP (Figure 35B). The large fraction of prolonged openings in 1-633 plus 837-1480(K1250A) channels seems paradoxical, because only a small fraction of the bursts of 1-633 plus 837-1480 channels belonged to the slow component of the distribution (Figure 33), implying that few bursts involved binding of ATP to the stabilizing site. Intriguingly, the same paradox seems to apply to continuous K1250A channels, which also showed predominantly long openings under conditions where WT channels were only inefficiently locked by AMPPNP (cf. Carson et al., 1993, 1995). Despite technical difficulties, such as excessive numbers of flickery closures coupled with the small number of bursts obtained, the distribution of burst durations of 1-633 plus 837-1480(K1250A) indicated a mixture of two populations, both with lifetimes longer than the corresponding populations for 1-633 plus 837-1480 channels (Figure 35C). In accordance with Scheme I, the slower components of those distributions are different, and reflect k_3 for 1-633 plus 837-1480 channels, but k_{-2} for 1-633 plus 837-1480(K1250A) channels. But the observation that the faster component was ~5-fold prolonged for 1-633 plus 837-1480(K1250A) channels, if correct, suggests that rate k_{-1} is also slowed in these channels, which would provide, during each burst, a longer time window for ATP to bind to NBD2.

Strictly, an invariant slower k_{-1} would predict bursts at very low [ATP] longer than the ~250-ms bursts seen for WT channels in the absence of PKA. However, continuous K1250A CFTR channels showed brief (~200-ms) bursts at 10 μM ATP comparable to WT (Zeltwanger et al., 1999), and we occasionally saw comparably brief reopenings of 1-633 plus 837-1480(K1250A) channels in macropatches after ATP washout, when [ATP] was extremely low. In any event, an influence of the Walker-A mutation on more than one rate constant is not unexpected, since 1-633 plus 837-1480(K1250A) channels were also ~10-fold slower in opening (τ_{ib} = 25±12 s in the absence of PKA, n=4) than 1-633 plus 837-1480 channels (τ_{ib} = 3055±666 ms in the absence of PKA, n=18), just like full-length K1250A channels, which reportedly open far more slowly than WT (Carson et al., 1995). Propagated effects of the Walker-A mutation on protein structure, or possible contribution of other regions to the catalytic sites (including a second CFTR molecule in a putative dimer; cf. Zerhusen et al., 1999), might eventually explain this and other, similarly intriguing, findings. For instance, K464A CFTR channels, mutated at the Walker-A lysine in NBD1, display relatively normal gating despite greatly impaired ATPase activity, which prompted the interpretation that, at least in those mutant channels, opening might be uncoupled from ATP hydrolysis (Ramjeesingh et al., 1999).

7.3.8. Interpretation of kinetic observations by fits to a gating scheme

Scheme I was adopted for semi-quantitative interpretation of the parameters estimated from fits to macroscopic current relaxations, and steady-state kinetic analysis of records with one or a few channels, for WT and all of the severed channels. From Scheme I, the opening rate at saturating [ATP] is equal to k_1, i.e., $k_1 = 1/\tau_{ib}$. If r_{OC} does not depend on [ATP], and $r_{OC} >> r_{CO,max}$ (an approximation likely to hold both for the split channels

and for WT in the absence of PKA), then $K_{r_{CO}} \approx K_{P_o}$ (see above). Depending on $k_{off,ATP}$, $K_{r_{CO}}$ is $\geq K_d$ for step $C_1 \rightarrow C_2$; but alterations in $K_{r_{CO}}$ (K_{P_o}) will parallel changes in K_d, as long as k_1 is unaffected. The remaining four rate constants, k_{-1}, k_2, k_{-2}, and k_3, determine observable parameters related to the open state, such as mean burst duration (τ_b), distribution of burst durations (characterized by short and long time constants τ_{sh} and τ_l, and fractional amplitudes a_{sh} and a_l, where $a_{sh}+a_l=1$), slow decay time constant following AMPPNP removal (τ_{AMPPNP}), and fractional amplitude of that slowly decaying component (a_{locked}). τ_{sh}, τ_l, a_{sh}, and a_l are obtained from the survivor function, of the form $surv(t) = a_{sh}e^{-t/\tau_{sh}} + a_l e^{-t/\tau_l}$ $(a_{sh} + a_l = 1)$, for the set of states $\{O_1, O_2\}$ (Chapter 4, Eq. 2; cf. Colquhoun and Hawkes, 1981). τ_b is obtained either as the mean of that distribution, or by elementary combinatorics. The dependence of these observable parameters on the rate constants is as follows (see derivations in Appendix C):

$$\tau_b = (k_{-2} + k_2 + k_3)/(k_2k_3 + k_{-1}k_{-2} + k_{-1}k_3) \quad (18)$$

$$a_{sh} = (\sqrt{D} - k_2 - k_{-2} - k_3 + k_{-1})/(2\sqrt{D}) \quad (19)$$

$$\tau_{sh} = 2/(k_{-1} + k_2 + k_{-2} + k_3 + \sqrt{D}) \quad (20)$$

$$\tau_l = 2/(k_{-1} + k_2 + k_{-2} + k_3 - \sqrt{D}) \quad (21)$$

where $D = (k_{-1} + k_2 + k_{-2} + k_3)^2 - 4(k_{-1}k_3 + k_{-1}k_{-2} + k_2k_3)$.

To validate the use of multi-channel patches and a fit to a Closed-Open-Blocked scheme (see Methods) for estimating mean burst durations, Scheme I was extended by adding two brief blocked states B_1 and B_2, communicating only with O_1 and O_2, respectively. When simulations of this extended scheme with multiple channels were

fitted assuming the *C-O-B* scheme, the fit gave rate constants that predicted mean burst durations similar to those expected from Eq. 18.

To obtain the two parameters describing the slowly decaying current component following exposure to AMPPNP, the following simplifications were made. Since AMPPNP was applied at 10-fold excess over ATP (0.1 mM ATP plus 1 mM AMPPNP), it was assumed that all channels in state O_2 at any time have AMPPNP (not ATP) bound at NBD-B. As AMPPNP cannot be hydrolyzed, k_3=0, and a fraction $k_{-2}/(k_2+k_{-2})$ of all *open* channels is expected to be in state O_1, and the complementary fraction $k_2/(k_2+k_{-2})$ in O_2, at steady state. (This assumption of an equilibrium between O_1 and O_2 may not strictly hold, if step $O_1 \rightarrow O_2$ is irreversible, see above.) When all nucleotides are then suddenly removed, k_1 and k_2 fall to zero, and Scheme I reduces to $O_2 \overset{k_{-2}}{\rightarrow} O_1 \overset{k_{-1}}{\rightarrow} C_1$. Solving the differential equation describing this scheme, with initial conditions given by the above steady-state occupancies of O_1 and O_2, the time course of the current decay is obtained as the sum of $O_1(t)$ and $O_2(t)$ (see derivation in Appendix C). The normalized current decay is a double-exponential, with slower time constant

$$\tau_{\text{AMPPNP}} = 1 / k_{-2} \tag{22}$$

with fractional amplitude

$$a_{\text{locked}} = (k_2 / (k_2 + k_{-2})) \cdot (k_{-1} / (k_{-1} - k_{-2})). \tag{23}$$

Note that a_{locked} is not exactly equal to, but approximates, the fraction of open channels locked at steady state, as long as $k_{-1} >> k_{-2}$. The time constant of the fast component, predicted to be $1/k_{-1}$, was not used, since it was comparable to the solution exchange time.

Figure 37 shows fits to Scheme I of the six (free) observable parameters measured in the presence of PKA for WT CFTR and the split channels. The set of rate constants that provided the most reasonable overall fit to the set of observed parameters is printed on the schemes for each construct, and the measured and predicted (Eqs. 18-23, above) parameters are compared on the right. Because no short component could be resolved in the burst durations of WT and 1-633 plus 634-1480 channels in the presence of PKA, for those constructs k_{-1} was fixed to the inverse of the burst durations measured in the absence of PKA, on the assumption that under those conditions $k_2 << k_{-1}$. For the same two constructs a very high k_2 of ~200 s^{-1} optimized the fit by causing the fractional amplitude of the predicted brief component to vanish. In practice, for k_2 higher than ~20 s^{-1} the brief component was already at the limit of detection, as shown by simulations of Scheme I, followed by analysis identical to that used for the real data. In particular, simulating ~500 openings for Scheme I, with rate constants as shown in Figure 37 for WT, except that k_2=40 s^{-1} or 20 s^{-1} was used, gave two components in the distribution of openings, readily detectable by subsequent analysis. However, since in real data flickery closures are also present necessitating burst analysis, Scheme I was modified by including brief closed states B_1 and B_2, linked to O_1 and O_2, respectively (see above), via typical rate constants $r_{O1,B1}=r_{O2,B2}=3$ s^{-1}, $r_{B1,O1}=r_{B2,O2}=100$ s^{-1}. Following simulation of ~500 bursts, burst analysis was performed using a cutoff of 50 ms to exclude flickery closures. Scheme I with rate constants like that shown for WT, but k_2=20 s^{-1}, predicts τ_{sh}=42 ms, τ_l =771 ms, a_{sh}=0.11, and a_l =0.89 for the time constants and fractional amplitudes of the survivor function of open times. Indeed, when the distribution of bursts obtained from a simulation including flickers was fitted with a mixture of two exponentials, the fit converged to

parameters τ_{sh}=35 ms, τ_l =712 ms, a_{sh}=0.11, and a_l =0.89, and the logarithm of the likelihood was ~20 units higher than that of a single exponential fit. When the same simulation was repeated with k_2=40 s^{-1}, followed by burst analysis as above, a double exponential fit found parameters τ_{sh}=12 ms, τ_l =846 ms, a_{sh}=0.03, and a_l =0.97 (for predicted parameters τ_{sh}=23 ms, τ_l =771 ms, a_{sh}=0.06, and a_l =0.94), but the likelihood was only 3 log units higher than that of a single exponential fit, indicating no significant improvement by assuming a second component. Thus, as expected, burst analysis, necessitated by inclusion of flickery closures, decreased the sensitivity of detection of subsequent fitting. Hence, only a lower estimate of k_2 >~20 s^{-1} could be established with confidence for WT and 1-633 plus 634-1480 channels in PKA. The fact that a mixture of two components in the distribution of bursts was never observed for WT (and 1-633 plus 634-1480) suggests that the transition of rate k_2, from a value >20 s^{-1} in the presence of PKA to a value <<k_{-1} in the absence of PKA, occured very rapidly upon removal of PKA, consistent with the observed rapid decline in P_o within 3-5 s (Figures 27A, B), such that the transition period was too short to be observed experimentally.

For 1-835 plus 837-1480, 1-633 plus 837-1480, and Flag3-633 plus 837-1480 channels, the printed rate constants are those representative of the behavior in the presence of PKA, as reflected by their opening rate (k_1). However, as there was no discernible effect of PKA on their burst durations (Figure 28C), the six measured parameters used for the fit to Scheme I are averages of values obtained with and without PKA. Instead of K_d for the equilibrium between C_1 and C_2, K_{P_o} values are printed (measured in PKA for WT, without PKA for the other constructs).

Figure 37. Model fit of Scheme I, to data of WT CFTR and CFTR channels severed around the R domain, in the presence of PKA.

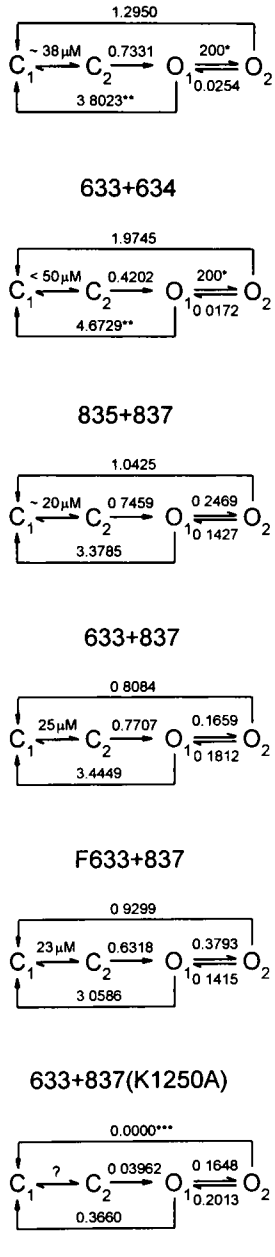

	OBSERVED			MODEL
WT				
a_{sh}	0.00	+/-	0.00	0.01
a_l	1.00	+/-	0.00	0.99
τ_{sh}	--			5
τ_l	778	+/-	48	772
τ_b	771	+/-	92	763
τ_{AMPPNP}	39316	+/-	3646	39316
a_{locked}	0.90	+/-	0.07	1.00
633+634				
a_{sh}	0.00	+/-	0.00	0.01
a_l	1.00	+/-	0.00	0.99
τ_{sh}	--			5
τ_l	461	+/-	25	506
τ_b	554	+/-	21	500
τ_{AMPPNP}	58052	+/-	14447	58052
a_{locked}	1.00	+/-	0.00	1.00
835+837				
a_{sh}	0.74	+/-	0.05	0.89
a_l	0.26	+/-	0.05	0.11
τ_{sh}	266	+/-	28	275
τ_l	987	+/-	147	854
τ_b	325	+/-	29	336
τ_{AMPPNP}	7310	+/-	1027	7010
a_{locked}	0.59	+/-	0.09	0.66
633+837				
a_{sh}	0.92	+/-	0.01	0.93
a_l	0.08	+/-	0.01	0.07
τ_{sh}	210	+/-	8	276
τ_l	1020	+/-	131	1022
τ_b	380	+/-	38	326
τ_{AMPPNP}	5841	+/-	423	5518
a_{locked}	0.47	+/-	0.04	0.50
F633+837				
a_{sh}	0.83	+/-	0.02	0.83
a_l	0.17	+/-	0.02	0.17
τ_{sh}	261	+/-	12	289
τ_l	944	+/-	85	953
τ_b	456	+/-	41	400
τ_{AMPPNP}	8161	+/-	2203	7067
a_{locked}	0.65	+/-	0.11	0.76
633+837(K1250A)				
a_{sh}	0.37	+/-	0.09	0.50
a_l	0.63	+/-	0.09	0.50
τ_{sh}	961	+/-	338	1635
τ_l	6869	+/-	1192	8303
τ_b	4969	+/-	654	4969
τ_{relax}	6669	+/-	117	4969
a_{relax}	1.00	+/-	0.00	1.00

Scheme I with set of rate constants (s^{-1}) giving closest overall fit to indicated set of observed parameters for each construct. a_{sh}, a_l, τ_{sh}, τ_l, fractional amplitudes and time constants of exponentials fitted to distributions of burst durations; τ_b mean burst duration, in PKA for WT and 1-633 plus 634-1480, or pooled for 1-835 plus 837-1480, 1-633 plus 837-1480, and Flag3-633 plus 837-1480; τ_{AMPPNP}, a_{lock}, time constant and fractional amplitude of slowly relaxing current component after removal of AMPPNP and ATP; τ_{relax}, a_{relax}, similar, after just ATP, for 1-633 plus 837-1480(K1250A). For step $C_1 \rightarrow C_2$, K_{P_o} is printed instead of K_d. Errors for a_{sh}, a_l, τ_{sh}, and τ_l are half-widths of 0.5 unit likelihood intervals, calculated separately for each parameter; for τ_b, τ_{AMPPNP}, and a_{locked} errors are s.e.m.. k_1 was obtained as $1/\tau_{ib}$ (τ_{ib}, mean interburst duration) in PKA and 2 mM MgATP. (Except for 1-633 plus 837-1480(K1250A), for which all data are in the absence of PKA.) * k_2 for WT and 1-633 plus 634-1480 may be <200 s^{-1}, k_2>20 s^{-1} accounts for uniform distribution of burst durations in PKA. ** k_{-1} for WT and 1-633 plus 634-1480 was fixed to $1/\tau_{ib}$ after PKA removal, assuming $k_2 << k_{-1}$. *** k_3 was set to zero for 1-633 plus 837-1480(K1250A).

For 1-633 plus 837-1480(K1250A) channels, all parameters were measured in the absence of PKA. k_3=0 was assumed for this construct, since this rate represents a (compound) step including ATP hydrolysis likely at NBD2 (NBD-B). τ_{relax} and a_{relax}, substituted for τ_{AMPPNP} and a_{locked}, represent the quasi-macroscopic decay current observed on removing ATP. Because k_3=0, the action of ATP at NBD-B is expected to be analogous to the action of AMPPNP at NBD-B of WT channels.

The numerical values of the rates should be taken as, at best, a qualitative description, because of experimental limitations (variability, temperature effects, etc.) and simplifying assumptions (e.g., on- and off-rates at NBD-B were assumed identical for AMPPNP and ATP). Nevertheless, several interesting comparisons can be made. 1-633 plus 634-1480 seems almost identical to WT, except for a <2-fold increase in rate k_3, accounting for shortened bursts. (The apparent lower rate k_1 reflects collection of all 1-633 plus 634-1480 data in the lower temperature pool (~22°C); opening rates were not significantly different from WT when compared at the same temperatures; see Chapter 6, Figure 22 and Table III.) Since a 2-fold change in rate corresponds to a change in activation energy of less than 1 kT, it may be concluded that the cut between residues 633 and 634 has very little effect on gating, and, likely, on channel structure. On the other hand, constructs 1-835 plus 837-1480, 1-633 plus 837-1480, and Flag3-633 plus 837-1480 differed from WT by a decrease of at least two orders of magnitude of the rate k_2, and a more than 5 fold increase in k_{-2}, corresponding to changes in activation energy of >5 kT for the on-rate and ~1.6 kT for the off-rate, consistent with a structural destabilization of NBD-B caused by the cut before residue 837. Smaller K_{P_o} values, but unaltered rates k_1, for these same constructs (Figures 29, 37) suggest increased affinities for ATP at NBD-A,

compared to partially phosphorylated WT (or 1-633 plus 634-1480) channels. Comparing 1-633 plus 837-1480(K1250A) with 1-633 plus 837-1480, the fit for the Walker-A mutant predicted nucleotide on- and off-rates at NBD-B (k_2 and k_{-2}) similar to those of 1-633 plus 837-1480. However, to account for the observed distribution of bursts of the Walker mutant, k_{-1} had to be slowed by an order of magnitude compared to 1-633 plus 837-1480 channels, which, together with a similar decrease in opening rate (compare k_1 with basal opening rate of 1-633 plus 837-1480), calls into question the assumed local nature of the effect on channel structure of the Walker-A mutation.

8. CONCLUSION

By exploiting the modular ABC-transporter design of CFTR, we have defined functional boundaries for CFTR's NBD1, by monitoring functional co-assembly of co-expressed severed CFTR half-molecules. No sever points were tolerated between residues 448 and 623, but up to 18 residues could be discarded N-proximal to Phe433, or 34 residues distal to Leu633, without destroying channel function. Thus, the N-terminal boundary of NBD1 can be confidently assigned to lie within the stretch of a.a.s 433-448, while the C-terminus of NBD1 maps within a.a.s 623-633.

The observation that severed CFTR channels which lack residues 415-432 (i.e. co-expressed Flag3-414 plus 433-1480; the missing piece is predicted to form β1, Figure 25, *gray*) are opened by MgATP with the same apparent affinity as seen for WT CFTR channels ($K_{1/2}$ ~50 μM; Figure 24D-E) is intriguing. This is because a number of observations have suggested that binding and hydrolysis of ATP are responsible for CFTR channel opening, and that this binding site, NBD-A, is formed by NBD1 (reviewed in Gadsby and Nairn, 1999; Csanády and Gadsby, 1999, see also Chapters 4 and 5). For example, CFTR 1-835 channels, truncated after the R domain and hence lacking NBD2, are opened by MgATP with μM apparent affinity (Sheppard et al., 1994), and CFTR 1-1218 channels, which also lack NBD2, yield large currents in whole oocytes and robust gating of channels in excised patches (Chan et al., 1999). Also, mutant K1250A CFTR channels, in which ATP hydrolysis at NBD2 is severely impaired (Ramjeesingh et al., 1999), show brief WT-like openings at low μM [ATP], but extremely long openings at higher [ATP] that reflect binding at NBD2 of ATP that cannot be hydrolyzed (Zeltwanger

et al., 1999); those results imply that the brief openings observed at low [ATP] involve only NBD1. If, indeed, the relatively high affinity action of MgATP to open CFTR channels occurs at NBD1 (i.e., if NBD-A is formed entirely, or largely, by NBD1) even in Flag3-414 plus 433-1480 channels, then our findings prompt a new series of questions. Thus, although the overall organization of the NBDs of all ABC transporters may be similar, does the detailed structure of the nucleotide binding pocket of NBD1 in CFTR perhaps differ from that of HisP or RbsA? Or, perhaps, are the detailed structures similar, and our expectations of the consequences of deleting β1 unwarranted? Alternatively, perhaps substantial contributions to the binding energy for ATP at NBD-A are made by regions of the polypeptide other than NBD1, such as NBD2 (e.g., Jones and George, 1999) or even cytoplasmic loops from the transmembrane domains (e.g. Mourez et al., 1998). Point mutations at residues believed to lie in or near the catalytic sites of CFTR's NBDs, chosen on the basis of the HisP and RbsA structures, should soon resolve some of these questions (cf. Vergani et al., 2000).

The functional studies on WT CFTR in parallel with CFTR channels severed just N- and/or C-proximal to the R domain, intended to shed light on the mechanism by which the R domain interacts with the NBDs to gate CFTR channels (Chapter 7), support the following model. The unphosphorylated R domain inhibits opening of WT channels by interference both with nucleotide binding at NBD-A (likely NBD1) and with the subsequent rate-limiting step for channel opening (presumably ATP hydrolysis, or perhaps formation of the pre-hydrolysis complex). The inhibitory influence on ATP binding, normally relieved through phosphorylation, depends on physical linkage of the R domain to residues which follow 837, because channels split between residues 835 and 837

display a high affinity for ATP even in the absence of PKA (Figure 29D). The inhibition of the post-binding step also partially depends on the same linkage, because partial disinhibition is observed in split channels 1-835 plus 837-1480, signalled by their opening at a low rate (of ~0.1 s^{-1}) in the presence of ATP prior to exposure to PKA (Figures 27, 28). Both types of inhibition are lost in severed channels which lack the R domain (1-633 plus 837-1480 and Flag3-633 plus 837-1480), and this results in high apparent affinity for ATP (Figure 29) and relatively rapid channel opening (~0.35 s^{-1}; Figure 28D, and Table IV) without phosphorylation by PKA. The stimulatory effect of PKA on the rate-limiting step for CFTR-channel opening is only partially due to disinhibition by R-domain phosphorylation, and could also involve phosphorylation event(s) outside the R domain, because the opening rate of severed channels with no R domain is further accelerated ~2 fold by PKA (to ~0.7 s^{-1}, comparable to that of strongly phosphorylated WT; Figures 27, 28, 31). This similarity of the maximal opening rate of split channels with no R domain to that of phosphorylated WT channels refutes the previously proposed stimulatory effect of the phosphorylated R domain on opening rate. An interaction between CFTR's N terminus and the R domain (Naren et al, 1999) is supported by our observations that the gating kinetics of severed channels without an R domain are unaffected by an N-terminal Flag epitope (Figure 28), whereas that same Flag slowed (2-3 fold) the opening of WT channels, or of split channels that do contain an R domain (Chapter 6).

Binding of ATP to NBD-B also seems inhibited by the unphosphorylated (or partially phosphorylated) R domain in WT channels, and this results in short open bursts (Figures 28C, 33), and impaired locking by AMPPNP (Hwang et al., 1994). Severed channels without an R domain seem capable of binding ATP at NBD-B, evident, e.g.,

from the locking effect of AMPPNP on those channels, but the affinity of this binding site for nucleotide seems considerably lower than in phosphorylated WT channels (Figures 31, 32, 33, 35). Although this could reflect loss of a facilitatory influence of the phosphorylated R domain, a more likely explanation is that simply cutting before residue 837 destabilizes NBD-B (likely NBD2) structure: this is supported by the similarly decreased nucleotide affinity of NBD-B in 1-835 plus 837-1480 channels (Figures 31, 33), which contain an R domain capable of at least partial function (cf. substantially lower basal opening rate of these channels compared to 1-633 plus 837-1480, and large response to PKA; Figures 27, 28), and also by their similarly increased sensitivity to temperature changes (Figure 34).

These chapters have explored structural boundaries of CFTR's NBD1, have presented an initial broad description of the gating characteristics of CFTR channels with and without an R domain, and have provided an internally consistent framework for rationalizing them and for planning further experiments. The information extracted from these measurements allows some preliminary insight into how structural interactions among CFTR's intracellular domains might be linked to various gating steps, and how those interactions might be modulated by phosphorylation.

APPENDIX

A. Likelihood function in the case of binning limits

Suppose that lower and upper bin limits $t_{k,min}$ and $t_{k,max}$ are imposed. Quantities analogous to those in Eqs. 5, 6, and 4, conditional on being binned, are defined as

$$pctlvl'(k) = P(\text{event is level } k \mid \text{event is binned}), \tag{A1}$$

$$p'_{ki} = P(t_{k,i} \le \textit{dwell time} < t_{k,i+1} | \text{event is level } k \textbf{ and } \text{event is binned}), \tag{A2}$$

$$P'(k,i) = P(\text{event is level } k \textbf{ and } t_{k,i} \le \textit{dwell time} < t_{k,i+1} \mid \text{event is binned}). \tag{A3}$$

Next, $P_{k,binned}$ is defined as the fraction of all observed level k events predicted to be binned given bin limits $t_{k,min}$ and $t_{k,max}$:

$$\begin{aligned} P_{k,binned} &= P(\text{event is binned} \mid \text{event is level } k) = \\ &= surv_{\{k\}}(t_{k,min}) - surv_{\{k\}}(t_{k,max}). \end{aligned} \tag{A4}$$

It follows from the theory of probabilities that

$$pctlvl'(k) = \frac{pctlvl(k) \cdot P_{k,binned}}{\sum_{j=0}^{N} pctlvl(j) \cdot P_{j,binned}} \quad , \tag{A5}$$

and

$$p'_{ki} = \frac{p_{ki}}{P_{k,binned}} \quad . \tag{A6}$$

The probability of an event falling into the i^{th} bin of the level k histogram, conditional on being binned, is

$$P'(k,i) = pctlvl'(k) \cdot p'_{ki} = \frac{pctlvl(k) \cdot p_{k,i}}{\sum_{j=0}^{N} pctlvl(j) \cdot P_{j,binned}} \quad . \tag{A7}$$

Proceeding in an analogous way to steps 7 and 8 in the main text, the likelihood function becomes

$$L'(\Theta) = \prod_{k=0}^{N} \prod_{i=1}^{r_k} P'(k,i)^{n_{k,i}} = \prod_{k=0}^{N} \prod_{i=1}^{r_k} \left[\frac{pctlvl(k) \cdot p_{k,i}}{\sum_{j=0}^{N} pctlvl(j) \cdot P_{j,binned}} \right]^{n_{k,i}} , \tag{A8}$$

while $LL'(\Theta)$, defined as $LL'(\Theta) = \ln(L'(\Theta))$, is

$$LL'(\Theta) = \sum_{k=0}^{N} \sum_{i=1}^{r_k} n_{k,i} \cdot \ln p_{k,i} + \sum_{k=0}^{N} n_k \cdot \ln pctlvl(k) - n_t \cdot \ln \left[\sum_{k=0}^{N} pctlvl(k) \cdot P_{k,binned} \right], \tag{A9}$$

where $n_t = \sum_{k=0}^{N} n_k$ is the total number of binned events.

B. Introducing additional constraint of first dwell > t_d

Because of the properties of a stationary Markov system (see e.g. Colquhoun and Hawkes, 1977), Eq. 13 can be rewritten in the form:

$$\begin{aligned} surv_{\{k\}}(t,t_d) = P(&\text{no observable leaving from } \{k\} \text{ before time } t - t_d | \\ &\text{entered } \{k\} \text{ at time } -t_d \text{ after an observable stay in } \{\bar{k}\} \textbf{ and} \\ &\text{stayed in } \{k\} \text{ until time } 0) \end{aligned} \tag{B1}$$

The expression in Eq. B1 has the form

$P(C|\,A$ **and** $B) = P(C$ **and** A **and** $B) \,/\, P(A$ **and** $B)$, where C is "no observable leaving from $\{k\}$ before time t-t_d", A is "entered $\{k\}$ at time -t_d after an observable stay in $\{\bar{k}\}$ ", B is "stayed in $\{k\}$ between time -t_d and 0". Following the reasoning of Roux and Sauvé (1985),

$$P(C \textbf{ and } A \textbf{ and } B) = \frac{\mathbf{p}_k(\infty)^T \mathbf{Q}_{k\bar{k}} e^{\mathbf{Q}_{\bar{k}\bar{k}} t_d} (-\mathbf{Q}_{\bar{k}\bar{k}}^{-1}) \mathbf{Q}_{\bar{k}k} e^{\mathbf{Q}_{kk} t_d}}{\mathbf{p}_k(\infty)^T \mathbf{Q}_{k\bar{k}} \mathbf{1}_{\bar{k}}} e^{\hat{\mathbf{Q}}_{kk}(t-t_d)} \mathbf{1}_k \quad , \tag{B2}$$

$$P(A \textbf{ and } B) = \frac{\mathbf{p}_k(\infty)^T \mathbf{Q}_{k\bar{k}} e^{\mathbf{Q}_{\bar{k}\bar{k}} t_d} (-\mathbf{Q}_{\bar{k}\bar{k}}^{-1}) \mathbf{Q}_{\bar{k}k} e^{\mathbf{Q}_{kk} t_d} \mathbf{1}_k}{\mathbf{p}_k(\infty)^T \mathbf{Q}_{k\bar{k}} \mathbf{1}_{\bar{k}}} \quad , \tag{B3}$$

from which the survivor function can be assembled:

$$surv_{\{k\}}(t, t_d) = \begin{cases} 1 & \text{for } t < t_d \\ [\textbf{initial}]_k^T e^{\hat{\mathbf{Q}}_{kk}(t-t_d)} \mathbf{1}_k & \text{for } t \geq t_d \end{cases} \quad , \tag{B4}$$

where

$$[\textbf{initial}]_k^T = \frac{\mathbf{p}_k(\infty)^T \mathbf{Q}_{k\bar{k}} e^{\mathbf{Q}_{\bar{k}\bar{k}} t_d} (-\mathbf{Q}_{\bar{k}\bar{k}}^{-1}) \mathbf{Q}_{\bar{k}k} e^{\mathbf{Q}_{kk} t_d}}{\mathbf{p}_k(\infty)^T \mathbf{Q}_{k\bar{k}} e^{\mathbf{Q}_{\bar{k}\bar{k}} t_d} (-\mathbf{Q}_{\bar{k}\bar{k}}^{-1}) \mathbf{Q}_{\bar{k}k} e^{\mathbf{Q}_{kk} t_d} \mathbf{1}_k} \quad , \tag{B4a}$$

$$\hat{\mathbf{Q}}_{kk} = \mathbf{Q}_{kk} - \mathbf{Q}_{k\bar{k}} (\mathbf{I}_{\bar{k}} - e^{\mathbf{Q}_{\bar{k}\bar{k}} t_d}) \mathbf{Q}_{\bar{k}\bar{k}}^{-1} \mathbf{Q}_{\bar{k}k} \qquad \text{(as in Eq. 12b).} \tag{B4b}$$

C. Derivation of observable parameters for Scheme I.

C.1. Mean open time / burst duration

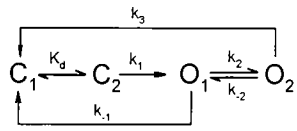

(Scheme I)

The mean open time (cf. τ_b in text) is the weighted average of the durations of various types of openings, weighted by their fractional occurrences. Openings either close from O_1, after venturing m times to O_2, m=0,...∞, "type 1_m"; or from O_2, upon entering O_2 the m^{th} time, m=1,...∞, "type 2_m". The mean durations of individual dwells at O_1 or O_2 are $\tau_{O1} = 1/(k_{-1} + k_2)$, and $\tau_{O2} = 1/(k_{-2} + k_3)$, respectively. Let π_{-1} be the probability that a channel in O_1 will next exit to C_1, π_2 the probability that it will next exit to O_2. Similarly, π_{-2} and π_3 denote probabilities that a channel in O_2 next exits to O_1 or to C_1, respectively. Thus, $\pi_{-1} = k_{-1}/(k_{-1} + k_2)$, $\pi_2 = k_2/(k_{-1} + k_2)$, $\pi_{-2} = k_{-2}/(k_{-2} + k_3)$, and $\pi_3 = k_3/(k_{-2} + k_3)$. The mean duration of a type 1_m opening is $(m+1)\cdot\tau_{O1} + m\cdot\tau_{O2}$, with fractional occurrence $\pi_2^m \pi_{-2}^m \pi_{-1}$, while type 2_m openings last for $m\cdot(\tau_{O1} + \tau_{O2})$, and occur with $\pi_2^m \pi_{-2}^{m-1} \pi_3$ probability. Hence,

$$\tau_b = \sum_{m=0}^{\infty} \pi_2^m \pi_{-2}^m \pi_{-1}[(m+1)\cdot\tau_{O1} + m\cdot\tau_{O2}] + \sum_{m=1}^{\infty} \pi_2^m \pi_{-2}^{m-1} \pi_3[m\cdot(\tau_{O1} + \tau_{O2})] =$$

$$= (\pi_{-1} + \pi_3/\pi_{-2})\cdot(\tau_{O1} + \tau_{O2})\cdot \sum_{m=0}^{\infty} m\cdot(\pi_2\pi_{-2})^m + \pi_{-1}\cdot\tau_{O1}\cdot \sum_{m=0}^{\infty}(\pi_2\pi_{-2})^m \quad ,$$

from which, using identities $\sum_{m=0}^{\infty} m\cdot q^m = q/(1-q)^2$ and $\sum_{m=0}^{\infty} q^m = 1/(1-q)$ for q<1,

$$\tau_b = (\pi_{-1} + \pi_3/\pi_{-2})\cdot(\tau_{O1} + \tau_{O2})\cdot \pi_2\pi_{-2}/(1-\pi_2\pi_{-2})^2 + \pi_{-1}\cdot\tau_{O1}/(1-\pi_2\pi_{-2}). \qquad (C1)$$

Substituting for π_{-1}, π_2, π_{-2}, π_3, τ_{O1}, and τ_{O2} from the rates, Eq. C1 reduces to Eq.18.

C.2. Survivor function of open times / burst durations

Numbering the states of Scheme I in the order C_1, C_2, O_1, O_2, the **Q**-matrix of the system is

$$\mathbf{Q} = \left|\begin{array}{cc|cc} -k'_{on} & k'_{on} & 0 & 0 \\ k_{off} & -(k_{off}+k_1) & k_1 & 0 \\ \hline k_{-1} & 0 & -(k_{-1}+k_2) & k_2 \\ k_3 & 0 & k_{-2} & -(k_3+k_{-2}) \end{array}\right| ,$$

in particular, the submatrix of the set of states $\{O_1,O_2\}$ is

$$\mathbf{Q}_{\{O_1,O_2\}\{O_1,O_2\}} = \left|\begin{array}{cc} -(k_{-1}+k_2) & k_2 \\ k_{-2} & -(k_3+k_2) \end{array}\right| .$$

The Eigenvalues of the submatrix are $\lambda_{\pm} = \frac{-(k_{-1}+k_2+k_{-2}+k_3) \pm \sqrt{D}}{2}$, where

$D = (k_{-1}+k_2+k_{-2}+k_3)^2 - 4(k_{-1}k_3 + k_{-1}k_{-2} + k_2k_3)$. The exponential of the submatrix is

$$e^{\mathbf{Q}_{\{O_1,O_2\}\{O_1,O_2\}}t} =$$

$$= \left|\begin{array}{cc} \frac{(e^{\lambda_+ t}+e^{\lambda_- t})}{2} - \frac{k_{-1}+k_2-k_{-2}-k_3}{2\sqrt{D}}\cdot(e^{\lambda_+ t}-e^{\lambda_- t}) & \frac{k_2}{\sqrt{D}}\cdot(e^{\lambda_+ t}-e^{\lambda_- t}) \\ \frac{k_{-2}}{\sqrt{D}}\cdot(e^{\lambda_+ t}-e^{\lambda_- t}) & \frac{(e^{\lambda_+ t}+e^{\lambda_- t})}{2} + \frac{k_{-1}+k_2-k_{-2}-k_3}{2\sqrt{D}}\cdot(e^{\lambda_+ t}-e^{\lambda_- t}) \end{array}\right|$$

The survivor function of $\{O_1,O_2\}$ is $surv_{\{O_1,O_2\}}(t) = \mathbf{p}_{\{O_1,O_2\}}(0)^{\mathrm{T}} e^{\mathbf{Q}_{\{O_1,O_2\}\{O_1,O_2\}}t} \mathbf{1}_{\{O_1,O_2\}}$

(cf. Chapter 3, Eq. 2), where $\mathbf{p}_{\{O_1,O_2\}}(0)^{\mathrm{T}} = [1, 0]$ (since all openings start in O_1). I.e., the survivor function simplifies to the sum of the first row of the submatrix:

$$surv_{\{O_1,O_2\}}(t) = \frac{\sqrt{D}-k_2-k_{-2}-k_3+k_{-1}}{2\sqrt{D}}\cdot e^{\lambda_- t} + \frac{\sqrt{D}+k_2+k_{-2}+k_3-k_{-1}}{2\sqrt{D}}\cdot e^{\lambda_+ t} . \qquad \text{(C2)}$$

The coefficient of the first term and $-\lambda_-^{-1}$ give a_{sh} and τ_{sh}, respectively (Eqs. 19 and 20), while the second coefficient and $-\lambda_+^{-1}$ yield a_l and τ_l (Eq. 21). As a check, the mean of the above distribution, $<t> = a_{sh}\tau_{sh} + a_l\tau_l$, is identical to τ_b in Eq. C1 (Eq. 18).

C.3. Time course of unlocking from AMPPNP-mediated lock

The predicted time course of unlocking is obtained by solving the differential equation describing scheme $O_2 \overset{k_{-2}}{\rightarrow} O_1 \overset{k_{-1}}{\rightarrow} C_1$, with initial condition $o_1(0) = k_{-2} / (k_2 + k_{-2})$, $o_2(0) = k_2 / (k_2 + k_{-2})$. The vector-solution of equation

$$\frac{d}{dt}\begin{bmatrix} o_1 \\ o_2 \end{bmatrix}(t) = \begin{bmatrix} -k_{-1} & k_{-2} \\ 0 & -k_{-2} \end{bmatrix}\begin{bmatrix} o_1 \\ o_2 \end{bmatrix}(t)$$

with the above initial condition is

$$\begin{bmatrix} o_1 \\ o_2 \end{bmatrix}(t) = \frac{k_{-2}}{k_2 + k_{-2}} \cdot \begin{bmatrix} 1 - \dfrac{k_2}{(k_{-1} - k_{-2})} \\ 0 \end{bmatrix} \cdot e^{-k_{-1}t} + \frac{k_2}{k_2 + k_{-2}} \cdot \begin{bmatrix} \dfrac{k_{-2}}{k_{-1} - k_{-2}} \\ 1 \end{bmatrix} \cdot e^{-k_{-2}t} \quad , \qquad \text{(C3)}$$

from which the time course, obtained as $o(t) = o_1(t) + o_2(t)$, contains a slow component with time constant $1 / k_{-2}$ (see Eq. 22) and fractional amplitude $(k_2 / (k_2 + k_{-2})) \cdot (k_{-1} / (k_{-1} - k_{-2}))$ (see Eq. 23); as well as a fast component with time constant $1 / k_{-1}$ and complementary fractional amplitude.

BIBLIOGRAPHY

Aleksandrov, A.A., and J.R. Riordan. 1998. Regulation of CFTR ion channel gating by MgATP. *FEBS Letters.* 431:97-101.

Al-Nakkash, L., and T.-C. Hwang. 1999. Activation of wild-type and deltaF508-CFTR by phosphodiesterase inhibitors through cAMP-dependent and -independent mechanisms. *Pflugers Arch.* 437:553-561.

Anderson, M.P., D.P. Rich, R.J. Gregory, A.E. Smith, and M.J. Welsh. 1991a. Generation of cAMP-activated chloride currents by expression of CFTR. *Science.* 251:679-82.

Anderson, M.P., H.A. Berger, D.P. Rich, R.J. Gregory, A.E. Smith, and M.J. Welsh. 1991b. Nucleoside triphosphates are required to open the CFTR chloride channel. *Cell.* 67:775-84.

Anderson, M.P., R.J. Gregory, S. Thompson, D.W. Souza, S. Paul, R.C. Mulligan, A.E. Smith, and M.J. Welsh. 1991c. Demonstration that CFTR is a chloride channel by alteration of its anion selectivity. *Science.* 253:202-205.

Armstrong, S., L. Tabernero, H. Zhang, M. Hermodson, and C. Stauffacher. 1998. The 2.5Å structure of the N-terminal ATP-binding cassette of the ribose ABC transporter. *Biophys. J.* 74:A338.

Ball, F.G., and M.S.P. Sansom. 1989. Ion-channel gating mechanisms: model identification and parameter estimation from single channel recordings. *Proc. R. Soc. Lond.* B 236:385-416.

Baukrowitz, T., T.-C. Hwang, A.C. Nairn, and D.C. Gadsby. 1994. Coupling of CFTR Cl^- channel gating to an ATP hydrolysis cycle. Neuron. 12:473-482.

Bear, C.E., F. Duguay, A.L. Naismith, N. Kartner, J.W. Hanrahan, and J.R. Riordan. 1991. Cl^- channel activity in Xenopus oocytes expressing the cystic fibrosis gene. *J. Biol. Chem.* 266:19142-19145.

Bear, C.E., C. Li, N. Kartner, R.J. Bridges, T.J. Jensen, M. Ramjeesingh, and J.R. Riordan. 1992. Purification and functional reconstitution of the cystic fibrosis transmembrane conductance regulator (CFTR). *Cell.* 68:809-818.

Berkower, C., and S. Michaelis. 1991. Mutational analysis of the yeast a-factor transporter STE6, a member of the ATP binding cassette (ABC) protein superfamily. *EMBO J.* 10:3777-3785.

Berkower, C., D. Taglicht, and S. Michaelis. 1996. Functional and physical interactions between partial molecules of STE6, a yeast ATP-binding cassette protein. *J. Biol. Chem.* 271:22983-22989.

Bibi, E., and H.R. Kaback. 1990. *In vivo* expression of the *lac*Y gene in two segments leads to functional *lac* permease. *Proc. Natl. Acad. Sci.* 87:4325-4329.

Blunck, R., U. Kirst, T. Riessner, and U.-P. Hansen. 1998. How powerful is the dwell-time analysis of multichannel records? *J. Membrane Biol.* 165:19-35.

Caceci M. S., and W. P. Cacheris. 1984. Fitting curves to data. The simplex algorithm is the answer. *Byte.* May 1984:340-348.

Carson, M.R., and M.J. Welsh. 1993. 5'-adenylylimidodiphosphate does not activate CFTR chloride channels in cell-free patches of membrane. *Am. J. Physiol.* 265:L27-L32.

Carson, M.R., S.M. Travis, and M.J. Welsh. 1995. The two nucleotide-binding domains of cystic fibrosis transmembrane conductance regulator (CFTR) have distinct functions in controlling channel activity. *J. Biol. Chem.* 270:1711-1717.

Chan, K.W., L. Csanády, A.C. Nairn, and D.C. Gadsby. 1999. Deletion analysis of CFTR channel R domain using severed molecules. *Biophys J.* 76:A405.

Chang, X.-B., J.A. Tabcharani, Y.-X. Hou, T.J. Jensen, N. Kartner, N. Alon, J.W. Hanrahan, and J.R. Riordan. 1993. Protein kinase A (PKA) still activates CFTR chloride channel after mutagenesis of all 10 PKA consensus phosphorylation sites. *J. Biol. Chem.* 268:11304-11311.

Chang, X.-B., Y.-X. Hou, T.J. Jensen, and J.R. Riordan. 1994. Mapping of cystic fibrosis transmembrane conductance regulator topology by glycosylation site insertion. *J. Biol. Chem.* 269:18572-18575.

Cheng, S.H., R.J. Gregory, J. Marshall, S. Paul, D.W. Souza, G.A. White, C.R. O'Riordan, and A.E. Smith. 1990. Defective intracellular transport and processing of CFTR is the molecular basis of most cystic fibrosis. *Cell.* 63:827-834.

Cheng S.H., D.P. Rich, J. Marshall, R.J. Gregory, M.J. Welsh, and A.E. Smith. 1991. Phosphorylation of the R domain by cAMP-dependent protein kinase regulates the CFTR chloride channel. *Cell.* 66:1027-36.

Cheung, M., and M.H. Akabas, 1996. Identification of CFTR channel-lining residues in and flanking the M6 membrane-spanning segment. *Biophys. J.* 70:2688-2695.

Clancy, J.P., J.S. Hong, Z. Bebök, S.A. King, S. Demolombe, D.M. Bedwell, and E.J. Sorscher. 1998. Cystic fibrosis transmembrane conductance regulator (CFTR) nucleotide-binding domain 1 (NBD-1) and CFTR truncated within NBD-1 target to the epithelial plasma membrane and increase anion permeability. *Biochem.* 37:15222-15230.

Colquhoun, D., and A. G. Hawkes. 1977. Relaxation and fluctuations of membrane currents that flow through drug-operated channels. *Proc. R. Soc. Lond.* B 199:231-262.

Colquhoun, D., and A.G. Hawkes. 1981. On the stochastic properties of single ion channels. *Proc. R. Soc. Lond.* B 211:205-235.

Colquhoun, D., and B. Sakmann, 1985. Fast events in single-channel currents activated by acetylcholine and its analogues at the frog muscle end-plate. *J. Physiol.* 369:501-557.

Colquhoun, D., and A.G. Hawkes. 1995. The principles of stochastic interpretation of ion-channel mechanisms. *In* Single channel recording. Second Edition. B. Sakmann and E. Neher, editors. Plenum Press, New York. 433-434.

Colquhoun, D., and F.J. Sigworth. 1995. Fitting and statistical analysis of single-channel records. *In* Single channel recording. Second Edition. B. Sakmann and E. Neher, editors. Plenum Press, New York. 483-587.

Csanády, L., and D.C. Gadsby. 1999. CFTR channel gating: Incremental progress in irreversible steps. *J. Gen. Physiol.* 114:49-53.

Csanády, L., K.W. Chan, D. Seto-Young, A.C. Nairn, and D.C. Gadsby. 1999. Co-expression of two halves of CFTR lacking the R domain results in near fully functional channels. *Pediatr. Pulmonol.* Suppl. 19:174.

Csanády, L. 2000. Rapid kinetic analysis of multichannel records by a simultaneous fit to all dwell-time histograms. *Biophys. J.* 78:785-799.

Dawson, D.C., S.S. Smith, and M.K. Mansoura. 1999. CFTR: Mechanism of anion conduction. *Physiol. Revs.* 79: S47-S75.

Devidas, S., H. Yue, and W.B. Guggino. 1998. The second half of the Cystic Fibrosis Transmembrane Conductance Regulator forms a functional chloride channel. *J. Biol. Chem.* 273:29373-29380.

Dousmanis, A.G., A.C. Nairn, and D.C. Gadsby. 1996a. [Mg^{2+}] governs CFTR Cl^- channel opening and closing rates, confirming hydrolysis of two ATP molecules per gating cycle. *Biophys. J.* 70:A127.

Dousmanis, A.G., A.C. Nairn, and D.C. Gadsby. 1996b. Three functionally different phosphoforms of CFTR identified by patterns of single-channel gating. *J. Gen. Physiol.* 108:11a.

Doyle, D.A., J.M. Cabral, R.A. Pfuetzner, A. Kuo, J.M. Gulbis, S.L. Cohen, B.T. Chait, and R. MacKinnon. 1998. The structure of the potassium channel: molecular basis of K^+ conduction and selectivity. *Science.* 280:69-77.

Dulhanty, A.M., and J.R. Riordan. 1994. Phosphorylation by cAMP-dependent protein kinase causes a conformational change in the R domain of the cystic fibrosis transmembrane conductance regulator. *Biochem.* 33:4072-4079.

Eskandari, S., E.M. Wright, M. Kreman, D.M. Starace, and G.A. Zampighi. 1998. Structural analysis of cloned plasma membrane proteins by freeze-fracture electron microscopy. *Proc. Natl. Acad. Sci. U.S.A.* 95:11235-11240.

Gadsby, D.C., and A.C. Nairn. 1999. Control of CFTR channel gating by phosphorylation and nucleotide hydrolysis. *Physiol. Revs.* 79:S77-S107.

Gao, M., D.W. Loe, C.E. Grant, S.P.C. Cole, and R.G. Deeley. 1996. Reconstitution of ATP-dependent leukotriene C_4 transport by co-expression of both half-molecules of human multidrug resistance protein in insect cells. *J. Biol. Chem.* 271:27782-27787.

Groves, J.D., L. Wang, and M.J.A. Tanner. 1998. Functional reassembly of the anion transport domain of human red cell band 3 (AE1) from multiple and non-complementary fragments. *FEBS Letts.* 433:223-227.

Grygorczyk R., J.A. Tabcharani, J.W. Hanrahan. 1996. CFTR channels expressed in CHO cells do not have detectable ATP conductance. *J. Membr. Biol.* 151:139-48.

Guggino, W.B. 1999. Cystic fibrosis and the salt controversy. *Cell.* 96:607-610.

Gunderson, K.L., and Kopito, R.R., 1994. Effects of pyrophosphate and nucleotide analogs suggest a role for ATP hydrolysis in cystic fibrosis transmembrane conductance regulator channel gating. *J. Biol. Chem.* 269:19349-19353.

Gunderson, K.L., and Kopito, R.R., 1995. Conformational states of CFTR associated with channel gating: The role of ATP binding and hydrolysis. *Cell.* 82:231-239.

Haardt, M., M. Benharouga, D. Lechardeur, N. Kartner, and G.L. Lukacs. 1999. C-terminal truncations destabilize the cystic fibrosis transmembrane conductance regulator without impairing its biogenesis. *J. Biol. Chem.* 274:21873-21877.

Hall., R.A., R.T. Premont, C.-W. Chow, J.T. Blitzer, J.A. Pitcher, A. Claing, R.H. Stoffel, L.S. Barak, S. Shenolikar, E.J. Weinman, S. Grinstein, and R.J. Lefkowitz. The β_2-adrenergic receptor interacts with the Na^+/H^+-exchanger regulatory factor to control Na^+/H^+ exchange. 1998. *Nature.* 392:626-630.

Hallows, K.R., V. Raghuram, J. Tazelaar, L.A. Witters, B.E. Kemp, and J.K. Foskett. 1999. AMP-activated protein kinase, a novel interactor with the C-terminal tail of CFTR. *Pediatr. Pulmonol.* Suppl. 19:166.

Hartman, J., Z. Huang, T.A. Rado, S. Peng, T. Jilling, D.D. Muccio, and E.J. Sorscher. 1992. Recombinant synthesis, purification, and nucleotide binding characteristics of the

first nucleotide binding domain of the cystic fibrosis gene product. *J. Biol. Chem.* 267:6455-6458.

Heginbotham L., T. Abramson, and R. MacKinnon. 1992. A functional connection between the pores of distantly related ion channels as revealed by mutant K^+ channels. *Science.* 258:1152-5.

Higgins, C.F. 1992. ABC transporters: from microorganisms to man. *Annu. Rev. Cell Biol.* 8:67-113.

Honkanen, R.E., J.Zwiller, R.E. Moore, S. Dailty, B.S. Khatra, M. Dukelow, and A.L. Boynton. 1990. Characterization of microcystin-LR, a potent inhibitor of type 1 and type 2a protein phosphatases. *J. Biol. Chem.* 265:19401-19404.

Horn, R., and K. Lange. 1983. Estimating kinetic constants from single channel data. *Biophys. J.* 43:207-223.

Huang, P., K. Trotter, R.C. Boucher, S.L. Milgram, and M.J. Stutts. 1998. Protein kinase A activity closely associated with CFTR channels in excised patches. *Pediatr. Pulmonol.* Suppl. 17:208.

Hung, L.-W., I.X. Wang, K. Nikaido, P.-Q. Liu, G.F. Ames, and S.-H. Kim. 1998. Crystal structure of the ATP-binding subunit of an ABC transporter. *Nature* 396:703-707.

Hwang, T.C., M. Horie, and D.C. Gadsby. 1993. Functionally distinct phospho-forms underlie incremental activation of protein kinase-regulated Cl^- conductance in mammalian heart. *J. Gen. Physiol.* 101:629-50.

Hwang, T.C., G. Nagel, A.C. Nairn, and D.C. Gadsby. 1994. Regulation of the gating of cystic fibrosis transmembrane conductance regulator Cl channels by phosphorylation and ATP hydrolysis. *Proc. Natl. Acad. Sci. USA.* 91:4698-4702.

Ishihara, H., and M.J. Welsh. 1997. Block by MOPS reveals a conformational change in the CFTR pore produced by ATP hydrolysis. *Am. J. Physiol.* 273:C1278-1289.

Jackson, M.B., B.S. Wong, C.E. Morris, H. Lecar, and C.N. Christian. 1983. Successive openings of the same acetylcholine receptor channel are correlated in open time. *Biophys. J.* 42:109-114.

Jackson, M. B. 1985. Stochastic behaviour of a many channel membrane system. *Biophys. J.* 47:129-137.

Jia, Y., C.J. Mathews, and J.W. Hanrahan. 1997. Phosphorylation by protein kinase C is required for acute activation of cystic fibrosis transmembrane conductance regulator by protein kinase A. *J. Biol. Chem.* 272:4978-4984.

Jones, P.M., and A.M. George. 1999. Subunit interactions in ABC transporters: towards a functional architecture. *FEMS Microbiol. Letts.* 179:187-202.

Kaczmarek, L.K., K.R. Jennings, F. Strumwasser, A.C. Nairn, U. Walter, F.D. Wilson, and P. Greengard. 1980. Microinjection of catalytic subunit of cyclic AMP-dependent protein kinase enhances calcium action potentials of bag cell neurons in cell culture. *Proc. Natl. Acad. Sci. U.S.A.* 77:7487-7491.

Kartner, N., J.W. Hanrahan, T.J. Jensen, A.L. Naismith, S. Sun, C.A. Ackerley, E.F. Reyes, L.-C. Tsui, J.M. Rommens, C.E. Bear, and J.R. Riordan. 1991. Expression of the cystic fibrosis gene in non-epithelial invertebrate cells produces a regulated anion conductance. *Cell.* 64:681-691.

Ko, Y.H., M. Delannoy, and P.L. Pedersen. 1997. Cystic fibrosis transmembrane conductance regulator: the first nucleotide binding fold targets the membrane with retention of its ATP binding function. *Biochem.* 36:5053-5064.

Ko, Y.H., and P.L. Pedersen. 1995. The first nucleotide binding fold of the cystic fibrosis transmembrane conductance regulator can function as an active ATPase. *J. Biol. Chem.* 270:22093-22096.

Li, C., M. Ramjeesingh, W. Wang, E. Garami, M. Hewryk, D. Lee, J.M. Rommens, K. Galley, and C.E. Bear. 1996. ATPase activity of the cystic fibrosis transmembrane conductance regulator. *J. Biol. Chem.* 271:28463-28468.

Liman, E.R., J. Tytgat, and P. Hess. 1992. Subunit stoichiometry of a mammalian K^+ channel determined by construction of multimeric cDNAs. *Neuron* 9:861-871.

Loo, T.W., and D.M. Clarke. 1994. Reconstitution of drug-stimulated ATPase activity following co-expression of each half of human P-glycoprotein as separate polypeptides. *J. Biol. Chem.* 269:7750-7755.

Loo, T.W., and D.M. Clarke. 1995. Rapid purification of human P-glycoprotein mutants expressed transiently in HEK 293 cells by nickel-chelate chromatography and characterization of their drug-stimulated ATPase activities. *J. Biol. Chem.* 270:21449-21452.

Luo, J., M.D. Pato, J.R. Riordan, and J.W. Hanrahan. 1998. Differential regulation of single CFTR channels by PP2C, PP2A, and other phosphatases. *Am. J. Physiol.* C1397-C1410.

Ma, J., J.E. Tasch, T. Tao, J. Zhao, J. Xie, M.L. Drumm, and P.B. Davis. 1996. Phosphorylation-dependent block of cystic fibrosis transmembrane conductance regulator chloride channel by exogenous R domain peptide. *J. Biol. Chem.* 271:7351-7356.

Ma, J., J. Zhao, M.L. Drumm, J. Xie, and P.B. Davis. 1997. Function of the R domain in the cystic fibrosis transmembrane conductance regulator chloride channel. *J. Biol. Chem.* 272:28133-28141.

MacKinnon, R. 1995. Pore loops: An emerging theme in ion channel structure. *Neuron.* 14:889-892.

Magleby, K.L., and B.S. Pallotta, 1983. Burst kinetics of single calcium-activated potassium channels in cultured rat muscle. *J. Physiol.* 344:605-623.

Magleby, K. L., and L. Song. 1992. Dependency plots suggest the kinetic structure of ion channels. *Proc. R. Soc. Lond.* B 249:133-142.

Mansoura, M.K., S.S. Smith, A.D. Choi, N.W. Richards, T.V. Strong, M.L. Drumm, F.S. Collins, and D.C. Dawson. 1998. Cystic fibrosis transmembrane conductance regulator (CFTR) anion binding as a probe of the pore. *Biophys. J.* 74:1320-1332.

Marshall, J., S. Fang, L.S. Ostedgaard, C.R. O'Riordan, D. Ferrara, J.F. Amara, H. IV. Hoppe, R.K. Scheule, M.J. Welsh, A.E. Smith, and S.H. Cheng. 1994. Stoichiometry of recombinant cystic fibrosis transmembrane conductance regulator in epithelial cells and its functional reconstitution into cells in vitro. *J. Biol. Chem.* 269:2987-2995.

Mathews, C.J., J.A. Tabcharani, X.-B. Chang, T.J. Jensen, J.R. Riordan, and J.W. Hanrahan. 1998a. Dibasic protein kinase A sites regulate bursting rate and nucleotide sensitivity of the cystic fibrosis transmembrane conductance regulator chloride channel. *J. Physiol.* 508:365-377.

Mathews, C.J., J.A. Tabcharani, and J.W. Hanrahan. 1998b. The CFTR chloride channel: Nucleotide interactions and temperature-dependent gating. *J. Membr. Biol.* 163:55-66.

McDonough, S., N. Davidson, H.A. Lester, N.A. McCarty. 1994. Novel pore-lining residues in CFTR that govern permeation and open-channel block. *Neuron.* 13:623-634.

Mourez, M., M. Hofnung, and E. Dassa. 1997. Subunit interactions in ABC transporters: a conserved sequence in hydrophobic membrane proteins of periplasmic permeases defines an important site of interaction with the ATPase subunits. 1997. *EMBO J.*, 16:3066-3077.

Moyer, B.D., J. Loffing, E.M. Schwiebert, D. Loffing-Cueni, P.A. Halpin, K.H. Karlson, I.I. Ismailov, W.B. Guggino, G.M. Langford, and B.A. Stanton. 1998. Membrane trafficking of the cystic fibrosis gene product, cystic fibrosis transmembrane conductance regulator, tagged with green fluorescent protein in madin-darby canine kidney cells. *J. Biol. Chem.* 273:21759-21768.

Moyer B.D., J. Denton, K.H. Karlson, D. Reynolds, S. Wang, J.E. Mickle, M. Milewski, G.R. Cutting, W.B. Guggino, M. Li, B.A. Stanton. 1999. A PDZ-interacting domain in CFTR is an apical membrane polarization signal. *J. Clin. Invest.* 104:1353-61.

Müller, M., É. Bakos, E. Welker, A, Váradi, U.A. Germann, M.M. Gottesman, B.S. Morse, I.B. Roninson, and B. Sarkadi. 1996. Altered drug-stimulated ATPase activity in mutants of the human multidrug resistance protein. *J. Biol. Chem.* 271:1877-1883.

Nagel, G., T.C. Hwang, K.L. Nastiuk, A.C. Nairn, and D.C. Gadsby. 1992. The protein kinase A-regulated cardiac Cl^- channel resembles the cystic fibrosis transmembrane conductance regulator. *Nature.* 360:81-84.

Naren, A.P., M.W. Quick, J.F. Collawn, D.J. Nelson, and K.L. Kirk. 1998. Syntaxin 1A inhibits CFTR chloride channels by means of domain-specific protein-protein interactions. *Proc. Natl. Acad. Sci. U.S.A.* 95:10972-10977.

Naren, A.P., E. Cormet-Boyaka, J. Fu, M. Villain, J.E. Blalock, M.W. Quick, and K.L. Kirk. 1999. CFTR chloride channel regulation by an interdomain interaction. *Science* 286:544-548.

Neville, D.C.A., C.R. Rozanas, E.M. Price, D.B. Gruis, A.S. Verkman, and R.R. Townsend. 1997. Evidence for phosphorylation of serine 753 in CFTR using a novel metal-ion affinity resin and matrix-assisted laser desorption mass spectrmetry. *Protein Science* 6:2436-2445.

Ng I.S., R. Pace, M.V. Richard, K. Kobayashi, B. Kerem, L.C. Tsui, and A.L. Beaudet. 1991. Methods for analysis of multiple cystic fibrosis mutations. *Hum. Gen.* 87:613-7.

Ostedgaard, L.S., D.P. Rich, L.G. DeBerg, and M.J. Welsh. 1997. Association of domains within the cystic fibrosis transmembrane conductance regulator. *Biochem.* 36:1287-1294.

Picciotto, M.R., J.A. Cohn, G. Bertuzzi, P. Greengard, and A.C. Nairn. 1992. Phosphorylation of the cystic fibrosis transmembrane conductance regulator. *J. Biol. Chem.* 267:12742-12752.

Qin, F., A. Auerbach, and F. Sachs. 1996. Estimating single-channel kinetic parameters from idealized patch-clamp data containing missed events. *Biophys. J.* 70:264-280.

Qin, F., A. Auerbach, and F. Sachs. 1997. Maximum likelihood estimation of aggregated Markov processes. *Proc. R. Soc. Lond.* B 264:375-383.

Quinton, P.M., 1983. Chloride impermeability in cystic fibrosis. *Nature.* 301:421-422.

Ramjeesingh M., C. Li, E. Garami, L.-J. Huan, K. Galley, Y. Wang, and C.E. Bear. 1999. Walker mutations reveal loose relationship between catalytic and channel-gating

activities of purified CFTR (cystic fibrosis transmembrane conductance regulator). *Biochem.* 38:1463-1468.

Randak, C., P. Neth, E.A. Auerswald, I. Assfalg-Machleidt, A.A. Roscher, H.B. Hadorn, and W. Machleidt. 1996. A recombinant polypeptide model of the second predicted nucleotide binding fold of the cystic fibrosis transmembrane conductance regulator is a GTP-binding protein. *FEBS Lett.* 398:97-100.

Randak, C., P. Neth, E.A. Auerswald, C. Eckerskorn, I. Assfalg-Machleidt, and W. Machleidt. 1997. A recombinant polypeptide model of the second nucleotide-binding fold of the cystic fibrosis transmembrane conductance regulator functions as an active ATPase, GTPase and adenylate kinase. *FEBS Lett.* 410:180-186.

Rich, D.P., R.J. Gregory, M.P. Anderson, P. Manavalan, A.E. Smith, and M.J. Welsh. 1991. Effect of deleting the R domain on CFTR-generated chloride channels. *Science.* 253:205-207.

Rich, D.P., H.A. Berger, S.H. Cheng, S.M. Travis, M. Saxena, A.E. Smith, and M.J. Welsh. 1993. Regulation of the cystic fibrosis transmembrane conductance regulator Cl^- channel by negative charge in the R domain. *J. Biol. Chem.* 268:20259-20267.

Riordan, J.R., J.M. Rommens, B.S. Kerem, N. Alon, R. Rozmahel, Z. Grzelczak, J. Zielinski, S. Lok, N. Plavsic, J.L. Chou, M.L. Drumm, M.C. Ianuzzi, F.S. Collins, and L.C. Tsui. 1989. Identification of the cystic fibrosis gene: cloning and characterization of complementary DNA. *Science.* 245:1066-1073.

Rosenberg, M.F., R. Callaghan, R.C. Ford, and C.F. Higgins. 1997. Structure of the Multidrug Resistance P-glycoprotein to 2.5nm Resolution Determined by Electron Microscopy and Image Analysis. *J. Biol. Chem.* 272:10685-10694.

Rothberg, B. S., R. A. Bello, and K. L. Magleby. 1997. Two-dimensional components and hidden dependencies provide insight into ion channel gating mechanisms. *Biophys. J.* 72:2524-2544.

Roux, B., and R. Sauvé. 1985. A general solution for the time interval omission problem applied to single channel analysis. *Biophys. J.* 48:149-158.

Schwiebert, E.M., M.E. Egan, T.H. Hwang, S.B. Fulmer, S.S. Allen, G.R. Cutting, and W.B. Guggino. 1995. CFTR regulates outwardly rectifying chloride channels through an autocrine mechanism involving ATP. *Cell.* 81:1063-1073.

Seibert, F.S., J.A. Tabcharani, X.-B. Chang, A.M. Dulhanty, C. Mathews, J.W. Hanrahan, and J.R. Riordan. 1995. cAMP-dependent protein kinase-mediated phosphorylation of cystic fibrosis transmembrane conductance regulator residue Ser-753 and its role in channel activation. *J. Biol. Chem.* 270:2158-2162.

Seibert, F.S., X.-B. Chang, A.A. Aleksandrov, D.M. Clarke, J.W. Hanrahan, and J.R. Riordan. 1999. Influence of phosphorylation by protein kinase A on CFTR at the cell surface and endoplasmic reticulum. *Biochim. Biophys. Acta.* 1461:275-283.

Senior, A.E., and D.C. Gadsby. 1997. ATP hydrolysis cycle and mechanism in P-glycoprotein and CFTR. *Semin. Cancer Biol.* 8:143-150.

Sheppard, D.N., L.S. Ostedgaard, D.P. Rich, and M.J. Welsh. 1994. The amino-terminal portion of CFTR forms a regulated Cl^- channel. *Cell.* 76:1091-1098.

Sheppard, D.N., and M.J. Welsh. 1999. Structure and function of the CFTR chloride channel. *Physiol. Revs.* 79:S23-45.

Short, D.B., K.W. Trotter, D. Reczek, S.M. Kreda, A. Bretscher, R.C. Boucher, M.J. Stutts, and S.L. Milgram. 1998. An apical PDZ protein anchors the cystic fibrosis

transmembrane conductance regulator to the cytoskeleton. *J. Biol. Chem.* 273:19797-19801.

Shyamala, V., V. Baichwal, E. Beall, and G.F. Ames. 1991. Structure-function analysis of the histidine permease and comparison with cystic fibrosis mutations. *J. Biol. Chem.* 266:18714-18719.

Sigworth, F. J., and S. M. Sine. 1987. Data transformations for improved display and fitting of single-channel dwell-time histograms. *Biophys. J.* 52:1047-1054.

Smit, L.S., D.J. Wilkinson, M.K. Mansoura, F.S. Collins, and D.C. Dawson. 1993. Functional roles of the nucleotide-binding folds in the activation of the cystic fibrosis transmembrane conductance regulator. *Proc. Natl. Acad. Sci. USA* 90:9963-9967.

Stutts M.J., C.M. Canessa, J.C. Olsen, M. Hamrick, J.A. Cohn, B.C. Rossier, and R.C. Boucher. 1995. CFTR as a cAMP-dependent regulator of sodium channels. *Science.* 269:847-50.

Stutts, M.J., B.C. Rossier, and R.C. Boucher. 1997. Cystic fibrosis transmembrane conductance regulator inverts protein kinase A-mediated regulation of epithelial sodium channel single channel kinetics. *J. Biol. Chem.* 272:14037-14040.

Stühmer, W., F. Conti, H. Suzuki, X. Wang, M. Noda, N. Yahagi, H. Kubo, and S. Numa. 1989. Structural parts involved in activation and inactivation of the sodium channel. Nature 339: 597-603.

Sugita, M., Y. Yue, and J.K. Foskett. 1998. CFTR Cl^- channel and CFTR-associated ATP channel: distinct pores regulated by common gates. *EMBO J.* 17:898-908.

Sun, F., M.J. Hug, C.H. Yun, N.A. Bradbury, and R.A. Frizzell. 1999. The PDZ domain-containing protein, E3KARP couples ezrin to cystic fibrosis transmembrane conductance regulator (CFTR). *Pediatr. Pulmonol.* Suppl. 19:165.

Tabcharani, J.A., X.-B. Chang, J.R. Riordan, and J.W. Hanrahan. 1991. Phosphorylation-regulated Cl^- channel in CHO cells stably expressing the cystic fibrosis gene. *Nature.* 352:628-631.

Tabcharani, J.A., J.M. Rommens, Y.-X. Hou, X.-B. Chang, L.C. Tsui, J.R. Riordan, and J.W. Hanrahan. 1993. Multi-ion pore behaviour in the CFTR chloride channel. *Nature.* 366:79-82.

Tabcharani J.A., Linsdell, P., and J.W. Hanrahan. 1997. Halide permeation in wild-type and mutant cystic fibrosis transmembrane conductance regulator chloride channels. *J. Gen. Physiol.* 110:341-354.

Townsend, R.R., P.H. Lipniunas, B.M. Tulk, and A.S. Verkman. 1996. Identification of protein kinase A phosphorylation sites on NBD1 and R domains of CFTR using electrospray mass spectrometry with selective phosphate ion monitoring. *Protein Science.* 5:1865-1873.

Travis, S.M., H.A. Berger, and M.J. Welsh. 1997. Protein phosphatase 2C dephosphorylates and inactivates cystic fibrosis transmembrane conductance regulator. *Proc. Natl. Acad. Sci. U.S.A.* 94:11055-11060.

Venglarik, C.J., B.D. Schultz, R.A. Frizzell, and R.J. Bridges. 1994. ATP alters current fluctuations of cystic fibrosis transmembrane conductance regulator: Evidence for a three-state activation mechanism. *J. Gen. Physiol.* 104:123-146.

Vergani, P., L. Csanády, C. Basso, R. Sánchez, A.C. Nairn, and D.C. Gadsby. 2000. Mutations near the predicted catalytic site of NBD1 affect CFTR Cl^- channel function surprisingly little. *Biophys. J.* 78:264A.

Walker, J.E., M. Saraste, M.J. Runswick, and N.J. Gay. 1982. Distantly related sequences in the α- and ß- subunits of ATP synthase, myosin, kinases and other ATP-requiring enzymes and a common nucleotide binding fold. *EMBO J.* 8:945-951, 1982.

Weinreich, F., J.R. Riordan, and G. Nagel. 1999. Dual effects of ADP and adenylylimidodiphosphate on CFTR channel kinetics show binding to two different nucleotide binding sites. *J. Gen. Physiol.* 114(1):55-70.

Wilkinson, D.J., M.K. Mansoura, P.Y. Watson, L.S. Smit, F.S. Collins, and D.C. Dawson. 1996. CFTR: The nucleotide binding folds regulate the accessibility and stability of the active state. *J. Gen. Physiol.* 107:103-119.

Winter, M.C., D.N. Sheppard, M.R. Carson, and M.J. Welsh. 1994. Effect of ATP concentration on CFTR Cl^- channels: A kinetic analysis of channel regulation. *Biophys. J.* 66:1398-1403.

Winter, M.C., and M.J. Welsh. 1997. Stimulation of CFTR activity by its phosphorylated R domain. *Nature.* 389:294-296.

Yang Y. D.C. Devor, J.F. Engelhard, S.A. Ernst, T.V. Strong, F.S. Collins, J.A. Cohn, R.A. Frizzell, and J.M. Wilson. 1993. Molecular basis of defective anion transport in L cells expressing recombinant forms of CFTR. *Hum. Mol. Gen.* 2:1253-61.

Yike, I., J. Ye, Y. Zhang, P. Manavalan, T.A. Gerken, and D.G. Dearborn. 1996. A recombinant peptide model of the first nucleotide-binding fold of the cystic fibrosis transmembrane conductance regulator: comparison of wild-type and delta F508 mutant forms. *Protein Sci.* 5:89-97.

Yount, R.G. 1975. ATP Analogs. *Adv. Enzymol.* 43:1-565.

Yun, C.H.C., S. Oh, M. Zizak, D. Steplock, S. Tsao, C.-M. Tse, E.J. Weinman, and M. Donowitz. 1997. cAMP-mediated inhibition of the epithelial brush border Na^+/H^+ exchanger, NHE3, requires an associated regulatory protein. *Proc. Natl. Acad. Sci. U.S.A.* 94:3010-3015.

Zeltwanger, S., F. Wang, G.T. Wang, K.D. Willis, and T.C. Hwang. 1999. Gating of cystic fibrosis transmembrane conductance regulator chloride channels by adenosine triphosphate hydrolysis. Quantitative analysis of a cyclic gating scheme. *J. Gen. Physiol.* 113:541-554.

Zerhusen, B., J. Zhao, J. Xie, P.B. Davis, and J. Ma. 1999. A single conduction pore for chloride ions formed by two cystic fibrosis transmembrane conductance regulator molecules. *J. Biol. Chem.* 274:7627-7630.

Zhu, T., D. Dahan, A. Evangelidis, S. Zheng, J. Luo, and J.W. Hanrahan. 1999. Association of cystic fibrosis transmembrane conductance regulator and protein phosphatase 2C. *J. Biol. Chem.* 274:29102-29107.